



HAL
open science

Dynamics of early stages of cell adhesion on fluid substrates

Oleg Mikhajlov

► **To cite this version:**

Oleg Mikhajlov. Dynamics of early stages of cell adhesion on fluid substrates. Biological Physics [physics.bio-ph]. PSL Université, 2021. English. NNT: . tel-04057091

HAL Id: tel-04057091

<https://hal.science/tel-04057091>

Submitted on 3 Apr 2023

HAL is a multi-disciplinary open access archive for the deposit and dissemination of scientific research documents, whether they are published or not. The documents may come from teaching and research institutions in France or abroad, or from public or private research centers.

L'archive ouverte pluridisciplinaire **HAL**, est destinée au dépôt et à la diffusion de documents scientifiques de niveau recherche, publiés ou non, émanant des établissements d'enseignement et de recherche français ou étrangers, des laboratoires publics ou privés.

Copyright



PSL Université

Ecole doctorale Physique en Ile-de-France

Laboratoire Physico Chimie Curie — Institut Curie

Dynamics of early stages of cell adhesion on fluid substrates

Par Oleg Mikhajlov

Thèse de doctorat de Physique

Dirigée par Patricia Bassereau et Guy Tran van Nhieu

Présentée et soutenue publiquement le 11 mars 2021

Devant un jury composé de :

Françoise	Brochard	Professeure émérite	Presidente du jury
Johanna	Ivaska	Professeure	Rapportrice
Jay	Groves	Professeur	Rapporteur
René-Marc	Mège	Directeur de recherche	Examineur
Patricia	Bassereau	Directrice de recherche	Directeur de thèse
Guy	Tran van Nhieu	Directeur de recherche	Co-directeur de thèse

Abbreviations


- **AFM**: atomic force microscopy.
- **APC**: antigen-presenting cell.
- **AU**: arbitrary unit.
- **AZ**: adhesion zone.
- **DDM**: n-dodecyl β -D-maltoside.
- **DHPE**: 1,2-dihexadecanoyl-sn-glycero-3-phosphoethanolamine.
- **DGS-NTA**: 1,2-dioleoyl-sn-glycero-3-[(N-(5-amino-1-carboxypentyl)iminodiacetic acid)succinyl].
- **DMEM**: Dulbecco's Modified Eagle's Medium.
- **DOPC**: 1,2-dioleoyl-sn-glycero-3-phosphocholine.
- **DOPE**: 1,2-di-(9Z-octadecenoyl)-sn-glycero-3-phosphoethanolamine.
- **DPPC**: 1,2-dipalmitoyl-sn-glycero-3-phosphocholine.
- **ECM**: extracellular matrix.
- **EDTA**: ethylenediaminetetraacetic acid.
- **EGFP**: enhanced green fluorescent protein.
- **EMT**: epithelial-to-mesenchymal transition.
- **EtOH**: ethanol.
- **FA**: focal adhesion.
- **FACS**: Fluorescence-activated Cell Sorting.

- **FN:** fibronectin.
- **FRAP:** Fluorescence Recovery After Photobleaching.
- **FRET:** Fluorescence Resonance Energy Transfer.
- **FWHM:** full width at half maximum.
- **HEPES:** 4-(2-hydroxyethyl)-1-piperazineethanesulfonic acid.
- **I-CAM1:** Intercellular Adhesion Molecule 1.
- **IPTG:** isopropyl β -D-1-thiogalactopyranoside.
- **ITO:** indium tin oxide.
- **IS:** immunological synapse.
- **KO:** knockout.
- **LFA-1:** Lymphocyte function-associated antigen 1.
- **MBP:** maltose-binding protein.
- **MEF:** mouse embryonic fibroblast.
- **MFM:** molecular force microscopy.
- **MHC:** major histocompatibility complex.
- **Mn:** manganese.
- **NA:** nascent adhesion.
- **RGD:** tripeptide Arg-Gly-Asp.
- **SD:** standard deviation.
- **SEM:** standard error of the mean.
- **SLB:** supported lipid bilayer.
- **TCR:** T-cell receptor.
- **TEV protease:** Tobacco Etch Virus protease.
- **PCR:** Polymerase chain reaction.

- **PFA**: paraformaldehyde.
- **PM**: plasma membrane.
- **PSF**: point spread function.
- **SDS-PAGE**: sodium dodecyl sulphate–polyacrylamide gel electrophoresis.
- **SE**: succinimidyl ester.
- **SUV**: small unilamellar vesicle.

Contents

Abbreviations	i
List of figures	viii
List of tables	xiv
Preface	1
I Introduction	3
1 Interactions between cells and their environment	5
2 Mechanisms of cell-cell and cell-ECM adhesions	9
2.1 Integrin-mediated cell-ECM adhesions	10
2.2 Integrins and their ligands	11
2.2.1 Adhesiveness regulation	14
2.2.2 Integrin activation	15
2.3 Integrin adhesion plaque-associated proteins	16
2.4 Acto-myosin contraction unit	19
3 Mechanotransduction in cell adhesion	23
3.1 Mechanosensing	23
3.2 Rigidity sensing and reinforcement	24
3.3 Adhesion maturation	27

4	Cell-cell adhesion 	29
4.1	Supported lipid bilayers (SLBs), some mechanical and rheological properties	29
4.2	Cell-SLB hybrid systems	31
4.3	Immunological synapse	32
4.4	RGD-mediated adhesions on fluid substrates	33
4.5	A molecular clutch associated with membrane viscosity	36
II	Materials and Methods	39
5	Sample preparations	41
5.1	Substrate preparation	41
5.1.1	Glass coverslip cleaning	41
5.1.2	Sample chamber assembly	41
5.1.3	SUV preparation	42
5.1.4	SLB preparation	43
5.1.5	SLB functionalization	44
5.1.6	SLB quality control	44
5.2	Invasin production	47
5.2.1	Invasin cloning	47
5.2.2	Invasin expression	48
5.2.3	Invasin purification and labelling	48
5.3	Cell culture preparation	51
5.3.1	Cell line description	51
5.3.2	Cell transfection	53
5.3.3	Cell culture and preparation for the adhesion experiment	53
6	Microscopy imaging	55
6.1	Setup	55
6.1.1	Imaging conditions	55

6.1.2	Optical resolution	56
6.2	Fluorescence calibration	57
6.2.1	Calibration principle	58
6.2.2	Fluorophore preparation	59
6.2.3	Imaging of the fluorophores in bulk and on SLBs	60
7	Image analysis	65
7.1	Cell contour detection	65
7.2	Protein cluster detection	66
7.3	Protein cluster quantification	67
III	Results	69
8	Cell adhesion. Role of substrate properties	71
8.1	Cell spreading	72
8.2	Adhesion index	74
9	Dynamics of adhesion zone maturation on SLBs	83
9.1	Adhesion zone quantification. Role of the nature of ligand	84
9.2	Effect of integrin activation by Mn^{2+}	88
10	Characterization of individual integrin clusters	97
10.1	Integrin amount in individual adhesion clusters	98
10.2	Integrin densities in individual adhesion clusters	100
11	Radial distribution of adhesion proteins in <i>AZ</i>	107
11.1	Adhesion cluster radial distribution on different substrates	109
11.2	Radial distribution of actin in the <i>AZ</i>	114
11.3	Invasin clustering and depletion in the <i>AZ</i>	117
11.4	SLB deformation by pulling membrane tethers	122

12	Localization of other adhesion proteins in integrin clusters	127
12.1	Adhesion proteins' co-clustering	129
12.2	Adhesion protein recruitment as a function of the size of integrin cluster . .	131
12.3	Role of integrin activation by Mn^{2+} on adhesion protein recruitment dy- namics	134
IV	Discussion, Conclusion, Perspectives	137
13	Discussion	139
13.1	Integrin activation and clustering on rigid and fluid substrates	140
13.2	Integrin cluster growth on RGD-coated SLBs	140
13.3	Integrin cluster movement in the <i>AZ</i> on RGD-coated SLBs	142
13.4	Recruitment of integrin adaptor proteins to adhesion clusters	143
13.5	Role of integrin activation by ligands	144
13.6	Membrane deformations	145
13.7	Cluster morphology	146
13.8	Ligand reorganization on the SLB surface	147
14	Conclusion	151
15	Longer-term perspectives	155
	Appendices	159
A	Uncertainty estimation for protein densities and protein numbers	161
B	GUV preparation	163
	Bibliography	165

List of Figures

1.1	A summary of the various cell junctions in a vertebrate epithelial cell . . .	7
1.2	Bacterial infection of a host cell induced by the zipper mechanism	8
2.1	Transmembrane adhesion proteins link the cytoskeleton to extracellular structures	9
2.2	Map of integrin-based adhesion structures as a function of traction force .	11
2.3	Ribbon diagram of the extracellular segment of the $\alpha_V\beta_3$ integrin	12
2.4	Integrin family and their ligands	13
2.5	Comparison of integrin-binding regions of Invasin and fibronectin	14
2.6	Integrin conformational changes associated with affinity regulation	15
2.7	Representative scheme of integrin adhesome	17
2.8	Nanoscale architecture of focal adhesions	17
2.9	Force generation and transmission through the molecular clutch	18
2.10	Force orientation and magnitude at the single integrin level	19
2.11	Force orientation in FAs	20
3.1	Role of substrate geometry in the cellular mechanoreponse during cell adhesion	24
3.2	Generation of periodic interruptions depends on substrate rigidity	25
3.3	Lifetime of slip and catch bonds under load	25
3.4	Mechanisms of rigidity sensing	26
3.5	Local formation of focal contacts in response to an external force	27
3.6	Cell adhesion on rigid and soft substrates	28

4.1	Supported lipid bilayer (SLB)	30
4.2	SLB stiffness in comparison to tissues, hydrogels, and glass substrates	30
4.3	Hybrid live cell–SLB system	31
4.4	Model immunological synapse	32
4.5	TCR/MHC micro-clusters exclude and displace ICAM-1/LFA-1 complexes	33
4.6	Podosome Formation on RGD Membrane	34
4.7	Early adhesion integrin clusters on SLB and glass	34
4.8	Stages of cell adhesion on SLB and glass	35
5.1	Sample chamber	42
5.2	Possible mechanisms of supported bilayer formation	43
5.3	Fluorescent microgram of an Invasin-coated SLB	44
5.4	Measuring the rate of lateral diffusion of molecules on SLB by FRAP	45
5.5	Results of the FRAP of Invasin-coated SLBs	47
5.6	SDS-PAGE gel with protein samples from Invasin expression till MBP cleavage by TEV protease	49
5.7	SDS-PAGE gel with protein samples from MBP cleavage by TEV protease till the purification by size exclusion	50
5.8	Design of an Halo-tagged β_1 integrin	51
5.9	Halo-tagged β_1 integrins translocate to the cell surface and target to FAs	52
5.10	Flow cytometry histogram of β_1 -Halotag fibroblasts binding to RGD	52
6.1	Measurement of the point spread function with fluorescent beads	57
6.2	Illumination inhomogeneity in the field of view of the microscope	60
6.3	Fluorescence calibration curves	62
7.1	Cell contour detection	65
7.2	Histogram-based image segmentation	66
7.3	Detection of Integrin clusters and Invasin holes	67
7.4	Integrin cluster quantification	68

7.5	Radial segmentation of a fluorescence image	68
8.1	Cell shape evolution during adhesion.	73
8.2	Area and shape of adherent cells	74
8.3	Definition of a “trembling” cell	75
8.4	Cell adhesion control	76
8.5	Evolution of cell adhesion on glass and SLB.	77
8.6	Role of Mn^{2+} -mediated integrin activation in cell adhesion on different substrates	79
8.7	Role of Mn^{2+} -mediated integrin pre-activation in non-specific cell adhesion.	80
9.1	Visualization of the <i>AZ</i> of the cell	84
9.2	Quantification of the <i>AZ</i>	85
9.3	Characterization of the clusters in the <i>AZ</i>	86
9.4	Total number of clusters in the <i>AZ</i> and integrin density in them	87
9.5	Effect of integrin activation by Mn^{2+} on the evolution of the <i>AZ</i> ratio	89
9.6	Effect of integrin activation by Mn^{2+} on the total area of integrin clusters in the <i>AZ</i>	90
9.7	Effect of integrin activation by Mn^{2+} on the total number of integrin clus- ters in the <i>AZ</i>	90
9.8	Effect of integrin activation by Mn^{2+} on the average integrin cluster area	91
9.9	Effect of integrin activation by Mn^{2+} on the number of integrins in the <i>AZ</i>	92
9.10	Effect of integrin activation by Mn^{2+} on the integrin density in the <i>AZ</i>	93
9.11	Evolution of adhesion maturation	94
10.1	Number of integrin receptors in adhesion clusters of cells adhering on dif- ferent substrates	99
10.2	Number of integrins per individual adhesion cluster and the effect of inte- grin activation by Mn^{2+}	100
10.3	Relationship between the number of integrins in the clusters and the cluster area	101

10.4	Effect of integrin activation by Mn^{2+} on the averaged integrin density in individual adhesion clusters	102
10.5	Time lapse distributions of the adhesion cluster sizes as a function of integrin density in individual adhesion clusters	103
10.6	Evolution of integrin density distributions	105
11.1	Focal adhesions in cells on rigid substrates	107
11.2	Analysis of the adhesion protein radial distribution in the <i>AZ</i>	108
11.3	Normalized radial distribution of integrin numbers in the <i>AZ</i>	110
11.4	Distribution of the integrin densities in the clusters as a function of their radial localization in the cells, in the different conditions	111
11.5	Cell rings' areas.	112
11.6	Radial distribution of the global integrin densities in the cells in the different conditions	113
11.7	Fluorescence microscopy images of three cells adhering on RGD with <i>AZ</i> of different sizes	115
11.8	Radial distribution of the normalized actin intensity signal	116
11.9	Co-existence of integrin clusters, Invasin clusters and Invasin holes in the <i>AZ</i>	119
11.10	Radial distribution of the proportion of area occupied by Invasin holes	120
11.11	Inter-distances between the integrin clusters and the Invasin holes	121
11.12	Fluorescence image of cells in two focal planes	123
11.13	Fluorescence images of SLB protrusions in orthogonal planes	125
12.1	Cluster detection in the <i>AZ</i> in two fluorescence channels	128
12.2	Adhesion cluster intersection	129
12.3	Number of adhesion proteins in the <i>AZ</i>	130
12.4	Number of adhesion proteins as a function of number of β_1 -integrins in the clusters	132
12.5	Number of talin and vinculin proteins as a function of number of β_1 -integrins in the clusters	133

12.6	Number of paxillin proteins in adhesion clusters in cells treated with(out) Mn^{2+}	134
12.7	Number of paxillin proteins as a function of number of β_1 -integrins in the clusters. Role of Mn^{2+}	135
13.1	Length-dependent protein exclusion at the contact of two membranes . . .	148
15.1	Adhesion between a cell and a GUV	156
B.1	Sketch of the chamber for the vesicle preparation	163
B.2	GUVs added to cells in culture	164

List of Tables

2.1	Anchoring junctions	10
2.2	Integrin-ligand affinities (K_d)	13
6.1	Fluorescence channels	56
6.2	Optical resolution for different fluorophores	56
6.3	Imaging conditions for fluorescence calibrations	60
6.4	Fluorescence calibration coefficients	62
12.1	Ratio between the number of adhesion proteins and integrins in clusters (from linear fits in the Figure 12.4	132
A.1	Fractional uncertainties due to calibration	162

Preface

Adhesion is a ubiquitous process for virtually all cells from those that form together tissues and organs of multicellular organisms to single immune cells that migrate adhering to the extracellular matrix in search of pathogenic cells or tiny bacteria that adhere to their host cell's membrane in order to infect them. Cells adhere to substrates or other cells not only to maintain physical cohesion, but also to receive information on their microenvironment. Adhesion is thus a platform for communication (chemical and mechanical) between a cell and a substrate or another cell.

In this work, we are interested in integrin-mediated adhesion. Integrins and multiple proteins that are associated with them (integrin adhesome) are thoroughly described in the Introduction (Part I) of this thesis. The adhesion proteins are the main players of this mechano-chemical communication. During cell adhesion they assemble in clusters and in a process called mechanotransduction convert mechanical stimuli into biochemical signals and transmit them inside the cell. In this part we also describe the principles of mechanotransduction on rigid substrates where cells manage to develop mature adhesion structures, namely focal adhesions. Although cell adhesion on rigid substrates is very well studied, much about adhesion on soft fluid substrates like membranes remains unknown.

In this project, we have studied the dynamics of early steps of cell adhesion on fluid substrates (supported lipid bilayers, or SLBs). The aim of the project is to understand the formation and evolution of integrin clusters in cells adhering on fluid lipid bilayers functionalized with ligands of different affinities (RGD, Invasin). Ligand affinity to integrins appears to be very important in integrin activation and consequent formation of adhesion clusters. In this study, we have also investigated the role of integrin pre-activation by manganese on cluster evolution during cell adhesion.

We have used a mouse embryonic fibroblast (MEF) cell line in which the endogenous β_1 -integrin subunit was replaced by β_1 -Halotag (gift from David Calderwood, Yale University). We can, thus, label only the β_1 -integrins that are on the cell surface by using

cell non-permeable dyes functionalized with Halotag ligands. We have developed an approach based on fluorescence calibration that allows to quantify the amount of integrins in adhesive structures.

In the Materials and Methods (Part II), we have described our experimental system presenting its main components (cell culture and functionalized SLBs). We have also detailed the main technical aspects of the experiment (sample preparation, test of SLB fluidity by FRAP, fluorescence calibrations on SLB surfaces and microscopy imaging). Finally, we have described our post image processing analysis.

In the chapter 8 of the Results we have compared cell adhesion on rigid and fluid substrates. Next, we have studied the evolution of the cell area containing integrin clusters (adhesion zone, or **AZ**) in the chapter 9. The chapter 10 is devoted to the characterization of individual integrin clusters in the adhesion zone. In the chapter 11 we have mapped the radial distributions of integrin clusters and the actin organization. In this chapter we have also mapped the location of the inhomogeneities of Invasin on the SLB that occurred during cell adhesion and detected the deformations of SLBs coated with Invasin. In the final chapter 12, we have studied the recruitment of the integrin adaptor proteins to adhesion clusters.

Finally, we discuss our findings through the prism of already existing knowledge on adhesions on rigid glass or adhesion on other ligands (Part IV). We also discuss the limitations of our cell-SLB adhesion experiments. As a perspective, we formulate the remaining questions that can be addressed with our cell-SLB hybrid system and a different system based on giant unilamellar vesicle (GUV) that was developed during this thesis is described in the B.

Part I

Introduction

Chapter 1

Interactions between cells and their environment

Adhesion is a ubiquitous phenomenon in the cellular world. Except some circulating cell types, most of the cells in pluricellular organisms, are bound to other cells or are attached to biological fibers of the extracellular matrix (ECM). Adhesion is the main means of interaction between cells and their external environment. Adhesion is involved in many important aspects of cellular life, such as cell migration (Lauffenburger and Horwitz [1996], Yamada and Sixt [2019]), cell differentiation (Khalil et al. [2014]) and at a larger scale, tissue formation and development (Gumbiner [1996]). Perturbation of cell adhesion is an important aspect in cancer cell metastasis (Matsuyoshi et al. [1992]). Each of these cellular processes results from a complex network of biochemical reactions triggered by different means. As we will see later in this introduction, the interactions between cells and their microenvironments can be described in terms of mechanics and molecular biochemistry. Cells interact with a large variety of substrates from micron-size protein fibers of the ECM to other cell membranes that contain many transmembrane proteins and surrounded by a glycocalyx layer (Alberts et al. [2008]). We detail below these different types of interactions.

- **Cells' membranes-membrane adhesion**

Every higher organism is composed of multicellular structures, such as organs and tissues. To keep the integrity of such cell assemblies and maintain proper interactions between them, different types of cell adhesion proteins are employed (Alberts et al. [2008]). These proteins are assembled in multi-protein complexes, which are located at the contacts between the neighboring cells. In vertebrates we can distinguish four different types

of complexes, which serve specific functions in cell-cell interaction and rely on a specific protein composition (cf. Figure 1.1). First ones are desmosomes, strong hyper-adhesive intercellular junctions containing transmembrane proteins from the cadherin super family linked to intermediary filaments. Desmosomes are found in tissues under mechanical stress like epithelia, cardiac muscle tissue or bladder tissue (Delva et al. [2009]). They resist mechanical stress and act as signaling centers in fundamental processes such as cell proliferation, differentiation and morphogenesis (Garrod and Chidgey [2008], Perez et al. [2008]). Second ones are adherens junctions or cadherin-based junctions, containing cadherins that establish homotypic interactions between cells. Cadherins can associate with the actin cytoskeleton and together with desmosomes, determine the strength of intercellular adhesion required for the establishment of the other junctional complexes. Third ones are gap junctions, specialized protein complexes forming channels that directly connect the cytoplasm of two cells, allowing the intercellular transport of various molecules, ions and electrical impulses (Lampe and Lau [2000]). Fourth ones are tight junctions, the occludin protein complexes that function as a diffusion barrier for transmembrane proteins and lipids at the surface of polarized cells. They also seal the neighboring cells together, making the intercellular space impermeable for proteins and other macromolecules (Andersson et al. [2003]). The cell junctions are incredibly complex structures and even a minor genetic alteration of any of its components can lead to serious disorders, as substantial body of research shows (Lai-Cheong et al. [2007]).

- **Cells adhesion on the ECM**

Another common example of cell-exterior interaction is the one between cells and the extracellular matrix (cf. Figure 1.1). The ECM is a three-dimensional network composed of five classes of macromolecules – collagens, elastin, proteoglycans, hyaluronan and adhesive glycoproteins (Alberts et al. [2008]). Cells can produce these molecules in a number of variants (encoded by different genes or produces by alternative splicing). Moreover, depending on the cell type and cellular microenvironment, they can secrete these isoforms in different proportions. Therefore, the ECM exhibits a high variety of molecular composition and vastly different mechanical properties (Pollard et al. [2017]). The ECM provides mechanical support to different cells and tissues (Frantz et al. [2010]), influences embryonic development (Rozario and DeSimone [2010]), plays an important role in cell self-renewal and differentiation (Sheehy and Parker [2011]), regulate and guide cell migration (Moore and Sheetz [2011]). Cell migration can be viewed as a repeated cycle of adhesions, protrusions at the front and retractions at the back (Giannone et al. [2007]). Cells adhere to the ECM to establish stable contact points on which they can pull

propelling themselves forward. These adhesions are based on the molecular interactions between the ECM proteins and cellular receptors. Cells use a variety of receptors, and integrins are the best-characterized ones (Huttenlocher and Horwitz [2011]). They vary their expression profiles to accomplish the required degree and strength of adhesion with the specific ECM. When cell adhesion is impaired, cell migration through connective tissue gets compromised, which leads to the increase of the risk of infections (immune cells cannot properly respond to inflammation stimuli) (Wehrle-Haller and Imhof [2003]).

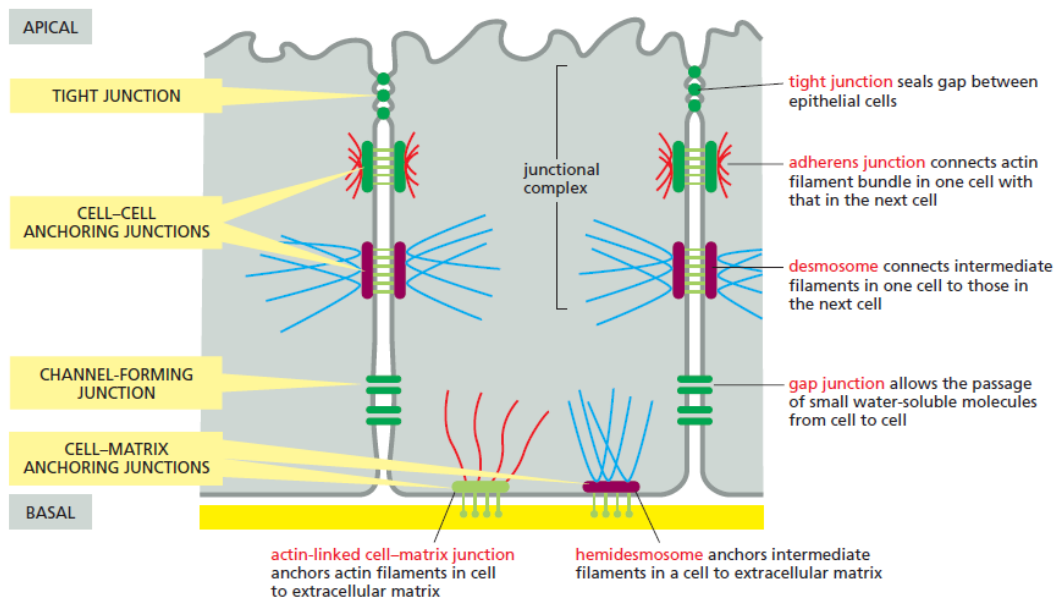


Figure 1.1: A summary of the various cell junctions in a vertebrate epithelial cell. Illustration of the major types of cell-cell and cell-matrix junctions. Cell junctions are classified according to their primary functions. The drawing is based on epithelial cells of the small intestine. Figure taken from Alberts et al. [2008].

- **Cells and bacteria**

We can distinguish another remarkable type of cell-cell interactions, those between host cells and bacteria. In case of infection, pathogens exploit common cell adhesion mechanisms in order to infect host cells. For example, some of them enter mammalian cells in a so-called “zippering” manner (Isberg [1991], Cossart and Sansonetti [2004]). Adhesion proteins, expressed on the bacterial surfaces, bind cell receptors with high affinity: for instance, the Invasin of *Yersinia pseudotuberculosis* binds β_1 -integrins (Isberg and Barnes [2001]), or Internalin A of *Listeria monocytogenes* binds E-cadherin (Mengaud et al. [1996]). The gradual binding of bacterial adhesion proteins to cell receptors results in the tight wrapping of the cell membrane around the bacterial body, which resembles a zipper lock closure (Sansonetti [2002]) (cf. Figure 1.2).

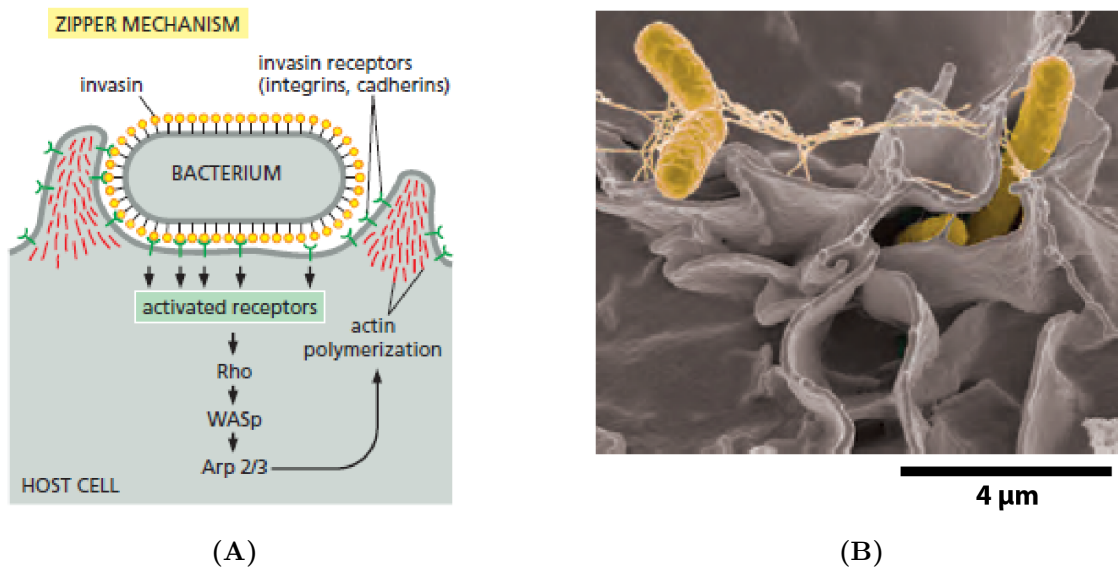


Figure 1.2: Bacterial infection of a host cell induced by the zipper mechanism.

A) In the zipper mechanism, bacteria express an invasion protein Invasin that binds with high affinity to a host-cell receptor, which is often a cell–cell or cell–matrix adhesion protein.

B) A scanning electron micrograph showing a very early stage of *Salmonella enterica* invasion of a host cell. Bacteria (pseudocolored yellow) are shown surrounded by a small membrane ruffle.

Figure taken from Alberts et al. [2008].

Chapter 2

Mechanisms of cell-cell and cell-ECM adhesions

Cell adhesion can be described as a superposition of multiple weak and dynamic receptor-ligand bonds in the mean field of non-specific interaction caused by van der Waals, electrostatic and steric interactions between the cell and the substrate (more in Boal [2012]). From here on we will focus on the specific part of this interaction.

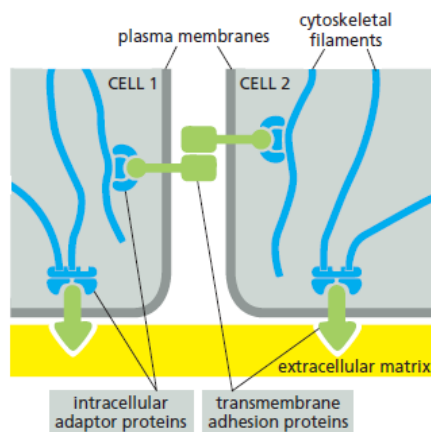


Figure 2.1: Transmembrane adhesion proteins link the cytoskeleton to extracellular structures.


The external linkage is typically mediated by cadherins (cell-cell junctions) or integrins (cell-matrix junctions). The internal linkage to the cytoskeleton is generally indirect, via intracellular adaptor proteins, to be discussed in the section 2.3.

Figure taken from Alberts et al. [2008].

Cells adhere through adhesion proteins (cell receptors) that span the plasma membrane (PM) with the cytosolic end linking to the cytoskeletal filaments and the ectodomain binding to specific molecules (ligands) of the ECM or of the other cells' membranes (cf. Figure 2.1). Two large superfamilies, the cadherins and integrins, are paradigms to these

two kinds of external attachment. Cadherins mediate cell-cell adhesion, whereas integrins mediate adhesions between cells and ECM, and in some cases, they mediate cell-cell rather than cell-ECM adhesions (cf. Table 2.1). In this work, we will focus on the cellular interactions between a cell and the ECM or the neighboring cells, mediated by integrins.

Table 2.1: Anchoring junctions (adapted from Alberts et al. [2008]).

Junction	Transmembrane adhesion protein	Extracellular ligand	Intracellular cytoskeletal attachment
Cell-cell 			
Adherens junction	Classical cadherins	Classical cadherin on neighboring cell	Actin filaments
Desmosome	Nonclassical cadherins (desmoglein, desmocollin)	Desmoglein and desmocollin on neighboring cell	Intermediate filaments
Cell-Matrix			
Actin-linked cell-matrix junction	Integrin	Extracellular matrix proteins	Actin filaments
Hemidesmosome	$\alpha_6\beta_4$ Integrin, type XVII collagen	Extracellular matrix proteins	Intermediate filaments

2.1 Integrin-mediated cell-ECM adhesions

The integrin adhesome is the ensemble of molecules that compose and regulate integrin mediated adhesion sites and forms a complex adhesive platform at the interface between ECM and actin cytoskeleton. This adhesive platform consists of integrin clusters that recruit adaptor proteins connecting them with the actin cytoskeleton. Integrin clustering is important because it increases local concentrations of the proteins in clusters in order to accelerate biochemical reactions in which they take part. Consequently, clustering enhances mechano-biochemical communication signals between cells and substrates. Mechanical load on adhesion clusters can induce their growth in a dynamic manner. In the example of the cell migrating on a rigid surface (cf. Figure 2.2), one can observe a co-existence of different types of adhesion clusters: nascent adhesions at the very edge of the cell, focal adhesions a little further away and fibrillar adhesions in the cell body.

Nascent adhesions (NAs) are small (less than $1 \mu m$ in diameter) dot-like clusters that emerge at the edge of the cell. They dynamically assemble and disassemble within a lifespan of about 1 minute. When connected to the actin cytoskeleton, NAs are stabilized,

move centripetally from the cell edge and grow to larger (up to $10 \mu m^2$) and long-lived (several minutes) focal adhesions (FAs) (Riveline et al. [2001], Vicente-Manzanares et al. [2009]) (cf. Figure 2.2).

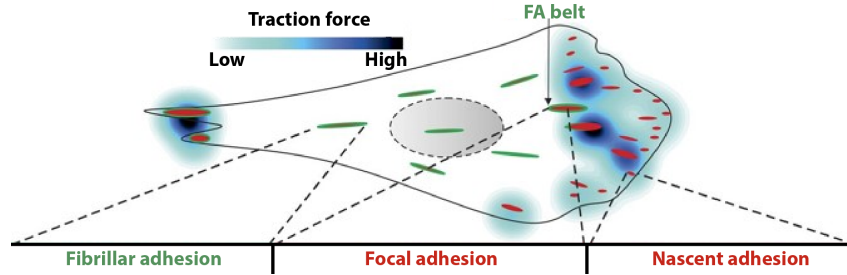




Figure 2.2: Map of integrin-based adhesion structures as a function of traction force. Model of a migrating cell containing three types of integrin-based adhesion structures: nascent adhesions (NAs) at the leading edge of cell protrusions (red, dot-like), focal adhesions (FAs) emerge from mature NAs closer to the cell center (red, elongated) and fibrillar adhesions at the cell center (red and green, elongated). The highest traction force transmission is at the FAs as they are strongly engaged with actin through a "molecular clutch". At NAs and fibrillar adhesions the traction force transmission is low due to the less developed connection to actin in the first case, and decreased connection to actin by the FA belt proteins in the second case. Figure adapted from Sun et al. [2016].

Cells apply physical forces to stabilize NAs, to mature them to FAs and to m  them from the cell edge. These forces are transmitted from the actin cytoskeleton to integrin clusters through cytoskeletal linkers forming a "molecular clutch" (Mitchison and Kirschner [1988], Case and Waterman [2015]). Behind the lamella, the transmission force between integrins and their ligands is enzymatically decreased and FA transform into fibrillar (or central) adhesions (Sun et al. [2016]).

Cells use the molecular clutch as a coupling mechanism between integrins and actin to transduce physical forces to the external environment. The most important molecular players that are involved in force transmission can be split into 3 adhesion units: the **receptor unit** (integrins and ligands), the **cytoskeletal linker unit** (proteins linking receptors to actin cytoskeleton) and the **force generation unit** (actomyosin assemblies). Next, we will describe all the three units and explain the integrin cluster maturation mechanism and how it depends on mechanical properties of the substrate.

2.2 Integrins and their ligands

Integrins are the major metazoan cell adhesion receptors that mediate both adhesion to the extracellular matrix (ECM) and cell-cell adhesion. First desc  ed by Richard Hynes in 1987, the integrins' super-family is among the best-characterized cell receptors (Hynes

[1987]). Integrins are (α , β) heterodimer transmembrane proteins that link the ECM to the cytoskeleton. Each of the subunits has an external (ectodomain) and internal (cytoplasmic domain) (cf. Figure 2.3). The cytoplasmic domain is short (20-50 amino acids), whereas the ectodomain may be between 90 and 1600 amino acid long (Hynes [2002]).

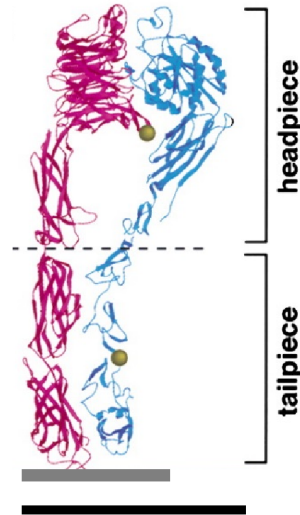


Figure 2.3: Ribbon diagram of the extracellular segment of the $\alpha_V\beta_3$ integrin.

The model of the extended conformation of the extracellular segment of $\alpha_V\beta_3$ integrin (α_V in pink, β_3 in blue) was reconstructed from the crystal structure (PDB: 1JV2) of the bent conformation by breaking the bent form at the junction between the headpiece and tailpiece (dashed line), and moving the headpiece relative to the tailpiece. The approximate position of the cell membrane is indicated by a gray line. Black bar indicates 100 Å.

Figure adapted from Takagi et al. [2002].

Mammalian cells have 24 unique integrin receptors build from 18 alpha and 8 beta subunits. Most integrins are known to bind a wide variety of ligands (of ECM nature, or cell surface adhesion proteins). Moreover, many ligands bind to multiple integrin receptors. This binding promiscuity is explained by the fact that different classes of integrins recognize specific interaction motives that their ligands share (Humphries et al. [2006]) (cf. Figure 2.4). One of them is a tripeptide Arg-Gly-Asp (RGD), a common binding motif among the ECM proteins (fibronectin (FN), vitronectin) and von Willebrand factor. All five α_V -integrins, two β_1 -integrins (α_5 , α_8) and $\alpha_{IIb}\beta_3$ share the ability to recognise ligands containing RGD.

Integrins also interact with non-ECM ligands: ICAM-1 molecules on cell surface mediate cell-cell adhesion (Gothlein et al. [1986]). They are also targeted by a number of bacterial pathogens, to promote adhesion to host cells or invasion, as illustrated by the Invasin protein at the surface of the bacteria *Yersinia pseudotuberculosis* (Hauck et al. [2012], Isberg et al. [1987]). Invasin binds to β_1 -integrins with much higher affinity than

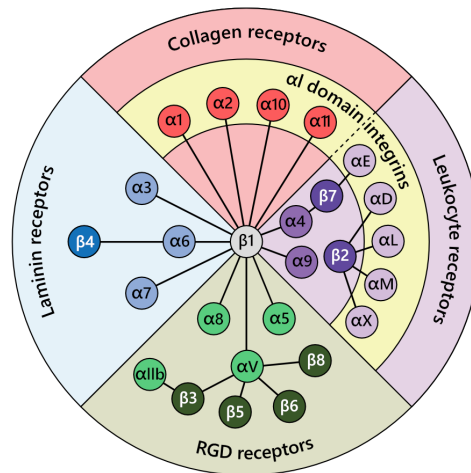


Figure 2.4: Integrin family and their ligands.
 Taken from morphictx.com (time of access February 3, 2021).

does fibronectin, through a mutually exclusive (thus probably the same) binding site confirmed by crystal structure (Hamburger et al. [1999]). Similarities between Invasin and fibronectin structures confirm their common integrin-binding properties (cf. Figure 2.5). Moreover, structural analysis suggests that Invasin has a larger binding surface area with integrins than fibronectin, providing an explanation for the increased integrin-binding affinity of Invasin compared to fibronectin.

The range of the dissociation constants (K_d) between integrins and their ligands is very large (cf. Table 2.2): from as low as several nM for bacterial Invasin to high μM for cell-ECM and cell-cell interactions.

Table 2.2: Integrin-ligand affinities (K_d).

K_d	Protein	Reference
5 nM	Invasin	Van Nhieu and Isberg [1991]
0.7 μM	Fibronectin	Akiyama and Yamada [1985]
1.7 μM	Linear RGD	Pfaff et al. [1994]
1.3 μM	Cyclic RGD	Pfaff et al. [1994]
3 μM	ICAM-1	Carman and Springer [2003]

Bacterial pathogens take advantage of their high affinity for binding to the cell membrane for cell invasion. In contrast, weaker affinity bonds between cells and ECM are needed in cell migration when the dynamics of bond formation and disruption is important.

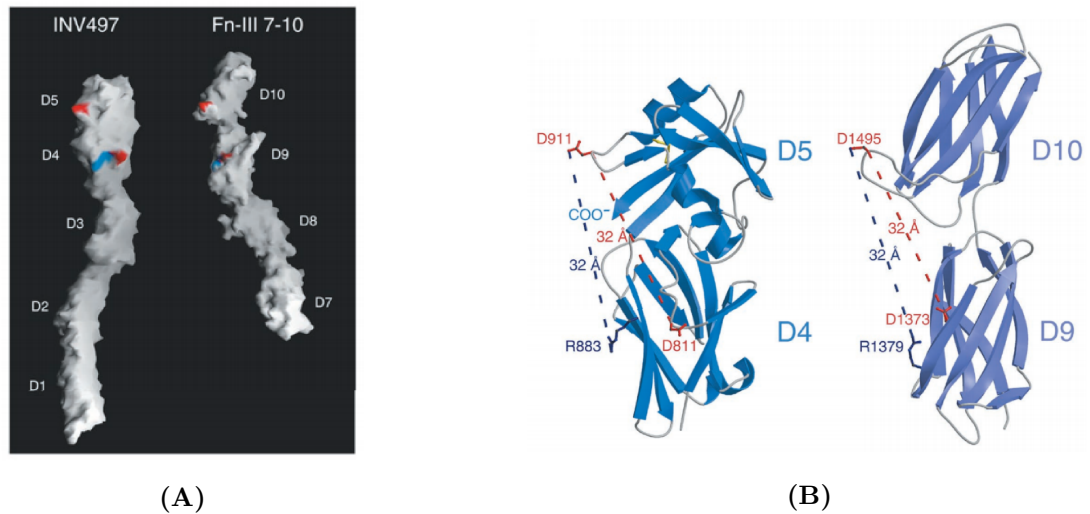


Figure 2.5: Comparison of integrin-binding regions of Invasin and fibronectin.

A) Invasin (Inv497) and fibronectin (Fn-III 7-10) structures. The relative positions of several residues implicated in interactions with integrins are similar [Asp811, Asp911, and Arg883 in Inv497; Asp1373, Asp1495, and Arg1379 in Fn-III 9 and 10; (aspartates are red; arginines are blue)].

B) Ribbon diagrams of D4, D5 domains of Invasin and D9, D10 domains of fibronectin. Invasin contain a rather flat region at the integrin-binding interface (between Asp811 and Asp911). In contrast, the integrin-binding surface of fibronectin contains a cleft resulting from the narrow link between Fn-III 9 and 10.

Figure taken from Hamburger et al. [1999].

2.2.1 Adhesiveness regulation

Cells may regulate the overall strength of adhesiveness (**avidity**) in a robust and dynamic way through the local number of receptor-ligand bonds (**valency**), as well as by regulating the **affinities** between receptors and their ligands. These mechanisms are most likely coupled between each other as there is evidence that integrin activation (increase of integrin affinity due to its conformational change) may stimulate integrin clustering and vice versa (Isenberg et al. [1987], Li et al. [2003]). Integrin valency, or the local densities of the receptors, can be regulated by changing their ability to move passively by diffusion or actively, and by creating local clusters. The amount of integrins on the cell surface is tightly regulated by mechanisms of endocytic trafficking (Bridgewater et al. [2012], de Franceschi et al. [2015]). Integrins on the plasma membrane of the cell constantly undergo exo- and endocytosis. These two processes control integrin turnover and thus play an important role in integrin-mediated cell adhesion. Integrin affinity depends on its molecular conformation: closed (low ligand affinity), intermediate and open (high ligand affinity) (Carman and Springer [2003]) (cf. Figure 2.6). It has been shown that small ligands like RGD peptides can bind to integrins that are not fully activated, whereas

larger ligands like fibronectin cannot (Coller [1986], Juerg H. Beer et al. [1992], Mould et al. [1998]). Fibronectin binds synergistically to two integrin regions, one of which is hidden in a non-open conformation (García et al. [2002]), thus it has a lower affinity to inactive integrins than to active ones. The same is likely true for Invasin given the fact that bacterial pathogens mostly bind to the tips of filopodial protrusions and to the cell cortex where activated integrins are spatially present (Miihkinen et al. [2020], Romero et al. [2011], Romero et al. [2012]). EM studies demonstrated that multiple integrin conformations co-exist (Takagi et al. [2002]) and that their relative ratios depend on integrin activation driven by allosteric modulations at either its cytosolic or extracellular part (Hynes [2002], Calderwood [2004]).

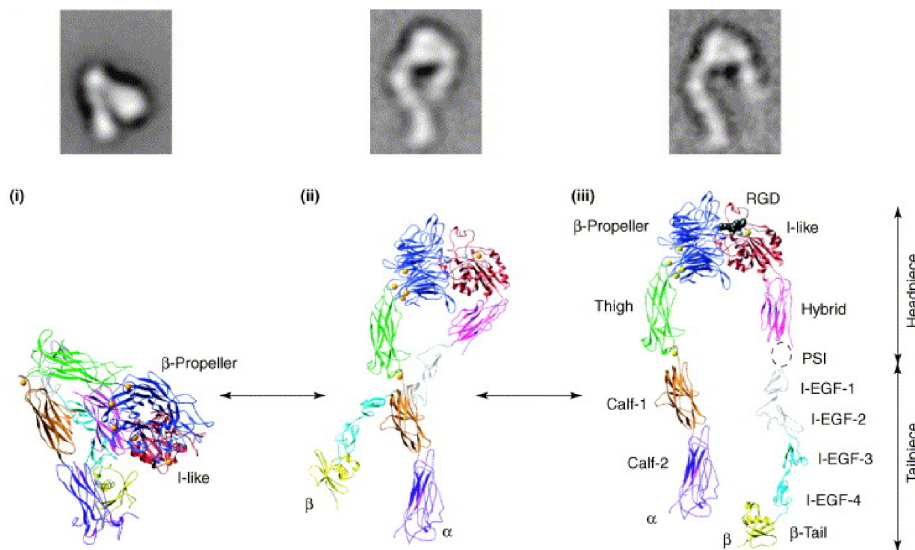


Figure 2.6: Integrin conformational changes associated with affinity regulation. The upper panels show EM averages and the lower panels show ribbon diagrams based on the bent crystal structure or fitting of the latter to the extended EM structures. (i) Bent conformation (low affinity). (ii) Extended conformation with closed headpiece (predicted to be of intermediate affinity). (iii) Extended conformation with open headpiece (high affinity). Figure adapted from Carman and Springer [2003].

2.2.2 Integrin activation

A so-called “**outside-in**” **integrin activation** pathway is induced when a ligand binds to the extracellular integrin domain, extending a closed conformation to a higher ligand-affinity one (cf. Figure 2.6). This striking conformational change of integrin ectodomain induces a separation of the cytosolic tails of the two integrin subunits. This conformational change can occur dependent or independent of ligand binding in a process named **integrin**

priming. Integrins can be primed by Mn^{2+} ions, binding to extracellular integrin domain and through “inside-out” integrin activation (Takagi et al. [2002]).

“Inside-out” integrin activation is mediated through the integrin cytoplasmic domains. Adaptor proteins of the integrin adhesome, talin and kindlin-2, induce the same conformational change as in outside-in signaling by binding to these domains (Calderwood [2004], Montanez et al. [2008]). A number of adaptor proteins either reinforces talin binding (RIAM, kindlin-2) (Klapholz and Brown [2017], Li et al. [2017]) or inhibits it by competitive binding leading to no conformational change (PTP-domain proteins), or by phosphorylation of integrin NPxY motif (Src kinase) (Calderwood [2004]). Integrin activation is tightly regulated and is important in many biological processes like hemostasis, during which the activation of platelet integrin $\alpha_{IIb}\beta_3$ mediates thrombus formation (Shattil et al. [1998]), leukocyte trafficking, during which β_1 and β_2 integrins become activated (Laudanna et al. [2002], Hogg et al. [2002]) and many others including cell migration (Huttenlocher et al. [1996]), also during assembly of an ECM (Pelecsek et al. [1997]) and cell adhesion (Wu et al. [1995]).

2.3 Integrin adhesion plaque-associated proteins

Complex assemblies of proteins become organized around the cytoplasmic tails of activated integrins, producing intracellular signals that regulate cell adhesion. An extensive number of proteins associate with integrin in adhesions, the integrin adhesion plaque proteins, discovered by a combination of bioinformatics (Zaidel-Bar et al. [2007], Zaidel-Bar and Geiger [2010]), immunocytochemistry (Zamir et al. [2008]) and proteomic analysis (Byron et al. [2011], Schiller et al. [2011], Kuo et al. [2011], Geiger and Zaidel-Bar [2012], Schiller et al. [2013]). These studies showed that about 200 proteins belong to the integrin adhesion plaque in the most mature FAs. They have either a “structural” or “signaling” role in adhesion.

The first ones, marked with a yellow shading in Figure 2.7, insure a structural connection between the adhesion receptors and the actin cytoskeleton or have a scaffolding role forming bridges between adhesion proteins. Talin, kindlin, vinculin, zyxin and paxillin belong to this group of adaptor proteins. The recruitment of the adaptor proteins at adhesion sites is regulated by the second type of proteins, the “signaling” molecules. They promptly change the binding affinities between the structural proteins by inducing conformational changes. This signaling is governed by a number of kinases and phosphatases

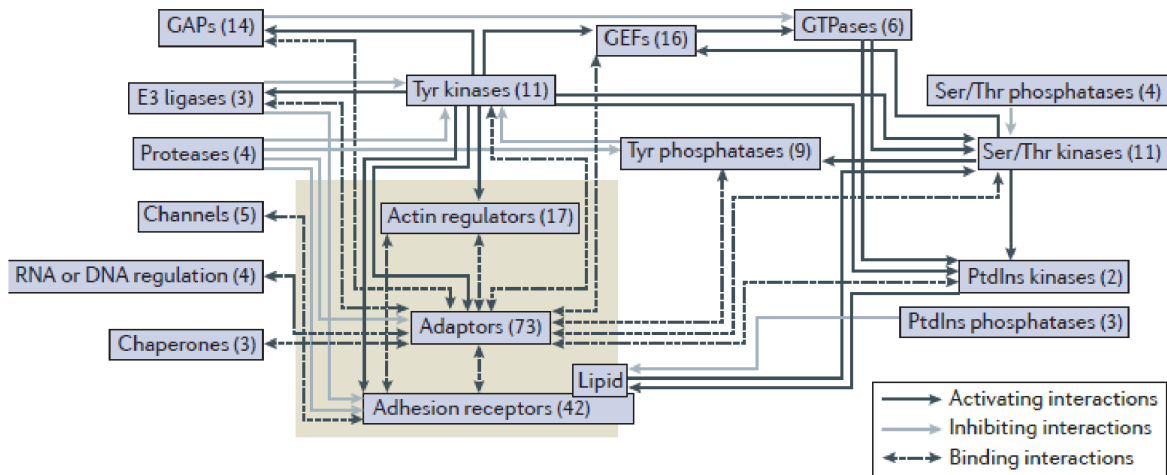


Figure 2.7: Representative scheme of integrin adhesome.

Schematic representation of the adhesome. The functional categories of the different adhesome components are shown, with the number of family members in the adhesome given in brackets. The yellow shading includes all the adhesome components that perform scaffolding function, and they are surrounded by the regulatory (signalling) adhesome components. Figure taken from Winograd-Katz et al. [2014].

that (de)phosphorylate different residues (tyrosine, serine, threonine) of adhesion proteins, activating or inhibiting their interactions. Some kinases like Src and focal adhesion kinase (FAK) are also phosphorylation targets and their activity is directly associated with their phosphorylation status (Panetti [2002]). The activity of some kinase/phosphatase signaling networks is regulated by Rho-GTPases, acting as molecular switches

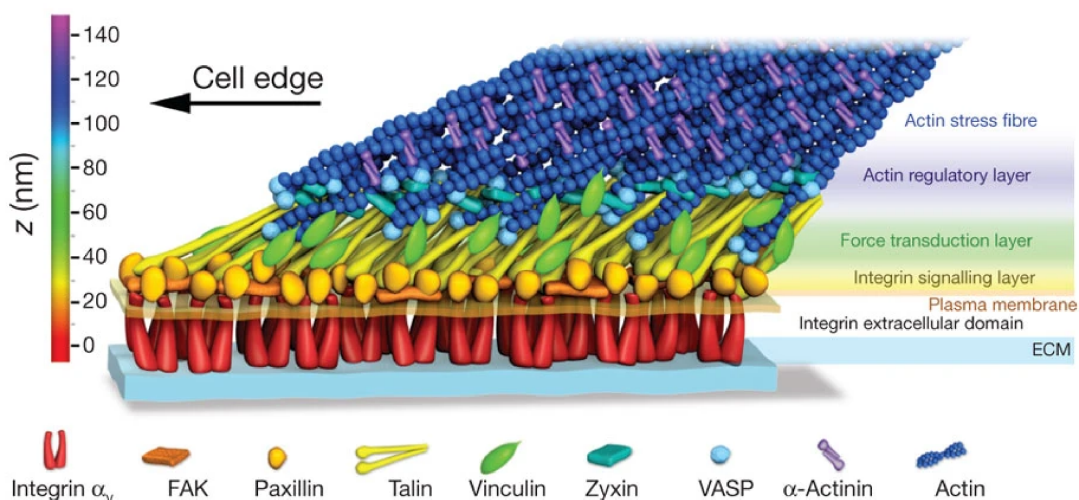


Figure 2.8: Nanoscale architecture of focal adhesions.

Schematic model of focal adhesion molecular architecture, depicting experimentally determined protein positions. Note that the model does not depict protein stoichiometry. Figure taken from Kanchanawong et al. [2010].

under the GTP-bound active and GDP-bound inactive forms (Hall [2005]). For more details on the adhesion regulation pathways please refer to (Zaidel-Bar and Geiger [2010], Horton et al. [2016]).

FAs are well organized structures and are conserved in many cell types (Geiger et al. [2009]). Another level of FA organization was revealed by the group of Clare Waterman. In their pioneering work, they have mapped a 3D-layered structure of FAs by using advanced super-resolution technique (Kanchanawong et al. [2010]) (cf. Figure 2.8).

These results provide evidence for the existence of several layers of interacting proteins in FAs. Indeed, integrins and actin are vertically (perpendicularly to the adhesion plane) separated by about a 40 nm wide region containing 3 multi-protein layers: an integrin signaling layer with FAK and paxillin; an intermediate force-transduction layer with talin and vinculin and an uppermost actin-regulatory layer containing zyxin, vasodilator-stimulated phosphoprotein (VASP) and alpha-actinin.

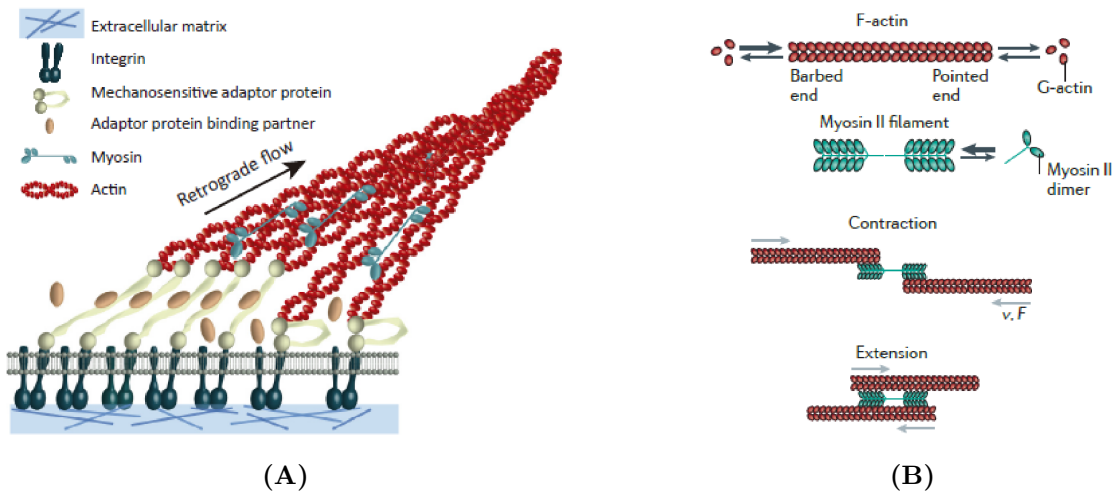


Figure 2.9: Force generation and transmission through the molecular clutch.

A) Serial connection between the ECM, integrins, mechanosensitive adaptor proteins, and actin. Myosin motors pull on actin filaments, transmitting the force to the different elements of the adhesion cluster leading to conformational changes in adaptor proteins and affecting unbinding events.

B) Myosin II filaments drive the translocation of F-actin filaments towards their barbed ends with a characteristic force (F) and gliding velocity (v). This can result in the contraction of two bound anti-parallel actin filaments. The forces generated by these contractions are transmitted to integrins and ECM through the molecular clutch.

Figure adapted from Elosegui-Artola et al. [2018], Murrell et al. [2015].

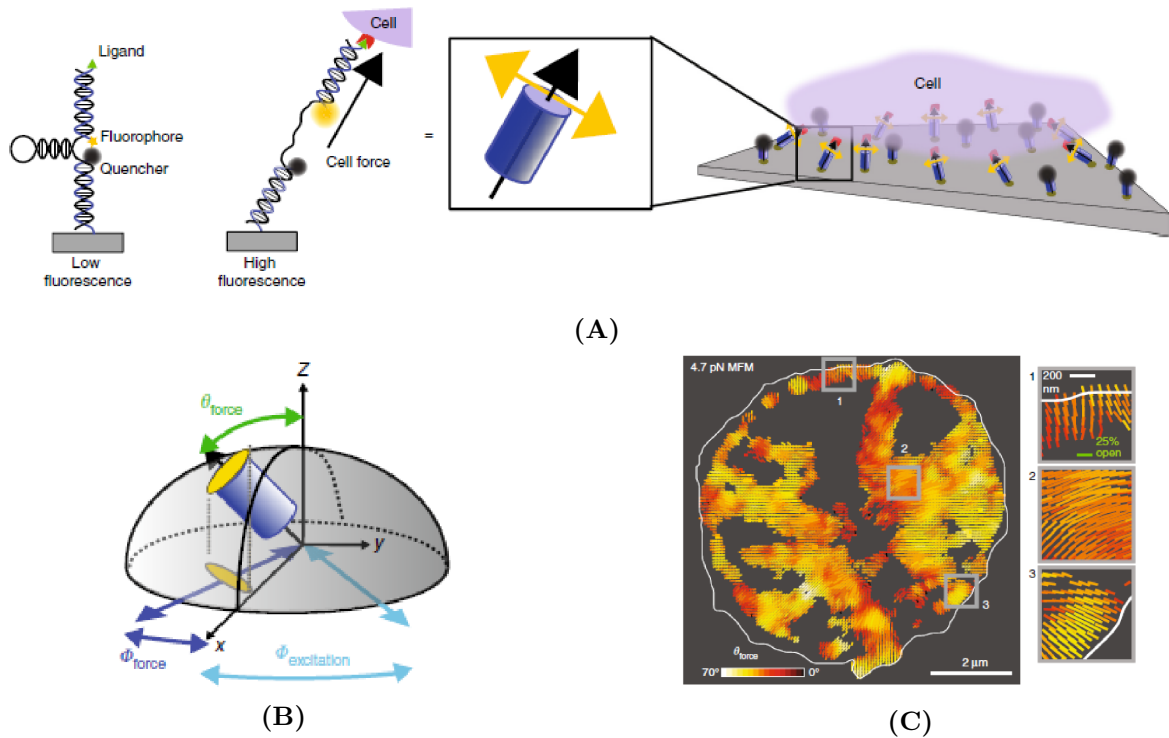


Figure 2.10: Force orientation and magnitude at the single integrin level.

Excitation-resolved fluorescence polarization microscopy and DNA-based FRET tension probes enable the measurement of molecular force orientation and magnitude.

A) Principle of molecular tension probes. Yellow arrows, fluorophore transition dipole moments; green triangles, RGD ligands; red polygon, integrin receptors.

B) Forces applied by the cell on the ligand dictate DNA probe orientation (gray hemisphere, possible orientations), fluorophore orientation, and the XY projection of Cy3B (yellow ellipse in the XY plane).

C) Molecular force microscopy (MFM) map of platelet integrin forces. Dipole orientation, Φ_{force} ; color, Θ_{force} ; length, percentage of open tension probes. Gray background represents intensity below a threshold of signal-to-noise ratio <5 .

Figure taken from Brockman et al. [2018].

2.4 Acto-myosin contraction unit

Cells can apply physical forces to the adhesion clusters. These forces may be generated by two processes: myosin-powered actin contractility and polymerization at the barbed-end of actin filaments at plasma membranes (Elosegui-Artola et al. [2018], Murrell et al. [2015]) (cf. Figure 2.9). These two phenomena drive the so-called actin ‘retrograde flow’, corresponding to a net flow of actin from the cell edge to the cell center. In a migrating cell, the forces that NAs and FAs can transmit to the ECM are different. NAs are only weakly attached to actin filaments and transmit the retrograde pushing forces from the polymerizing branched actin network. FAs are more mature clusters with reinforced connections between integrins and actin bundles; thus, FAs can transmit higher pulling

forces generated by myosin contractility. Moreover, forces generated by myosin contractility stabilize FA (Wolfenson et al. [2011]) and also align ligand-engaged integrins in the FA (Swaminathan et al. [2017]). Feedback processes between the pulling forces, the maturation of the adhesive structures, the reinforcement of the actin bundles into thick stress fibers that can exert higher forces allow the cells to exert strong forces on solid substrates, and conversely to resist to shear forces in flow for instance.

Cell forces have been measured at the level of the adhesion clusters by traction force microscopy (TMF) that detects the force exerted by the cells by measuring the deformation of deformable substrates or the deflection of pillars or cantilevers (Ganz et al. [2006], Bergert et al. [2016]) and on a single-molecule level by FRET sensors (Grashoff

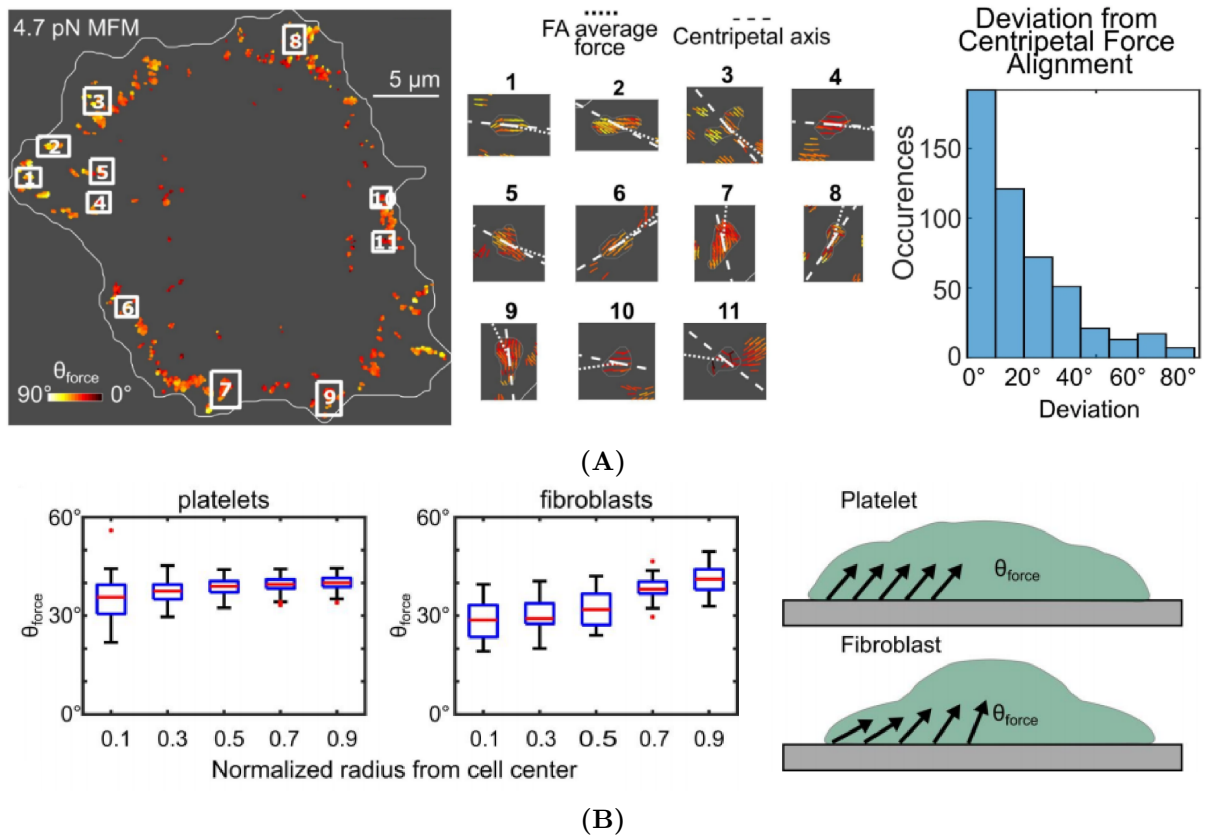


Figure 2.11: Force orientation in FAs.

A) Orientation of FAs with respect to the centripetal axis in the adhesion plane (FAs with the 0° orientation are developed along the centripetal axis) and tilt angle Θ_{force} of the force applied to the FA, (0° when the force is perpendicular to the adhesion plane and 90° when it is parallel to the plane).

B) Force tilt angle Θ_{force} as a function of the distance from the cell center in platelets and fibroblasts (0 is the cell center and 1 is the cell edge). The red lines indicate medians. The 25/75% quartiles are indicated by blue boxes, while whiskers extend to 1.5 times the interquartile range. Outliers are indicated by red “+” signs.

Figure taken from Brockman et al. [2018].

et al. [2010], Morimatsu et al. [2013], Roca-Cusachs et al. [2017]). The magnitudes of the forces applied to adhesion clusters are of the order of several nN, whereas at the level of single receptor ligand bond they are 1000 times smaller (in the range of several pN). The magnitude and orientation of integrin-based traction forces were first measured together in mouse fibroblasts and human platelets (Brockman et al. [2018]). Brockman et al. designed a molecular force microscopy assay (MFM) based on a combination of FRET and polarization microscopy, and applied it to study forces generated in FAs. A DNA-based FRET sensor allowed to measure the amplitude of the forces applied to integrin receptors by actin cytoskeleton and polarization imaging revealed the orientation of these forces with 2 angles of the spherical coordinate system $(\Theta_{force}, \Phi_{force})$ (cf. Figure 2.10).

In their work, the authors estimated the forces applied to each individual integrin-RGD bonds to be of several pN in amplitude. They also detected that the forces in the FA were radially directed towards the cell center and had a tilt angle (relative to the plane perpendicular to the adhesion plane), Θ_{force} between 30-40°. Interestingly, this tilt did not depend on the radial localization of the FA in human platelets, but it increased from the center to the edge of the cell for mouse fibroblasts (cf. Figure 2.11).

Chapter 3

Mechanotransduction in cell adhesion

Cell adhesion structures are mechanotransduction systems because they transduce physical signals into biochemical responses and, conversely, convert biochemical energy to generate physical forces. These mechanisms rely on conformation-dependent biochemical reactions that can be induced by physical forces and constraints from the external environment and that are further transmitted to the cell by the mechanotransduction systems. For example, an external mechanical stimulus can induce the recruitment of adhesion proteins to the site of contact. This recruitment can then trigger actomyosin contraction creating a mechanical response to the initial stimulus. These two mechanisms are coupled via feedback loops allowing cells to “respond” to force stimuli from outside in the same “language” – a physical force. This process is called mechanosensing.

3.1 Mechanosensing

Mechanosensing allows cells to sense physical cues and to distinguish substrates depending on their geometry or rigidity. Thus, for example, the same cells will develop dramatically different adhesion morphologies if they adhere on fiber-like or plain substrates (cf. Figure 3.1).

Substrate rigidity (which corresponds to the degree of deformation of the material per unit of applied force) is an important factor that influences the cell fate and behavior from stem cell differentiation (Engler et al. [2006], Wen et al. [2014]) to cell migration (Lo et al. [2000]). It is now well established that on substrates exhibiting stiffness gradients, most cell types will migrate towards the stiffest zone in a phenomenon called "durotaxis" (Discher et al. [2005]). Rigid and soft substrates induce different mechanotransduction signaling cascades leading to differential gene expression. For example, they can regulate the

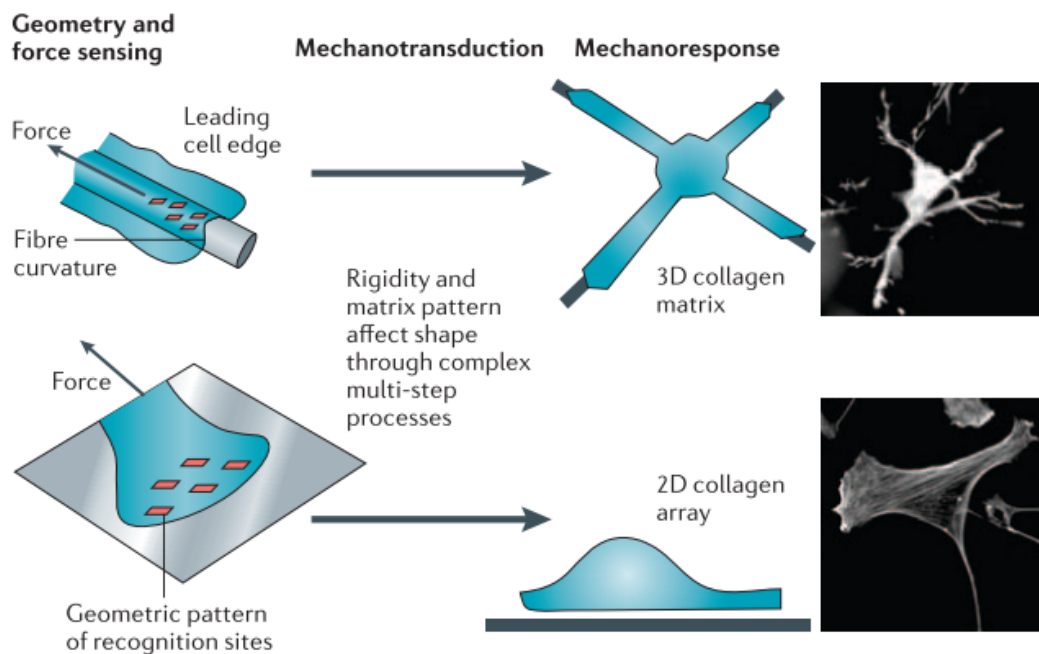


Figure 3.1: Role of substrate geometry in the cellular mechanoreponse during cell adhesion.

Geometry-dependent interactions are locally transduced into biochemical signals that activate various mechanosensitive signalling pathways, ultimately regulating cellular mechanoreponses. This figure emphasizes a dramatic difference in morphology that human fibroblasts assume after 4 hours on matrices of different geometry: collagen-coated plain surfaces (bottom panel) or collagen coated fibers (top panel).

Figure taken from Vogel and Sheetz [2006].



transcription of the Yap/Taz genes that are known to induce epithelial-to-mesenchymal transition (EMT) and thus contribute to cell proliferation (Dupont et al. [2011], Iskratsch et al. [2014]).



3.2 Rigidity sensing and reinforcement

Cells constantly probe their substrates' rigidity. For example, mouse embryonic fibroblasts (MEF) perform a periodic movement at the edge of the lamellipodia when they spread on fibronectin-coated glass (Giannone et al. [2004]). To sense the substrate rigidity, they pull on the substrate every time they adhere to it and extend their lamellipodia, adhering again when the adhesion bonds break. The periodicity of this process depends on substrate rigidity: the shortest period for the most rigid and the longest for the softest substrate (cf. Figure 3.2). This process suggests the existence of mechano-chemical feedback loops in cells that regulate local architecture at the adhesion site and generate forces proportional to the rigidity of the substrate (Galbraith and Sheetz [1998]). Thus,

this contracting-extending process allows the cell to discriminate between the substrates of different rigidity (Giannone et al. [2004], Ghassemi et al. [2012]).

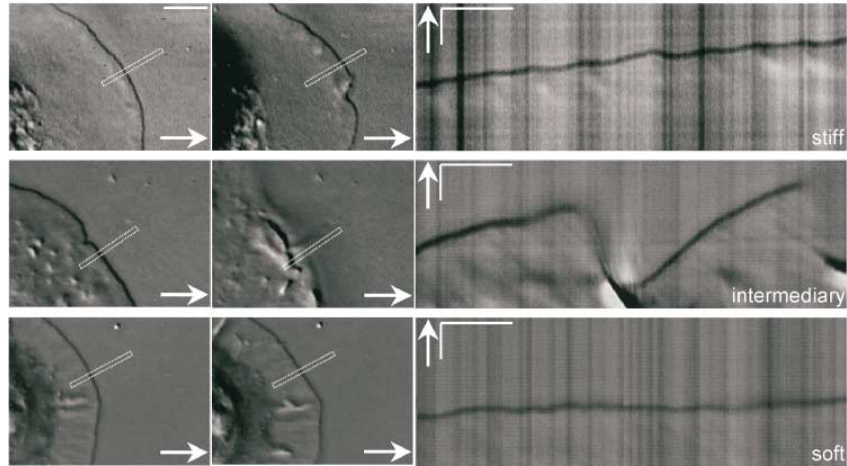


Figure 3.2: Generation of periodic interruptions depends on substrate rigidity.

From top to bottom:

DIC kymographs of MEF cells spreading on polyacrylamide gels covalently linked with FN, of different stiffness: stiff, intermediate and soft.

Left: Scale bars, $5 \mu m$. Right: time bars, 30 s; scale bars, $2 \mu m$. Arrows indicate the direction of protrusion.

Figure taken from Giannone et al. [2004].

This process continues until a sufficiently strong adhesion forms between the cell and the substrate and withstands the force applied by the cell. The bond strengthening phenomenon during cell adhesion on rigid substrates, called rigidity reinforcement, is well studied and characterized (Choquet et al. [1997], Jiang et al. [2006], Kong et al.

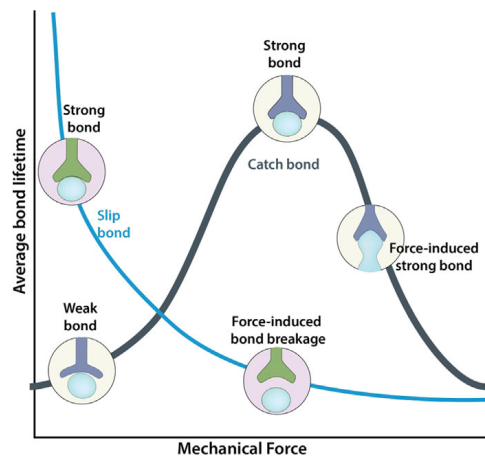


Figure 3.3: Lifetime of slip and catch bonds under load.

Life time of slip bonds (blue line) decreases under tension whereas the life time of catch bonds (gray line) increases under applied load up to a maximum force above which it behaves as a slip bond.

Figure taken from Changede and Sheetz [2016].

[2009]). The physical connections between the ECM through integrins and associated proteins and the contractile cytoskeleton are mediated by series of weak non-covalent bonds. Individually these bonds break when subjected to an external stress after a time period called bond-survival time. Nevertheless, cells can form force-sustaining adhesion sites through two mechanisms. The first is the integrin-ECM bond strengthening under force (Kong et al. [2009]). Their survival time increases under increasing external stress. Molecular bonds with such properties are called catch-bonds in contrast to slip-bonds that break faster when subjected to an increasing force (Vogel and Sheetz [2006]) (cf. Figure 3.3).

The second is the increase of the number of individual bonds to the adhesion sites under load. The force needed to break a cluster of N bonds in parallel is about a factor of N larger than that for a single bond. Thus, the recruitment of more receptors, adaptive proteins will strengthen the bond in the adhesion site (Vogel and Sheetz [2006]). Mechanotransduction pathways leading to the recruitment of proteins to adhesion sites are associated with the load-dependent increase of affinity in protein-protein interactions. It may be caused by a combination of mechanisms from molecular conformation changes induced directly by mechanical stress (opening cryptic domains of proteins) to enzymatic modifications like (de)phosphorylation, for example. Talin is a mechanosensitive protein that unveils up to 11 vinculin binding sites when mechanically stretched (VBSs) (del Rio et al. [2009]). When talin couples the cytoskeleton to the ECM and stretches, it recruits and activates vinculin, leading to association of this latter to actin filaments, strengthening the anchorage to the actin cytoskeleton as a function of substrate stiffness (Izard and Vorrhein [2004], del Rio et al. [2009]).

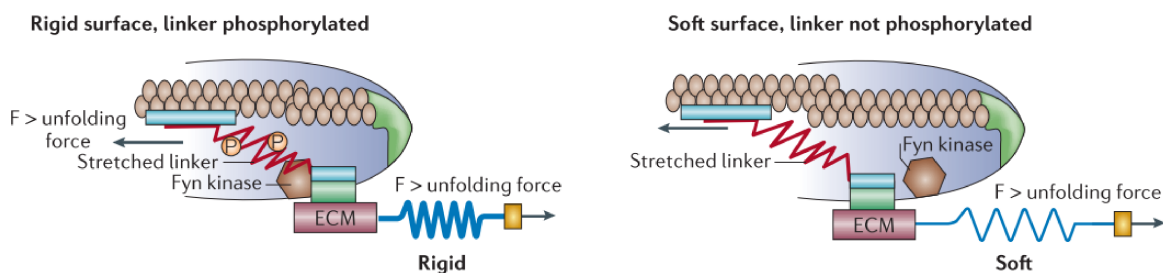


Figure 3.4: Mechanisms of rigidity sensing.

These panels illustrate the position-dependent mechanism of rigidity sensing. Depending on the rigidity of the substrate, the linker protein and the Fyn kinase will be more or less distant, affecting the phosphorylation of the linker.

Figure taken from Vogel and Sheetz [2006].

Figure 3.4 illustrates the role of phosphorylation in rigidity reinforcement through protein recruitment to the adhesion clusters on soft and rigid substrates. On both soft

and rigid substrates, the linker protein connecting integrins and actin is stretched by the applied mechanical force. But the same force will deform the soft substrate more than the rigid one, displacing integrins further from their initial position on the cell membrane. The displaced integrins on the soft substrate will displace the linker protein, which will have less chance to be phosphorylated by Fyn kinase located in the initial cluster. Conversely, on rigid substrate where integrins were not displaced from the initial cluster, the linker protein will stay in its initial place and will have more chances to be phosphorylated by Fyn kinase (cf. Figure 3.4).

3.3 Adhesion maturation

The idea that physical stresses induce maturation of the integrin clusters, i.e. the recruitment of proteins to the clusters to reinforce the adhesion bonds, was directly evidenced by Riveline et al. [2001]. In their experiments they have applied centripetal mechanical force to small dot-like NAs at the cell edge using a micropipette. The local force application induced the centripetal growth of focal complexes: new proteins were recruited and the focal complexes elongate and eventually become indistinguishable from focal adhesion structures (cf. Figure 3.5). Myosin activity is shown to be crucial in integrin cluster maturation. The inhibition of myosin contraction prevents the formation of

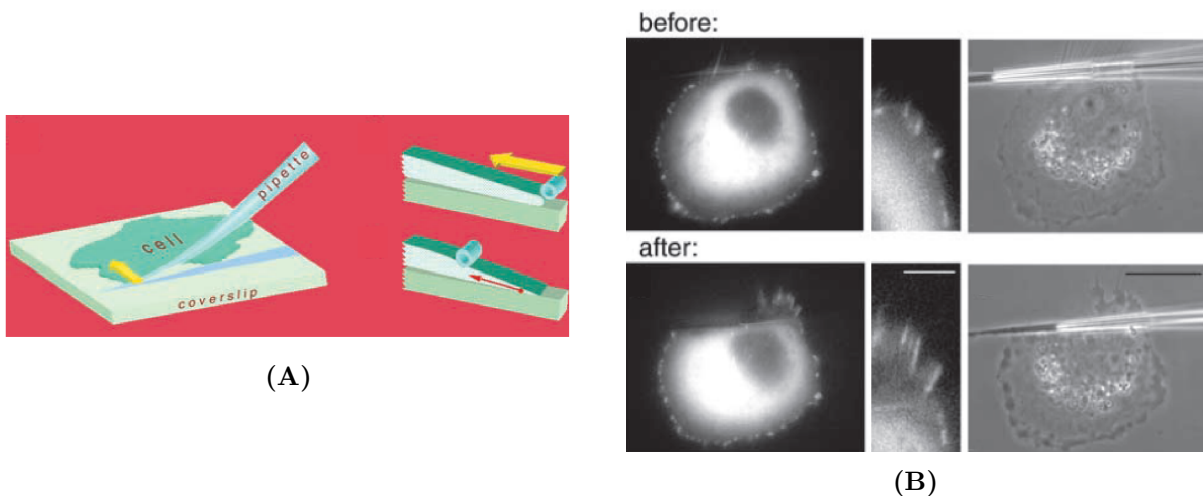


Figure 3.5: Local formation of focal contacts in response to an external force.

A) Scheme depicting the method of application of external force. The pipette, covered either with poly-L-lysine or fibronectin, was bent against the coverslip and moved along the chosen lamellipodium as indicated by the yellow arrow.

B) Fluorescence (GFP–vinculin) and DIC microscopy images were taken before (top panel) and after (bottom panel) pipette shift on the cell lamellipodium.

Figure adapted from Riveline et al. [2001].

large mature clusters, but not the formation of small NAs on the edge (Riveline et al. [2001], Wolfenson et al. [2011]).

Adhesion maturation has also been studied on adhering cells during rigidity probing. At early adhesion stage on RGD coated substrates elementary adhesion clusters within NAs were observed by super-resolution microscopy (Changede et al. [2015]). They form similarly on rigid and soft substrates. These clusters are around 100 nm in size and contain about 50 integrins. On rigid substrates where cells develop high force loads NAs can mature to large FAs, whereas on soft ones they do not (Saez et al. [2005]). At late adhesion stages on rigid substrates actin cytoskeleton is reorganized. Actomyosin bundles grow and strengthen and as a result pull harder on the adhesion sites that mature into FAs (cf. Figure 3.6). FAs are more stable and contain a more complex assembly of proteins (cf. section 2.3 for the adhesome) (Nathalie Q. Balaban et al. [2001], Geiger et al. [2009]). Integrin densities in FAs can reach more than 900 integrins/ μm^2 (Wiseman et al. [2004]). Since stress fibers are in general oriented across the cell (cf. Figure 3.6, right), FA are elongated structures (several microns in length) usually distributed along the periphery of the cell, where the rigidity sensing initially occurs, very close to the edge and directed radially. These directive adhesion structures break the isotropy of the cell shape, resulting in its non-isotropic spreading (Prager-Khoutorsky et al. [2011]). As on soft substrates (Young modulus below 10kPa), the integrin clusters do not mature to the similar extent as on rigid ones (Engler et al. [2004]) and actin stress fibers do not form, cells adhering on soft substrates have an isotropic shape during the time course of adhesion (cf. Figure 3.6).

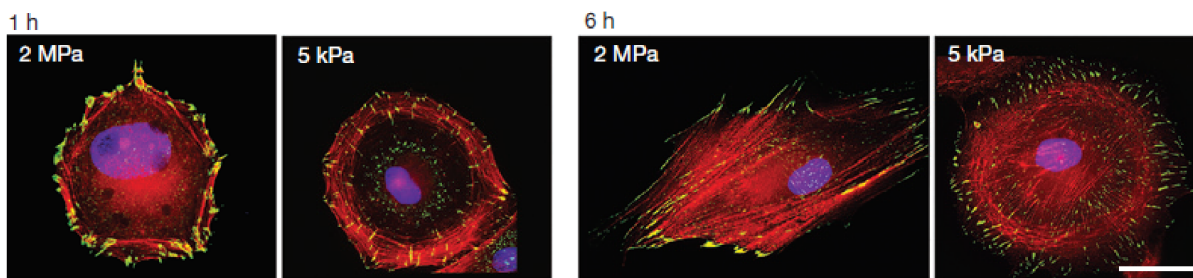


Figure 3.6: Cell adhesion on rigid and soft substrates.

HFF cells stably expressing paxillin-YFP (green) were plated on fibronectin-coated 2MPa or 5kPa PDMS substrates, and fixed at 1 and 6h following seeding. Cells were stained with TRITC-phalloidin (red) and DAPI (blue). Scale bar, 30 μm .

Figure adapted from Prager-Khoutorsky et al. [2011].

Chapter 4

Cell-cell adhesion

The majority of cell adhesion studies were performed on ECM-coated rigid surfaces that impose a biophysical environment differing from the physiological conditions. Immune T-cells and epithelial cells, for example, contact through receptors diffusing in the plasma membranes, with different mechanical properties than a surface of a petri-dish. The membranes are fluid and adhesion proteins on their surfaces can move passively (diffusion) or be moved by an active process imposed by the adhering cell.

Studying cell-cell adhesion represents a more challenging problem than cell-ECM adhesion because ligand mobility on the fluid substrate and more complicated, in general, 3D geometry of the contact. One approach to address this problem is to replace one cell by a reconstituted membrane that contains just the specific molecules responsible for adhesion (McConnell et al. [1986], Watts and McConnell [1987]).

4.1 Supported lipid bilayers (SLBs), some mechanical and rheological properties

The supported lipid bilayer is a 2D fluid system that consists of a lipid bilayer (in general, a single one) deposited over a solid substrate. The bilayer and the substrate are separated by a thin (few nm) layer of water or soft polymer cushions (Sackmann [1996]) (cf. Figure 4.1). SLBs can be made by vesicle fusion with the substrate. The efficiency of this process can be achieved by careful preparation of the samples described in the following protocol (Lin et al. [2010]). Indeed, the stability and fluidity of SLBs depend on the fine balance of van der Waals, hydration and electrostatic forces between the lipids and the solid substrate (Johnson et al. [2002], Richter et al. [2003]). Thus, the quality of

the SLBs depends on many factors such as lipid composition and quality, ionic strength of buffers, substrate hydrophilicity and thickness (cf. chapter 5 of the Materials and Methods), that should be well controlled during SLB formation. Supported lipid bilayers represent an excellent model to study cell-cell adhesion for several reasons.

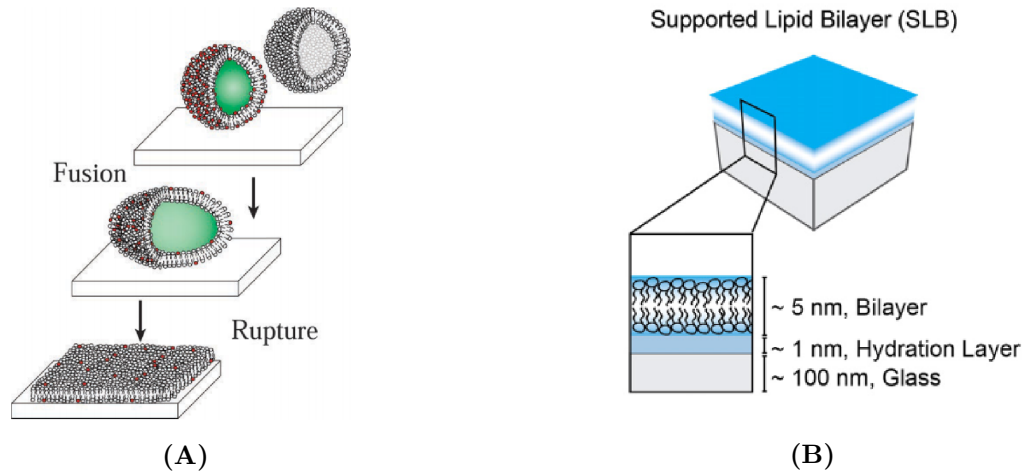


Figure 4.1: Supported lipid bilayer (SLB).

A) Schematic of the SLB formation proposed by Johnson et al. [2002]: adsorbed vesicles fuse among themselves until a critical size is reached, then rupture to form bilayer disks.

B) SLBs contain a bilayer separated from a rigid substrate by a thin layer of water. Figures taken from Johnson et al. [2002], Glazier and Salaita [2017].

First, the flat substrate allows to image the adhesive contact with conventional microscopy techniques. Second, the lipid composition of the bilayer can be controlled; it can contain fluorescent lipids or functionalized lipids that can be tagged with cell ligands. Finally, the key feature of SLBs that distinguishes them from other surfaces is their lateral fluidity. The lipids and thus the bound ligands can freely diffuse on the surface of the SLB. The diffusion coefficients of lipids in SLBs depend on their lipid composition and can also be controlled.

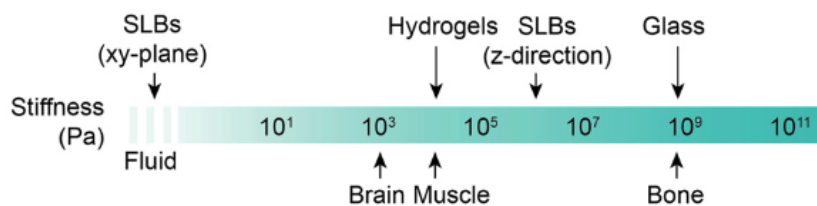


Figure 4.2: SLB stiffness in comparison to tissues, hydrogels, and glass substrates. SLBs are anisotropic, behaving like fluids in the XY-plane, but stiffer than hydrogels in the Z-direction.

Figure taken from Glazier and Salaita [2017].

Let's consider SLBs functionalized with cell ligands. From the mechanical point of view, an SLB behaves like viscous liquid in the plane of the bilayer (xy-plane). Its viscosity,

that is about 2 orders of magnitude higher than water, controls the ligand mobility on its surface (Block [2018]) if the ligand size is smaller than about $1 \mu\text{m}$ (the bulk viscosity can be neglected) (Mascalchi et al. [2012]). If a tangential force is applied to the ligand (for instance with a magnetic tweezers, see (Boulbitch [1999]) for instance), it experiences a drag force related to the bilayer viscosity. In contrast, along the axis perpendicular to the xy-plane (z-direction) SLBs are rather rigid when probed for compression (pushing onto the bilayer). Due to the presence of the glass under the bilayer, SLBs resist this type of deformation with approximately the same stiffness as the glass (several tens of MPa (Picas et al. [2012])). However, in the opposite direction when a pulling force is applied, SLBs can be deformed like any lipid membrane with deformations that depend on the bending rigidity of the membrane and on its tension (Derényi et al. [2002]) (cf. Figure 4.2). Such an experiment was done with atomic force microscopy (AFM) and a force of the order of 100 pN was measured to pull and extend a tube from a DOPC bilayer deposited on a mica surface (Armond et al. [2011]). Note that the force barrier required to form a tube is higher when the force is not punctual but applied on a membrane patch: it increases as the square root of the patch area, as compared to the point force (Koster et al. [2005]). Also, if a bilayer is compressed by depositing it on a stretched PDMS surface and by next relaxing the extension, this leads to a negative membrane tension and a spontaneous tubulation of the SLB can be observed (Staykova et al. [2011]).

4.2 Cell-SLB hybrid systems

SLBs can be coated with practically any type of cell ligands by anchoring them to Nickel-chelating lipids through a polyhistidine tag (Nye and Groves [2008]). The protein density on the surface can be controlled by tuning the protein incubation conditions and by the Ni-lipids concentration. This makes the SLBs a very useful and versatile hybrid system to study cell adhesion on fluid substrates (cf. Figure 4.3).

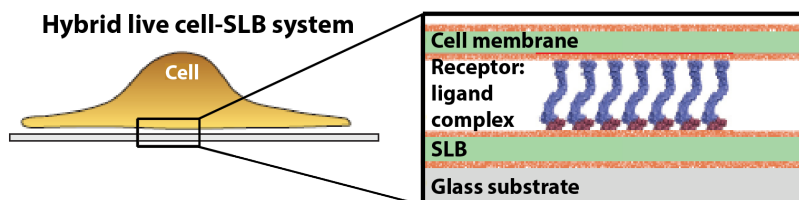


Figure 4.3: Hybrid live cell-SLB system.

Schematic of a cell interacting with an SLB through specific receptor-ligand interactions. Figure adapted from Biswas and Groves [2019].

Here we present two examples of cell-SLB hybrid systems that have been used to mimic cell adhesion on fluid membranes. The adhesion in these two cases is mediated by different adhesion receptor-ligand pairs.

4.3 Immunological synapse

One of the most studied examples of cell-cell adhesion is the immunological synapse (IS) (Dustin and Groves [2012], Dustin [2014]). The IS is a specialized adhesion structure between a T lymphocyte (T-cell) and an antigen-presenting cell (APC). The IS is composed of several receptors including T-cell receptors (TCRs) that bind to the major histocompatibility complex (MHC) of the APC and integrin receptors LFA-1 that bind to I-CAM1 of the APC. During the antigen recognition and T-cell activation TCR receptors recognize MHC and form microclusters of tens to hundreds molecules. Other proteins are recruited to the clusters to stimulate TCR signaling. TCR microcluster association with actin cytoskeleton leads to their reorganization and directed transport of the clusters to the cell center (cf. Figure 4.4).

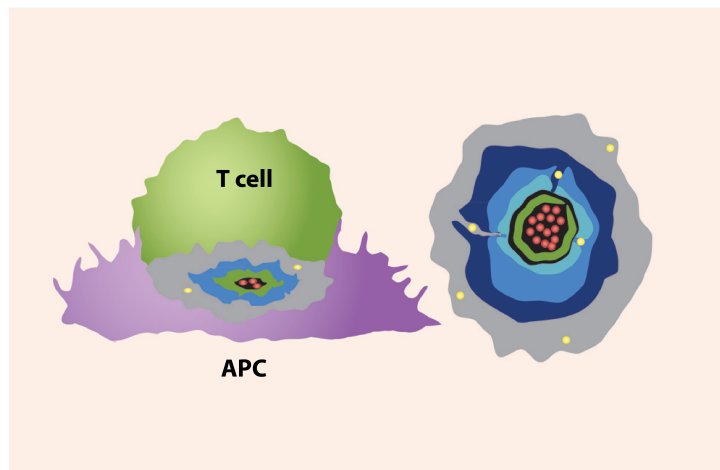


Figure 4.4: Model immunological synapse.

(left) T-cell in contact with an antigen-presenting cell (APC) during antigen recognition process. (right) Protein composition and their radial location in the synapse interface. From the periphery to the center: F-actin lamellipodium (gray); LFA-1-ICAM-1 adhesion (blue); CD28-CD80 costimulatory molecules (green); and TCR-MHC antigen recognition (red). The yellow dots are TCR microclusters that include both CD28 (green) and TCR (red).

Figure adapted from Dustin [2014].

During the antigen recognition process the adhesion proteins of the IS spatially organize and form a distinctive pattern with TCR/MHC in the center and cell adhesion proteins I-CAM1/LFA-1 on the periphery.

To study the formation of the IS in a more quantitative way, the Groves group studied the adhesion of T-cells on SLB coated with ICAM1 and MHC proteins (Hartman et al. [2009]). The evolution of the mutual distribution of the receptors was observed. A typical protein pattern that resembles that in the IS was formed within the first 15 minutes of adhesion (cf. Figure 4.5).

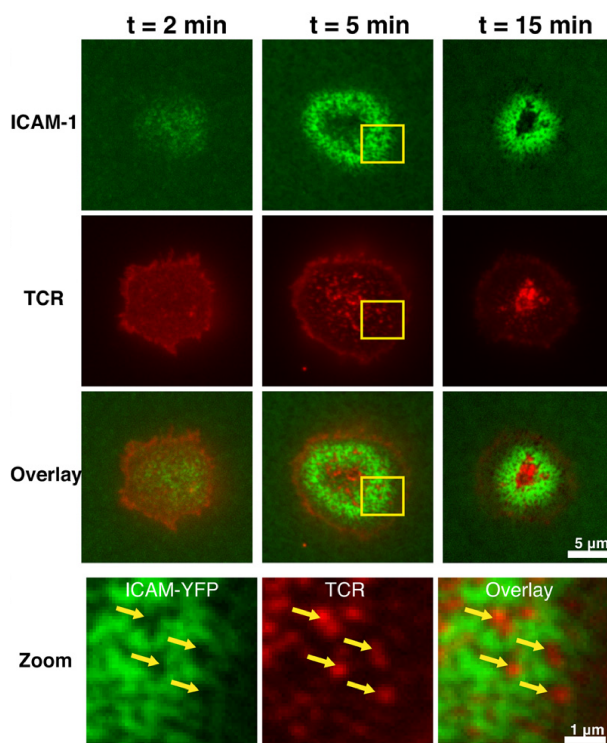


Figure 4.5: TCR/MHC micro-clusters exclude and displace ICAM-1/LFA-1 complexes.

Epifluorescence images of ICAM-1-YFP and T-cells labeled with labeled α TCR- f_{ab} (Alexa Fluor 568) that were fixed 2 min (column 1), 5 min (column 2), and 15 min (column 3) after contact with SLBs containing ICAM-1 and MHC. Upon formation, TCR micro-clusters exclude and displace ICAM-1 as they translocate to the center of the synapse. The ICAM-1 density within the excluded areas is comparable to the bulk density.

Figure adapted from Hartman et al. [2009].

4.4 RGD-mediated adhesions on fluid substrates

The same type of hybrid cell-SLB system was used to study integrin-RGD mediated cell adhesion by different groups (Marchi-Artzner et al. [2001], Yu et al. [2011], han Yu et al. [2013], Wolfenson et al. [2014], Bennett et al. [2018]). M. Sheetz and his collaborators have been particularly influential on these questions. They observed the formation of integrin clusters when REF52 fibroblast cells adhere on fluid RGD-coated SLBs. In these experiments, the neutravidin that carried the RGD peptides were labelled but not

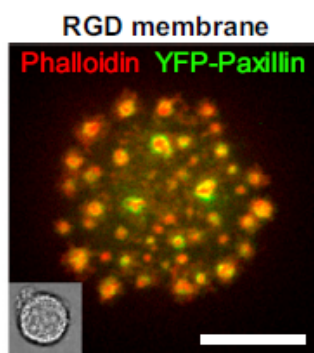


Figure 4.6: Podosome Formation on RGD Membrane.

REF52 fibroblast develops podosome-like structures on RGD membrane after 45 min of initial adhesion. The scale bar, 10 μm .

Figure taken from han Yu et al. [2013].

the RGD, and integrins were indirectly revealed using fluorescent YFP paxillin. The authors showed that after approximately 45 minutes since the beginning of cell adhesion, in contrast with the dense patches of FA on solid substrate, the integrin clusters exhibit a ring-like shape with no integrin in the center. Several adhesion proteins like paxillin and vinculin were recruited to these rings, whereas actin was detected in the center, globally reminiscent of podosome structures (cf. Figure 4.6).

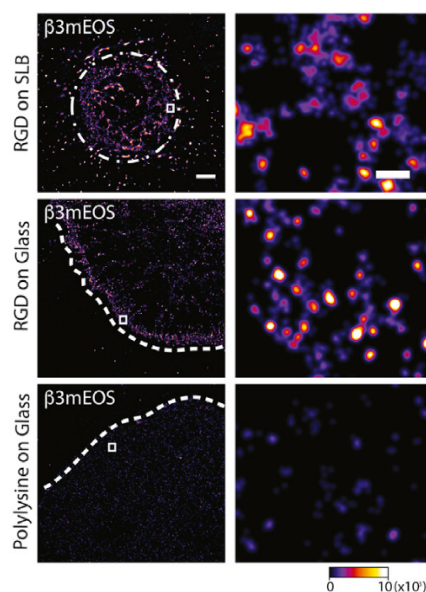


Figure 4.7: Early adhesion integrin clusters on SLB and glass.

From top to bottom: integrin ($\beta_3\text{mEOS}$) clusters formed on RGD-SLBs, glass and poly-lysine coated glass (Ctrl-) within the first minutes of adhesion. Images were acquired with photoactivated localization microscopy (PALM). The dotted lines indicate the cell boundary, and the white box indicates the zoomed-in region shown adjacent. Scale bars, 5 μm (left) and 200 nm (right).

Figure adapted from Changede et al. [2015].

Based on comparative studies of cell adhesion on RGD-coated surfaces, fluid or solid and the use of super resolution microscopies, the current view of the different stages of maturation of adhesion clusters is the following. Cell adhesion starts with integrins binding to their ECM ligands (RGD) and the formation of small dot-like NAs that contain about 50 integrins (Changede et al. [2015], Changede and Sheetz [2016]). These integrin clusters are formed on both rigid and fluid substrates (cf. Figure 4.7).

At the early stage of adhesion, activated integrins in the clusters recruit talin and several other proteins such as kindlin, FAK, ILK and paxillin. The clusters that are only loosely attached to the actin cytoskeleton recruit FHOD1, formin (cf. Figure 4.8 A1,A2).

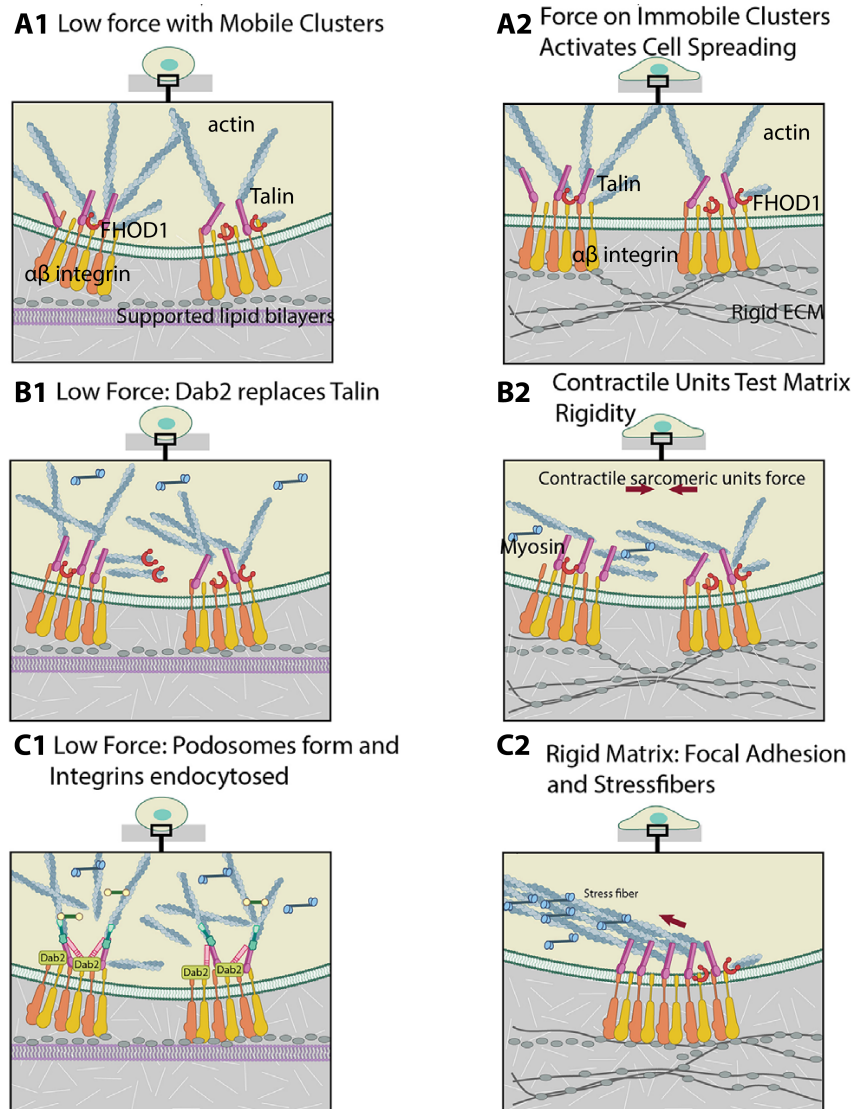


Figure 4.8: Stages of cell adhesion on SLB and glass.
 (left column: A1-B1-C1) Formation of integrin clusters on SLBs.
 (right column: A2-B2-C2) Formation of integrin clusters on glass.
 Figure adapted from Changede and Sheetz [2016].

At this stage NAs begin to sense the rigidity of the substrate by locally polymerizing actin. Negligibly small traction forces can be generated on fluid substrates, thus the clusters remain not mature and talin is replaced by Dab2, an adaptor protein that down-regulates integrin-mediated signaling (Finkelstein and Capelluto [2016]) (cf. Figure 4.8 B1). On rigid substrates, on the contrary, traction forces are higher and clusters mature more due to the mechanosensitivity of integrins and talins: new actin filaments assemble and myosin is recruited (cf. Figure 4.8 B2). Finally, NAs on fluid substrates form podosome-like structures with an actin core (cf. Figure 4.8 C1), whereas on rigid substrates sarcomeric actomyosin units assemble and exert “pinching” forces that stretch talin in the NAs and lead to further recruitment of integrin adaptor proteins and fuse the neighboring NAs to become FAs (Yang et al. [2016]) (cf. Figure 4.8 C2).

Therefore, the absence of cluster maturation on fluid substrates beyond the level of NAs is explained by Michael Sheetz and his collaborators by the absence of sufficient resisting physical force from the substrate to induce a mechano-dependent adhesion maturation. Moreover, no model explains how the podosome-like structures form. However, as explained above, cell membranes and SLB are viscous (100 times more viscous than water), thus dragging a ligand/receptor cluster inserted or bound to lipid membranes requires some force. Conversely, lipid membranes exert a resisting force on the integrin-ligand link sufficient to stretch talin molecules and induce integrin cluster maturation (Bennett et al. [2018]). Thus, membrane viscosity might be an important factor in cell adhesion and integrin cluster maturation on SLBs might to a certain extent depend on the bilayer viscosity as it does on the stiffness.

4.5 A molecular clutch associated with membrane viscosity

The molecular clutch model was adapted by Bennett et al. [2018], including the viscosity of the substrate: it explains that depending on the viscosity of the substrate, the loading rate might be able (or not) to activate the mechanosensitivity of the adhesive proteins. Force transduction in adhesion clusters was compared on RGD-coated SLBs in liquid (DOPC) and gel (DPPC) phases, with viscosities 10^{-6} Pa.s.m and 10^{-4} Pa.s.m, respectively (Bennett et al. [2018]). On SLBs with higher viscosity, the molecular clutch was assembled and the actin flow generated higher force loading rates than on SLBs with lower viscosities where the molecular clutch was not in place. Some maturation markers such the translocation of YAP to the nucleus also confirmed a higher level of

integrin cluster maturation on SLBs with higher viscosity. Nevertheless, it shows that when an adhesion cluster is moved within the cell contact area, it experiences mechanical forces due the viscosity of the bilayer. The cluster is also subjected to forces due to intracellular obstacles (i.e. regions with densely polymerized actin) that create a barrier to its displacement.

Thesis rationale

The molecular clutch model considers essentially forces applied tangentially to the surface. As already detailed above, SLBs can also be deformed in the direction perpendicular and away from the adhesion plane, because of the large anisotropy of mechanical properties of the SLB (Tang [2018]). This aspect has not been considered so far during interaction of cells with fluid membranes. Indeed, the SLB is almost incompressible under pushing force due to the glass below, but it can be deformed in the opposite direction (towards the cell). In cells, the forces applied to the clusters have both direction components, parallel and perpendicular to the adhesion plane (Brockman et al. [2018]).

We have thus set out to revisit the mechanism of adhesion cluster formation proposed by Changede and Sheetz [2016] and to study in more details the contribution of perpendicular components of pulling forces. It is possible that this component of the force is too weak on RGD coated SLBs, resulting in no adhesion maturation beyond the NAs. The stability (lifetime) of the adhesion bond could be a limiting factor in force transmission.

Thus, we decided to study cell adhesion with a ligand that binds more strongly to integrins than RGD, Invasin. In our project, we have compared cell adhesion on fluid substrates (SLBs) functionalized with ligands of different affinity, RGD and Invasin. Our objectives were to investigate:

- the effect of the integrin-ligand affinity on integrin activation and on the clustering process on SLBs;
- whether cluster maturation takes place;
- evidences for the action of orthogonal components of forces on adhesive structures.

Part II

Materials and Methods

Chapter 5

Sample preparations

5.1 Substrate preparation

5.1.1 Glass coverslip cleaning

Glass cleanness and absence of dust particles or residues is paramount for a defect-free bilayer formation. The SLB is observed on the coverslip, thus its cleaning is key. We clean and activate coverslips in a series of sonication steps of 30 min in the water bath sonicator (Elmasonic S 10 (H)): in distilled water, 2% Hellmanex III, distilled water, 1M KOH, distilled water. The KOH has a dual role of cleaning and glass activation. At the end of the cleaning steps the coverslip is dried under nitrogen flow and assembled to form the microscopy chamber. Coverglass slides are simply rinsed with EtOH, H₂O, EtOH and blow dried with nitrogen.

5.1.2 Sample chamber assembly

The bilayer should always be hydrated; thus it is formed in a sample flow chamber that always has buffer inside. The sample chamber for the cell adhesion experiment is a custom-made flow chamber that consists of a 26 mm x 76 mm coverglass slide and a 1.5 thickness coverslip from VWR glued together by two melted stripes of parafilm (cf. Figure 5.1). The distance between the two glass slides (the height of the channel) is about 250 μm . The chamber volume is about 50 μl . The chamber is assembled shortly after to glass cleaning and activation (cf. subsection 5.1.1). The assembled chambers can be stored in closed Petri dishes (protected from dust) at room temperature for about 3 days.

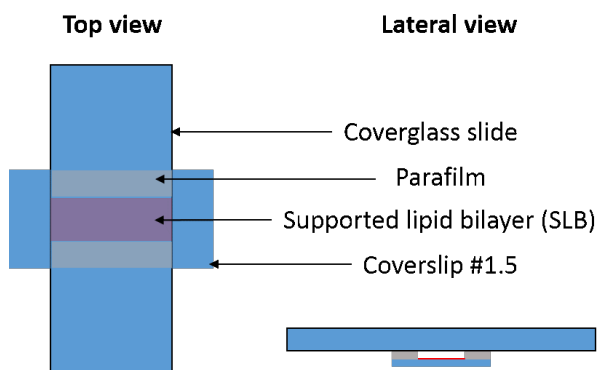


Figure 5.1: Sample chamber.
Scheme of the assembly of the sample chamber.

Next, the supported lipid bilayer is prepared on the activated coverslip and the chamber is ready for the cell adhesion experiment. Our protocol is inspired by the protocol developed in the group of Jay Groves (Lin et al. [2010]).

5.1.3 SUV preparation

SLBs are formed by fusion of Small Unilamellar Vesicles (SUVs) fusion on the coverslip. In our project we have used two lipid compositions to prepare SUVs and consequently SLBs:

1. DOPC/DGS-NTA(Ni)/DHPE-Marina Blue (94/2/4, mol/mol);
2. DOPC/DOPE-RGD/DHPE-Marina Blue (94/2/4).

Next, the first ones will be functionalized with Invasin. DOPC, DGS-NTA(Ni) and DOPE-RGD are purchased from Avanti Polar Lipids, and DHPE-Marina Blue is from Invitrogen. Similar lipid compositions were successfully used by other groups to prepare SLBs (Nye and Groves [2008]).

We have prepared the SUVs with the following protocol:

1. Lipids solubilized in chloroform are mixed together in a glass vial at 1 mg/ml, blow dried with a nitrogen flow, placed in vacuum desiccator for 1 hour, then rehydrated with distilled water for 15 min at room temperature, to a final lipid concentration of 1 mg/ml;
2. After rehydration, the glass vial is vortexed to detach the liposomes;

3. The solution is sonicated for 30 min in the water bath sonicator (Elmasonic S 10 (H));
4. The solution is then centrifuged at 20k RCF for 1 hour;
5. The solution is filtered through a 200 nm filter (Millipore) with a syringe;
6. The sample is dissolved in the **SUV fusion buffer** at the final composition: 10 mM Tris pH 7.3; 120 mM NaCl.

Lipids preparations are closed under with argon at all stages of SUV preparation to minimize their degradation by oxidation. The prepared SUVs were not stored but used immediately to prepare SLBs.

5.1.4 SLB preparation

The SUV solution is incubated in the sample chamber for 30 min to allow the SUV fusion on the substrate (cf. Figure 5.2).

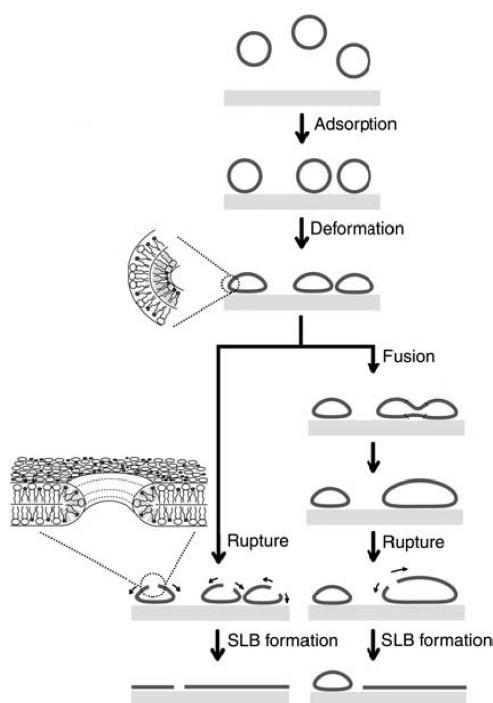


Figure 5.2: Possible mechanisms of supported bilayer formation.

Vesicles adsorb, deform, and rupture to form an SLB.

Figure adapted from Hamai et al. [2006].

Then the unfused vesicles are washed away with 10 x chamber volumes of the SUV fusion buffer. Next, the SLBs were washed with 10 x chamber volumes of the **cell buffer**:

25 mM HEPES pH 7.3; 120 mM NaCl; 7 mM KCl; 1.8 mM CaCl₂; 0.8 mM MgCl₂; 5 mM glucose. Any remaining defect on the surface is then passivated by incubation of the chamber in a "blocking" solution made of the cell buffer complemented with 1 mg/ml beta-casein for 15 min. Then the SLBs is washed again with 10 x chamber volumes of the cell buffer to remove the excess of the blocking solution.

5.1.5 SLB functionalization

To prepare Invasin-coated SLBs, SLBs containing Ni-lipids are functionalized with 6xHis-tagged Invasin (for Invasin production cf. section 5.2) following the protocol described by Nye and Groves [2008]. SLBs are incubated with 400 nM Invasin in the cell buffer for 1 hour at room temperature. Then the unbound proteins are washed away with 10 x chamber volumes of the cell buffer in two steps spaced in time by 30 min.

5.1.6 SLB quality control

To control the quality of the SLBs we first inspect them visually under the microscope (cf. chapter 6). We observe fluorophore distributions in both DHPE-Marina-Blue and

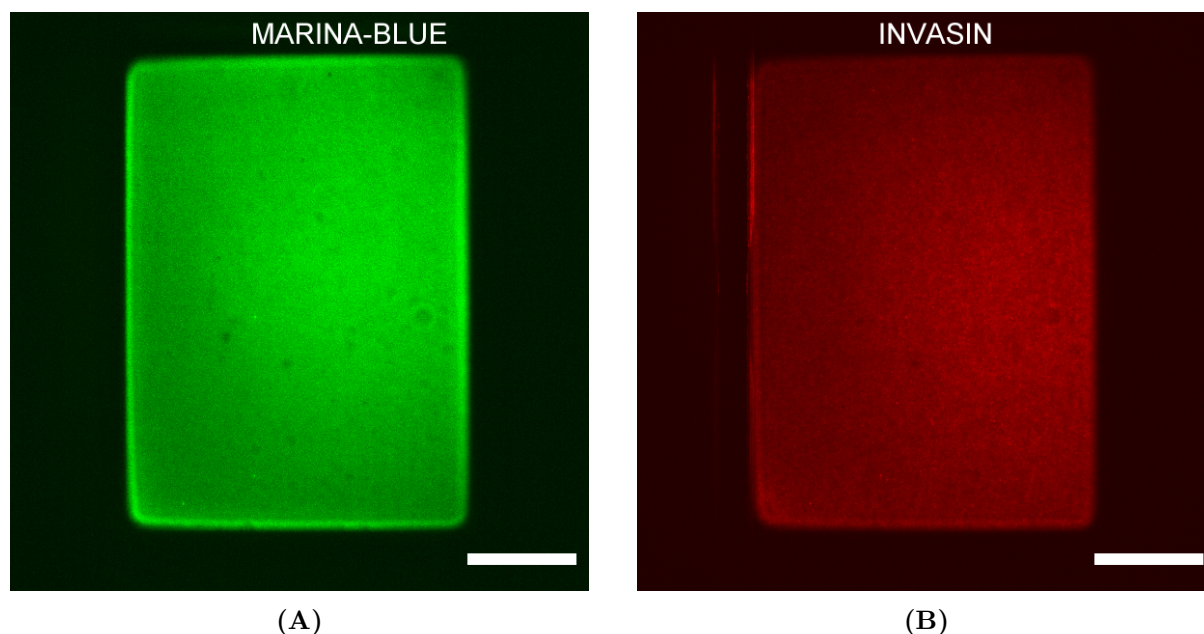


Figure 5.3: Fluorescent microgram of an Invasin-coated SLB.

20um The bilayer is imaged in two fluorescent channels:

A) Lipid channel (DHPE-Marina-Blue, green).

B) Protein channel (JF549-labelled Invasin, red).

Scale bars, 20 μm .

Invasin channels (cf. Figure 5.3). According to the fluorescence calibration (cf. section 6.2 of the microscopy imaging chapter in materials and methods) a homogeneous Invasin distribution on the SLB corresponds to approximately $600 \text{ Invasin}/\mu\text{m}^2$ (under our SLB preparation protocol). If no defaults are detected and in both DHPE-Marina-Blue and Invasin channels, we proceed further and test the SLBs on fluidity.

The fluidity of the prepared SLBs are checked by using the fluorescence recovery after photobleaching (FRAP) technique (cf. Figure 5.4). We can deduce the diffusion coefficients of fluorescent lipids or proteins attached to the bilayer by analysing the fluorescence recovery curves after photobleaching of a small area of the SLB (Soumpasis [1983]).

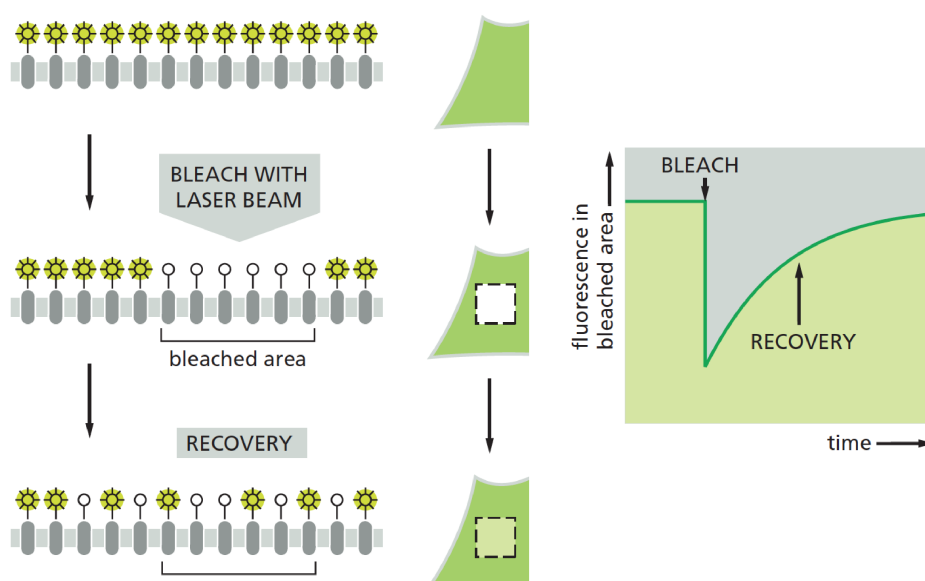


Figure 5.4: Measuring the rate of lateral diffusion of molecules on SLB by FRAP. The fluorescent molecules are bleached in a small area using a laser beam. The fluorescence intensity recovers as the bleached molecules diffuse away and unbleached molecules diffuse into the irradiated area. The diffusion coefficient is calculated from the rate of recovery (right). Figure adapted from Alberts et al. [2008].

We have analyzed the fluidity of both types of SLBs (RGD and Ni without and with bound proteins) with FRAP (cf. Figure 5.5). We have functionalized our SLB(Ni) with fluorescently labelled Invasin and EGFP (as a control). For each sample we have measured 10 FRAP curves in 2 experiments from a photobleached circular zone of approximately $20 \mu\text{m}^2$. Typical normalized fluorescence recovery curves for lipids (DHPE-Marina Blue) of the SLB(Ni) in presence of Invasin and Invasin on the SLB(Ni) are shown in the Figure 5.5A. They were fitted with the following function:

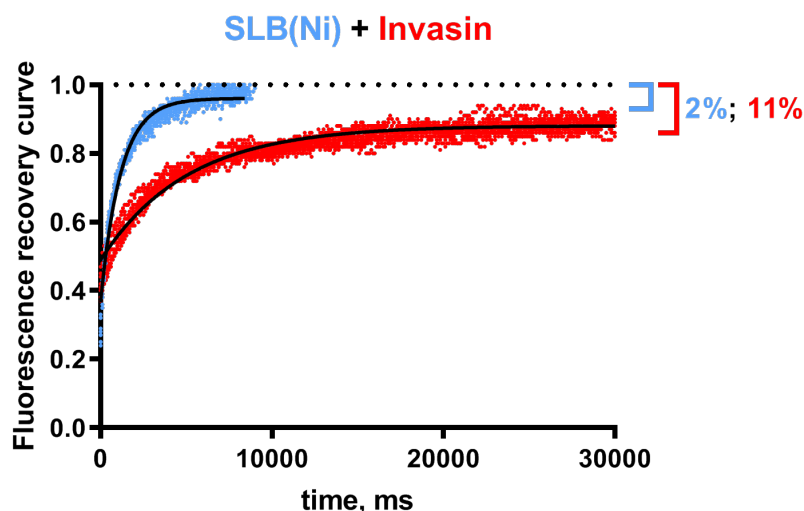
$$f(t) = f_0 + (f_{\text{plateau}} - f_0)(1 - e^{-kt}), \quad (5.1)$$

from which we can find the immobile fraction of fluors as $1 - f_{\text{plateau}}$. Figure 5.5 shows that the interaction of the lipid bilayer with the solid surface is limited since the immobile fraction (cf. Figure 5.5B) for fluorescent lipids is lower than 7% for SLB-RGD, and even lower for SLB-Ni. Lipids remain mobile when Invasin or EGFP is bound to the SLB-Ni. We also see that the immobile fraction of Invasin on the SLB is of the order of 11%, and 5% for EGFP.

The diffusion coefficient D , the radius of the bleached area r and the half-recovery time $t_{1/2}$ are link by the following expression:

$$D = 0.224 \cdot \frac{r^2}{t_{1/2}}. \quad (5.2)$$

The diffusion coefficients for lipids are approximately 75% lower in SLB(Ni) than in SLB(RGD), maybe due to electrostatic interactions between the glass and the Ni-lipids (0.8 versus 1.4 $\mu\text{m}^2/\text{s}$, respectively) (Figure 5.5C). These values are in fairly good agreement with the previous studies of lipid diffusion in lipid bilayer (SLBs or liposomes) (Guo et al. [2008], Pincet et al. [2016]).



(A)

Figure 5.5: Results of the FRAP of Invasin-coated SLBs.

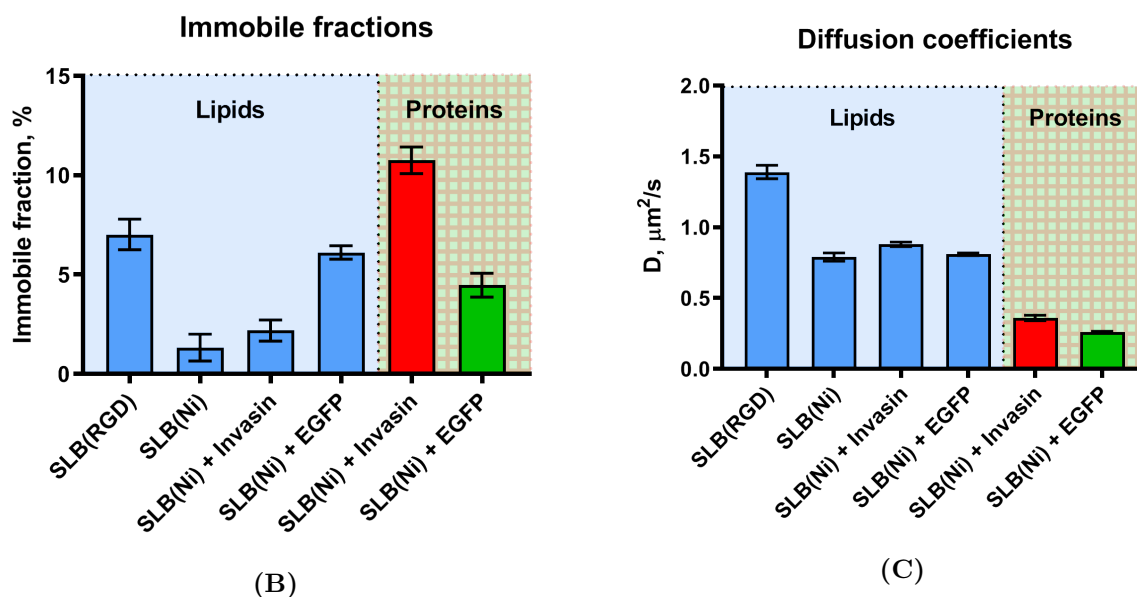


Figure 5.5: Results of the FRAP of Invasin-coated SLBs(cont).

- A) Fluorescence recovery curves normalized by the fluorescence of the neighbouring unbleached regions (diffusion on SLBs coated with Invasin (blue - lipids, red - Invasin)).
 B) Immobile fractions of proteins and lipids.
 C) Diffusion coefficients of proteins and lipids.

Binding of Invasin or EGFP to the bilayer does not change the lipid diffusion coefficient, showing that the bilayer is fluid. As expected, since proteins are bigger than lipids, the protein diffusion coefficients are lower, more than two times lower than that of the lipids (0.4 and $0.3 \mu\text{m}^2/\text{s}$ for Invasin and EGFP respectively). These results show that the RGD-lipids and Invasin-lipids complexes in our experiments are mobile in the bilayer.

5.2 Invasin production

Invasin cloning, expression and purification were performed in collaboration with research engineers at Institut Curie Fahima Di Federico and John Manzi.

5.2.1 Invasin cloning

The plasmid for Invasin expression was constructed in two steps. First, a DNA sequence coding for a TEV cleavage site followed by a 6xHis tag followed by the sequence coding for the last 474 amino acids of Invasin, inv474 (PDB: 1CWV) (in 5' – 3' direction) and flanked by *SacI* and *HindIII* restriction sites was synthesized and subcloned by

Thermo Fisher Scientific. Second, the insert of interest was cloned into a pMal p5x expression vector by digesting with *SacI* and *HindIII* enzymes and ligation. As a result, we have obtained the pOM474 plasmid that expresses a periplasmic maltose binding protein (MBP) fused to Invasin in *E. Coli* periplasm under IPTG inducible P_{tac} promoter.

5.2.2 Invasin expression

We have followed the protocols described in Leong et al 1990 and expressed Invasin in the periplasm to insure the oxidizing environment for the proper disulfide bond formation. We have used an *E. Coli* strain lacking *DegP* protease (Leong et al. [1990]). Proteins were expressed in 2YT medium + selection antibiotics (ampicillin for the plasmid and kanamycin for the *E. Coli* strain at final concentrations 100 $\mu\text{g}/\text{ml}$ and 50 $\mu\text{g}/\text{ml}$, respectively) + 0.2% glucose. Glucose is needed to inhibit amylase expression that can later perturb MBP-Invasin purification. Bacterial culture was inoculated from a single colony and incubated at 30 °C while shaking until the $OD_{600} = 0.5 - 0.6$. Then cells were induced with 0.5 mM IPTG for 4 hours. MBP-Invasin is well expressed at the right molecular size (approximately 96 kDa), thus we can proceed with the protein production, purification and labelling at the bigger scale.

5.2.3 Invasin purification and labelling

Invasin purification was performed in several steps:

1. Affinity purification using an amylose resin;
2. MBP cleavage by TEV protease;
3. Protein labeling with a succinimidyl ester (SE) reactive dye ;
4. Purification by size exclusion chromatography using a Superdex 75 column.

The more detailed protocol illustrates the purification process from 2 liters of bacterial culture that expressed MBP-Invasin:

Cell lysis

1. Resuspend cell pellets in approximately 80 mL **Lysis Buffer**: 25 mM HEPES pH 7.3, 500 mM NaCl, 1 mM EDTA;

2. Add a final of 1x EDTA Free cOmplete protease inhibitor tablet (Sigma Aldrich), 1 mM PMSF, 10 μ g/ml DNase and 10 μ g/ml lysozyme;
3. Cells were lysed via sonication (misonix sonicator ultrasonic processor XL, large probe at 20% intensity) on ice at 70% intensity: 3 sec - On, 3 Sec - Off for 5 minutes;
4. Sample was centrifuged at 20,000 RCF for 60 Min, 4°C and supernatants collected;

Affinity purification against the MBP

5. 10 mL Amylose Resin (NEB) were pre washed in water then Lysis buffer;
6. Cleared extracts were applied to Amylose Resin, and allowed to bind using an tube roller for 2h, 4°C;
7. Samples were washed 2x 40mL using batch method with Wash Buffer 1 (+EDTA);
8. Beads were applied to a column and washed a further 10x CV with the same buffer;
9. Proteins were eluted in 15 mL of Elution Buffer: 25 mM HEPES pH7.3, 500 mM NaCl, 10 mM maltose (the steps of the affinity purification against the MBP were repeated);
10. Protein concentration was estimated by measuring the absorbance spectrum at the Cary Eclipse Fluorescence spectrophotometer; the samples were analyzed by protein electrophoresis on SDS-PAGE gels (cf. Figure 5.6).

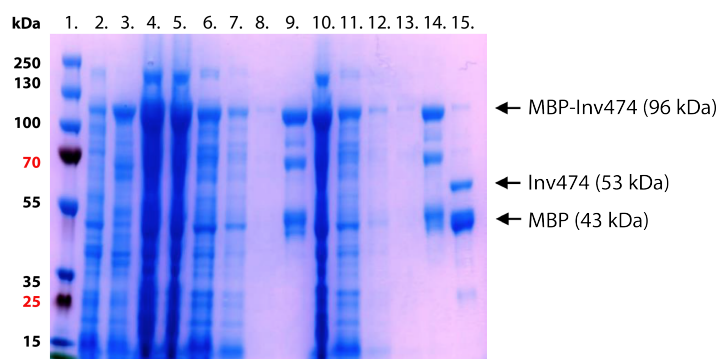


Figure 5.6: SDS-PAGE gel with protein samples from Invasin expression till MBP cleavage by TEV protease.

Lanes of the gel stained with Coomassie blue:

1. Markers; 2. Inv474 – 0h (before induction with IPTG); 3. Inv474 – 4h (after induction with IPTG); 4. Lysate supernatant; 5. MBP unbound; 6. MBP Wash 1; 7. MBP Wash 2; 8. MBP Wash 3; 9. MBP Elution 1; 10. MBP unbound 2; 11. MBP Wash 1; 12. MBP Wash 2; 13. MBP Wash 3; 14. MBP Elution 2; 15. Sample + TEV – O/N.

TEV Cleavage labelling

11. Add TEV protease at about 1:100 (TEV/Invasin, mol/mol);
12. Add JF549 SE dye (Tocris) at about 1:2 (Invasin/dye, mol/mol);
13. Incubate at 4°C in aluminum foil on the rolling table o/n;

Size exclusion purification

14. Labelled samples were concentrated down to approximately 500 μL and purified further by size exclusion chromatography using a Superdex75 column. Buffer: 25 mM HEPES pH 7.3, 120 mM NaCl. The elution fractions were analyzed by protein electrophoresis on SDS-PAGE gels (cf. Figure 5.7).

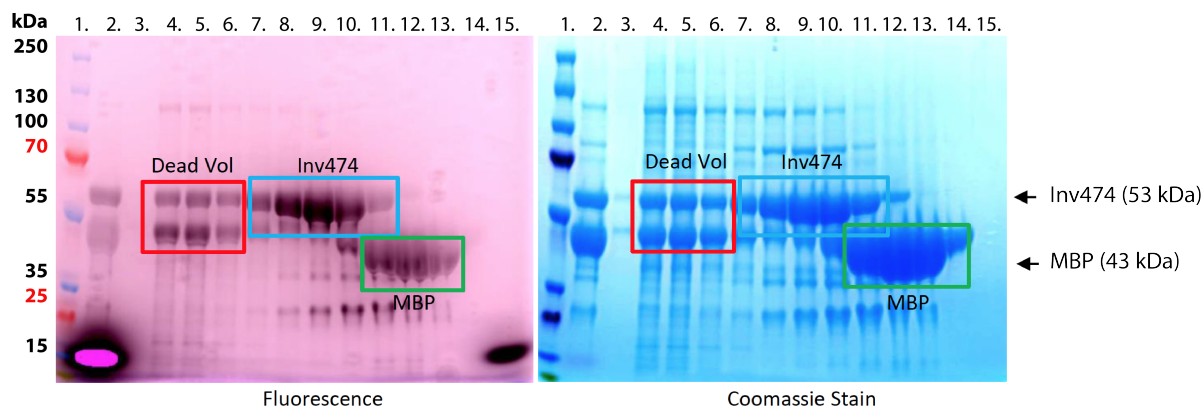


Figure 5.7: SDS-PAGE gel with protein samples from MBP cleavage by TEV protease till the purification by size exclusion.

Fluorescence image of the SDS-PAGE gel was taken (left), then the gel was stained with Coomassie blue (right). Lanes of the gel: 1. Markers; 2. TEV digested and labelled sample; 3. F9; 4. F10; 5. F11; 6. F12; 7. F13; 8. F14; 9. F15; 10. F16; 11. F17; 12. F18; 13. F19; 14. F20; 15. F21. F fractions are the elution fractions after the size exclusion column. F10-F12 correspond to the dead volume. F14-F16 correspond to Inv474. F17-F19 correspond to the MBP.

The fractions 8-10 corresponding to Invasin (cf. Figure 5.7) were collected and its absorbance spectrum was by measured at the Cary Eclipse Fluorescence spectrophotometer. Invasin concentration C and labelling ratio R were estimated from the sample absorbance measurements A_{280} and A_{max} (absorbances at $\lambda = 280$ nm and λ corresponding to the fluorescence of the dye which for the JF549 is 549 nm), the extinction coefficients of JF549 dye ϵ_{dye}^{-1} and Invasin ϵ_{prot}^{-2} ($101000M^{-1}cm^{-1}$ and $57995M^{-1}cm^{-1}$, respectively) and the CF correction coefficient³ that is equal to 0.169.

¹<https://www.tocris.com/products/janelia-fluor-549-se6147>

²<https://web.expasy.org/protparam/>

³<https://www.tocris.com/products/janelia-fluor-549-se6147>

$$C = \frac{A_{280} - A_{max} \cdot CF}{\epsilon_{dye}}; \quad (5.3)$$

$$R = \frac{A_{280}}{\epsilon_{prot} \cdot C}; \quad (5.4)$$

Therefore, we have obtained $C = 23.4 \mu M$ and $R = 43\%$.

5.3 Cell culture preparation

5.3.1 Cell line description

In this work, we have used a β_1 KO β_1 -Halotag MEF cell line (gift from David Calderwood, Yale University). The cell line was constructed by lentiviral transfection of a β_1 KO MEF cell line with an ecto-tag construct based on pLENTI expression vector. The Halotag

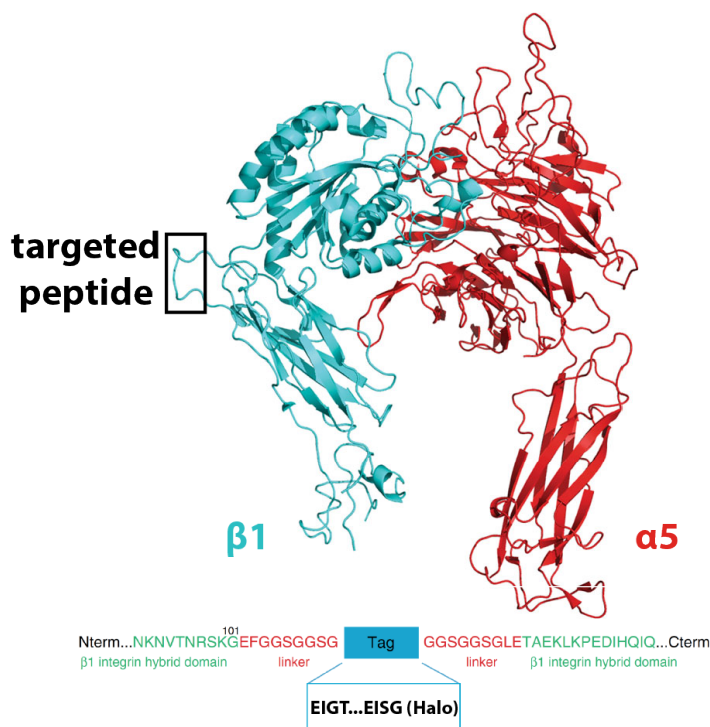


Figure 5.8: Design of an Halo-tagged β_1 integrin.

Ribbon diagram of the crystal structures of the $\alpha_5\beta_1$ integrin head piece (PDB: 3VI4). The hybrid domain loop into which the HaloTag[®] was inserted is indicated (black rectangle). Zoom-in on the amino acid sequence of human Halo-tagged- β_1 integrins at the tag insertion site. Figure adapted from Huet-Calderwood et al. [2017].

sequence was inserted on an exposed loop (β_1 residues 91-114) (Huet-Calderwood et al. [2017]) (cf. Figure 5.8).

Integrin expression levels and its targeting to the PM were controlled with immunoblots and FACS (Huet-Calderwood et al. [2017]). Ecto-tag β_1 integrins were shown to be targeted to FA colocalizing with vinculin (cf. Figure 5.9). Additionally, we have used a cell line stably expressing paxillin-mCherry (gift from David Calderwood, Yale University).

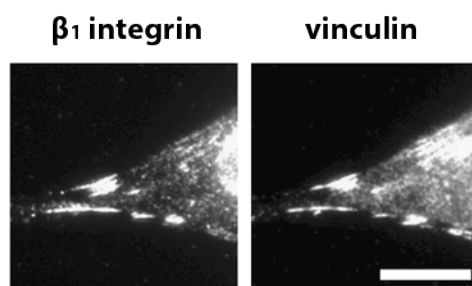


Figure 5.9: Halo-tagged β_1 integrins translocate to the cell surface and target to FAs.

Microscopy images of fibroblasts expressing Halo-tagged β_1 : integrin immunofluorescence with 9EG7 antibody (left), and vinculin immunofluorescence (right). Scale bar, 10 μm .

Figure adapted from Huet-Calderwood et al. [2017].

Integrin activation was not perturbed in the cell line. This was verified by assessing binding to fibronectin (FN) fragment containing FN type III repeats 9 and 10 (FN9-10) in a well-established FACS assay (Bouaouina et al. [2012]) (cf. Figure 5.10).

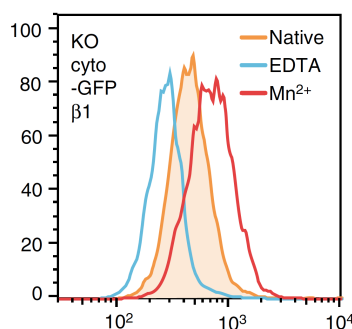


Figure 5.10: Flow cytometry histogram of β_1 -Halotag fibroblasts binding to RGD.

Flow cytometry histogram shows binding of soluble FN9-10 (% of max) to the β_1 KO β_1 -Halotag fibroblasts, in native conditions (filled orange peak), EDTA-inhibited conditions (blue peak), or Mn^{2+} -treated conditions (red peak).

Figure adapted from Huet-Calderwood et al. [2017].

5.3.2 Cell transfection

We have performed cell transfection by electroporation following the protocol described by (Gautreau et al. [2000]). For transfection, trypsinized cells were resuspended at a concentration of 2.5×10^7 cells/ml in 15 mM HEPES, pH 7.4, buffered medium. 200 μ l of cell suspension was added to 50 ml of a solution containing 210 mM NaCl, 5 mg of plasmid DNA, and 30 mg of salmon sperm DNA carrier (SigmaAldrich). LLC-PK1 cells were electroporated with a BioRad Gene Pulser at 950 mF and 240 V using 4-mm width cuvettes. Transiently transfected cells were analyzed after 24-48 h protein expression.

We have used the plasmids coding for the following proteins for cell transfection: talin-mCherry, vinculin-mCherry (both from Guy Tran van Nhieu, ENS Paris Saclay), zyxin-mCherry (gift from Danijela Vignjevic, Institut Curie), kindlin-2-mCherry (gift from Christof Hauck, Konstanz University).

5.3.3 Cell culture and preparation for the adhesion experiment

In cell adhesion experiments we have used mouse embryonic fibroblast (MEF) cells. They are cultured in Dulbecco's Modified Eagle's Medium (DMEM) high glucose with 10% fetal calf serum and 1% penicillin-streptomycin. Cells are serum starved for 24 hours before experiment. Cells are detached by Versene solution for 30 minutes at 37°C. Then they are incubated with a dye containing a Halotag[®] ligand (400 nM per 1 ml containing approximately 1.5-2 million cells) to label β_1 -integrin-Halotag for 10-15 minutes at room temperature. Then cells are spun down at low centrifuge speed (1000 rpm in Megafuge 16R centrifuge from Thermo Scientific), resuspended in the **cell buffer** (25 mM HEPES pH 7.3; 120 mM NaCl; 7 mM KCl; 1.8 mM CaCl₂; 0.8 mM MgCl₂; 5 mM glucose) to remove the Versene and the excess of dye and filtered with Falcon 40 μ m Cell Strainer (Corning) to remove cell clumps. Cells are then put to the imaging chamber just before the imaging starts (at the time point 0). In the experiments with manganese-treated cells, MnCl₂ was added (to the final 0.5mM concentration) just before putting cells into the imaging chamber. For fixed cell experiments, cells were fixed with 4% paraformaldehyde (PFA) for 30 minutes at room temperature. Actin in fixed cells was labelled with Alexa Fluor 647 Phalloidin (from ThermoFischer Scientific).

The cell line was shown to be mycoplasma free after testing it following a well-established PCR-based method (Young et al. [2010]) with the following primers: Myco-fw GGGAGCAAACAGGATTAGATACCCT; Myco-rev TGCACCATCTGTCACTCTGT-TAACCTC.

Chapter 6

Microscopy imaging

6.1 Setup

Microscopy experiments were done in the Nikon Imaging Center at Institut Curie. We have used a spinning disk microscope to image fluorescent lipid bilayers and cell adhesion on them. The microscope consists of a CSU-X1 Yokogawa head mounted on an inverted Ti-E Nikon microscope with a motorized XY stage (MadCity Lab[®]). Images were acquired with Metamorph software (Molecular Devices[®]) through a 100x NA1.45 objective with a Photometrics 95B-sCMOS camera. Live cell adhesion imaging was performed at 30°C using the stage top incubator (Tokai hit[®]). Fixed cells were imaged at RT with the same microscope.

The setup is equipped with 4 Cobolt lasers from Hübner Photonics: 405 nm (100mW), 488 nm (100mW), 561 nm (50mW) and 633 nm (100mW). They allow sample imaging in 4 fluorescence channels ('405', 'GFP', 'cy3' and 'cy5'). Samples can also be imaged in wide field mode using the transmission light from LED source. The setup is also equipped with a FRAP photoactivation module.

6.1.1 Imaging conditions

Unless it is staged otherwise we have used the same imaging conditions in our microscopy experiments (cf. Table 6.1). Z-stack images of 2.8 μm height are taken. The stack is centered at the SLB plane and its step is 0.4 μm . After that in all cases but one (cf. 11.4 of the Results) of the results) the maximum projection of the stack is made. Although we lose resolution in z-direction by doing the projection for many samples we would be less influenced by slight coverslip tilts that defocus the sample.

Table 6.1: Fluorescence channels.

Channels	405	GFP	Cy3	Cy5
Laser wavelength, nm	405	491	561	633
Laser power, %	15	30	30	30
Exposure time, ms	100	300	300	300

6.1.2 Optical resolution

We have used the following fluorophores in the project: Marina Blue-DHPE, Alexa Fluor 488, mCherry, JF549, Alexa Fluor 647.¹ The optical spatial resolution limit (lateral-xy and axial-z) for the spinning disk microscope can be estimated by the following formulas²:

$$Res_{xy} = 0.51 \cdot \frac{\lambda_{em}}{NA}; \quad (6.1)$$

$$Res_z = z_{FWHM} = 0.64 \cdot \frac{\bar{\lambda}}{n - \sqrt{n^2 - NA^2}}; \quad (6.2)$$

where $\bar{\lambda} = \sqrt{2} \cdot \frac{\lambda_{ex} \cdot \lambda_{em}}{\sqrt{\lambda_{ex}^2 + \lambda_{em}^2}}$ and $n = 1.52$ being refractive index of glass.

Table 6.2: Optical resolution for different fluorophores.

Fluorophore	λ_{ex}	λ_{em}	$\bar{\lambda}$	Res_{xy}	Res_z
DHPE-Marina Blue	365	460	404	162	243
Alexa Fluor 488 %	499	520	509	183	306
JF549	549	571	560	201	337
mCherry	587	610	598	215	360
Alexa Fluor 647	650	671	660	232	397

In practice, the optical resolution limit is larger than these theoretical values. To better estimate it we have imaged fluorescent beads that are smaller than the diffraction limit (TetraSpeck fluorescent microspheres of nominal diameter 100 nm from ThermoFisher Scientific) (cf. Figure 6.1). The beads are stained with a green dye ($\lambda_{ex}/\lambda_{em}$: 505/515 nm). We have segmented the image using the Renyi Entropy threshold method in ImageJ

¹www.aatbio.com/fluorescence-excitation-emission-spectrum-graph-viewer

²www.hi.helsinki.fi/amu

and measured w , the width of the point spread functions (PSFs). The width w is 339 ± 63 nm (from the 478 beads analyzed). If we approximate the PSF function with a Gaussian, the width is larger than the full width at half maximum (FWHM) that corresponds to the optical resolution limit (cf. Figure 6.1). Thus, we have obtained the lower and the upper values for the estimation of the optical resolution in the green channel and can conclude that the real optical resolution limit might be between 180 and 340 nm.

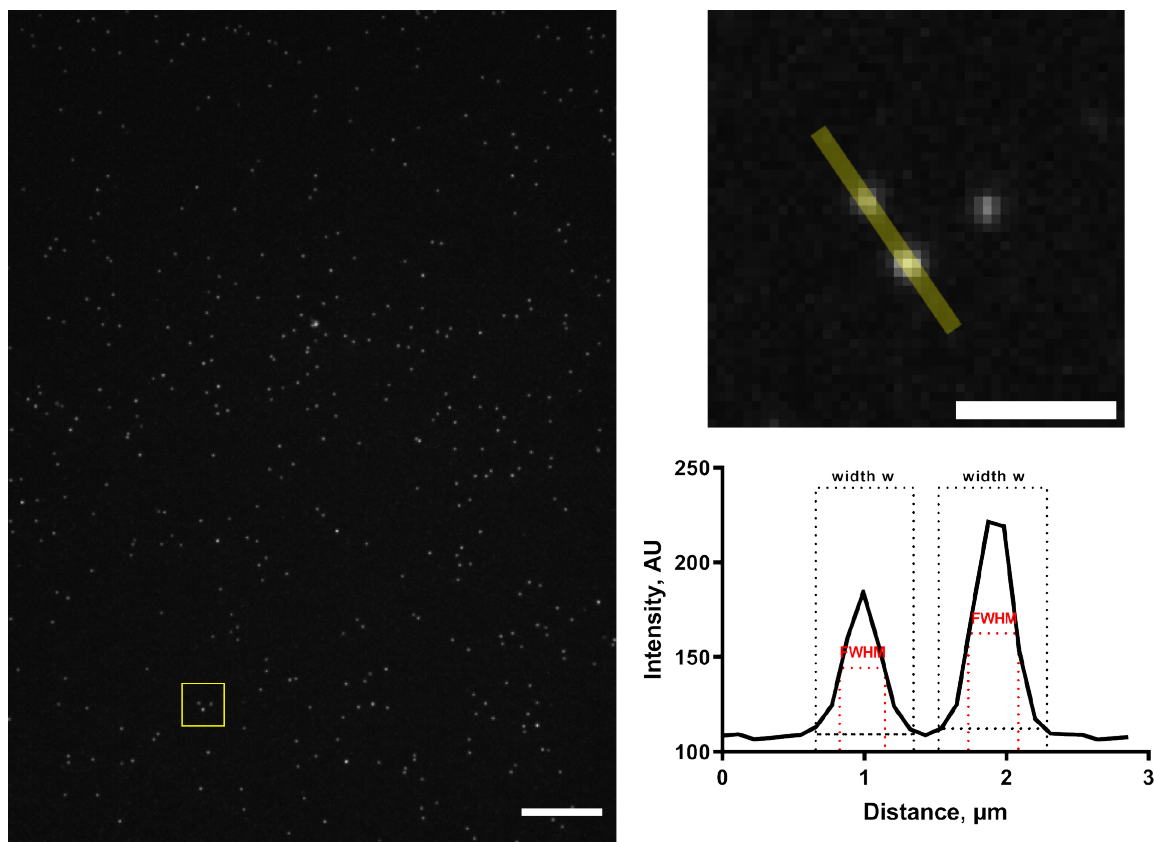


Figure 6.1: Measurement of the point spread function with fluorescent beads. Fluorescence image of green fluorescent beads of nominal diameter 100 nm (left). The zoomed area corresponding to the yellow square on the left image (top right). Intensity profile along across two beads (bottom right) on which the detected width w and FWHM are shown. Scale bars, $20 \mu\text{m}$ (left) and $2 \mu\text{m}$ (right).

6.2 Fluorescence calibration

The aim of the calibration is to quantify the density of fluorescence species in the cell adhesion plane by using supported lipid bilayers as fluorescence standards. The original protocol of the calibration is described in (Galush et al. [2008]).

6.2.1 Calibration principle

Within a certain range of fluorophore densities, we can relate the density of the fluorescence species n_{fl} [μm^{-2}] and the intensity I_{fl} [AU] of the fluorescence image of the cell surface in the adhesive contact by the following:

$$n_{fl} = A_{fl} \cdot I_{fl}; \quad (6.3)$$

where A_{fl} is the proportionality factor that depends on the fluorescent molecule and imaging conditions. This linear relationship holds for concentrations below the critical concentration at which fluorophores start to self-quench Dahim et al. [2002]. The range of densities of fluorescence species where this linear relationship holds is verified during the calibration process.

Standards have to be used to calibrate the fluorescence in membranes, in illumination conditions similar to the experiments. In practice, fluorescent lipids are convenient since they can be incorporated in the bilayer at controlled concentration, thus their density is known and the corresponding fluorescence can be measured as a function of their density. Here, SLBs are particularly suitable if the fluorescence intensity is measured in the exact same conditions as in the experiments where the contact zone between cells and SLBs are imaged. But, to account for differences in fluorescence yield between the fluorescent markers on the lipid and the protein, the fluorescence of the lipids and the proteins at known concentrations must be compared; for this, measurements in bulk are well-suited.

The proportionality factor A_{fl} is related to the proportionality factor of the calibration standard A_{st} by the following relation:

$$A_{fl} = \frac{A_{st}}{F \cdot n^*}; \quad (6.4)$$

where the correction factor $F = I_{fl}/I_{st}$ is the ratio between the intensities of the fluorescence species I_{fl} and the standard I_{st} at a given concentration in solution and n^* is the labeling molar ratio of the fluorescence species. $n^* = 1$ for lipids, but might be $\neq 1$ for proteins, depending on the efficiency of the labeling protocol. n^* must be measured for each preparation of proteins with a spectrophotometer.

F takes into account the optical properties of the microscope and spectral differences between the fluorophore and the standard. In order to determine A_{fl} for a given fluorophore, we need to do the following:

1. Calibrate our imaging system with a standard fluorophore and measure the proportionality factor A_{st} in SLB with fluorescent lipids;
2. Measure the correction factor F with experiments in solution.

More precisely, in the first step, we prepare a series of SLBs with fluorescence lipids (standard) incorporated at known densities. Then we image these SLBs with exactly the same imaging conditions (laser powers, exposure times and fluorescence channels, or sets of fluorescence filters) as we do for the fluorophore of interest. In the second step, we measure the correction factor F, the dimensionless factor that represents the efficiency of the fluorophore versus the standard. Practically, to calculate F, we measure the ratio of intensities between the fluorophore and the standard at a given concentration in solution (in bulk), or more precisely, the ratio of the slope of the plots Intensity versus bulk concentration, for both fluorophores, α_{st} and β_{fl} . This measurement must be done directly at the microscope with exactly the same imaging conditions as for the first step.

We have done 3 calibrations (1 in the green channel, 2 in the red channel) for the following molecules: AlexaFluor488, JF549 and mCherry protein. We have used Bodipy FL DHPE (Molecular probes, referred to as BodipyFL in the following) and Texas Red DHPE (Invitrogen, referred to as TexasRed in the following) lipidated dyes as standards for the green and the red calibrations, respectively.

6.2.2 Fluorophore preparation

All fluorophores, except the lipidated ones, were diluted in the working EM buffer. As lipids would aggregate in aqueous solution, we have solubilized them in detergent. Lipid solutions of BodipyFL or TexasRed were blow-dried under argon and vacuum for 30 minutes, and re-solubilized in the working EM buffer with 2.25 mM n-Dodecyl β -D-maltoside (DDM).

The accuracy of the calibration greatly relies on the precise knowledge of the fluorophore concentrations. The concentrations of all samples were checked on Cary Eclipse Fluorescence Spectrophotometer using the following published extinction coefficients: AlexaFluor488 ($73000 \text{ M}^{-1}\text{cm}^{-1}$), BodipyFL ($80000 \text{ M}^{-1}\text{cm}^{-1}$), JF549 ($101000 \text{ M}^{-1}\text{cm}^{-1}$), TexasRed ($116000 \text{ M}^{-1}\text{cm}^{-1}$), mCherry ($72000 \text{ M}^{-1}\text{cm}^{-1}$).

6.2.3 Imaging of the fluorophores in bulk and on SLBs

All the samples were imaged with our microscope and the precise imaging conditions corresponding to either green or red calibrations:

Table 6.3: Imaging conditions for fluorescence calibrations.

Calibration	Green	Red
Laser wavelength, nm	491	561
Laser power, %	30	30
Exposure time, ms	300	300
Excitation filters	ZET405/488/561/640xv2	same
Emission filters	525/50	585/40

The images of the fluorophores in bulk were taken approximately 10 μm above the coverslip. We have observed that the intensity distribution of the fluorescence signal of a dye in solution is not homogenous in the imaging plane (cf. Figure 6.2). This is related to the non-homogeneous illumination. The illumination seems to be more or less homogeneous in the middle of the illumination pattern (the plateau). For our analysis we have only considered the intensity in this region.

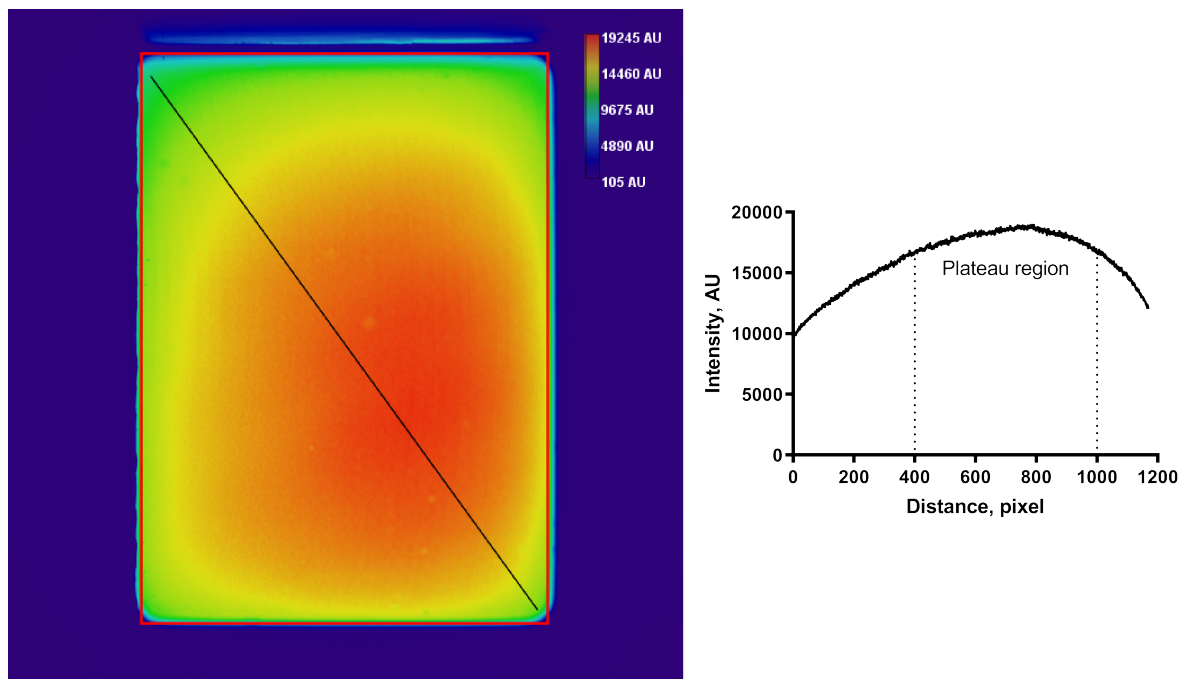
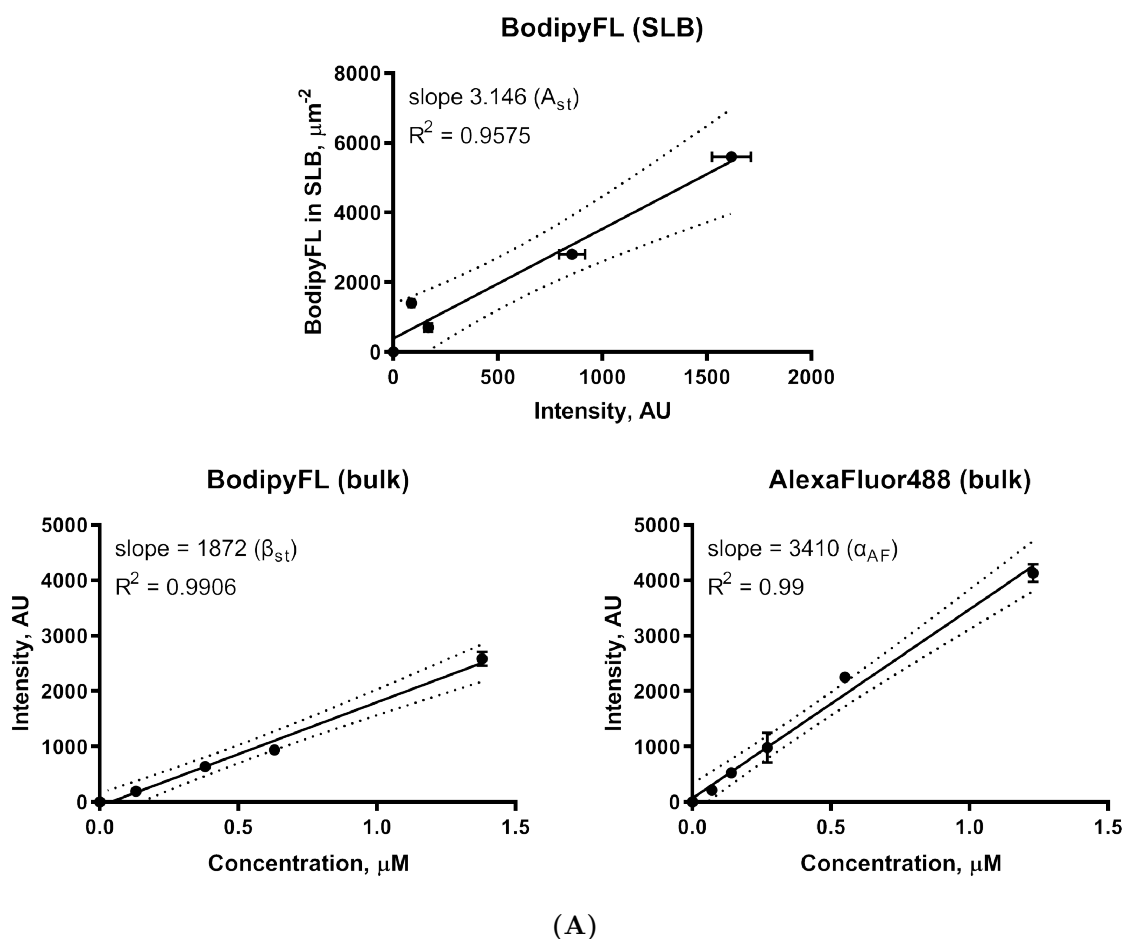


Figure 6.2: Illumination inhomogeneity in the field of view of the microscope. Pseudocolored fluorescence image of the dye solution (left). Intensity profile along the diagonal of the field of view (right).

The standard SLBs (DOPC + BodipyFL) with different concentrations of BodipyFL were prepared following the protocol described in this thesis (cf. section 5.1 in the Materials and Methods). We have calculated the surface densities of BodipyFL in the SLBs from their molar ratios and assuming the area of a DOPC lipid projected on the SLB plane to be 0.72 nm^2 and, thus, the number of lipids per μm^2 to be $2 \cdot \frac{\mu\text{m}^2}{0.72\text{nm}^2} = 2.8 \cdot 10^6$ (where the factor 2 is to take both bilayer leaflets into account) (Naglea and Tristram-Nagleb [2015]). For each sample 30 images were taken and the intensities of the plateau region were averaged. We have plotted the density-intensity standard curves for both calibrations and also intensity-concentration curves for all fluorophores in bulk (cf. Figure 6.3). Therefore, we obtain the following calibration values for our fluorescence species (cf. Table 6.4).

Note that the calibration factors were measured from fluorescent dyes in solution and not from fluorescent proteins. Galush et al. [2008] showed that, for instance, F was about 3 times higher with AlexaFluor488 bound to anti-biotin than to Streptavidin. But, weaker differences were observed in other cases. In practice, we should purify the proteins



(A)
Figure 6.3: Fluorescence calibration curves.

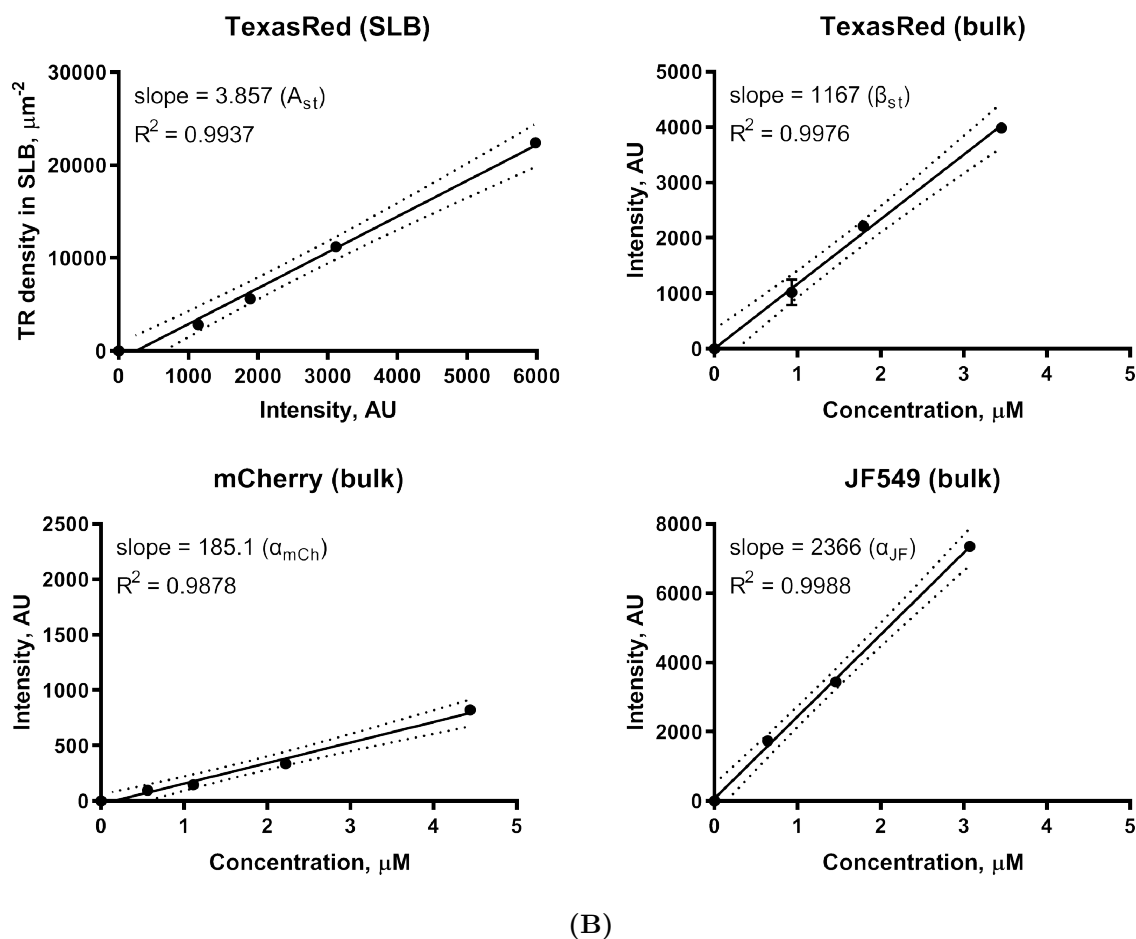


Figure 6.3: Fluorescence calibration curves(cont.).

Green (A) and red (B) calibrations were performed. The relationships between concentrations and detected intensities are plotted for fluorophores in bulk and on SLBs. They are fitted with linear curves. The slopes of the curves are shown on the graphs. Dots represent the 95% confidence bands of the fit.

Table 6.4: Fluorescence calibration coefficients.

Proteins	$A_{st}, \mu\text{m}^{-2}$	$\alpha_{fl}, \mu\text{M}^{-1}$	β_{st}	$F = \frac{\alpha_{fl}}{\beta_{st}}$	n^*	$A_{fl} = \frac{A_{st}}{F \cdot n^*}, \mu\text{m}^{-2}$
β_1 -integrin labelled with Alexa Fluor 488	3.146	3410	1872	1.82	1	1.73
JF549 labelled Invasin	3.857	2366	1167	2.03	0.427	4.45
mCherry labelled proteins	3.857	185	1167	0.16	1	24.11

of interest, label them and make the calibration, which is not possible. In addition, it is possible that the dye fluorescence is different in the cell environment as compared to

the buffer. Thus, the absolute values of the protein densities in the adhesion structures that we deduce from our experiments might be off by some systematic factor, however, it cannot be by an order of magnitude.

Chapter 7

Image analysis

Our image analysis pipeline consists of the following actions: cell contour detection in the wide field channel, protein clusters detection in the corresponding fluorescence channels, illumination correction, protein cluster quantification by using the fluorescence calibration and radial distributions of adhesion clusters. The programs were developed in collaboration with a research engineer at the Nikon Imaging Center at Institut Curie Anne-Sophie Macé. The source codes of the developed programs can be found [here](#).

7.1 Cell contour detection

We detect the cell contour in the wide field images semi-automatically. This means that the program applies an automatic routine to segment cells in the image (cf. Figure 7.1,

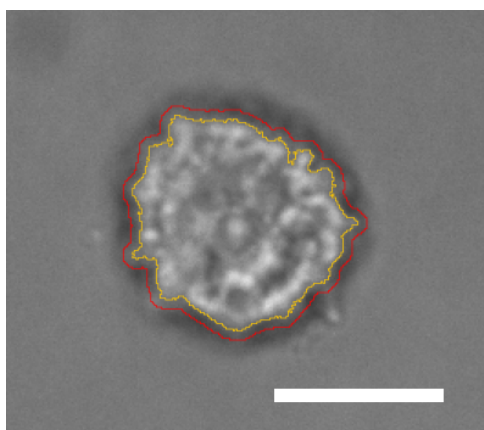


Figure 7.1: Cell contour detection.

Illustration of the result of the semi-automatic cell contour detection in a wide field image. The cell contour originally found by the program is depicted in yellow. The enlarged (and smoothed) by the program yellow cell contour is depicted in red. Scale bar, 10 μm .

yellow line). Then the user approves or not the segmentation. If the segmentation is wrong the program proposes a manual polygonal selection for cell segmentation. The automatic routine consists in thresholding wide field channel images with the ImageJ's auto threshold “*Mean white*” method and finding particles of the typical size of cells with ImageJ's “*Analyze particles*” plugin. “Cell contour” is then used to calculate the cell area and the cell circularity index $C = \frac{4\pi A}{P^2}$, where A is the cell area, P is the cell perimeter. The circularity index is computed on the “*enlarged*” by 5 pixels' contour (cf. Figure 7.1, red line). This is done to avoid contour roughness on the scale of several pixels.

7.2 Protein cluster detection

We have used an automatic image segmentation algorithm based on **Renyi's entropy thresholding** to detect protein clusters. This thresholding method was described in Kapur et al. [1985] and is now one of the standard threshold methods available in ImageJ. The method defines a threshold intensity value that separates two distributions (object and background) by maximizing the informational entropy and entropic correlation of those distributions (Sahoo et al. [1997]). Practically, for any given image of adhesion clusters the method based on the grey-level intensity histogram automatically defines an intensity threshold value Θ that separates the cluster signal from the background noise (cf. Figure 7.2).

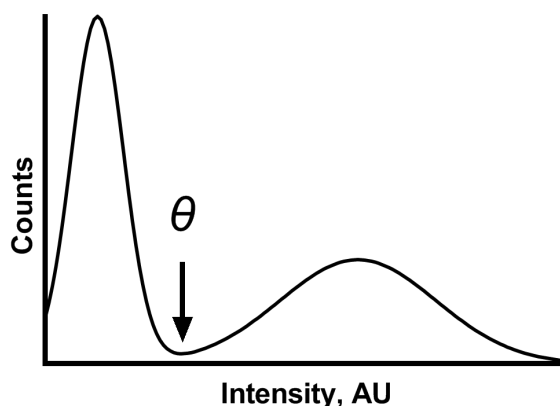


Figure 7.2: Histogram-based image segmentation.

Intensity threshold Θ separates the peaks of the background (low) and the signal (high) in the intensity histogram of a typical fluorescence image.

Thus, for example, we obtain the segmented integrin clusters (circled with yellow lines in Figure 7.3A). After the detection of the clusters we define the *adhesion zone* (**AZ**) of the cell as the smallest convex area that contains all the detected integrin clusters.

We use “*Convex hull*” function in ImageJ to select the **AZ** from the detected clusters (cf. Figure 7.3A, red line). Invasin holes can be detected with the same algorithm applied to the inversed image in Invasin fluorescence channel (when holes become clusters) (cf. Figure 7.3B).

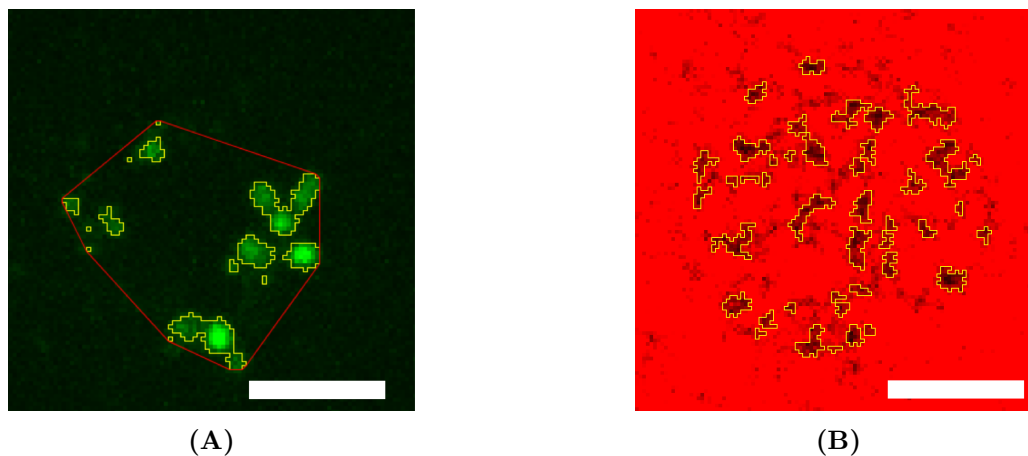


Figure 7.3: Detection of Integrin clusters and Invasin holes.

Illustration of the results of the automatic integrin clusters (A) and Invasin holes (B) detection in a fluorescence image. Clusters and holes are depicted with a yellow line. The red line in (A) shows the **AZ**.

Scale bars, $10 \mu m$.

7.3 Protein cluster quantification

To quantify the detected protein clusters we need to make a correction on the illumination inhomogeneity. The illumination is not homogeneous across the image (cf. Figure 6.2). Therefore, we have introduced the "illumination" map to correct this issue. It consists in normalizing the image by that of a fluorescent supported lipid bilayer (SLB). The SLB has a homogeneous distribution of fluorescent lipids in the image plane, so it is a perfect candidate for the illumination map. The intensities of the illumination map range between 0 (the dimmest illumination) and 1 (the brightest illumination). Therefore, the image correction for the illumination inhomogeneity is obtained by the division of pixels' intensities of the image by the intensities of the corresponding pixels of the illumination map.

After protein cluster detection, illumination correction and fluorescence calibration for the fluorophore labelling the protein, we can proceed with cluster quantification. First, we convert the pixel values of each cluster from AU of intensity to protein density [μm^{-2}] by dividing them by the corresponding pixels of the illumination map and multiplying

them by the proportionality calibration factor of the fluorophore (A_{fl}). The transformed image will represent the protein density map (cf. Figure 7.4).

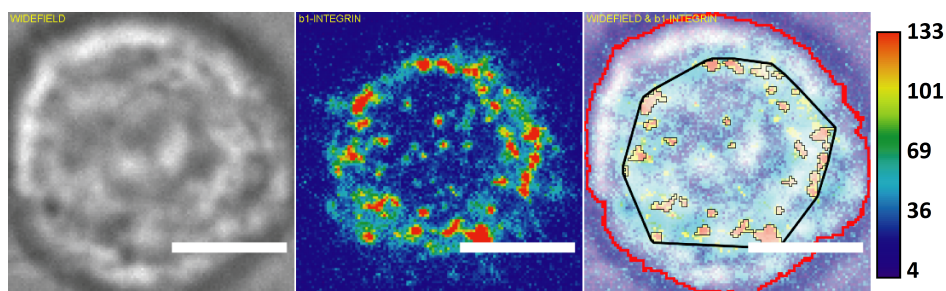


Figure 7.4: Integrin cluster quantification.

β_1 -integrin clusters are quantified based on a prior fluorescence calibration and illumination correction (cf. section 6.2 of Microscopy imaging chapter in materials and methods). Integrin density is represented with the pseudo-color (color code on the right in proteins/ μm^2). Scale bar, 10 μm .

Next, we can calculate the mean protein densities in the cluster as well as the number of proteins in the clusters by either taking the mean of the corrected values of the pixels in the clusters or multiplying this mean by the cluster area. Cells adhering on SLBs have a near round shape. We have divided the images of every cell into 10 sections (centered at the cell center of symmetry): 9 concentric rings of the same width $\frac{R}{10}$, where R is the cell radius and 1 circle in the center (cf. Figure 7.5). We have done that by taking the cell contour and scaling it down 9 times by 10% with an ImageJ command “*Enlarge*”. The protein clusters that are located in the same ring will have the same radial coordinate ($\pm \frac{R}{10}$).

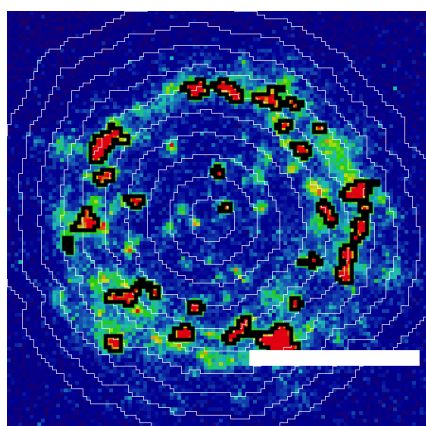


Figure 7.5: Radial segmentation of a fluorescence image.

Fluorescence image from the figure 7.4 is divided in 10 concentric rings. Scale bar, 10 μm .

Part III

Results

Chapter 8

Cell adhesion. Role of substrate properties

When cells are seeded on substrate, they sediment and reach the substrate surface and the cell adhesion begins. Cell adhesion is a complex process that can be viewed at different length scales:

- the largest scale (several microns) corresponding to the cell size;
- the intermediate scale corresponding to the adhesion zone, the contact area between the cell and the substrate (around $1 \mu m$);
- the scale corresponding to the individual clusters of adhesion molecules inside the adhesion zone (hundreds of nm). This is the smallest scale that can be reached with classical optical microscopy;
- the smallest scale corresponding to the individual adhesion molecules inside the adhesion clusters (tens of nm). This scale can be reached with super-resolution microscopy.

In this work we have characterized cell adhesion on the first three length scales by using classical fluorescence microscopy techniques. In this chapter we have focused on the largest scale. We have introduced two parameters that can be deduced at this scale: the shape of the spreading cell and the adhesion index of the cell. We have studied the role of the substrate nature in the cell adhesion using these parameters.

8.1 Cell spreading

The way cells spread depends on the substrate mechanical properties (Prager-Khoutorsky et al. [2011]). We can distinguish different spreading behaviours by comparing the areas of spreading and the shapes of adhering cells. In this section we have characterized and compared cell spreading on different substrates: solid (glass) and fluid (supported lipid bilayer, or SLB) substrates. Both types of substrates are coated with integrin ligands (fibronectin, RGD and Invasin). Ligands are immobilized on glass and freely diffusing on SLBs (cf. chapter 5 of the Materials and Methods).

We can follow the evolution of cell spreading on the typical fluorescence images (cf. Figure 8.1). We observe a transition in the cell shape for the cells adhering on glass. After approximately 1 hour of spreading it changes from a symmetric round shape to an irregular one (cf. Figure 8.1A-8.1B). Additionally, cells undergoing this transition flatten and their contact area with the substrate increases. On SLB cells remain round-shaped and their contact area with the substrate does not change during the whole time of observation (1 hour 30 minutes) (cf. Figure 8.1C-8.1D). These observations are consistent with the results of the previous studies of cell adhesion on SLBs (han Yu et al. [2013]).

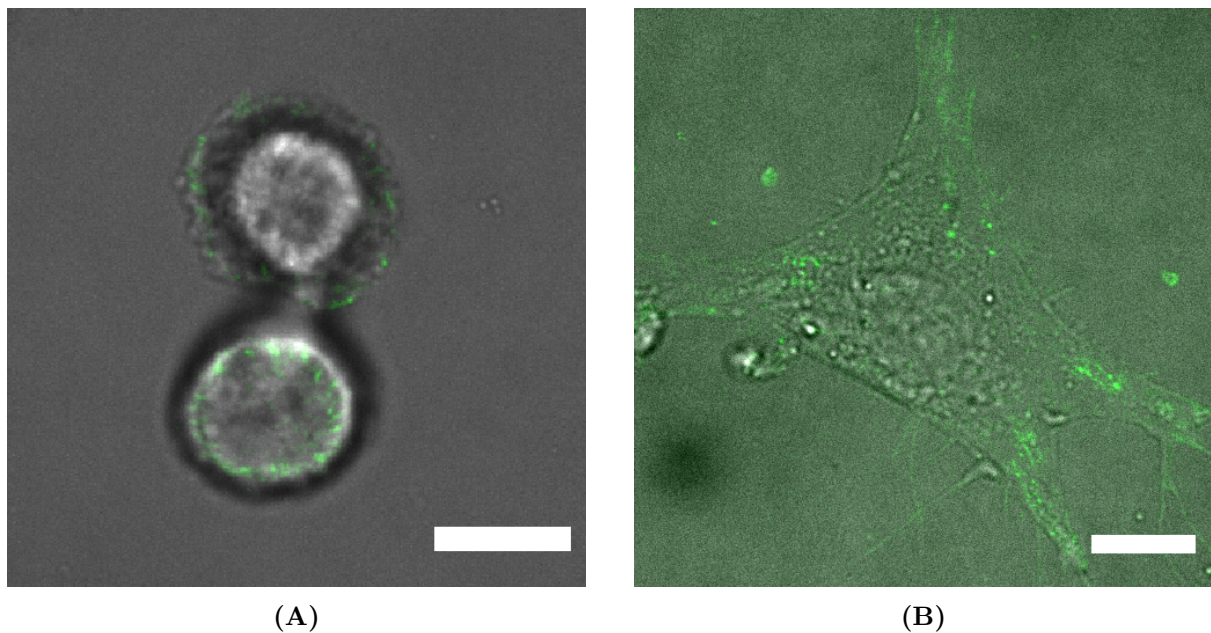


Figure 8.1: Cell shape evolution during adhesion.

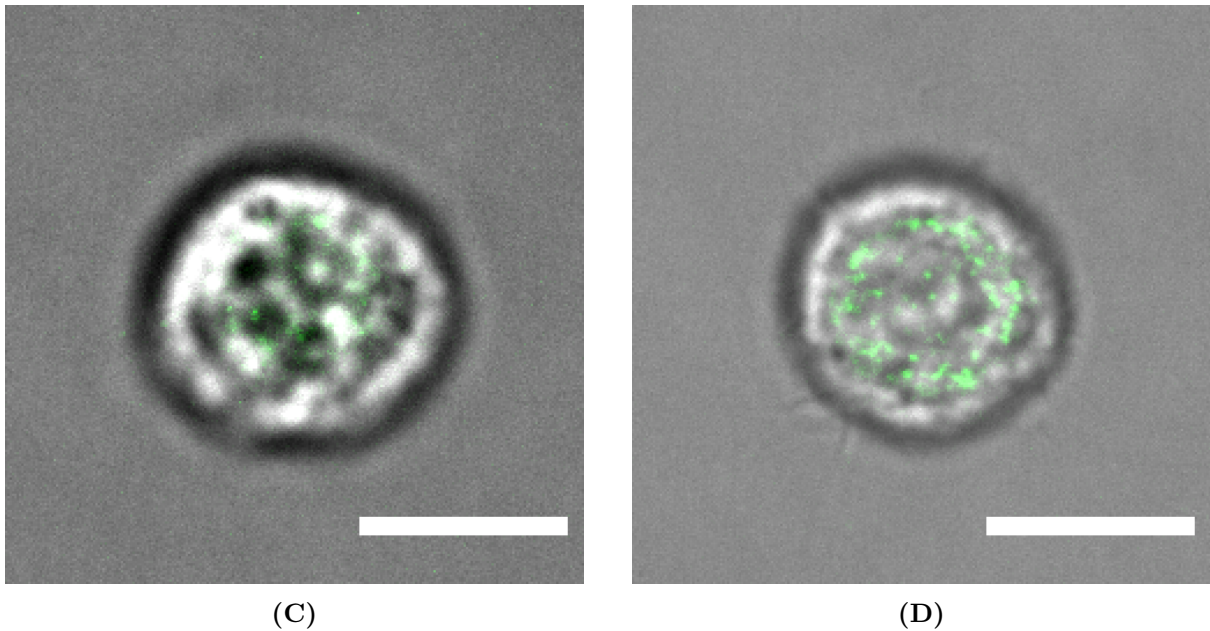


Figure 8.1: Cell shape evolution during adhesion(cont.).

Multi-channel images of cells adhering on Invasin-coated glass and Invasin-functionalized SLB: β_1 -integrin (green), cell contours in wide field (grey). Early stage - 30 minutes; late stage - 1 hour of adhesion. Scale bar, 10 μm .

- A) Early stage spreading on glass: a round shaped cell with FA forming at the edge.
- B) Late stage spreading on glass: an irregular shaped cell with developed FA.
- C) Early stage spreading on SLB: a round shaped cell with integrin adhesion structures (not FA) forming further from the cell edge.
- D) Late stage spreading on SLB: a round shaped cell with integrin adhesion structures (not FA) forming further from the cell edge.

Furthermore we have quantified the degree of irregularity of the shape of adhering cells on solid and fluid substrates. More specifically, we have measured the cell circularity index $C = \frac{4\pi A}{P^2}$, where A is the cell area (manually segmented from the wide field image of the cell), P is the cell perimeter (Figure 8.2). For a perfectly round cell it is equal to 1. For a cell with a more irregular shape it is less than 1. For instance, the circularity indexes of the round shaped cells on glass and on SLB (cf. Figure 8.1A, 8.1C, 8.1D) are 0.96, 0.97 and 0.97, and of the irregular shaped cell (cf. Figure 8.1B) – 0.25.

Next, we have compared the spreading in terms of circularity index and cell contact area for cells adhering 1 hour on glass and SLB, and coated with fibronectin, RGD or Invasin (cf. Figure 8.2). We can appreciate that independently of the ligand cells spread better on glass than on SLB, since they have a larger area on average (cf. Figure 8.2A). In addition, cells spread even less on SLB functionalized with Invasin than functionalized with RGD. Moreover, cells become less round on glass than on SLB (cf. Figure 8.2B). These observations suggest a different mode of cell spreading on glass and on SLB. Indeed, since the ligands are immobile on glass and freely diffusing on SLB, integrin organisation in

the contact zone of cell adhesion will be different for these substrates (Prager-Khoutorsky et al. [2011], han Yu et al. [2013]). For instance, cells that adhere on glass develop specific adhesion structures (focal adhesions, or FA) that anchor them to the substrate and set a specific direction for a cell to spread along (cf. Figure 8.1A-8.1B). Thus, cells on glass spread in a non-isotropic manner. Conversely, cells that adhere on SLB develop different types of adhesion structures that do not anchor them to the substrate as strongly as FA do (Prager-Khoutorsky et al. [2011], han Yu et al. [2013]). These weaker adhesions are more mobile making the shape of a spreading cell more isotropic or round.

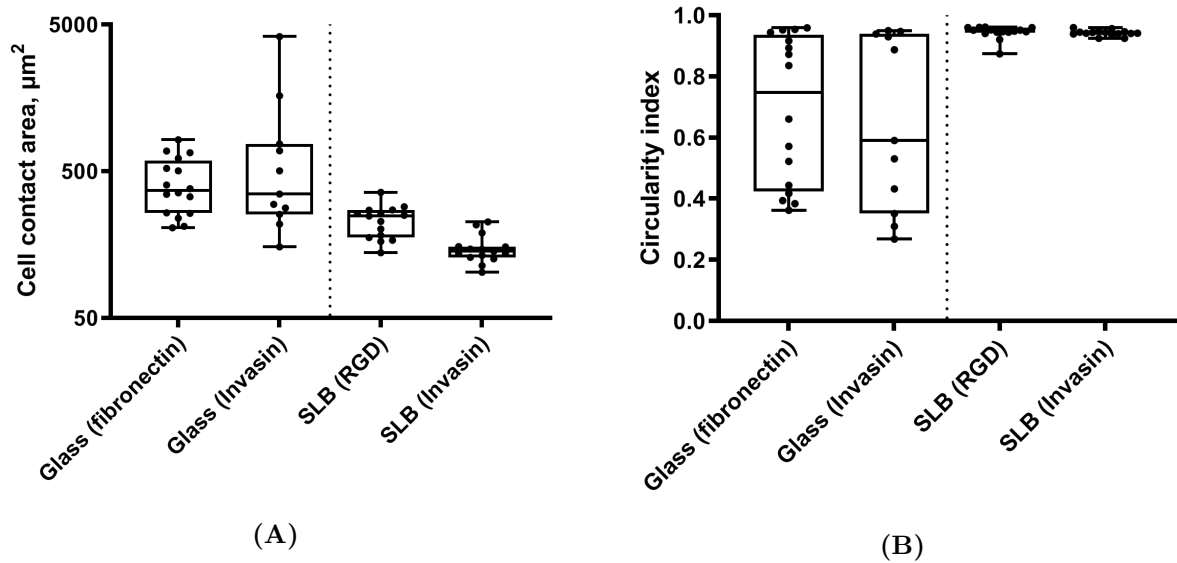


Figure 8.2: Area and shape of adherent cells.

A) Distribution of the area of cell-substrate contact

B) Distribution of circularity indices

for the cells after 1 hour of adhesion on different substrates: glass(fibronectin) 16 cells; glass(Invasin) 11 cells; SLB(RGD) 15 cells; SLB(Invasin) 15 cells.

Box with whiskers (from min to max) plot.

8.2 Adhesion index

During the first stage of adhesion, cells reach the substrate and stabilize on its surface. They have no translational speed at this stage, but they are not completely still yet. The cell border still moves around its adhesion position making the cell to “tremble” (cf. Figure 8.3). The “trembling” cell phenotype can be easily identified from transmission light time-lapse microscopy films recorded at 10 Hz. The cell “trembling” phenotype converts into *bona fide* cell adhesion when the “trembling” movement of the cell edge is no longer detected. We will use the “trembling” state as a proxy of pre-adhering cells.

In practice, we consider that a cell is “trembling” if we detect a movement of its edge by a few pixels (less than $1 \mu\text{m}$) during 5 seconds.

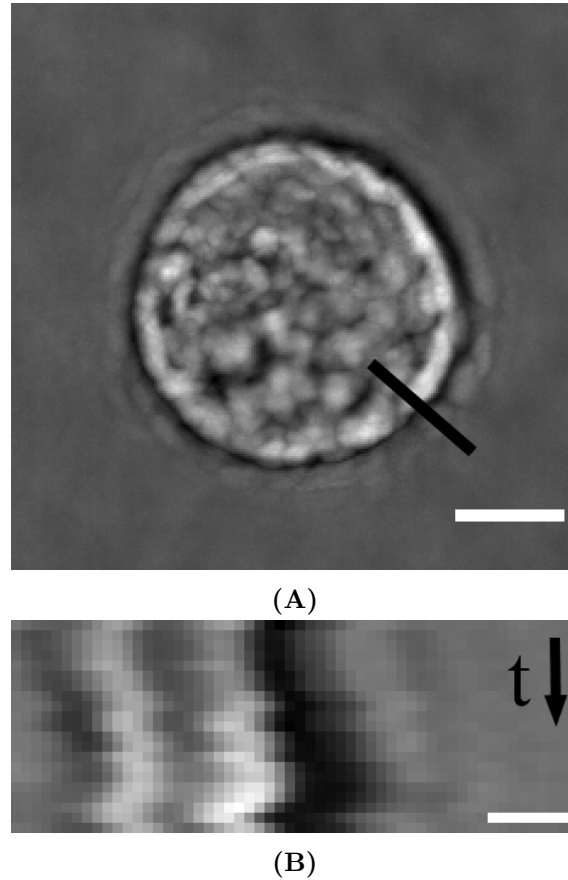


Figure 8.3: Definition of a “trembling” cell.
A) A micrograph of a “trembling” cell. Scale bar, $10 \mu\text{m}$.
B) A kymograph across the cell edge over 2 seconds.

We have quantified the dynamics of this early adhesion stage on different substrates by estimating the time it takes for a “trembling” cell to properly adhere to the substrate. For this, we have introduced an adhesion index \mathbf{A} , i.e. the fraction of properly adhered cells (“non-trembling”). In practice, $\mathbf{A} = 100\%$ when all cells adhere (do not tremble anymore) and $\mathbf{A} = 0\%$ when all cells “tremble”. In reality, as cells adhere independently of each other, \mathbf{A} is normally distributed.

First, we have verified the specificity of cell adhesion to all the studied substrates. We have measured in the same conditions the cell adhesion index \mathbf{A} for the late stage of adhesion (1 hour 30 minutes) for solid and fluid substrates (glass and SLB) functionalized with different cell ligands: fibronectin (on glass) that we compare to RGD peptide functionalized SLBs, and Invasin (either adsorbed on glass, or bound to a SLB). As a negative control, we compared with the cell adhesion index for non-adhering substrates,

glass coated with β -casein that is known to prevent cell adhesion or a pure DOPC bilayer (cf. Figure 8.4). The cell adhesion indexes for substrates functionalized with cell specific ligands are significantly higher than for these controls, confirming that the cells interact specifically with ligands on the different surfaces.

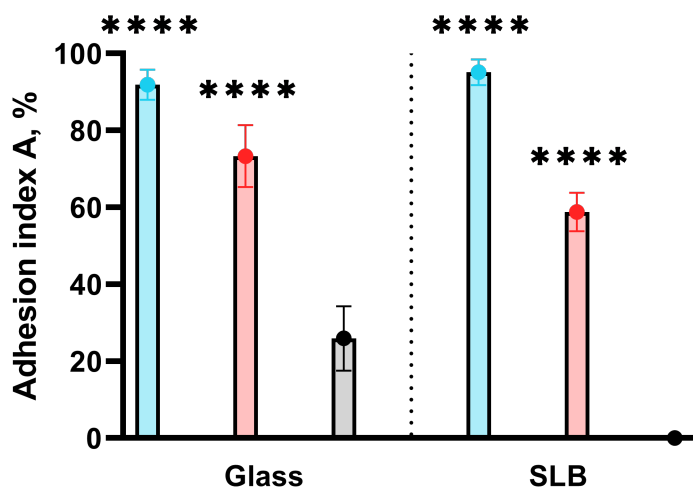




Figure 8.4: Cell adhesion control.

Adhesion index of cells after 1 hour on different substrates:

Glass	SLB	
fibronectin (49 cells, N=2)	RGD (41 cells, N=2)	Blue
Invasin (30 cells, N=2)	Invasin (97 cells, N=2)	Red
β -casein (Ctrl-) (27 cells, N=1)	SLB-DOPC (Ctrl-) (24 cells, N=1)	Black

N - number of experiments. Statistical t -tests were performed to compare the mean values of the adhesion indexes with their negative controls. Scatter plot (mean with SEM).

Next, we have characterized the dynamics of cell adhesion on these different substrates. On glass, during the first 45 minutes, cells exhibit similar adhesion dynamics for both ligands: fibronectin and Invasin (mean index A is not significantly different according to the t -test analysis). After 45 minutes, there is a larger proportion of cells properly adhered on fibronectin-coated glass than on Invasin-coated glass (92% and 73% respectively) (cf. Figure 8.5A). In comparison, the cell adhesion dynamics on fluid SLB depends more on the ligand. Cells adhere much faster on the SLBs coated with RGD than Invasin, reaching adhesion indexes of 70% after 30 minutes, while they fail to adhere at all on Invasin-coated SLBs at the same period of time. Generally, for every time point cells adhere less on Invasin than on RGD-coated SLBs (mean index A is significantly different according to the t -test analysis) (Figure 8.5B). This might seem counter-intuitive considering the fact that Invasin has higher affinity to integrins than fibronectin or RGD (Tran Van Nhieu and Isberg [1993]). On the other hand, Invasin binds to a more narrow range of integrin receptors than RGD. Indeed, it only binds to $\alpha_3\beta_1$, $\alpha_4\beta_1$, $\alpha_5\beta_1$ and $\alpha_6\beta_1$

(Leong et al. [1990]), whereas there are  known RGD-binding integrins  (Humphries et al. [2006]). Therefore, RGD peptides dispose more potential interaction partners that get activated. Moreover, integrins on RGD fluid substrates are more mobile than on Invasin fluid substrates because Invasin diffuses 2 times more slowly than a lipid (cf. subsection 5.1.6 of the Materials and Methods). Thus, this can facilitate binding of RGD to integrins as compared to Invasin as well as the formation of adhesion clusters. Overall these factors may initiate a faster cell adhesion on SLB (RGD) than on SLB (Invasin).

Noteworthy, cells adhere very similarly on fibronectin-coated glass and on fluid RGD-coated SLB (mean index A is not statistically different). Conversely, on Invasin immobilized on glass substrates, the adhesion index remains relatively stable along the whole adhesion process (between 50% and 70%), while on mobile Invasin on SLB, it is equal to zero for the first 30 minutes of adhesion then after 1 hour it rises to about 50%, close to the adhesion index on Invasin-coated glass. These results suggest a role of the ligand at the first stages of cell adhesion on fluid substrates as opposed to the ligand-immobilized substrates.

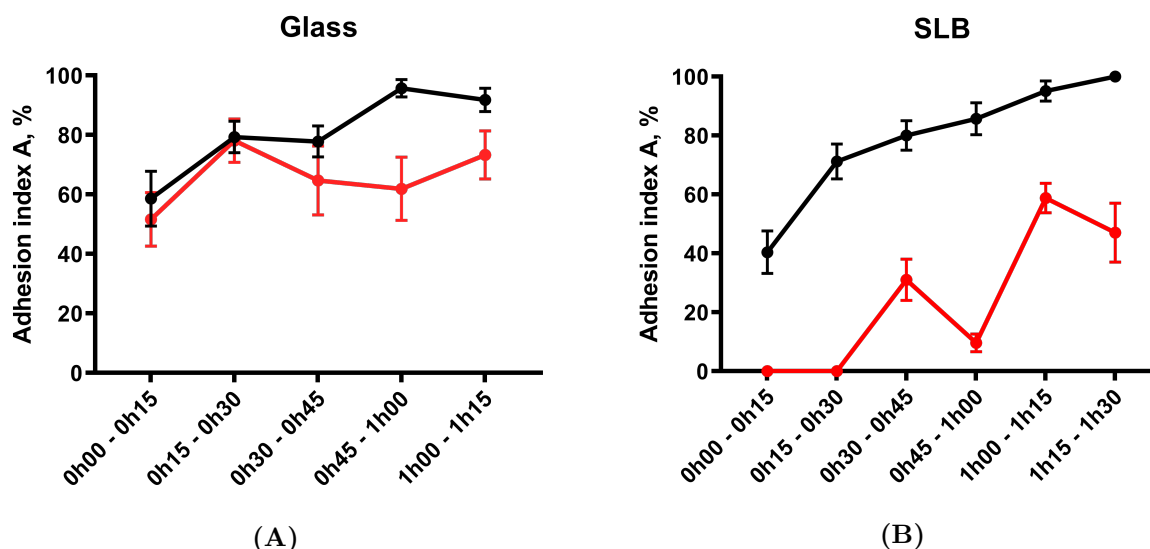


Figure 8.5: Evolution of cell adhesion on glass and SLB.

Cell adhesion index A versus time on

A) glass coated with fibronectin (black) (246 cells, $N=2$) and Invasin (red) (131 cells, $N=4$) immobilized on glass.

B) SLBs coated with RGD (black) (276 cells, $N=4$) and Invasin (red) (362 cells, $N=3$).

N - number of experiments. Statistical t -tests were performed to compare the mean values of the adhesion indexes for fibronectin/RGD and Invasin at every time point: for glass at all the time points (ns), except at 45-60 minutes (***), for SLBs at all the time points (****). Scatter line plot (mean with SEM).

Next, we have studied the role of integrin pre-activation (priming) by manganese ions (Mn^{2+}) on the dynamics of this first stage of cell adhesion. Cells were seeded without or

with 0.5 mM Mn^{2+} and their adhesion was quantified by measuring the adhesion indexes (cf. section 5.3 of the Materials and Methods). We have not found any significant change in cell adhesion dynamics on glass substrates for both ligands upon integrin activation by Mn^{2+} : according to the *t*-test analysis, the mean index A and its dynamics are similar, with one exception at 45-60 minutes for adhesion on fibronectin (cf. Figure 8.6A-8.6B). Conversely, the Mn^{2+} effect on cell adhesion dynamics is more pronounced for the fluid Invasin-coated substrates. Cells adhere significantly more efficiently on Invasin coated SLBs in the presence of Mn^{2+} than in its absence (mean index A is significantly different according to the *t*-test analysis) (cf. Figure 8.6D). Interestingly, Mn^{2+} treatment increases the cell adhesion dynamics on Invasin-coated fluid substrates to levels of adhesion on RGD-coated fluid substrates. But there is no significant increase of adhesion index due to the Mn^{2+} treatment for adhesion on the RGD-coated SLBs (cf. Figure 8.6C). Additionally, the adhesion index on glass does not reach 100% on Invasin after 1.5 hour, even with Mn^{2+} . But on SLB (Invasin), adhesion reaches 90+% (like on RGD) when integrins are activated, in contrast to 50-60% without activation.

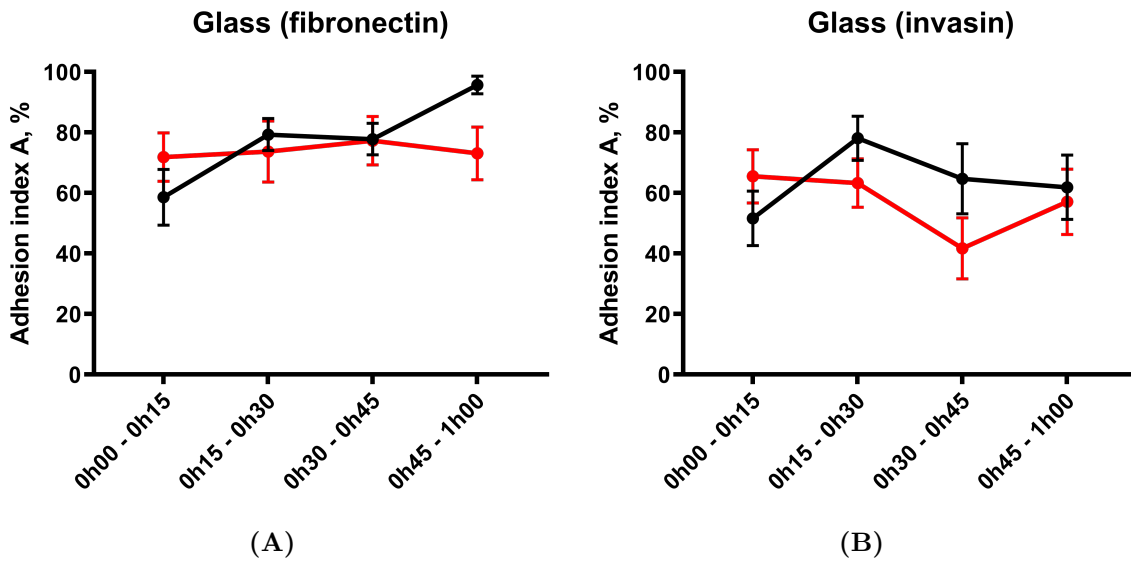


Figure 8.6: Role of Mn^{2+} -mediated integrin activation in cell adhesion on different substrates.

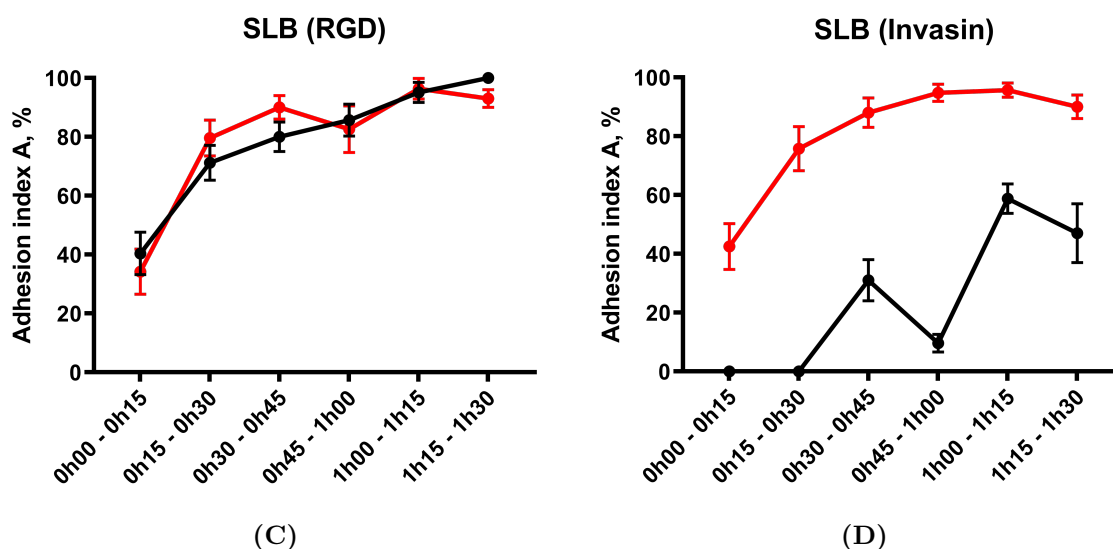


Figure 8.6: Role of Mn^{2+} -mediated integrin activation in cell adhesion on different substrates(cont.).

Cell adhesion index A versus time for:

A) Fibronectin-coated glass in presence (red) (282 cells, $N=2$) and absence (black) (99 cells, $N=2$) of Mn^{2+} .

B) Invasin-coated glass in presence (red) (131 cells, $N=4$) and absence (black) (112 cells, $N=4$) of Mn^{2+} .

C) RGD-functionalized fluid SLBs in presence (red) (276 cells, $N=4$) and absence (black) (233 cells, $N=6$) of Mn^{2+} .

D) Invasin-functionalized SLBs in presence (red) (362 cells, $N=3$) and absence (black) (283 cells, $N=3$) of Mn^{2+} .

N - number of experiments. Statistical t -tests were performed to compare the mean values of A for all substrates at every time point between the Mn^{2++} and Mn^{2+-} conditions: for glass at all the time points (ns), except for fibronectin at 45-60 minutes (**), for SLB-RGD at all the time points (ns) and for SLB-Invasin at all the time points (****). Scatter line plot (mean with SEM).

Since it is known that divalent ions can induce membrane-membrane adhesion (Leckband et al. [1993]), we have verified that this interaction does not play a role here. Indeed, in the Figure 8.7 we see that 1 hour after seeding the presence of Mn^{2+} does not induce non-specific adhesion for neither type of ligands, neither immobilized nor mobile.

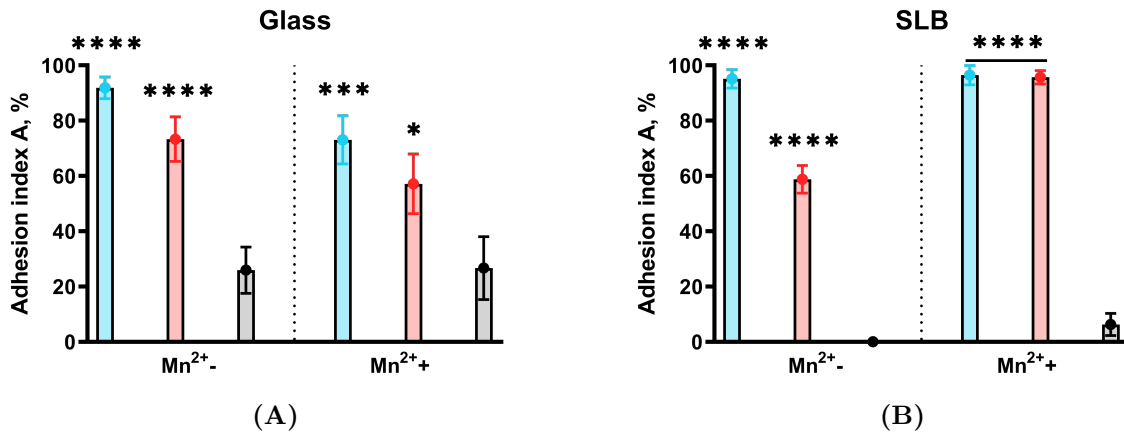


Figure 8.7: Role of Mn^{2+} -mediated integrin pre-activation in non-specific cell adhesion

A) Adhesion index of cells after 1 hour on glass:

Glass	Mn^{2+-}	Mn^{2++}	
fibronectin	49 cells, N=2	26 cells, N=2	Blue
Invasin	30 cells, N=2	21 cells, N=2	Red
β -casein (Ctrl-)	27 cells, N=1	21 cells, N=1	Black

B) Adhesion index of cells after 1 hour on SLB:

SLB	Mn^{2+-}	Mn^{2++}	
RGD	41 cells, N=2	28 cells, N=2	Blue
Invasin	97 cells, N=2	70 cells, N=1	Red
SLB-DOPC (Ctrl-)	24 cells, N=1	32 cells, N=1	Black

Statistical t -tests were performed to compare the mean values of the adhesion indexes with their negative controls. Scatter plot (mean with SEM).

chapter 8 conclusions:

In this chapter, we have studied cell adhesion at a large length scale (several microns) and demonstrated:

- A difference in the shape of the cell-substrate contact zone depending on the mechanical properties of the substrate. Cells that spread on solid substrates (glass) tend to adapt a more irregular shape than the ones that spread on fluid substrates (SLBs). These results are consistent with previous reports (Prager-Khoutorsky et al. [2011], Yu et al. [2011], han Yu et al. [2013]).
- A difference in the dynamics of cell adhesion for solid and fluid substrates of different ligand composition. While there is almost no difference in the adhesion index A of cells adhering on fibronectin and Invasin-coated glass, it differs significantly for cells adhering on SLBs functionalized with RGD and

Invasin. Cells adhere more readily on RGD fluid substrates than on Invasin ones.

- There is no significant effect of integrin activation by Mn^{2+} on cell adhesion dynamics on fibronectin or Invasin-coated glass. Mn^{2+} has no effect for adhesion on SLB (RGD), but drastically increases cell adhesion on SLB (Invasin).

Chapter 9

Dynamics of adhesion zone maturation on SLBs

From this chapter on, we have focused on cells adhering on the fluid substrates (SLBs coated with mobile ligands) as we believe they may reveal mechanical properties that cannot be studied on solid substrates with immobile ligands (glass).

We next investigated the “trembling-to-adhesion” transition in more details at a smaller micron scale. We study cell adhesion on the fluid substrates by imaging β_1 -integrins involved in adhesion with fluorescence microscopy (cf. chapter 6 of the Materials and Methods). We have labelled ectodomains of β_1 -integrins located at cell surfaces by Halotag[®] technology (cf. section 5.3 of the Materials and Methods). We have also used a calibration method to convert the raw intensity measurements to the actual integrin densities (cf. section 6.2 of the Materials and Methods). It allowed us to quantify the cell adhesion process in terms on integrin concentrations and distributions.

During cell adhesion on SLBs, the integrins are mostly concentrated in an area (black thick line in the Figure 9.1) smaller than the projected area of the whole cell (red line in the Figure 9.1) detected with wide field microscopy (cf. section 7.1 of the Materials and Methods). We call this area *the adhesion zone (AZ)* since it contains the majority of integrin receptors involved in the cell adhesion process. As we can see in the Figure 9.1, integrins are not homogeneously distributed in the *AZ* but form *clusters*. Integrin cluster formation during cell adhesion was previously shown on glass (cf. section 3.3 of the Introduction) and on SLB (cf. section 4.4 of the Introduction). We have developed an automatic program run by ImageJ that allows to segment the fluorescence image and find integrin clusters in it (cf. section 7.2 of the Material and Methods). Practically, we detect integrin clusters by our program and then define the *AZ* as the smallest convex

area containing the clusters.

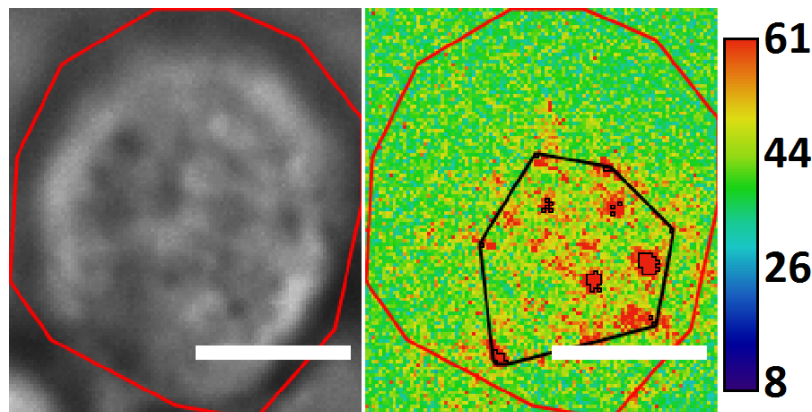


Figure 9.1: Visualization of the *AZ* of the cell.

Microscopy images of an adherent cell. Left to right: widefield image and pseudo-colored heat map of β_1 -integrin density based on a fluorescence microscopy image. The contour of the cell as detected by our program is represented in red. The *AZ* is represented as a thick black line. The thin black contours delimitate integrin clusters inside the zone. Both the *AZ* and integrin clusters are detected by our program. Integrin density scale (in $\text{integrins}/\mu\text{m}^2$) based on a prior fluorescence calibration (cf. section 7.2 of the Material and Methods). Scale bars, $5 \mu\text{m}$.

In this section we have studied how the *AZ* evolves during the time course of cell adhesion on the fluid substrates as a function of the bound ligand. We have also characterized the average integrin distribution in the *AZ* and the effect of integrin pre-activation by manganese ions. First, we have distinguished **three stages of cell adhesion**: the **early “trembling”**, the **intermediate** and the **late adhesion**. All “trembling” cells are in a pre-adhesion stage, the adhered (“non-trembling”) cells that are observed between the cell seeding (time 0) and 45 minutes belong to the intermediate stage, the adhered cells that are observed between 45 minutes and 1 hour 30 minutes are classified to the late adhesion stage. Consequently, we have obtained a general view on the time course of cell adhesion dynamics.

9.1 Adhesion zone quantification. Role of the nature of ligand

We have studied 280 cells adhering on fluid substrates: 201 on RGD and 79 on Invasin. We have characterized the *AZ* and followed its evolution from **early “trembling”** to **late** adhered cells. We have measured the ratio between the *AZ* area and the cell contact area (the *AZ ratio*) for the cells adhering on RGD and Invasin-coated fluid substrates and

detected its statistically significant decrease¹ for both of them (cf. Figure 9.2), suggesting a "contraction" of the **AZ**. The ratio drops by 38% (from 65% to 40%) for the cells adhering on RGD-coated bilayers and by 33% (from 58% to 39%) for the cells adhering on Invasin-coated bilayers. Moreover, it is worth noting that this reduction occurs during the first period (0h00 - 0h45) and remains more or less constant afterwards when cells adhere of RGD (cf. Figure 9.2A). In contrast, the **AZ ratio** changes mostly during the second period (0h45 - 1h30) for Invasin (cf. Figure 9.2B).

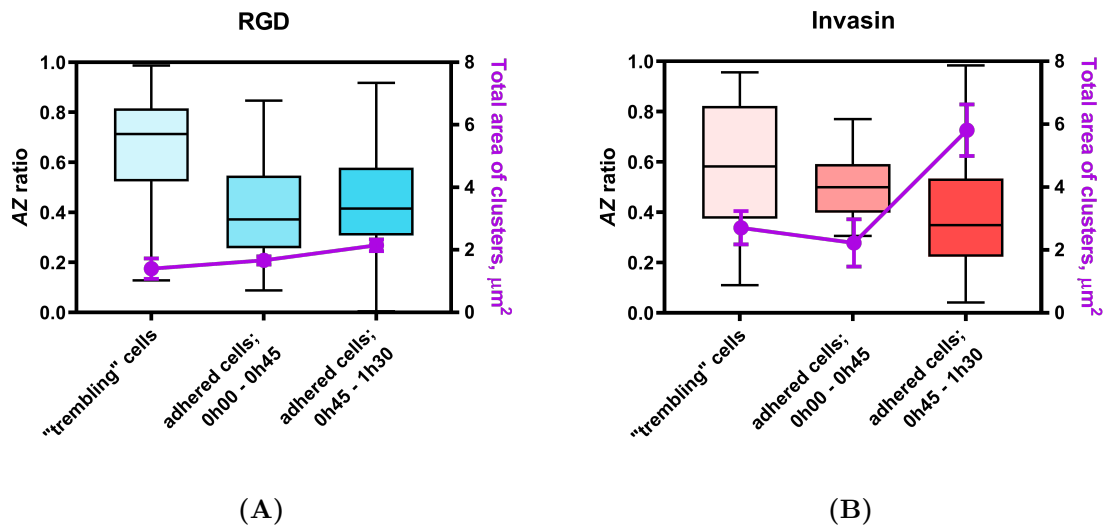


Figure 9.2: Quantification of the **AZ.**

The color gradation, from clear to dark, corresponds to the different stages, trembling, early (<0h45) and late (>0h45).

A) (left Y axis) Evolution of **AZ ratio** for cells on RGD-coated fluid substrates. Box and whiskers (from min to max) plot.

(right Y axis, magenta plot) Area of integrin clusters in the cell adhesion zone. Line plot (mean with SEM).

B) (left Y axis) Evolution of **AZ ratio** for cells on Invasin-coated fluid substrates. Box and whiskers (from min to max) plot.

(right Y axis, magenta plot) Area of integrin clusters in the cell adhesion zone. Line plot (mean with SEM).

Then, we have focused on the total area occupied by the integrin clusters inside of the **AZ**. This is the sum of the area of all integrin clusters in the **AZ**. It increases during cell adhesion. However, the dynamics of this increase is very different for the two types of ligands. The mean total area of integrin clusters increases by 57% for the cells adhering on RGD-coated substrates and by 115% on Invasin-coated substrates over 90 minutes (cf. Figure 9.2). Also during cell adhesion on RGD substrates the mean total area of integrin clusters increases weakly throughout the time course of cell adhesion, while during cell adhesion on Invasin substrates, it stays constant for the first 45 minutes and starts to

¹AZ ratios are normally distributed (d'Agostino Pearson test); then compared with ANOVA test

strongly increase after that (cf. Figure 9.2A-9.2B). Note that at long time (90 minutes), the average total cluster area is about 3 times higher on Invasin than on RGD.

To summarize, these results show the relative contraction of the cell **AZ** and the increase of the average total area of the integrin clusters for both types of studied fluid substrates. This might suggest the presence of contractile forces that move integrin clusters towards the cell center (han Yu et al. [2013]). Interestingly, the dynamics of these two processes differ depending on the nature of the substrate. It reaches a steady-state faster on RGD than on Invasin, but the total area of integrin clusters on Invasin increases more in relative and absolute numbers than on RGD.

Next, we zoomed in the **AZ** of an adhering cell. It contains integrin clusters of different sizes. The number of clusters per **AZ** decreases during cell adhesion independently of the type of substrate (cf. Figure 9.3).

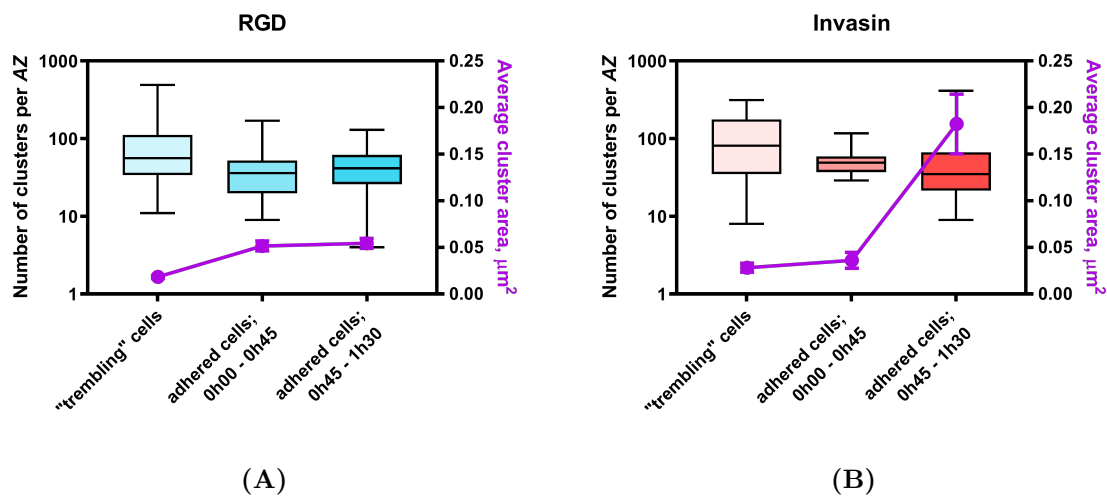


Figure 9.3: Characterization of the clusters in the **AZ.**

We use the same color codes as in Figure 9.2, from clear to dark.

A) (left Y axis) Number of integrin clusters in the **AZ** on RGD at different time periods. Log representation. Box and whiskers (from min to max) plot.

(right Y axis, magenta plot) Corresponding average area of the integrin clusters. Line plot (mean with SEM).

B) (left Y axis) Number of integrin clusters in the **AZ** on Invasin at different time periods. Log representation. Box and whiskers (from min to max) plot.

(right Y axis, magenta plot) Corresponding mean area of the integrin clusters. Line plot (mean with SEM).

This number has a broad log-normal distribution² with median values of 56 and 81 integrin clusters for the “trembling” cells on RGD and Invasin, respectively. The log-normal

²number of integrin clusters are log-normally distributed (Andersen-Darling test); then their log transformed values compared with ANOVA test

nature of the distribution suggests that at a given time point the number of integrin clusters is determined by the number of clusters at previous time points, suggesting a process in which adhesion clusters fuse with each other (Koch [1966]). At the late adhesion stage (after 90 minutes) on RGD the median number of integrin clusters decreases by 33% to 42 clusters (statistically non-significant²), whereas on Invasin it decreases by 2.3 fold to 35 clusters (statistically significant²). At the same time the mean cluster size significantly increases for both types of substrates during cell adhesion (cf. Figure 9.3A-9.3B). For the cells adhering on RGD, it increases by 2 fold and by 5.5 fold on Invasin. The mean cluster size is much higher on Invasin ($0.183 \mu m^2$) than on RGD ($0.055 \mu m^2$).

In the next step, we have quantified the amount of β_1 -integrin receptors in the **AZ**, based on our calibration of the fluorescence (cf. section 7.2 of the Materials and Methods). During cell adhesion the total number of integrins in the cell **AZ** increases (cf. Figure 9.4). We can observe a difference in the dynamics of this increase depending on the substrate ligand. On RGD-coated fluid substrates, the total number of integrins in the **AZ** starts increasing during the first 45 minutes of adhesion. In contrast, on Invasin, it increases only after a delay of around 45 minutes.

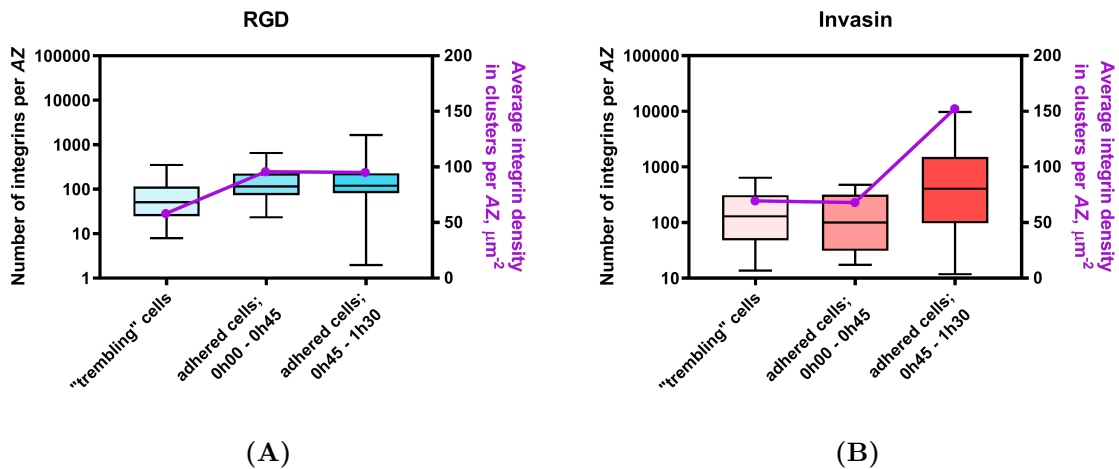


Figure 9.4: Total number of clusters in the AZ and integrin density in them.

We use the same color codes as in Figure 9.2, from clear to dark.

A) (left Y axis) Total number of integrins in the **AZ** on RGD over time. Log representation. Box and whiskers (from min to max) plot.

(right Y axis, magenta plot) Average integrin density in the clusters of the **AZ**. Line plot (mean with SEM).

B) (left Y axis) Total number of integrins in the **AZ** on Invasin over time. Log representation. Box and whiskers (from min to max) plot.

(right Y axis, magenta plot) Mean integrin density in the clusters of the **AZ**. Line plot (mean with SEM).

Moreover, the absolute number of integrins per **AZ** at any stage of adhesion is different between the cells adhering on RGD or Invasin ligated fluid substrates. Thus, poorly

adhered “trembling” cells on average have less integrins in the **AZ** when they adhere on RGD than on Invasin-coated fluid substrates (median values: 51 and 129 respectively) (cf. Figure 9.4). This indicates a difference in the “trembling-adhesion” transition of cells adhering on different fluid substrates, suggesting that more integrins need to be recruited to engage the cell in a stable adhesion on Invasin than on RGD. Additionally, the number of integrins recruited to the **AZ** during 1 hour 30 minutes of adhesion increases more for the (“non-trembling”) cells adhering on Invasin than on RGD (as compared to the “trembling” cells): median values increase by 2.4 fold (from 51 to 119) and by 3.2 fold (from 129 to 407), respectively (cf. Figure 9.4A-9.4B).

Finally, we have calculated the average integrin density in the **AZ** by dividing the total number of integrins in the **AZ** by the total area of integrin clusters in the **AZ**. It increases significantly for cells adhering on both types of ligands (cf. Figure 9.4A-reffig:res2:4B, right axes). We observe a relatively fast increase in integrin density over the first 45 minutes and a plateau on RGD while the increase occurs only after 45 minutes on Invasin. The increase is lower on RGD: 63% against 118% on Invasin, reaching 95 and 152 μm^{-2} in mean values respectively (cf. Figure 9.4A-9.4B, right axes).

To summarize, we have observed a reminiscent process of maturation of the **AZ** for cells adhering on a fluid substrate: the relative area of the **AZ** contracts, the number of integrin clusters in it decreases and their area becomes on average bigger. Both the number of integrins and integrin density in the clusters of the **AZ** increases during cell adhesion. This increase is “fast” and “low” for the RGD and “slow” and “high” for Invasin.

Finally, in the subsequent sections we have provided a more time-resolved analysis of the adhesion zone maturation together with the adhesion quantification at a single integrin cluster level.

9.2 Effect of integrin activation by Mn^{2+}

In this section, we have investigated the role of integrin pre-activation or “priming” by manganese ions (Mn^{2+}) on the dynamics of cell adhesion and integrin recruitment on fluid substrates. Cells treated with Mn^{2+} were seeded on fluid substrates of different ligand composition (RGD or Invasin) (cf. Materials and methods “integrin activation by manganese”) and their adhesion was analyzed as in the previous section. Here we have focused on the adhering cells following the “trembling-adhesion” transition. We have also refined the temporal resolution of cell adhesion grouping adhering cells in periods of 15 minutes.

During the time course of cell adhesion we observe the decrease of the **AZ** ratio for both types of ligands in response to integrin activation by Mn^{2+} (cf. Figure 9.5). This effect is less pronounced for RGD than for Invasin. The cells adhering on RGD substrates have their median **AZ ratio** decreased by 27% due to the Mn^{2+} treatment only at the very early adhesion stage (0 – 15 minutes after cell seeding) (cf. Figure 9.5A). In contrast, on Invasin, the median **AZ ratio** decrease reaches 36% at a later adhesion stage (45 minutes – 1 hour after cell seeding) (cf. Figure 9.5B). It is worth reminding that we did not observe any cell adherent on Invasin at an early stage (before 30 minutes) without Mn^{2+} .

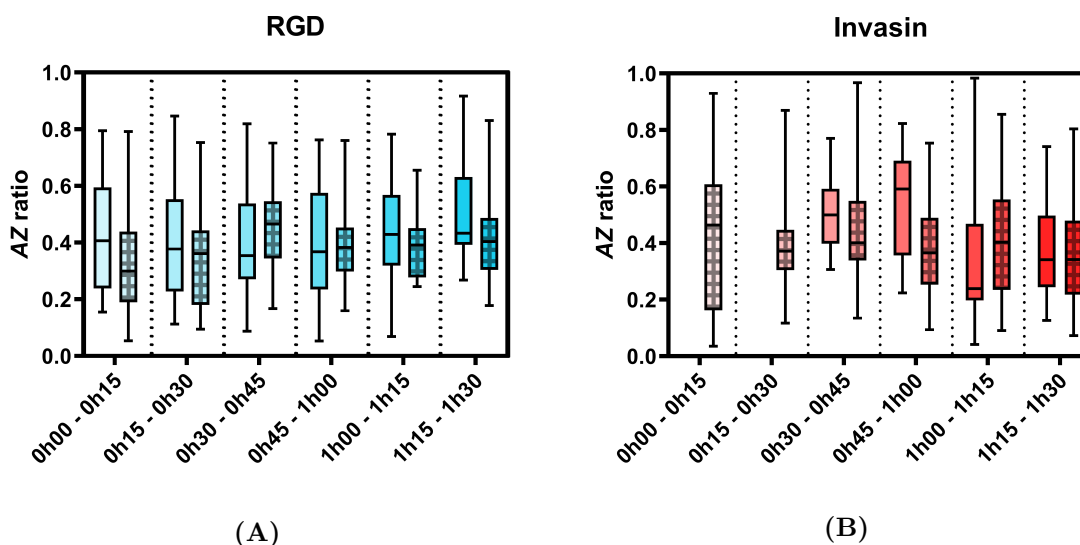


Figure 9.5: Effect of integrin activation by Mn^{2+} on the evolution of the **AZ ratio.** The color gradation, from clear to dark, corresponds to the different time points of adhesion. A) Evolution of the **AZ ratio** without Mn^{2+} (Mn^{2+} -, *non-striped boxes*) and with Mn^{2+} (Mn^{2+} +, *striped boxes*) for cells adhering on RGD-coated SLBs. B) Evolution of the **AZ ratio** without Mn^{2+} (Mn^{2+} -, *non-striped boxes*) and with Mn^{2+} (Mn^{2+} +, *striped boxes*) for cells adhering on Invasin-coated SLBs. Box and whiskers (from min to max) plot.

We have also observed an effect of cell treatment by Mn^{2+} on the total area of integrin clusters. The total area of integrin clusters increases over the first hour of cell adhesion for both ligands (cf. Figure 9.6). Thus, for the cells adhering on RGD coated fluid substrates the median area of integrin clusters increases by 14 to 27% depending on the time point (cf. Figure 9.6A). And for the cells adhering on Invasin coated fluid substrates we observe an increase by 93 to 136% depending on the time point (cf. Figure 9.6B).

The number of integrin clusters in the **AZ** is also affected by Mn^{2+} (cf. Figure 9.7). For RGD, the effect of integrin activation by Mn^{2+} only takes place after 45 minutes: depending on the time point, the mean number of integrin clusters decreases by 27 to 41% depending on the time point: from 44-51 to 26-36 clusters (the range of the mean

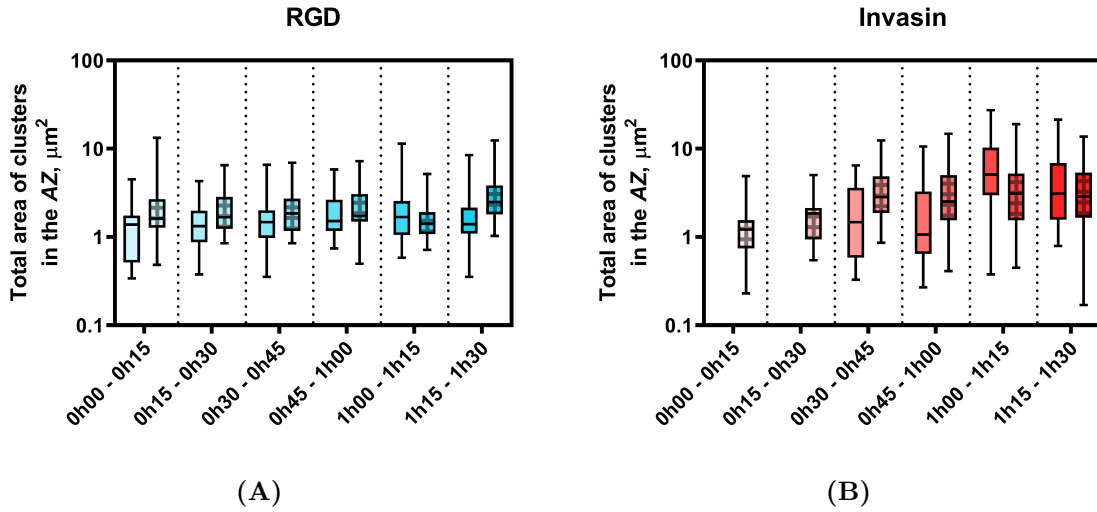


Figure 9.6: Effect of integrin activation by Mn^{2+} on the total area of integrin clusters in the **AZ**.

We use the same color codes as in Figure 9.5, from clear to dark.

A) Evolution of the total area of integrin clusters in the **AZ** without Mn^{2+} (Mn^{2+} -, *non-striped boxes*) and with Mn^{2+} (Mn^{2+} +, *striped boxes*) for cells adhering on RGD-coated SLBs. Log representation.

B) Evolution of the total area of integrin clusters in the **AZ** without Mn^{2+} (Mn^{2+} -, *non-striped boxes*) and with Mn^{2+} (Mn^{2+} +, *striped boxes*) for cells adhering on Invasin-coated SLBs. Log representation. Box and whiskers (from min to max) plot.

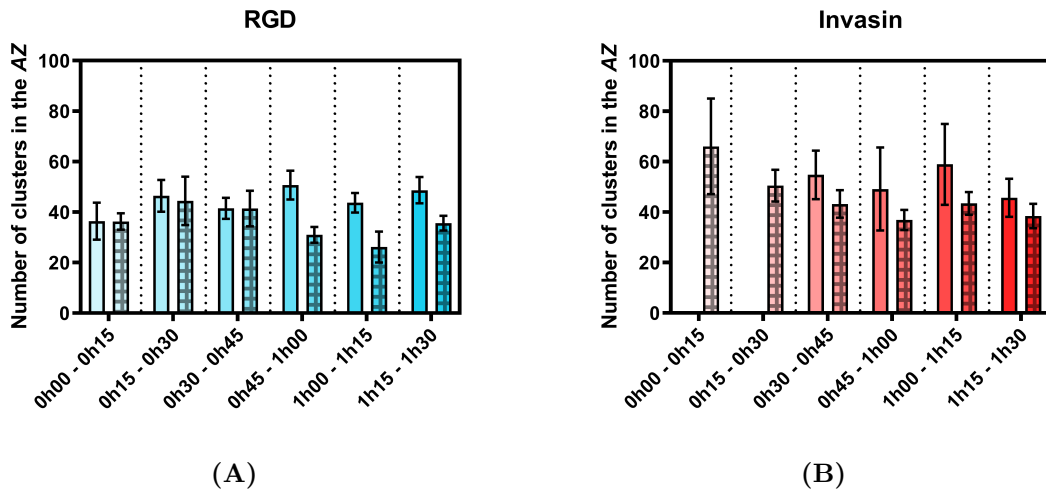


Figure 9.7: Effect of integrin activation by Mn^{2+} on the total number of integrin clusters in the **AZ**.

We use the same color codes as in the Figure 9.5, from clear to dark.

A) Evolution of the total number of integrin clusters in the **AZ** without Mn^{2+} (Mn^{2+} -, *non-striped bars*) and with Mn^{2+} (Mn^{2+} +, *striped bars*) for cells adhering on RGD-coated SLBs.

B) Evolution of the total number of integrin clusters in the **AZ** without Mn^{2+} (Mn^{2+} -, *non-striped bars*) and with Mn^{2+} (Mn^{2+} +, *striped bars*) for cells adhering on Invasin coated fluid substrates. Bar plots (mean with SEM).

values at different time points) (cf. Figure 9.7A). For Invasin, the effect takes place after 30 minutes (we do not observe cell adhesion on Invasin without Mn^{2+} before): depending on the time point, the mean number of integrin clusters decreases by 24-28% (from 46-59 to 37-43 clusters) (cf. Figure 9.7B).

Next, we have discovered that the Mn^{2+} treatment makes the area of an individual integrin cluster larger on average independently of the ligand (cf. Figure 9.8).

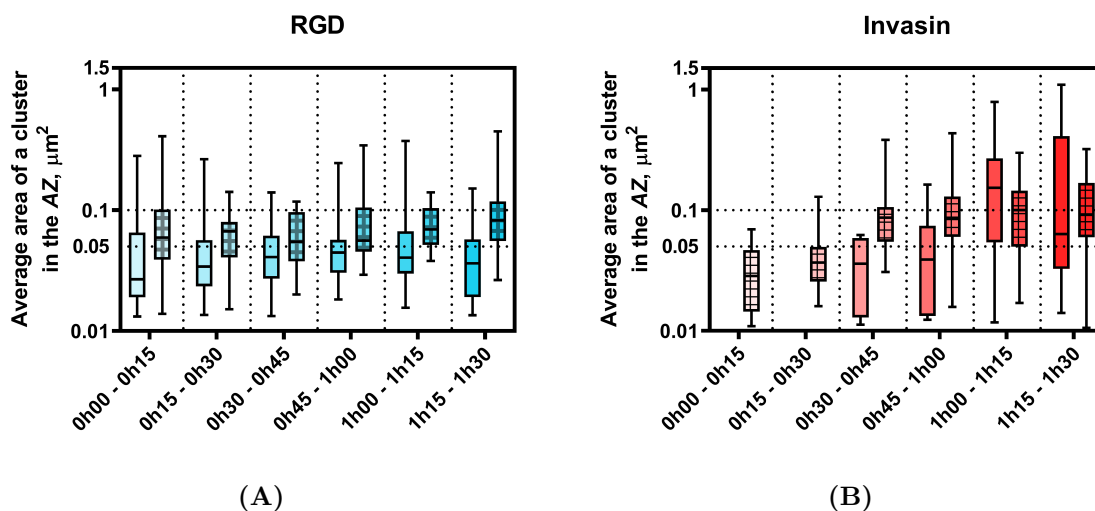


Figure 9.8: Effect of integrin activation by Mn^{2+} on the average integrin cluster area.

We use the same color codes as in the Figure 9.5, from clear to dark.

The dotted lines are a guide for the eyes, corresponding to $0.05 \mu m^2$ (the diffraction limit) and to $0.1 \mu m^2$ as a size reference.

A) Evolution of the average area of an integrin cluster in the **AZ** without Mn^{2+} (Mn^{2+} -, *non-striped boxes*) and with Mn^{2+} (Mn^{2+} +, *striped boxes*) for cells adhering on Invasin coated fluid substrates. Log representation.

B) Evolution of the average area of an integrin cluster in the **AZ** without Mn^{2+} (Mn^{2+} -, *non-striped boxes*) and with Mn^{2+} (Mn^{2+} +, *striped boxes*) for cells adhering on Invasin coated fluid substrates. Log representation. Box and whiskers (from min to max) plots.

More precisely, on RGD in response to integrin activation by Mn^{2+} the average area of clusters increases by 1.2-2.2 fold (depending on the time point) throughout the time course of cell adhesion (with median values increasing from 0.027 - $0.045 \mu m^2$ to 0.055 - $0.082 \mu m^2$). It is worth noting, that without Mn^{2+} treatment at any time point between 50% and 75% of integrin clusters are smaller than $0.05 \mu m^2$, which is approximately the limit of optical resolution due to diffraction. Whereas, with Mn^{2+} treatment at any time point between 50% and 75% of integrin clusters are larger $0.05 \mu m^2$ and about 25% of clusters are larger than $0.1 \mu m^2$ (cf. Figure 9.8A, dotted lines). On Invasin the effect of Mn^{2+} is bigger: between 30 minutes and 1 hour of adhesion the average area of individual integrin clusters increases by 2.2-2.4 fold (with median values increasing from 0.036 - 0.039

μm^2 to $0.086\text{-}0.087 \mu\text{m}^2$). Similarly to RDG, at this time period without Mn^{2+} treatment, we have detected between 50% and 75% of integrin clusters are smaller than $0.05 \mu\text{m}^2$, whereas with Mn^{2+} treatment between 75% and 100% of integrin clusters are larger $0.05 \mu\text{m}^2$ and between 25% and 50% are larger than $0.1 \mu\text{m}^2$ (cf. Figure 9.8B). After 1 hour we have not observed any significant effect of Mn^{2+} for Invasin. Nevertheless, clusters for both Mn^{2+} treated and non-treated cells are larger on average on Invasin than on RGD.

Next, we have compared the number of integrin receptors in the **AZ** of cells treated with and without Mn^{2+} (cf. Figure 9.9).

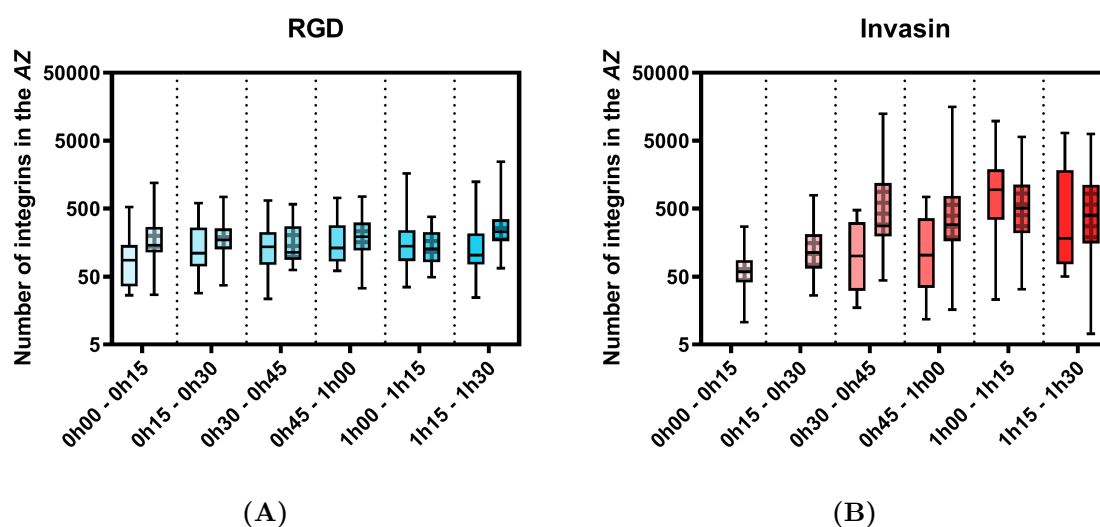


Figure 9.9: Effect of integrin activation by Mn^{2+} on the number of integrins in the **AZ**.

We use the same color codes as in Figure 9.5, from clear to dark.

A) Evolution of the number of integrins in the **AZ** without Mn^{2+} (Mn^{2+-} , *non-striped boxes*) and with Mn^{2+} (Mn^{2++} , *striped boxes*) for cells adhering on RGD coated fluid substrates. Log representation.

B) Evolution of the number of integrins in the **AZ** without Mn^{2+} (Mn^{2+-} , *non-striped boxes*) and with Mn^{2+} (Mn^{2++} , *striped boxes*) for cells adhering on Invasin coated fluid substrates. Log representation. Box and whiskers (from min to max) plots.

Integrin activation by Mn^{2+} increases the number of integrins in the **AZ** for both RGD and Invasin. For RGD we can observe this effect at the very early stage of adhesion (during the first 30 minutes after cell seeding), whereas for Invasin the effect is delayed as we have already observed for different quantities and differences are observed between 30 minutes and 1 hour. Thus, for the RGD in response to integrin activation by Mn^{2+} the median number of integrins in the **AZ** increases by 67% from approximately 87 to 145 molecules for the first 15 minutes of adhesion and remains higher than for non-treated cells for most of the time points (cf. Figure 9.9A). For Invasin, in response to integrin activation by Mn^{2+} the median number of integrins in the **AZ** increases by 2.8 fold (from

approximately 100 to 280 molecules) in the period between 30 minutes and 1 hour of adhesion (cf. Figure 9.9B).

Integrin density in the **AZ** is affected by integrin activation by Mn^{2+} but differently for each ligand (cf. Figure 9.10). For RGD the density is almost not changed and remains constant during the course of adhesion (cf. Figure 9.10A). For Invasin the median integrin density in the **AZ** increases by 71% from approximately 70 to 120 molecules per μm^{-2} in the period between 30 minutes and 1 hour of adhesion (cf. Figure 9.10B).

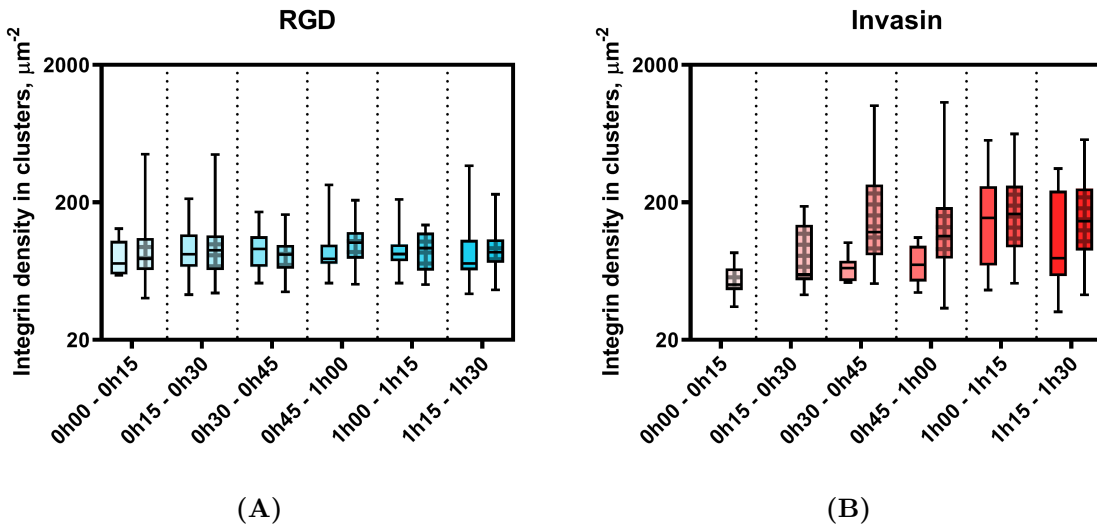


Figure 9.10: Effect of integrin activation by Mn^{2+} on the integrin density in the **AZ.** We use the same color codes as in the Figure 9.5, from clear to dark.

A) Evolution of integrin density in the **AZ** without Mn^{2+} ($Mn^{2+,-}$, *non-striped boxes*) and with Mn^{2+} ($Mn^{2+,+}$, *striped boxes*) for cells adhering on RGD coated fluid substrates. Log representation.

B) Evolution of integrin density in the **AZ** without Mn^{2+} ($Mn^{2+,-}$, *non-striped boxes*) and with Mn^{2+} ($Mn^{2+,+}$, *striped boxes*) for cells adhering on Invasin coated fluid substrates. Log representation. Box and whiskers (from min to max) plots.

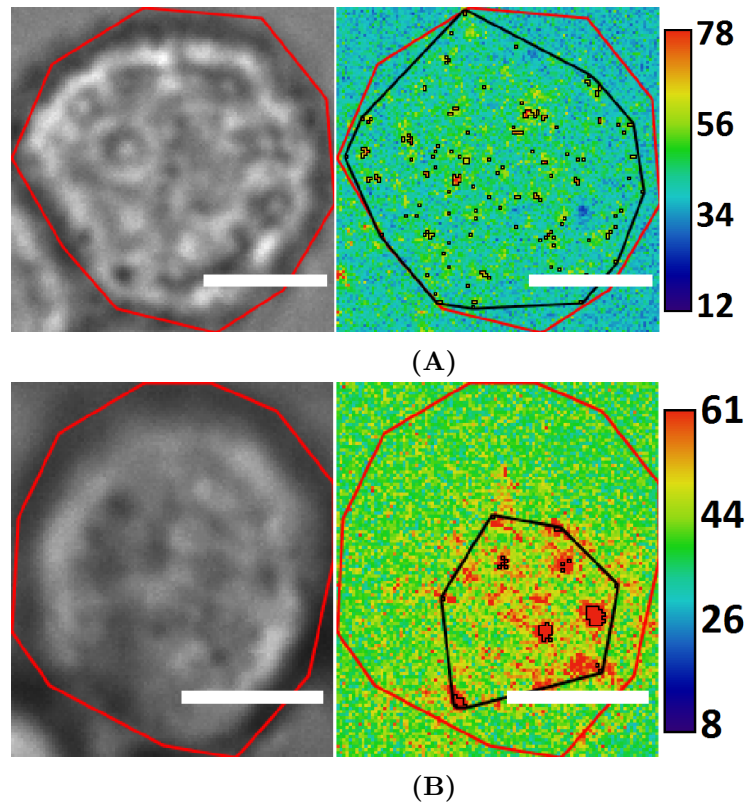


Figure 9.11: Evolution of adhesion maturation.

A) Early stage of cell adhesion on a fluid substrate.

B) Late stage of cell adhesion on a fluid substrate.

Integrin density scale (in integrins/ μm^2) based on a prior fluorescence calibration (cf. section 7.2 of the Materials and Methods). The contour of the cell is represented in red. The adhesion zone is represented as a thick black line. The thin black contours delimitate integrin clusters inside the zone. Scale bars, $5 \mu\text{m}$.

chapter 9 conclusions:

In this chapter we have studied cell adhesion of fluid substrates (SLBs) and have observed and characterized the adhesion maturation at two different length scales: the micron scale for the **AZ** and the sub-micron scale for the integrin clusters. We have demonstrated:

- The transition from “trembling” to “adhesive” stages of cell adhesion is accompanied with a decrease of **AZ** and number of integrin clusters, an increase of integrin clusters’ area, integrin numbers and densities in the **AZ** (cf. Figure 9.11).
- The dynamics of this maturation depends on ligands: on RGD it starts within the first 15 minutes of adhesion, whereas on Invasin there is a delay of 1 hour. Moreover, it leads to larger clusters, higher number of integrins and higher integrin densities for Invasin than RGD.
- Integrin activation by Mn^{2+} accelerates the maturation dynamics on RGD at the very early stage of adhesion (first 30 minutes): with Mn^{2+} , the integrin numbers and densities in the **AZ** are set in the first 15 minutes and remain about constant, slightly higher than without Mn^{2+} , where it takes 30 minutes to reach a plateau. On Invasin there is a delay (more than 30 minutes) for the engagement of integrins in the **AZ** that is strongly shortened by Mn^{2+} . When the plateau is reached (after 1 hour without Mn^{2+}), the number of integrins in the **AZ** and the density is the same with and without Mn^{2+} , 2 fold higher than on RGD.

Chapter 10

Characterization of individual integrin clusters

In this chapter we have focused on the individual integrin clusters and studied their maturation during the time course of cell adhesion. We have detected and analyzed 16'471 and 13'736 clusters in the **AZ** of cells adhering on RGD and Invasin-coated fluid substrates, respectively. Integrin clusters' maturation have been characterized by two parameters: their areas and the number of integrin receptors they contain.

When we detect and characterize individual clusters, we are limited by two factors: the optical resolution of the microscope and the ability of our software, to discriminate clusters from the background in our microscopy images.

The first limitation is related to the fact that we cannot determine the sizes of clusters that are smaller than the diffraction limit of our optical system (cf. subsection 6.1.2 of the Materials and Methods). Thus, we constantly underestimate integrin densities in the clusters that are smaller than optical resolution. Here, in our experimental conditions we have estimated the lateral optical resolution limit due to diffraction - 180 nm (cf. subsection 6.1.2 of the Materials and Methods). Thus, it prevents us to precisely characterize the clusters smaller than $0.05 \mu m^2$.

The second limitation is related to the imprecise detection cluster detection by our program. The program uses intensity histograms of images for cluster segmentation (cf. materials and methods "protein cluster detection"). For every image it defines an intensity threshold Θ that segments the image into the background ($I < \Theta$) and clusters ($I > \Theta$). Thus, we do not analyze clusters with the intensities lower than Θ . After converting Θ from AU of intensity to integrin density by using "fluorescence calibration", we deduce a threshold integrin concentration of 52 ± 18 integrins/ μm^2 (*mean* \pm σ) for the images of

our experiments (229 images of adhering cells were analyzed).

The setting of Θ lower or higher than its ‘true’ value leads to imprecise image segmentation: detects false positive (taking background pixels as clusters) or false negative (taking cluster pixels as background) clusters. Our program is more prone to these mistakes for images with low signal to noise ratio (S/N) (with low number of integrins). In this case the program detects clusters with the intensities corresponding to noise fluctuations of the camera. These clusters are predominantly very small in size (about 1 pixel) and they contain very small numbers of integrins. To mitigate these issues, we have decided to consider only the clusters larger than optical resolution in our analysis. They account for approximately 14 and 21% of all detected integrin clusters on RGD and Invasin respectively.

In the following section we have analyzed the evolution of the amount of integrin receptors inside individual adhesion clusters during cell adhesion on RGD and Invasin-coated fluid substrates. As in the previous part, we have also focused on the role of Mn^{2+} treatment on the individual cluster evolution.

10.1 Integrin amount in individual adhesion clusters

For RGD substrates the median value corresponds to 10-13 integrins per cluster depending on the time point and remains more or less constant between the moment of cell seeding and 1 hour 30 minutes later. We observe the similar adhesion clusters that were described by Changede et al. [2015]. The fact that the number of integrins we detect in our clusters is smaller than 52 ± 43 integrins that was detected previously can be explained by two things. First, we detect specifically β_1 -integrins while in the previous studies the integrin ligand (RGD) was detected and therefore, we underestimate the number of integrins in the clusters not considering other integrins that interact with RGD. Second, we have not used super-resolution microscopy, thus we might overestimate the real area of the clusters and consequently underestimate the number of integrins in them.

On the contrary, for Invasin we observe an increase of more than 2-fold in terms of the number of integrins per adhesion cluster: the median value increases from 8-9 integrins per cluster for the time points when adhesion starts, to 22-26 integrins after 1 hour of adhesion (cf. Figure 10.1).

Integrin activation by Mn^{2+} has a similar effect as on the maturation of the **AZ**, described in the previous chapter (cf. Figure 10.2). We do not observe any significant effect on the adhesion clusters on RGD throughout the time course of cell adhesion:

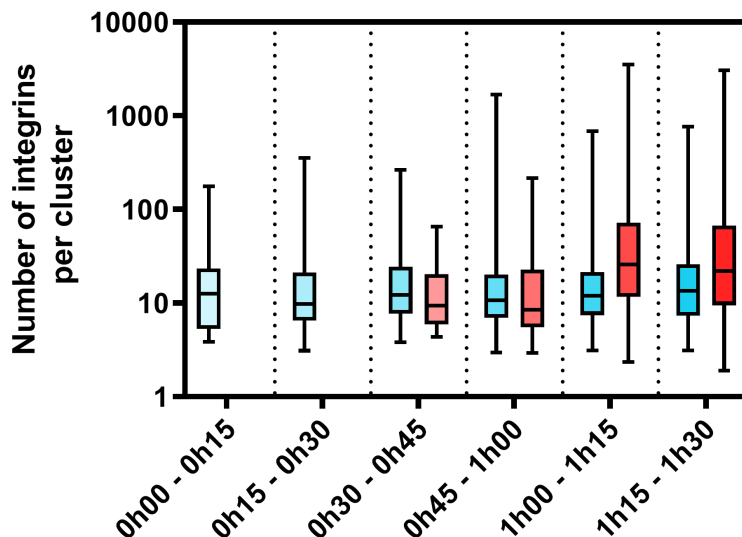


Figure 10.1: Number of integrin receptors in adhesion clusters of cells adhering on different substrates.

The color gradation, from clear to dark, corresponds to the different time points of adhesion. Evolution of the number of integrins in adhesion clusters for cells adhering on RGD- (blue) and Invasin-coated (red) fluid substrates. Log representation. Box and whiskers (from min to max) plot.

without Mn^{2+} median values range between 10 and 13 integrins per adhesion cluster depending on the time point, and with Mn^{2+} - 9-17 integrins per adhesion cluster (cf. Figure 10.2A).

In contrast, on Invasin, Mn^{2+} reduces the delay for integrin recruitment to the clusters (similar to the reduction of the delay for the **AZ** maturation). More specifically, in response to integrin activation by Mn^{2+} we obtain adhesion clusters with 6-13 integrins (median values) at the early stages of cell adhesion (first 30 minutes) and adhesion clusters with 18-37 integrins (next 30 minutes), corresponding to more than a 2-fold increase and significantly higher than in absence of Mn^{2+} (cf. Figure 10.2B). These results suggest that integrin activation by Mn^{2+} has a different effect on the dynamics of adhesion cluster maturation depending on the ligand composition of the fluid substrate.

Consequently, since we have measured an increase of the number of integrins in the clusters over time, we aimed at determining whether integrin density in the clusters increases as well over time. First, we have analyzed the relationship between the amount of integrin receptors in the adhesion cluster and the cluster area. We have run a Pearson correlation analysis between the number of integrins and the cluster area for both ligands and for the cells treated with(out) Mn^{2+} . These variables are positively correlated for both ligands and Mn^{2+} conditions. For RGD, the Pearson's correlation coefficients r are

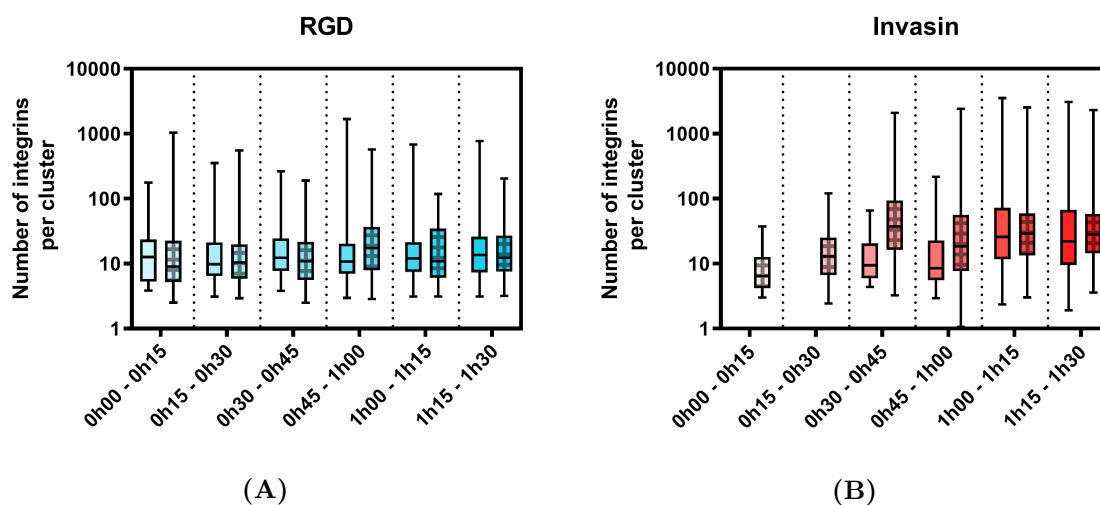


Figure 10.2: Number of integrins per individual adhesion cluster and the effect of integrin activation by Mn^{2+} .

We use the same color codes as in Figure 10.1, from clear to dark.

A) Evolution of the number of integrins per adhesion cluster without Mn^{2+} (Mn^{2+-} , *non-striped boxes*) and with Mn^{2+} (Mn^{2++} , *striped boxes*) for cells adhering on RGD coated fluid substrates. Log representation. Box and whiskers (from min to max) plot.

B) Evolution of the number of integrins per adhesion cluster without Mn^{2+} (Mn^{2+-} , *non-striped boxes*) and with Mn^{2+} (Mn^{2++} , *striped boxes*) for cells adhering on Invasin coated fluid substrates. Log representation. Box and whiskers (from min to max) plot.

0.79 and 0.92 with and without Mn^{2+} , respectively. For Invasin, r is equal to 0.74 and 0.93 with and without Mn^{2+} , respectively (cf. Figure 10.3). These results suggest an approximately linear relationship between the number of integrins in adhesion clusters and their areas, thus a constant integrin density, in the absence of Mn^{2+} . This is less the case when integrins are pre-activated by the Mn^{2+} .

10.2 Integrin densities in individual adhesion clusters

In this section we have calculated the integrin density at the level of individual adhesion clusters for both ligands at different time periods and with(out) Mn^{2+} . During the time course of cell adhesion, as observed for the average values in the **AZ**, we have observed an appreciably different evolution of integrin density for the cells adhering on RGD and on Invasin (cf. Figure 10.4).

For the RGD and without Mn^{2+} the median integrin density levels remain relatively stable (ranging between 84 and 99 integrins/ μm^2 throughout the time course of the experiment) (cf. Figure 10.4A). On the contrary, for Invasin, we have observed a step-like increase of integrin density after 1 hour: the median integrin density increases from

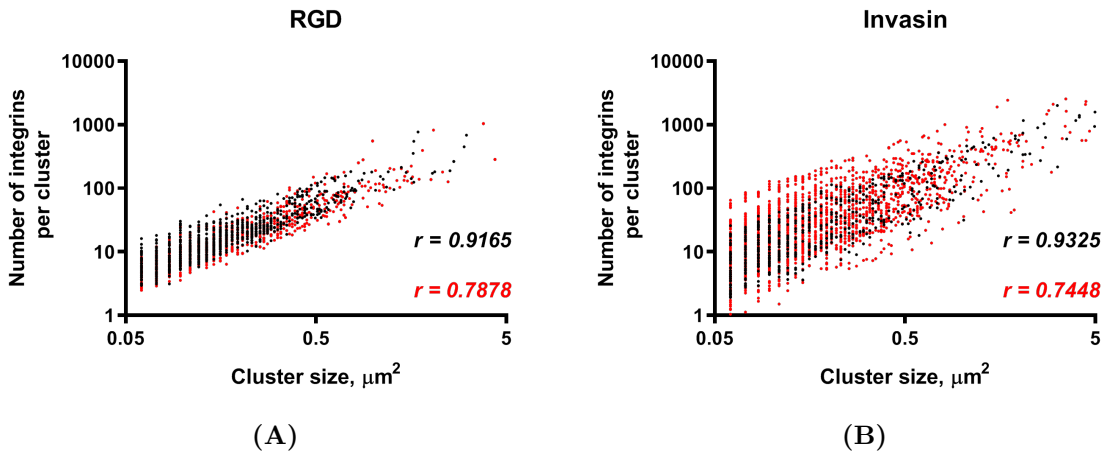


Figure 10.3: Relationship between the number of integrins in the clusters and the cluster area.

A) Amount of integrin receptors in the adhesion clusters as a function of the cluster area without Mn^{2+} (Mn^{2+-} , black dots) and with Mn^{2+} (Mn^{2++} , red dots) for cells adhering on RGD coated fluid substrates. Pearson's correlation coefficients are indicated. Log-log representation. Scatter plot.

B) Amount of integrin receptors in the adhesion clusters as a function of the cluster area without Mn^{2+} (Mn^{2+-} , black dots) and with Mn^{2+} (Mn^{2++} , red dots) for cells adhering on Invasin coated fluid substrates. Pearson's correlation coefficients are indicated. Log-log representation. Scatter plot.

73-76 integrins/ μm^2 (before 1 hour) to 158-188 integrins/ μm^2 (after 1 hour). The Mn^{2+} treatment has a different effect on the two ligands, as already described at the larger scale. For RGD we have not observed any significant differences in integrin densities (median values throughout the time of adhesion: 68-102 integrins/ μm^2) compared to the ones with no treatment. Conversely, for Invasin Mn^{2+} reduces the delay in the step-like increase of integrin density that is observed in its absence. Moreover, it increases the median integrin densities at the stage between 30 minutes and 1 hour of adhesion by 1.5-3.5-fold (from 73-76 integrins/ μm^2 without Mn^{2+} to 108-270 integrins/ μm^2 with Mn^{2+}) (cf. Figure 10.4B). Thus, Mn^{2+} treatment does not result in any significant increase in integrin density in adhesion clusters on RGD. On contrary, for Invasin it significantly increases integrin density and speeds up cluster maturation.

Next, we have analyzed the evolution of the integrin density in the individual adhesion clusters as a function of the area of the clusters (cf. Figure 10.5). The following cloud plots illustrate the difference between RGD and Invasin in individual clusters during the time course of cell adhesion. On RGD, we observe the presence of large clusters, around 1 μm^2 very early in the adhesion process. The cluster size remains mostly lower than 1 μm^2 and the integrin density less than 500 integrins/ μm^2 . Moreover, the distribution remains broad over time and the integrin activation by Mn^{2+} does not change the size and density

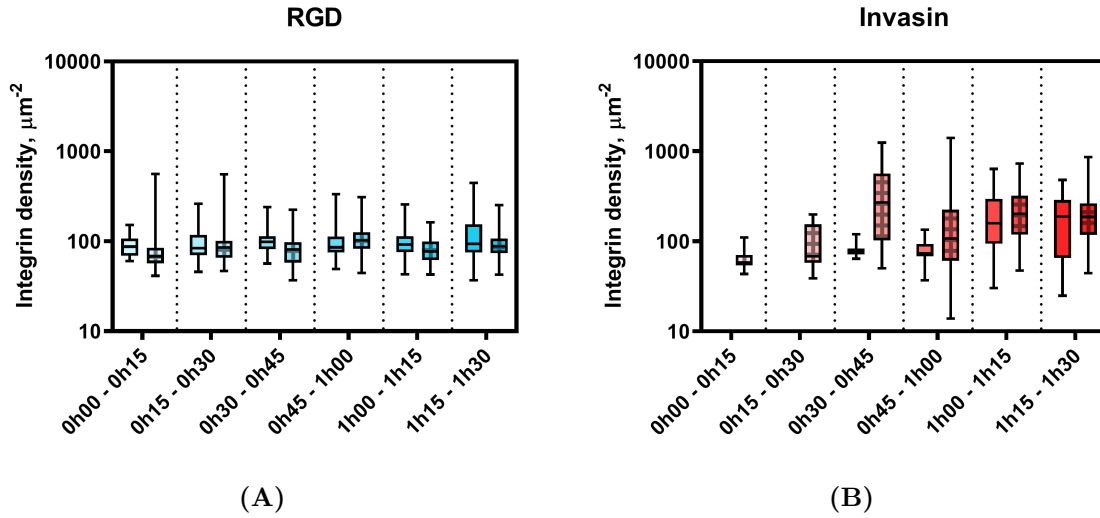


Figure 10.4: Effect of integrin activation by Mn^{2+} on the averaged integrin density in individual adhesion clusters.

We use the same color codes as in Figure 10.1, from clear to dark.

A) Evolution of integrin density in adhesion clusters without Mn^{2+} (Mn^{2+-} , *non-striped boxes*) and with Mn^{2+} (Mn^{2++} , *striped boxes*) for cells adhering on RGD coated fluid substrates. Log representation. Box and whiskers (from min to max) plot.

B) Evolution of integrin density in adhesion clusters without Mn^{2+} (Mn^{2+-} , *non-striped boxes*) and with Mn^{2+} (Mn^{2++} , *striped boxes*) for cells adhering on Invasin coated fluid substrates. Log representation. Box and whiskers (from min to max) plot.

distribution. In contrast, on Invasin, we observe a clear increase of the integrin density over time reaching values over $500 \text{ integrins}/\mu\text{m}^2$, as well as of the cluster size, with a higher number of clusters larger than $1 \mu\text{m}^2$ than on RGD after 1 hour of adhesion. In addition, integrin activation by Mn^{2+} increases integrin density in the individual adhesion clusters.

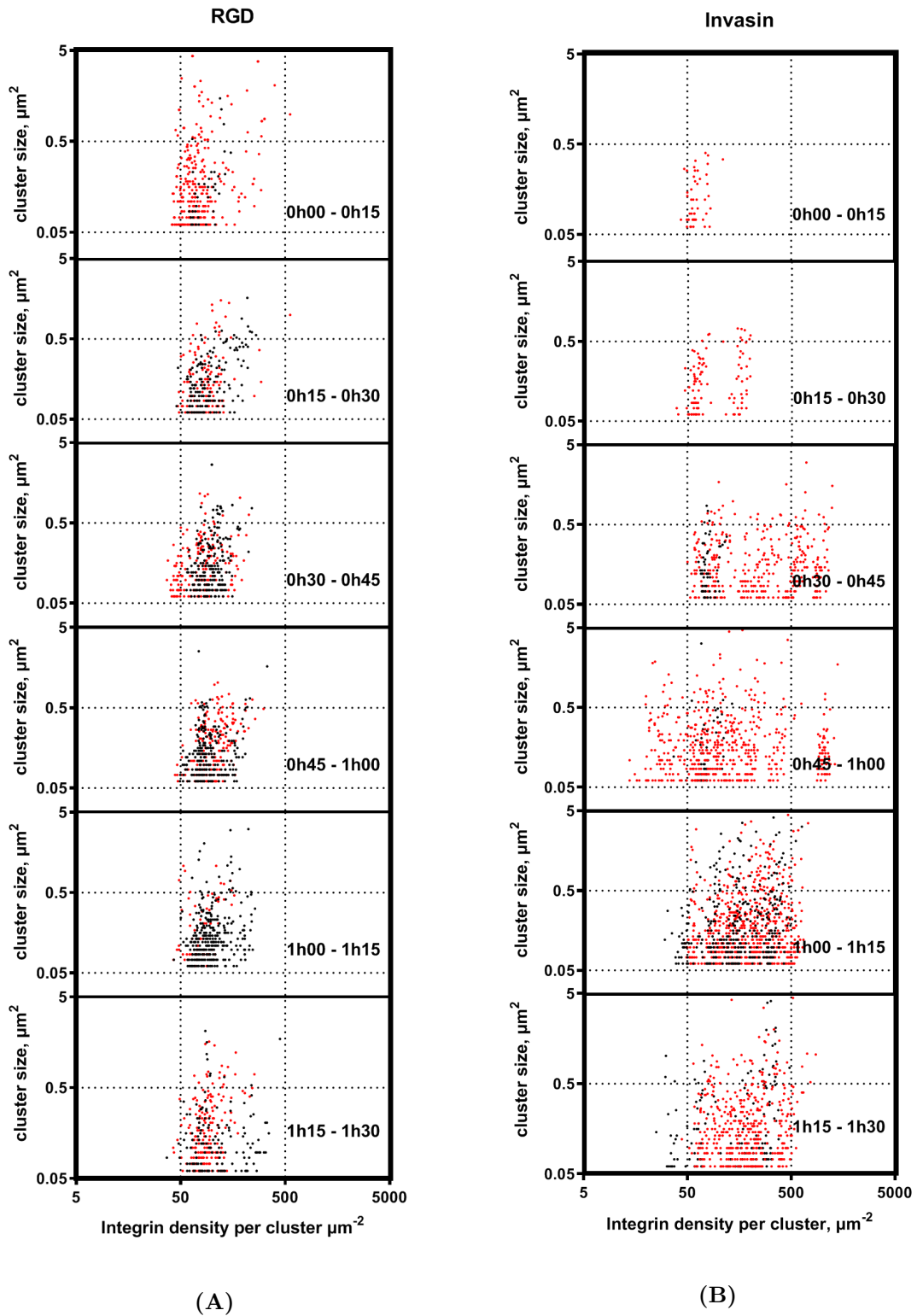


Figure 10.5: Time lapse distributions of the adhesion cluster sizes as a function of integrin density in individual adhesion clusters.

A) Cluster sizes versus integrin density in the clusters without Mn^{2+} (black) and with Mn^{2+} (red) for cells adhering on RGD-coated fluid substrates. Log-log representation.

B) Cluster sizes versus integrin density in the clusters without Mn^{2+} (black) and with Mn^{2+} (red) for cells adhering on Invasin-coated fluid substrates. Log-log representation.

Interestingly, we have observed multi-modal integrin density distributions for the clusters on Invasin and with Mn^{2+} treatment at different time points (cf. Figure 10.6). We have not observed them neither for RGD, nor for Invasin without Mn^{2+} treatment. In order to characterize these distributions we have fitted them as a sum of several Gaussians and followed their evolution during the time course of cell adhesion. At short time, less than 15 minutes, we observe only 2 classes corresponding to low densities: 56 and 78 integrins/ μm^2 . Gradually, more classes with higher integrin densities appear with time (with mean values 150-250, 400-500 and 900-1000 integrins/ μm^2), coexisting with a low density class. Integrin density in these more mature clusters are comparable to those in FA (Wiseman et al. [2004]). At time longer than 1 hour, we observe only populations with medium densities (100-250 and 400-500 integrins/ μm^2 , but no class at high density is visible in the distribution, possibly indicating that their number continues to decrease as their density increases.

The co-existence of populations of clusters with different integrin densities may be explained by the asynchrony of cell adhesion on Invasin. As we have seen in the Figure 8.6B of the chapter 8 of the Results, it takes 1 hour for having 90% of the cells adhering on Invasin with Mn^{2+} , and only about 40% of the cells adhere at 15 minutes. This implies that the cells at a given time are at different stages of their adhesion. Thus, they might have clusters at different maturation stage. The degree of asynchrony is obviously higher for the late adhesion time points (after 1 hour), when all the sub-populations are probably mixed. For the earlier adhesion time points (before 1 hour) we can appreciate a step-like evolution of integrin density sub-populations.

These results might suggest that integrin clusters maturation occurs by integrin reorganization in clusters leading to step-like increases of integrin density.

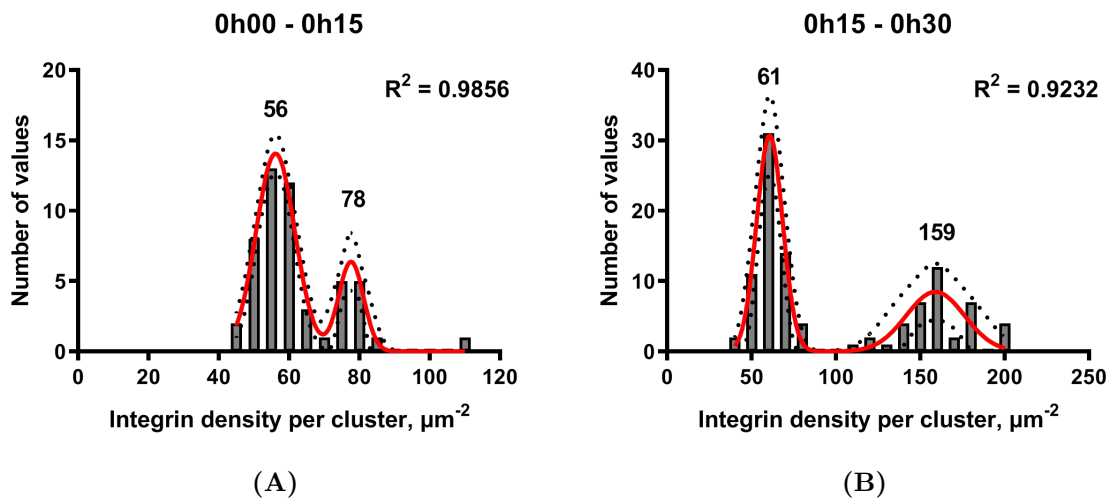


Figure 10.6: Evolution of integrin density distributions.

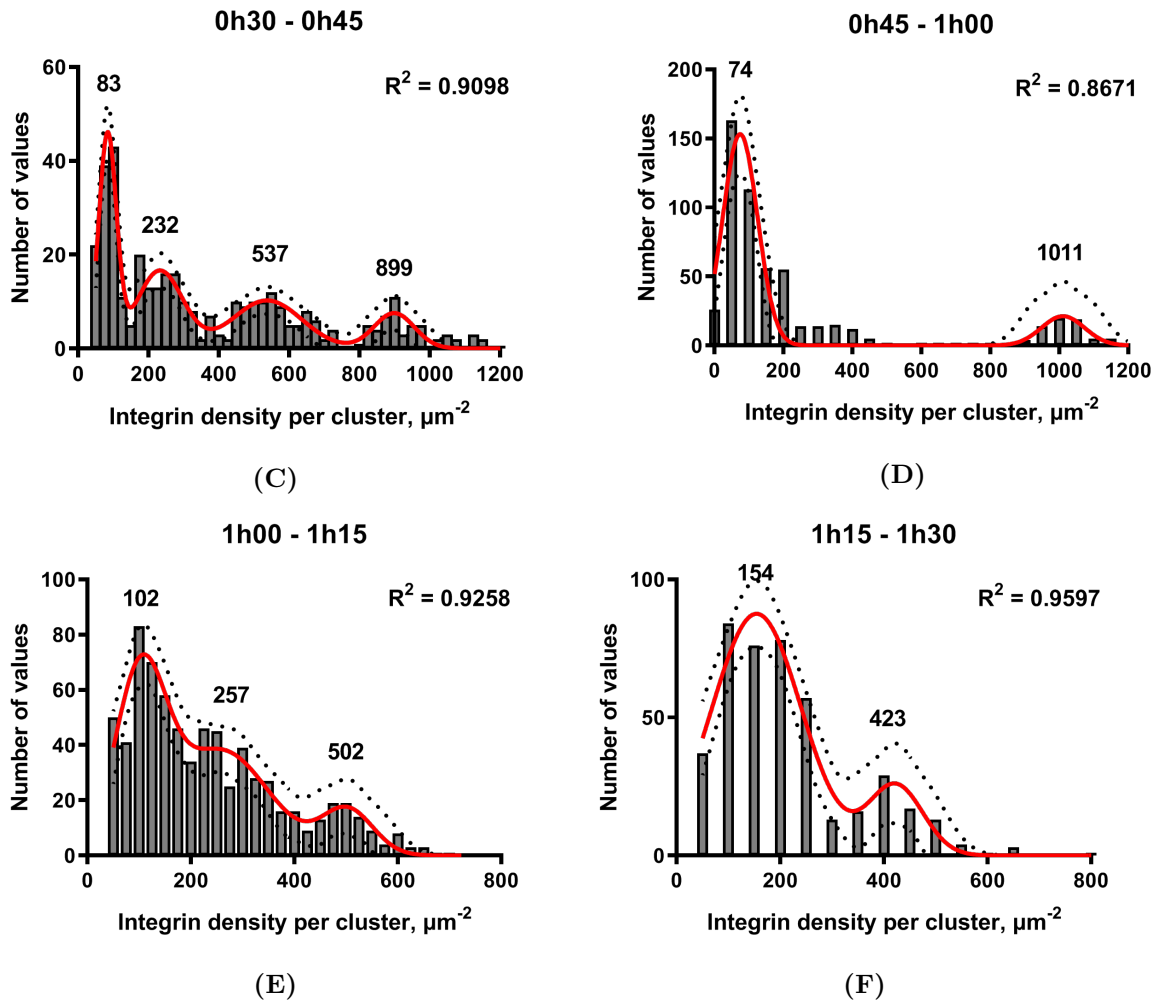


Figure 10.6: Evolution of integrin density distributions(cont.).

A)-E) Histograms of integrin density distributions on Invasin with Mn^{2+} treatment. Fits with a sum of Gaussian functions (red). 95% CI is indicated by black dots. Goodness of these fits is indicated with R^2 values. Mean values of Gaussian functions from the fits are indicated by numbers.

In the following part, we will focus on the adhesion clusters' locations in the **AZ** of the cell.

chapter 10 conclusions:

In this chapter, we have studied the maturation of the individual integrin clusters during cell adhesion by measuring the cluster area, the number of integrins and integrin density in clusters over time for RGD and Invasin-coated fluid substrates. Integrin cluster maturation happens differently for the two ligands. We have obtained the following results at the scale of single clusters, that are consistent with our previous results obtained at a larger scale:

- Integrin clusters are formed much faster on RGD than on Invasin. For RGD we observe a significant number of clusters larger than the diffraction limit at very short time (first 30 minutes), whereas it takes at least 30 minutes for the clusters to form on Invasin.
- Integrin clusters are on average smaller on RGD than on Invasin, suggesting that fusion of clusters is less efficient on RGD than on Invasin.
- Integrin activation by Mn^{2+} has a stronger effect on Invasin than on RGD. It accelerates and increases adhesion cluster maturation process, increasing integrin density in a step-like manner.

Chapter 11

Radial distribution of adhesion proteins in *AZ*

In this chapter we have focused on a detailed map of adhesion proteins' distribution in the *AZ*. It is known that on rigid substrate (glass) cells have irregular shapes and they develop mature FAs that are located close to the cell periphery (cf. Figure 11.1).

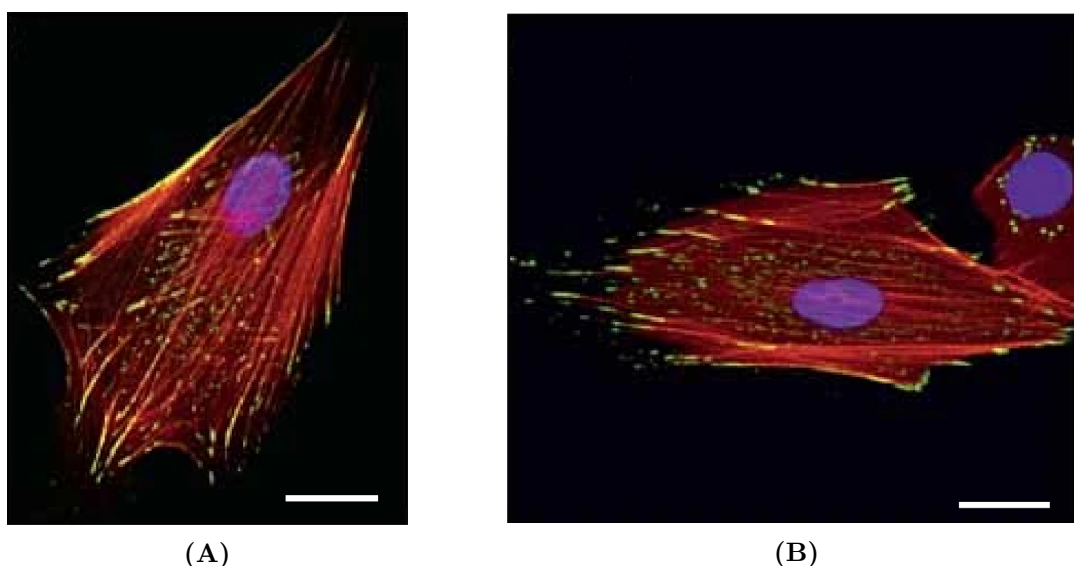


Figure 11.1: Focal adhesions in cells on rigid substrates (adapted from Prager-Khoutorsky et al. [2011]).

A-B) Focal adhesions in HFF cells stably expressing paxillin-YFP (green) on rigid substrates. Cells were stained with TRITC-phalloidin (red) and DAPI (blue).

Scale bar, 25 μm

We wanted to compare the distribution of adhesion sites on fluid SLBs with the FAs on rigid glass. Considering that cells adhering on fluid SLBs have a round shape (cf. section 8.1 of the Results), we have introduced polar coordinates (r, θ) and described the

adhesion protein localization with them. After taking into account the isotropy of the system, we have focused on the radial distribution of the proteins in the **AZ**.

Based on the cell contour detected from the wide field image, we have divided the contour in 10 concentric rings, each with a width equal to $\frac{1}{10}$ of the cell radius (cf. section 7.3 of the Materials and Methods) and centered on the center of symmetry of the cell contour. 0 corresponds to the center, 1 to the first ring and 10 to the external contour as detected from the wide field image (cf. Figure 11.2).

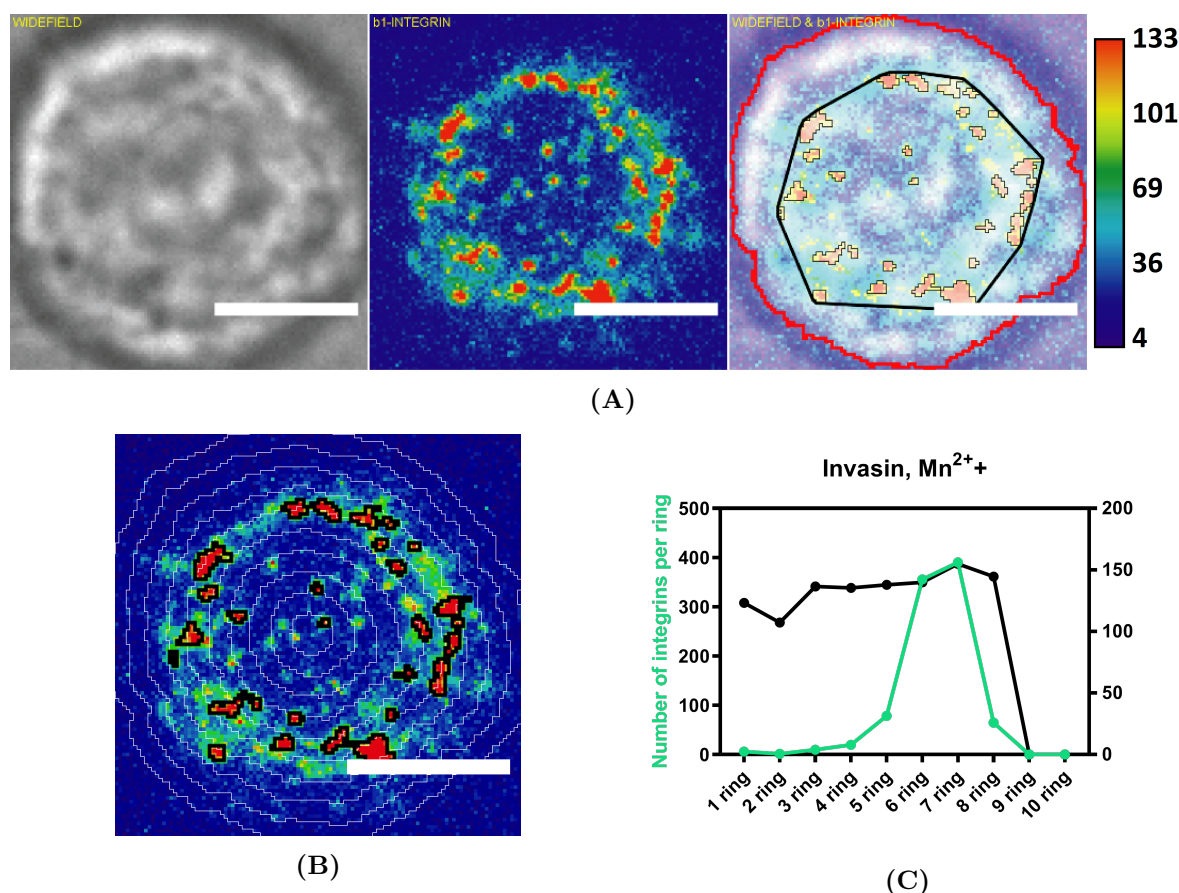


Figure 11.2: Analysis of the adhesion protein radial distribution in the **AZ.**

A) β_1 -integrin clusters in the **AZ** for a Mn^{2+} treated cell adhering on Invasin-coated fluid substrate. Pseudo-colored heat map of β_1 -integrin density based on a fluorescence microscopy image. Scale bar, $5 \mu\text{m}$. Integrin density scale based on a prior fluorescence calibration (cf. section 6.2 of the Materials and Methods).

B) **AZ** delimited by the external contour and with concentric rings (thin white lines) and integrin clusters inside the zone (thick black contours). Scale bar, $5 \mu\text{m}$.

C) β_1 -integrin numbers (green) and densities in the clusters (black) radial distribution profiles across the concentric rings, corresponding to the image in B). 0 corresponds to the center and 10 ring to the external contour of the cell (detected by wide field microscopy).

We have then plotted where the detected adhesion proteins are distributed (cf. Figure 11.2C). For the ring i , we count the proteins with radial location between $\frac{R(i-1)}{10}$ and $\frac{Ri}{10}$, where R is the cell radius. A peak in the distribution around the 6th and 7th rings

for instance indicates that most of β_1 -integrins are detected in a ring located between 0.6 and 0.7 cell radii from the cell center.

We have first applied this mapping procedure to integrins in the **AZ** of cells adhering on RGD and Invasin.

11.1 Adhesion cluster radial distribution on different substrates

We have analyzed 305 cells adhering on RGD and 206 cells on Invasin. We have also tested the role of integrin activation by Mn^{2+} on the radial distribution of adhesion proteins in the **AZ** (cf. Figure 11.3). We have plotted the distributions of the proportion of integrins in each ring (total number of integrins per ring normalized by the total number of integrins in the **AZ**).

For the cells adhering on RGD fluid substrates we have not seen significant difference of the radial distribution of integrins over time. This corroborates well with our previous results that showed a relatively fast adhesion maturation on RGD. Therefore, we have pooled and analyzed together data corresponding to different times of adhesion. In the absence and in the presence of Mn^{2+} , we see a similar radial distribution of integrins for the cells adhering on RGD: the largest proportion of integrin receptors are located in the 4 – 5th rings, thus midway between the cell edge and the center (cf. Figure 11.3A-11.3B).

For the cells adhering on Invasin we could not properly compare the evolution of radial distribution over time and the role of integrin activation by Mn^{2+} in this distribution because of the poor adhesion of cells without Mn^{2+} treatment in the early times of the spreading. Nevertheless, we have not detected any significant difference of the radial distribution of integrins over time for the Mn^{2+} -treated cells on Invasin. Like for adhesion on RGD, we analyze the data altogether, independent of the time. We observe that, on average, the integrins are mainly located between the 3th and 6th rings, with a broader radial distribution than for RGD (cf. Figure 11.3C). In the case of the non-treated cells we observe a less broad integrin distribution (cf. Figure 11.3D), although the amount of studied cells is much more limited.

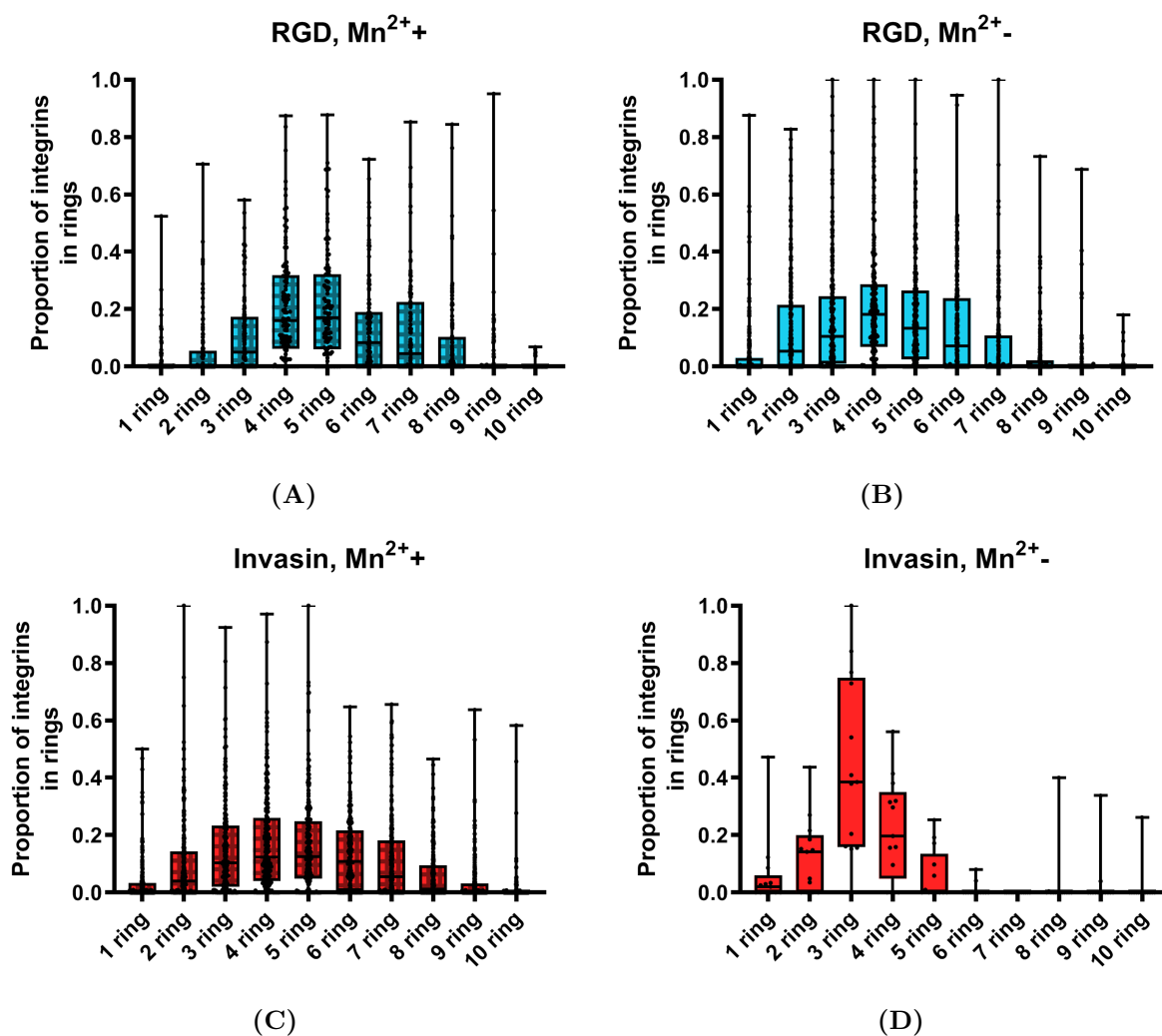


Figure 11.3: Normalized radial distribution of integrin numbers in the AZ.

A) Radial distribution of β_1 -integrin fractions across the concentric rings for the Mn^{2+} treated cells on RGD (104 cells). 10 ring corresponds to the external contour.

B) Radial distribution of β_1 -integrin fractions for the non-treated cells on RGD (201 cells).

C) Radial distribution profile of β_1 -integrin fractions for the Mn^{2+} treated cells on Invasin (192 cells).

D) Radial distribution profile of β_1 -integrin fractions for the non-treated cells on Invasin (14 cells).

Box and whiskers (from min to max) plots.

Next, we asked if the protein density in the clusters changes depending on their localization in the cells, which could correspond to different maturation levels of the clusters in the adhesion zone between the periphery and the center. For this, we have plotted the distribution of the protein densities in the clusters for each ring and for all cells (cf. Figure 11.4).

For both types of substrates and for both Mn^{2+} conditions the local integrin density appears to be independent of the radial coordinate. In other words, integrin clusters have

on average the same density independently of their position in the AZ (cf. Figure 11.4).

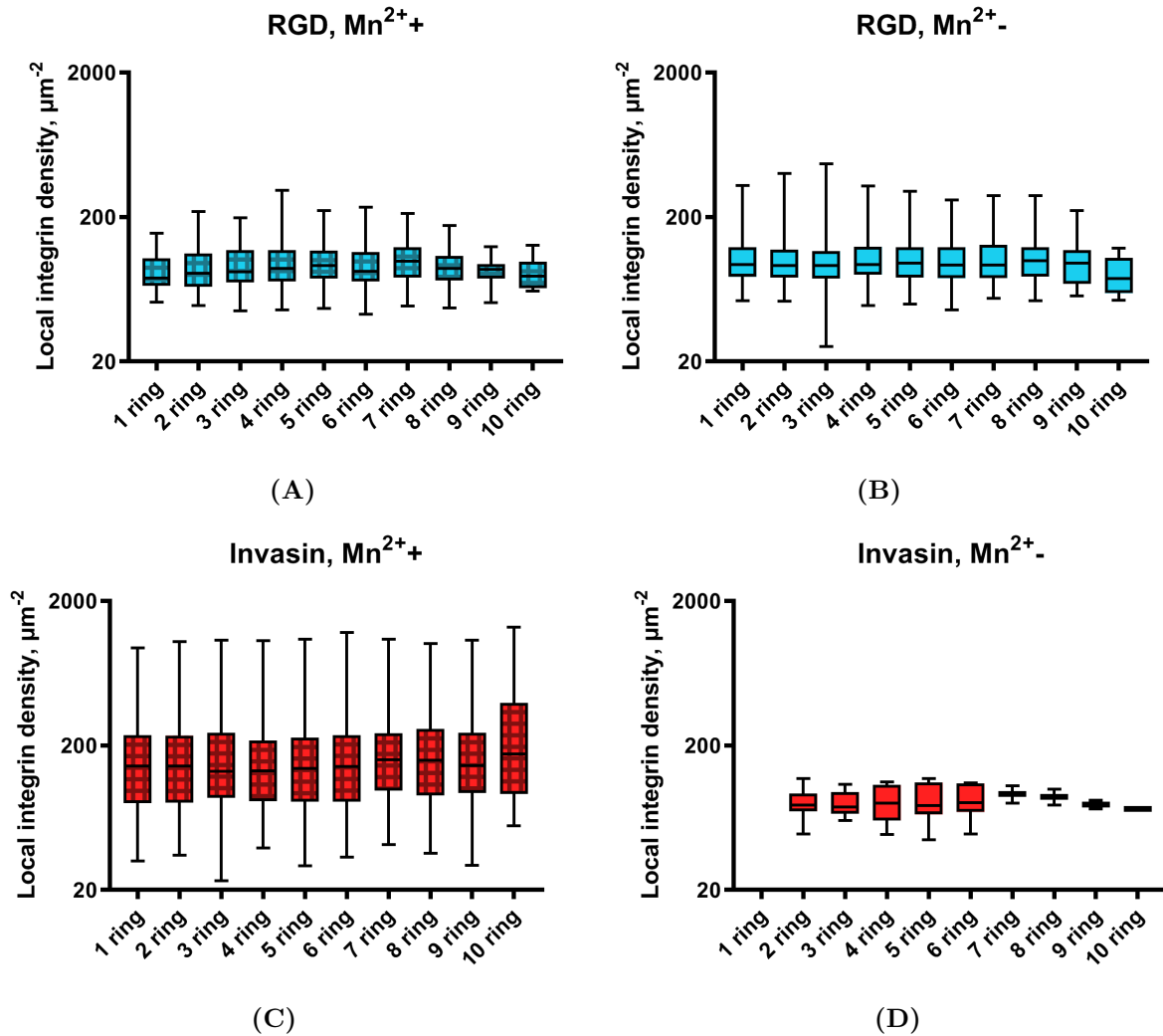


Figure 11.4: Distribution of the integrin densities in the clusters as a function of their radial localization in the cells, in the different conditions.

A) Distributions of β_1 -integrin densities in the clusters (local densities) for each concentric rings of the AZ for the Mn^{2+} treated cells on RGD (104 cells).

B) Same distributions for the non-treated cells on RGD (201 cells).

C) Same distributions for the Mn^{2+} treated cells on Invasin (192 cells).

D) Same distributions for the non-treated cells on Invasin (14 cells).

Box and whiskers (from min to max) plots.

We also calculated the average density of integrins per concentric ring/stripe, as a function of the ring number. We call it "global density", in contrast with the previous "local" density where we averaged the density of integrins per clusters. In contrast with the data in the Figure 11.3 representing the total number of integrins in each ring, which depends on the area of the ring, this representation cancels this dependence. We are able to compare those densities between the cells for different adhesion conditions because the

areas of the i^{th} ring (and cell areas detected from the wide field images) do not vary much between the adhering cells (cf. Figure 11.5).

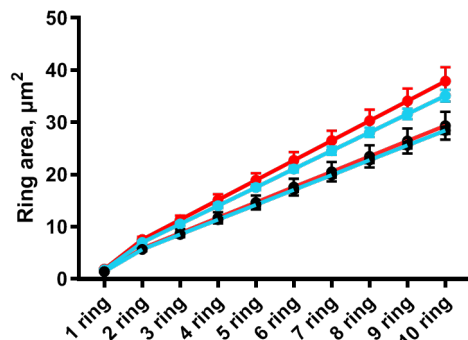


Figure 11.5: Cell rings' areas.

Area of the cell rings for the cells adhering on RGD (blue), or Invasin (red) and with (color dot) and without (black dot) Mn^{2+} treatment. Scatter line plot (mean with SEM).

With this representation, we find that for the cells adhering on RGD, integrin clusters are mainly located between the 2^{nd} and the 6^{th} ring for the non-treated cells with a maximum in ring 4 (cf. Figure 11.6B) and between 3^{rd} and 7^{th} ring for the Mn^{2+} treated cells with a maximum in rings 4 and 5 (cf. Figure 11.6A), with the median global densities ranging between $0.4\text{-}1.6 \mu\text{m}^{-2}$ and $0.2\text{-}1.2 \mu\text{m}^{-2}$, respectively.

For the cells adhering on Invasin the effect of the Mn^{2+} is stronger: integrin clusters are more centered (between the 1^{st} and the 4^{th} rings), and denser, (with median global density between $1.8\text{-}3.6 \mu\text{m}^{-2}$) for the non-treated cells (cf. Figure 11.6D) than for the cells treated with Mn^{2+} . Those have a broader radial distribution across the **AZ** (between the 2^{nd} and the 8^{th} rings) with a maximum between rings 3 and 5, and are less dense (with median global density between $0.1\text{-}2.7 \mu\text{m}^{-2}$) (cf. Figure 11.6C). However, note that the number of cells adhering in the absence of Mn^{2+} is much lower, and our statistics poor in this case. In addition, as already mentioned in chapter 10 of the Results, we observe that the local density of integrins recruited in the clusters is higher for cells adhering on Invasin than on RGD.

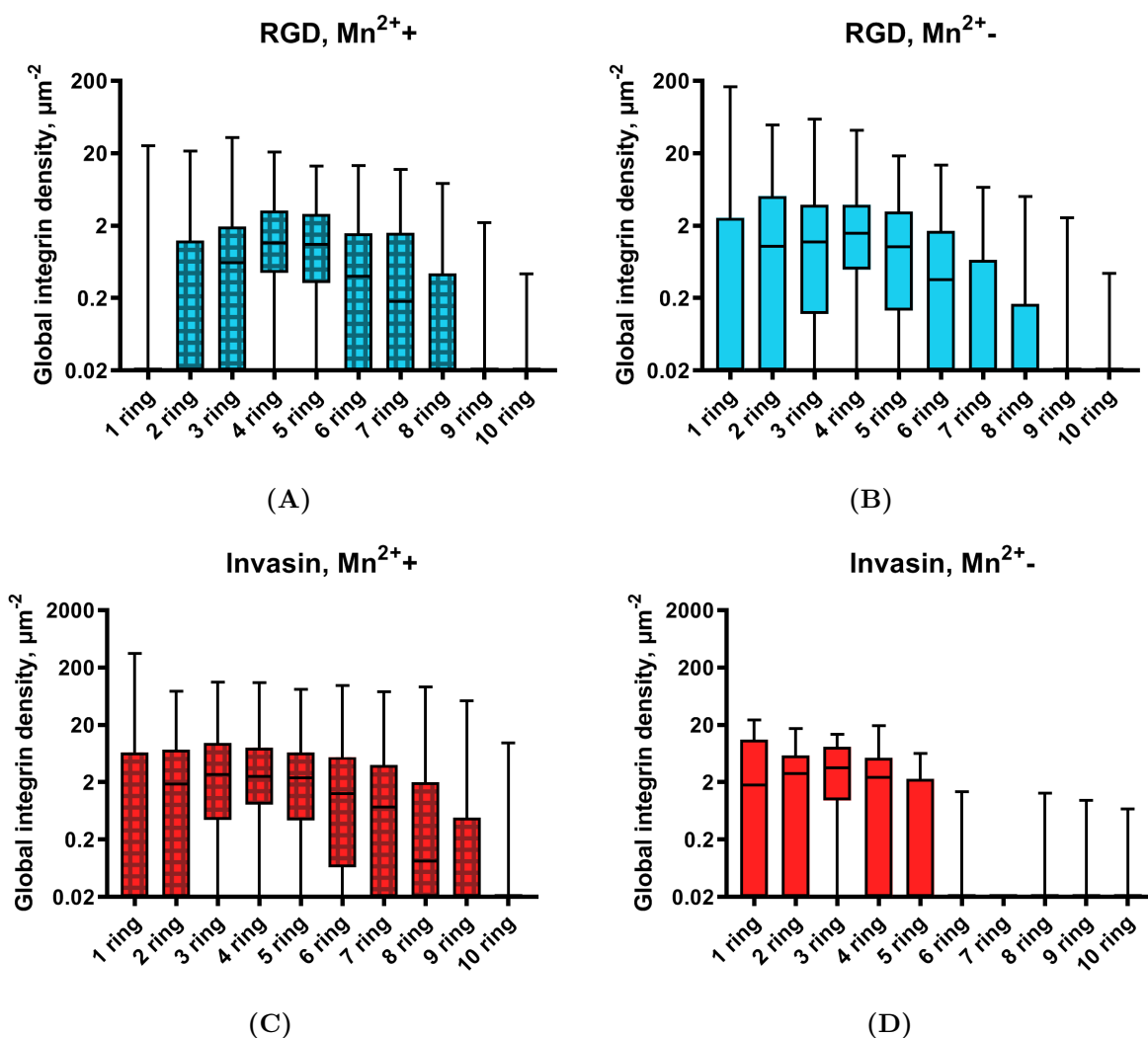


Figure 11.6: Radial distribution of the global integrin densities in the cells in the different conditions.

A) Distribution of the β_1 -integrin global densities (total number of integrins in the stripe/area of the stripe) as a function of the ring number for the Mn^{2+} treated cells on RGD (104 cells).
 B) Same distribution for the non-treated cells on RGD (201 cells).
 C) Same distribution for the Mn^{2+} treated cells on Invasin (192 cells).
 D) Same distribution for the non-treated cells on Invasin (14 cells).
 Box and whiskers (from min to max) plots.

To summarize these results, we have demonstrated that on average for fluid substrates (SLBs) integrin distribution is different from the mature one for the rigid substrate (glass). On SLBs, integrin clusters are located closer to the cell center than to its edge independently of the ligand or Mn^{2+} treatment, whereas on glass integrin is located in the bigger FA sites close to the periphery of the cell (cf. Figure 11.1). This is consistent with the contraction of the **AZ** by more than 30% (median value) during the adhesion process that we described in chapter 9 of the Results. The local density of integrins in the clusters does not depend on the cluster location in the **AZ**. The global radial integrin density localizes

the **AZ** of the cell. Globally, for the RGD the densest areas are between the 2nd and the 6th rings, whereas for the Invasin – between the 1st and the 4th rings. These areas broaden after Mn²⁺ treatment: for RGD, they are located less close to the center: 2-6 versus 3-7 without Mn²⁺; for Invasin, they are difficult to compare due to the very low number of points in Mn²⁺-, but they are broader than for RGD and also less "constricted".

11.2 Radial distribution of actin in the **AZ**

In this section, we have studied the organization of the actin cytoskeleton in the **AZ**. We have analyzed the radial distribution of actin in the **AZ** of the cell to characterize potential differences between SLBs and glass substrates (cf. Figure 11.1).

For that we have performed the same analysis as for radial distribution of integrins. In these experiments, we had to fix the cells on the SLBs to label them with with fluorescent phalloidin (cf. section 5.3 of the Materials and Methods). Moreover, for lack of time, we have only performed these experiments on RGD-coated SLB, and not on Invasin. Cells adhered on the RGD fluid substrates for 1 hour and were then fixed with PFA. Actin was stained with phalloidin-Alexa Fluor 647 and the cell **AZ** was imaged as previously described. We have often observed the presence of holes in the SLB under the **AZ** of the cell after fixation (cf. Figure 11.7, lipid channel - magenta). These holes were never observed in absence of cell fixation, but were not present when the same treatment was applied in the absence of cells, or next to the adhering cells. We suspect that they could result from forces exerted by the cells on the SLB during chemical fixation. Therefore, since the lipid bilayer was not uniform in these experiments, we could not quantify the actin signal as we did before for integrins.

Nevertheless, we could analyze the actin radial distribution based on raw fluorescence images (without fluorescence calibration). We observe that in most cases the **AZ** of the cell is delimited by the actin ring: no integrin clusters or actin structures could be detected outside of the **AZ** (cf. Figure 11.7, red channel). The **AZ** can vary in size depending on the degree of adhesion maturation and in general is not centered in the center of symmetry of the cell.

We have next analyzed the radial distribution of actin in the **AZ** on 120 cells fixed and adhering on RGD cells with labelled actin (46 non-treated and 74 treated with Mn²⁺). Without and with Mn²⁺, the global actin fluorescence signal density is stably high for $r < \frac{R}{2}$ (where R is the cell radius), reaching the highest median density in the ring 3 and monotonously decaying for the $r > \frac{R}{2}$, reaching the lowest median density in the ring 10

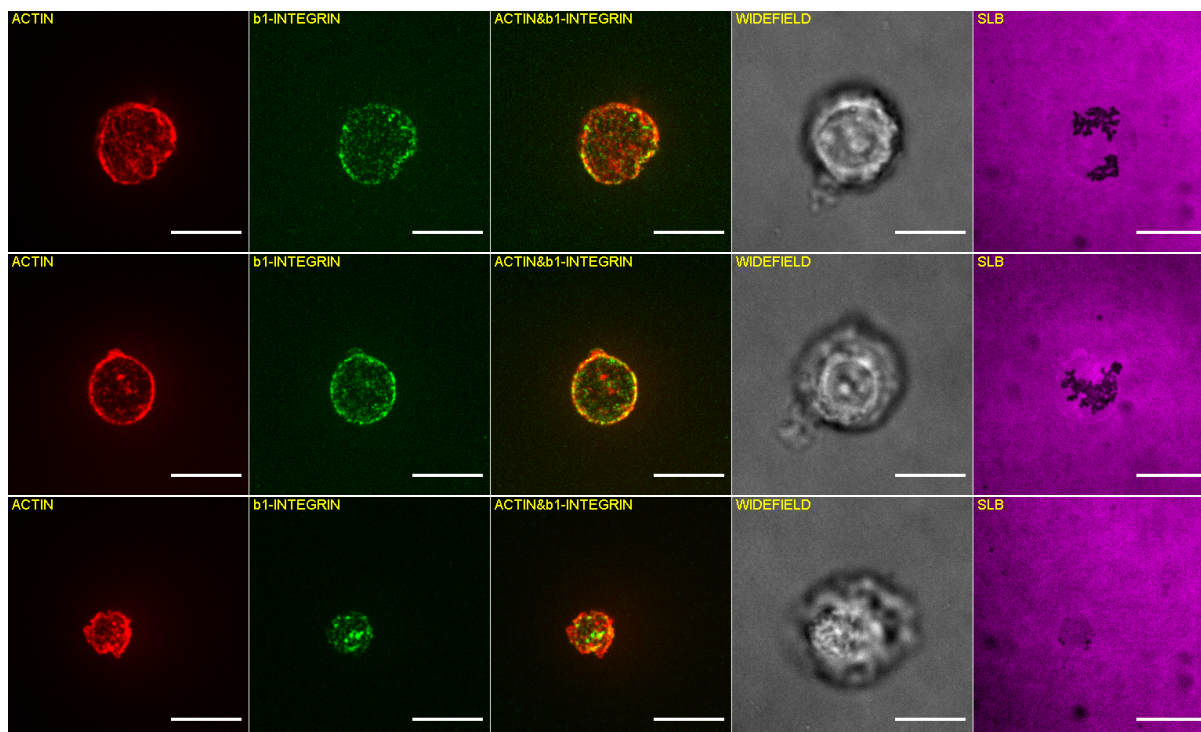


Figure 11.7: Fluorescence microscopy images of three cells adhering on RGD with *AZ* of different sizes.

From left to right: actin labelled with phalloidin-Alexa Fluor 647 (red), β_1 -integrin labelled with Halotag ligand-Alexa Fluor 488 (green), merge of actin and β_1 -integrin (red and green), cell contour in wide field (grey), SLB containing Marina-Blue DHPE lipids (magenta).

From top to bottom: a cell with a large, medium and small *AZ* (*AZ ratio*). Scale bars, 10 μm .

(cf. Figure 11.8A-11.8B). Integrin clusters in the same cells are predominantly located in the same rings as actin with a maximum around rings 2 to 4 (cf. Figure 11.8C-11.8D). These results suggest that after 1 hour of adhesion, integrin clusters and actin are mostly located in the same parts of the cell: closer to the cell center rather than to the cell edge.

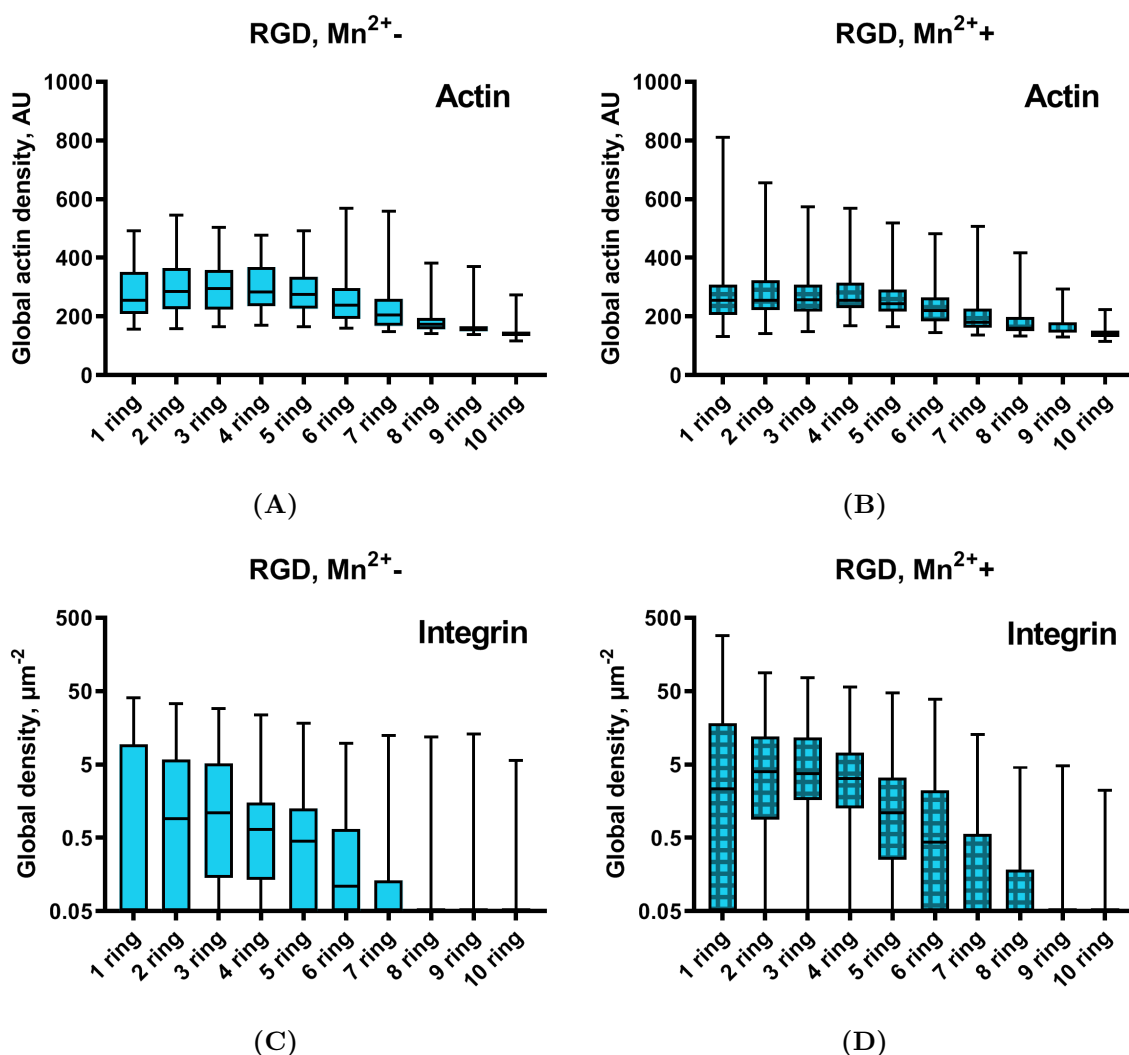


Figure 11.8: Radial distribution of the normalized actin intensity signal.

A) Radial distribution profile of the normalized actin signal across the concentric rings for the non-treated cells on RGD (46 cells).

B) Same distribution for the cells treated with Mn^{2+} on RGD (74 cells).

C) Distribution of the β_1 -integrin global densities (total number of integrins in the stripe/area of the stripe) as a function of the ring number for the Mn^{2+} non-treated cells on RGD (46 cells).

D) Same distribution for the Mn^{2+} treated cells on RGD (74 cells).

Box and whiskers (from min to max) plot.

To summarize this section, we have shown that at least for the cells adhering on RGD fluid substrates, the bulk of F-actin is located closer to the cell center than to the cell edge, and its maximum concentration corresponds to that of integrins. We observed an actin ring that encompasses the **AZ** of the cell and less organized actin structures inside the **AZ**. Moreover, we have not observed any significant difference in its radial distribution in the cells treated with(out) Mn^{2+} .

In the following section we have studied the evolution of the ligand distribution on the substrate during the time course of cell adhesion.

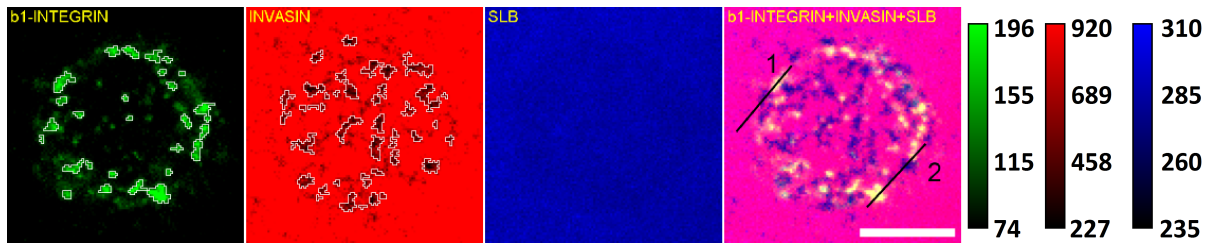
11.3 Invasin clustering and depletion in the **AZ**

In this section, we have characterized how cells act on the fluid surface coated with ligands. We have focused on Invasin remodeling underneath the cell during its adhesion. The same analysis could not be performed with RGD, since we did not have fluorescent lipidated peptides. Since cells very weakly adhere on Invasin in the absence of Mn^{2+} , we have essentially studied here the distribution of Invasin when integrins are activated by Mn^{2+} .

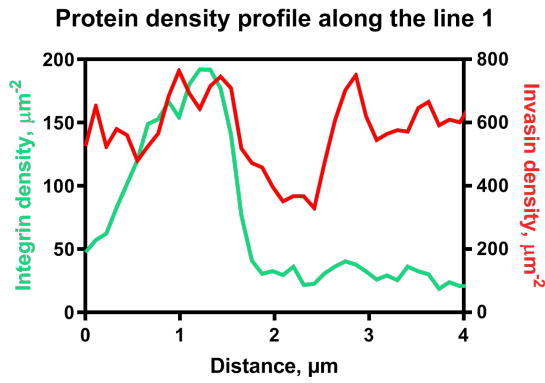
We have observed that Invasin density on the SLB under the adhering cells is not homogeneous: it is higher at the locations of integrin clusters but in some areas of the **AZ**, Invasin is strongly depleted (cf. Figure 11.9). The first observation is expected and likely correspond to the co-clustering of ligand-receptor pairs on the fluid substrate during cell adhesion. But, the depletion of Invasin, however, is unexpected. We have called these Invasin depletion zones, Invasin “holes”. This phenomenon is striking and we have next characterized and tried to understand the nature of this phenomenon. We have ruled out that Invasin holes originate from the defects in the SLB below. In control experiments using labeled lipids, we found that the quality of the SLB is the same throughout the whole **AZ**. The SLBs are homogeneous and there are no defects in places where Invasin is depleted (cf. Figure 11.9A-11.9D).

RESULTS

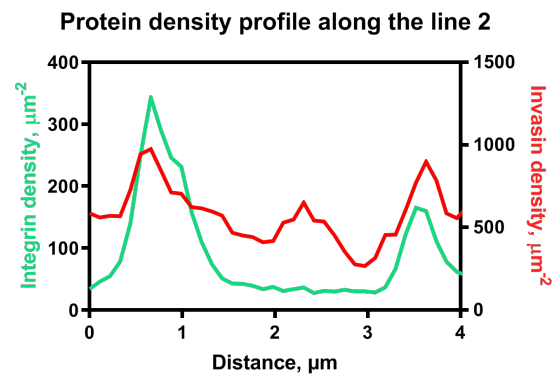
CHAPTER 11. RADIAL DISTRIBUTION OF ADHESION PROTEINS IN AZ



(A)

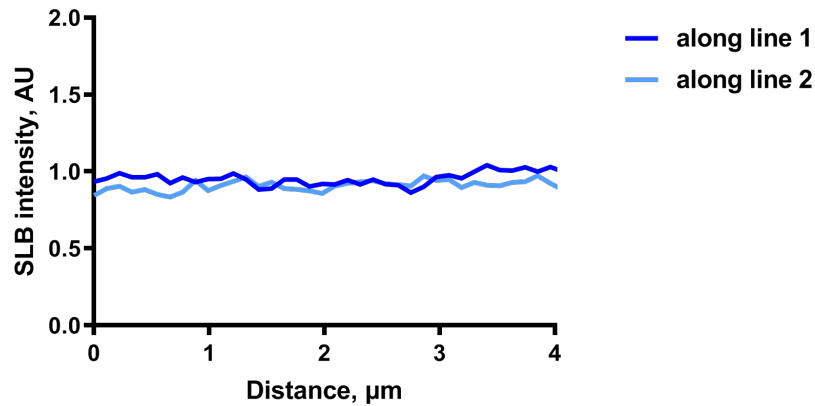


(B)



(C)

SLB intensity profiles



(D)

Figure 11.9: Co-existence of integrin clusters, Invasin clusters and Invasin holes in the AZ.

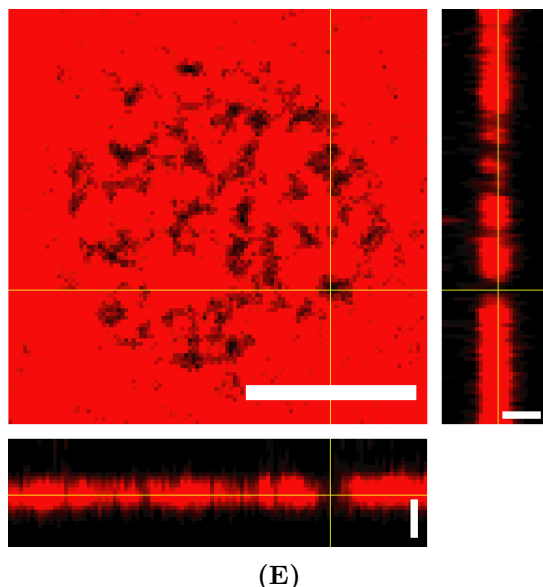


Figure 11.9: Co-existence of integrin clusters, Invasin clusters and Invasin holes in the **AZ.**

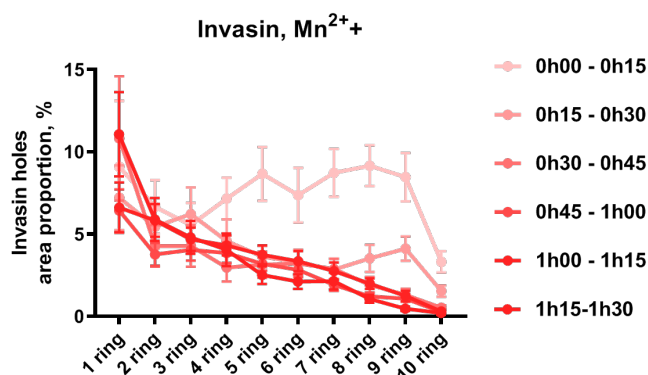
A) Characteristic fluorescence multi-channel image of a cell adhering on Invasin-coated SLB in the presence of Mn^{2+} . From left to right: β_1 -integrin labelled with Halotag ligand-Alexa Fluor 488 (green), Invasin labelled with JF549 (red), SLB containing Marina-Blue DHPE lipids (blue) and merge of β_1 -integrin, Invasin and SLB (green, red and blue). Integrin and Invasin density scales based on a prior fluorescence calibration (cf. Materials and methods “fluorescence calibration”). Marina-Blue lipid scale based on a raw fluorescence data (AU). Integrin clusters and Invasin holes (as detected by our software) are circled by a white line. Scale bar $5 \mu m$.

B-C) β_1 -integrin and Invasin density profiles across black lines 1 and 2 in A).

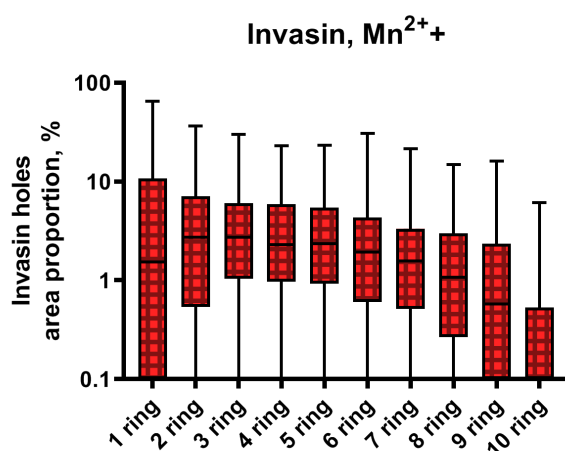
D) Normalized intensity profiles across the 2 lines in the SLB (lipid) channel.

E) Fluorescence image (same as in A)) of Invasin depletion in the **AZ** (xy coordinates) with two orthogonal views (yellow lines) (yz (right) and xz (bottom) coordinates). Scale bars (xy - $5 \mu m$, yz and xz - $1 \mu m$).

Next, we have analyzed 186 Mn^{2+} -treated cells adhering on Invasin. We have developed and applied an image treatment software that detects Invasin holes (cf. section 7.2 of the Materials and Methods) (cf. Figure 11.9A). Their shape is in general not discoid, but highly irregular and elongated, resembling a torn surface. Then, in a similar fashion as we did for integrins, we have studied the radial distribution of these Invasin depletion zones. We have plotted the fraction of the ring area occupied by Invasin holes as a function of the ring number at every time point of cell adhesion. We have observed that these holes are present since the early stages of cell adhesion (cf. Figure 11.10A). During the time course of cell adhesion, we observe on average a concentration of integrin holes close to the cell center and a reduction near the edge of the cell. Then we have integrated data acquired at all time points during adhesion. We see on the Figure 11.10B that the holes are radially located in the same part of the cell as integrins (cf. section 11.1 of the Results), mainly between rings 2 and 8, with a maximum at rings 3, thus essentially in the **AZ**.



(A)



(B)

Figure 11.10: Radial distribution of the proportion of area occupied by Invasin holes. A) Time lapse of the radial distribution profile of the proportion of area occupied by Invasin holes across the concentric rings for the cells treated with Mn^{2+} on Invasin (186 cells). B) Radial distribution profile of the proportion of area occupied by Invasin holes across the concentric rings for the cells treated with Mn^{2+} on Invasin (186 cells). This analysis includes all time data points. Box and whiskers (from min to max) plot.

Invasin holes seem to be formed adjacent to integrin clusters. We have analyzed the respective distribution of integrin clusters and Invasin holes (cf. Figure 11.11A). For every cell we have calculated the degree of area overlap between integrin clusters and Invasin holes (the ratio between the intersection of clusters and holes and their union). The mean value of this ratio is 1.2%, thus integrin clusters practically do not overlap with Invasin holes. Furthermore, we have asked how close Invasin holes are to integrin clusters. We have measured the smallest distance between each of integrin clusters and the closest Invasin hole (from border to border). We have focused on the clusters and holes with non-zero mutual distances to avoid the overlapping ones. We have plotted the cluster-hole distance distribution: we can fit it with a normal distribution ($R^2 = 0.94$) with a

mean of $0.7 \mu m$ and standard deviation $1 \mu m$, that can reach distances up to $8 \mu m$ (cf. Figure 11.11B).

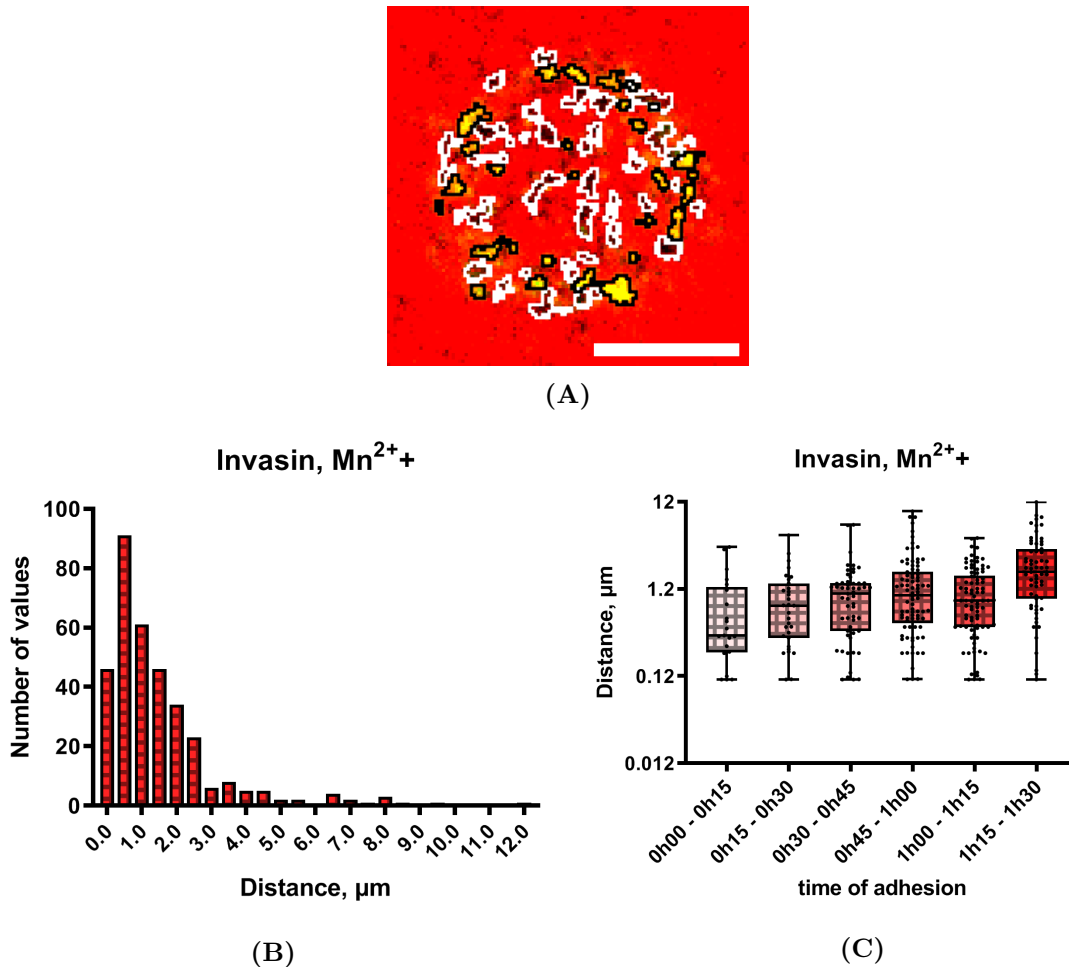


Figure 11.11: Inter-distances between the integrin clusters and the Invasin holes .
 A) Mutual distribution of integrin clusters (circled black) and Invasin holes (circled white) at the **AZ** of an adhering cell. Scale bar $5 \mu m$.
 B) Histogram of the distribution of distances between integrin clusters and the closest Invasin holes in the **AZ**. 342 pairs of integrin clusters and Invasin holes have been analyzed.
 C) Evolution the distances between integrin clusters and Invasin holes during the time course of cell adhesion. Log representation.

Additionally, we have analyzed the evolution of the clusters – holes distances during the time course of cell adhesion (cf. Figure 11.11C). We observe that the median distance increases over time: the holes are already present at the early stage (between 0 and 15 min) at a median distance of $0.35 \mu m$. This distance increases and reaches around $1 \mu m$ at 30 minutes after cell seeding. It is even larger, equal to $1.9 \mu m$ at the late stage of adhesion (1 hour 30 minutes after cell seeding).

To summarize these results, we have found that during the cell adhesion on Invasin coated SLB, the distribution of Invasin is altered. We have observed integrin-Invasin

co-clustering and also areas from which Invasin is depleted. These depletion zones, or Invasin holes, are not associated to any defect of the SLB. They are located in relative close proximity to integrin clusters, but do not overlap.

This ligand exclusion phenomenon might be related to the deformation of the SLB by the cell during adhesion. Indeed, as we have seen previously, the **AZ** contracts during cell adhesion. This could induce tangential stresses on the fluid membrane that might lead to a local buckling of the membrane next to the less mobile integrin clusters (points of support). This would bring the membrane slightly out of focus in these places, resulting in the apparent drop of intensity of the fluorescence signal. However, with the low signal in the lipid channel, we have not observed any important reduction of the fluorescent lipid signal in the areas where Invasin is depleted. Nevertheless, we have looked more closely at the different signal in z-sections of images with Invasin holes.

11.4 SLB deformation by pulling membrane tethers

We have imaged and compared cells in two focal planes (cf. Figure 11.12): one corresponding to the SLB and thus the adhesion zone of the cell, and one at $1.5 \mu\text{m}$ above the SLB (more than the optical resolution in z). In the SLB plane, we see the integrin clusters as well as the Invasin holes. Surprisingly, in the plane above, we observe some bright localized diffraction limited spots in the lipid, integrin and Invasin channels. These spots in the top plane are highlighted with black circles, the corresponding places (with the same x, y coordinates) in the SLB planes are highlighted in the same manner. These places do not correspond to neither integrin cluster, nor Invasin hole in the SLB plane. This suggests that adhesion does induce localized deformation of the SLB towards the cell interior. We have observed this type of deformation in 13% of the Mn^{2+} treated cells on Invasin coated SLB at late stages of adhesion (45 minutes or more after seeding).

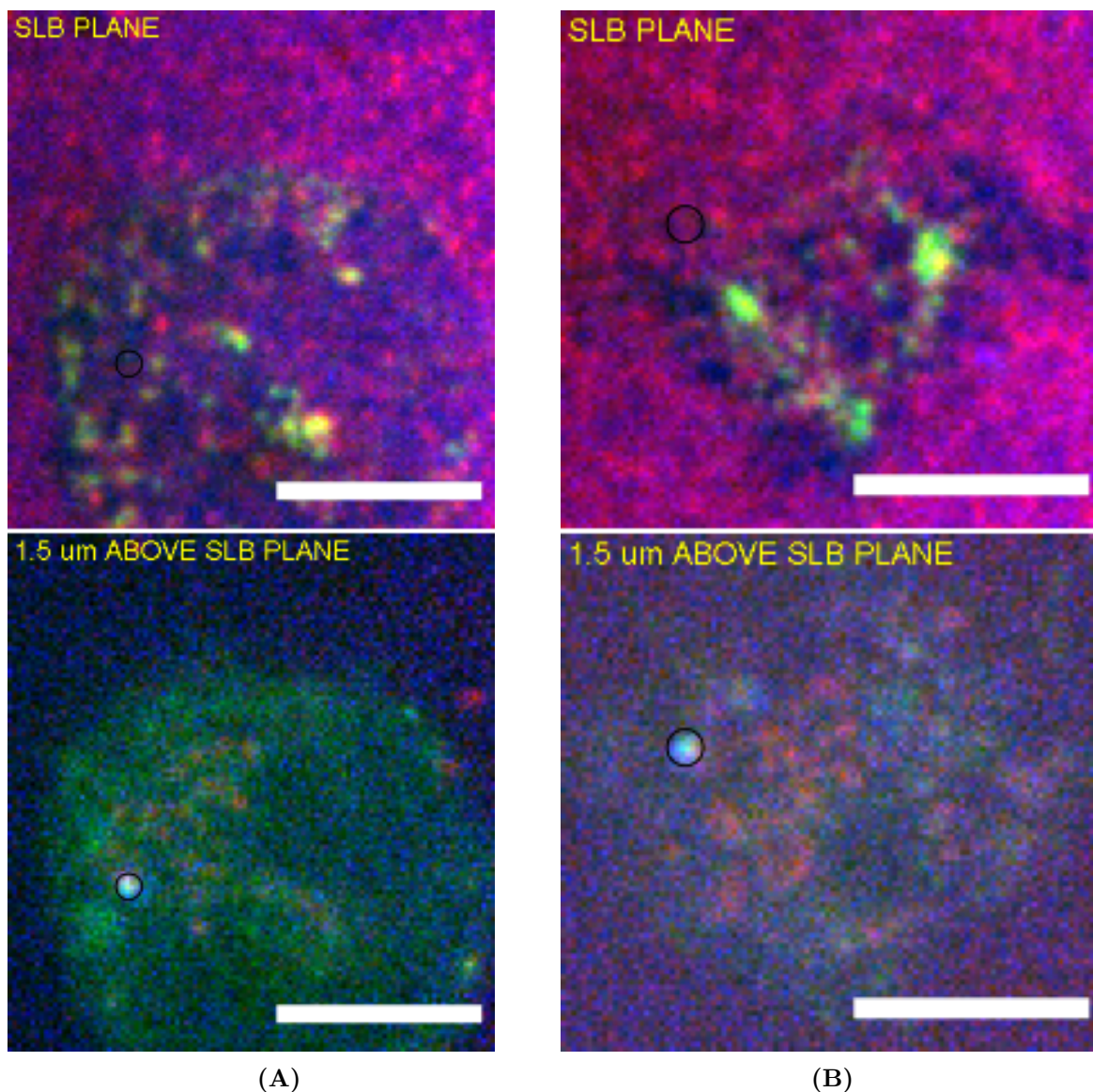


Figure 11.12: Fluorescence image of cells in two focal planes.

Multichannel confocal images of cell 1 (A) and cell 2 (B) adhering on Invasin coated SLB: β_1 -integrin labelled with Halotag ligand-Alexa Fluor 488 (green), Invasin labelled with JF549 (red), SLB containing Marina-Blue DHPE lipids (blue). 2 confocal sections are represented: the SLB (top) and a section 1.5 μm above the SLB (bottom). The area corresponding to the SLB protrusion is shown on both planes with a black circle.

The fact that the signal in the top plane is very localized suggests the formation of membrane tubes pulled from the SLB towards the cell upon the formation of integrin clusters. To check this hypothesis, we have imaged confocal sections along the z direction (cf. Figure 11.13).

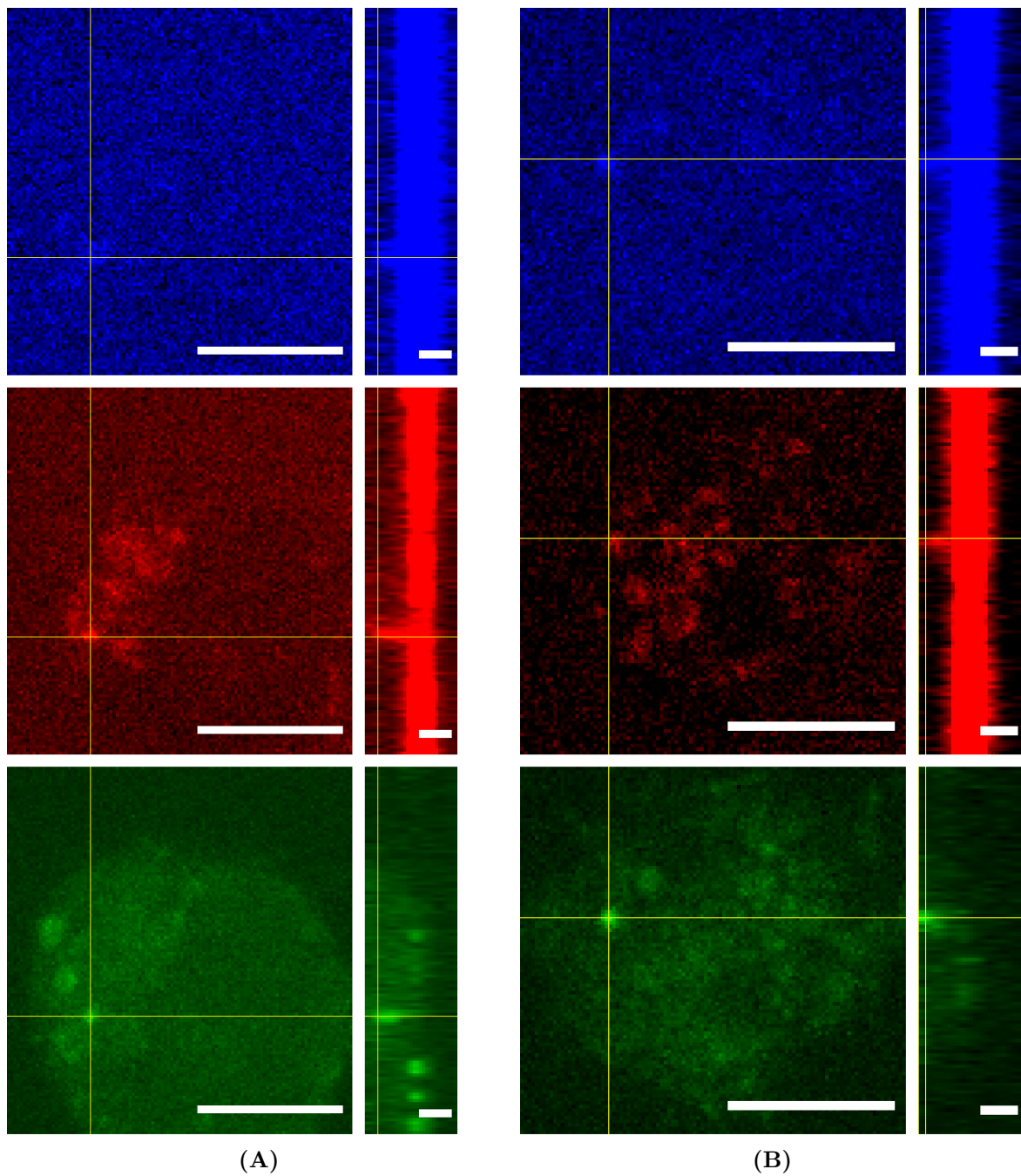


Figure 11.13: Fluorescence images of SLB protrusions in orthogonal planes.

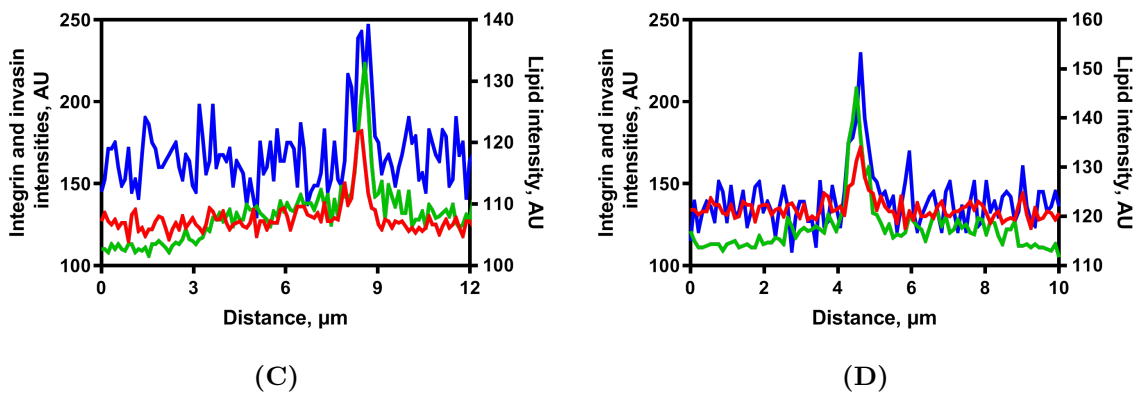


Figure 11.13: Fluorescence images of SLB protrusions in orthogonal planes(cont.). A-B) Confocal images for a cell 1 (A) and a cell 2 (B) adhering on Invasin coated SLB (1.5 μm above the SLB, xy plane): β_1 -integrin labelled with Halotag ligand-Alexa Fluor 488 (green), (top), Invasin labelled with JF549 (red) (medium), SLB containing Marina-Blue DHPE lipids (blue)), (bottom). Orthogonal views reconstructed from z-stack imaging (yz plane). C-D) Intensity profiles along the yellow line in the orthogonal views of corresponding cell images.

This confirms the formation of SLB invaginations bigger than 1 μm long covered with Invasin into the cell. We also see that in addition of the integrin clusters on the adhesion (SLB) plane, there are also integrin clusters at the tip of the invaginations (cf. Figure 11.13). These clusters contain in general less integrins than those in the *AZ*.

chapter 11 conclusions:


In this chapter, we have studied the radial organization of integrin clusters, Invasin and actin structures inside the **AZ**. We have shown the following:

- Local integrin densities in adhesion clusters do not depend on the cluster location in the **AZ**.
- On both substrates and independently of the Mn^{2+} treatment integrins are on average located closer to the cell centre than to the cell edge (at a distance of 0.3 to 0.5 of the cell radius from the cell center).
- On RGD substrates and independently of the Mn^{2+} treatment, actin cortex encompasses the **AZ**. Generally, actin and integrins are mostly located in the same area closer to the cell center than to the cell edge.
- On Invasin substrates and with Mn^{2+} treatment, Invasin on the surface of the SLB is remodelled in the **AZ**. It co-clusters with integrin, and it is also depleted in areas distinct from the integrin clusters, forming Invasin holes in spots devoid of integrin. These holes in general do not overlap with integrin clusters and the distance between them is of the order of μm .
- On Invasin substrates and with Mn^{2+} treatment, we have observed micron long membrane invaginations pulled out of the SLB surface towards the cell interior with an integrin- and Invasin-rich spot at the tip.

Chapter 12

Localization of other adhesion proteins in integrin clusters

In order to further investigate the adhesion maturation process at the level of adhesion clusters, in this chapter we have studied the recruitment of other proteins of the integrin adhesome (zyxin, vinculin, talin, kindlin-2 and paxillin) to integrin clusters (cf. section 2.3 of the Introduction). For the sake of time, we have focused on cells adhering on RGD-coated fluid substrates only.

We have analyzed the adhesion cluster composition for these five proteins and compared them with the β_1 -integrin composition. These proteins fused with fluorescence tags mCherry were co-expressed with the previously described β_1 -integrin after a transient cell transfection (except paxillin-mCherry that was stably expressed) (cf. subsection 5.3.2 of the Materials and Methods). The clusters were detected and analyzed in both fluorescence channels using the software program described earlier (cf. section 7.2 of the Materials and Methods). The determination of absolute numbers of adhesion proteins is even more challenging than for β_1 -integrins for several reasons. First, cells express both mCherry-labelled and unlabelled endogenous proteins. The ratio between them depends on transfection and is quite difficult to estimate at the single cell level. Second, the brightness of the mCherry-fusion constructs inside cells may be quite different from the one of mCherry protein outside the cell (as used in the calibration, cf. section 6.2 of the Materials and Methods). h fusion partners and microenvironment can greatly influence the fluorescence of the protein. We have thus analyzed the relative differences in recruitment of adhesion proteins. For the sake of time, we have not followed the time evolution of these adhesion clusters, so we have pooled all the adhesion time points together. Thus, we could analyze the degree of recruitment of adhesion proteins (in terms of cluster area

RESULTS
CHAPTER 12. LOCALIZATION OF OTHER ADHESION PROTEINS IN INTEGRIN CLUSTERS

and number of proteins per cluster) together with the number of integrins (as we did before) in the clusters.

In the figure 12.1 we can see the **AZ** of a typical cell that co-expresses paxillin and β_1 -integrin adhering on RGD coated SLB (cf. Figure 12.1). We have also analyzed the role of integrin activation by Mn^{2+} on the recruitment of paxillin.

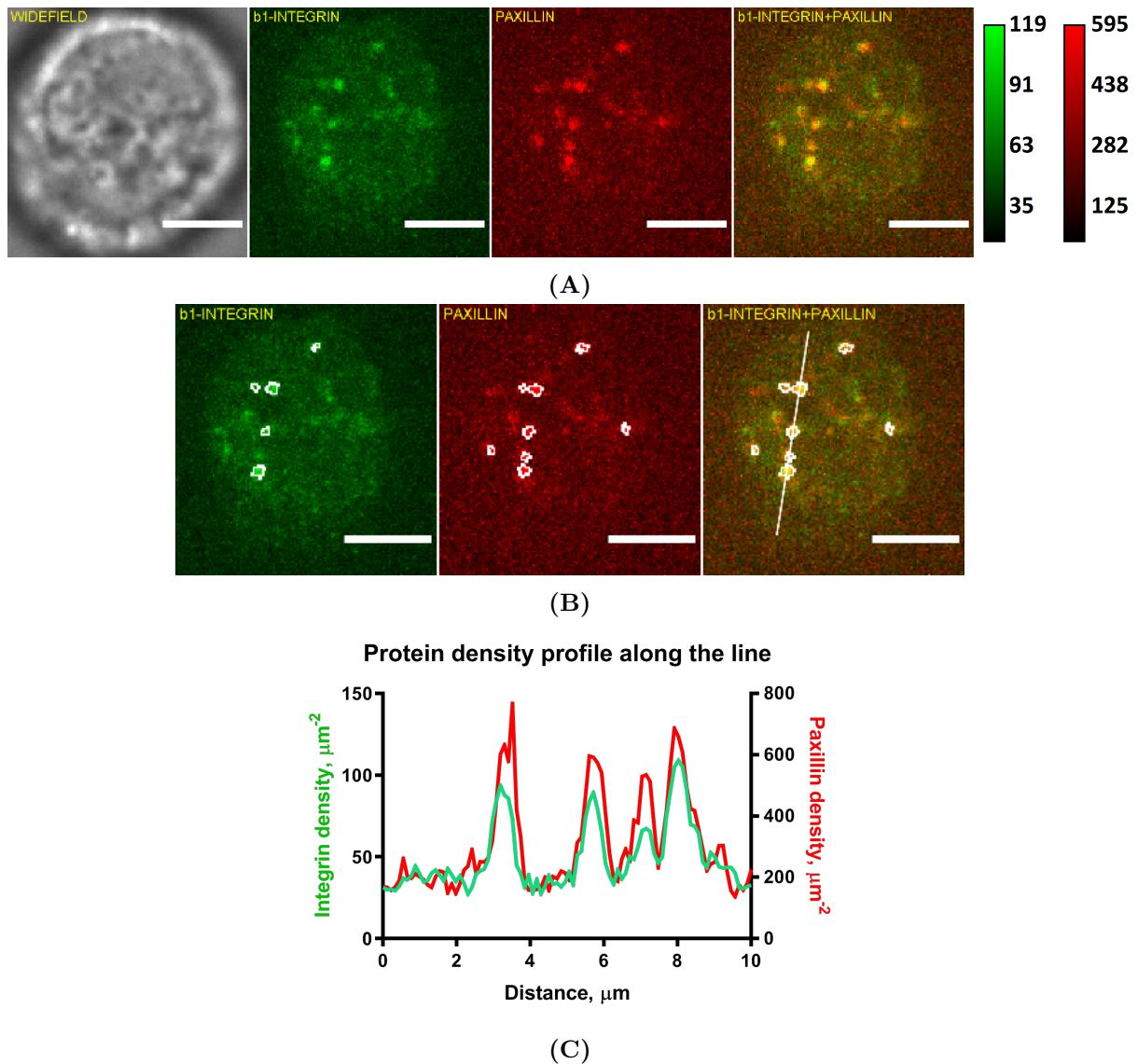


Figure 12.1: Cluster detection in the **AZ in two fluorescence channels.**

A) From left to right: cell contour on wide field image, **AZ** in integrin channel (green), **AZ** in paxillin channel (red), **AZ** in a merged channel of integrin and paxillin (green and red). Corresponding protein density scales (in proteins/ μm^2) based on a prior fluorescence calibration (cf. section 6.2 of the Materials and Methods).

B) From left to right: **AZ** in integrin channel (green) with detected clusters, **AZ** in paxillin channel (red) with detected clusters, **AZ** in a merged channel of integrin and paxillin (green and red) with clusters combined from both channels.

C) Protein density profiles along the white line scan in B) (green, integrin and red, paxillin). Scale bar, $5 = \mu m$.

12.1 Adhesion proteins' co-clustering

We have studied 16 zyxin, 13 vinculin, 25 talin, 7 kindlin-2 and 138 paxillin expressing cells. First, we have analyzed the overlap of the adhesion protein clusters with integrin clusters. For that for every adhesion protein we have measured the area of all clusters in the **AZ** and the intersection area between integrin clusters and other adhesion protein clusters (cf. Figure 12.2). We do observe some variation in total area of clusters in the **AZ** for different proteins. It can possibly be due to the fact these clusters were observed at different time points and also the expression levels might vary due to the differences in transfections. Nevertheless, the degree of cluster overlap, or the fraction between the total intersection area and the total area of the adhesion protein clusters, looks similar, ranging between 20-40% (with an exception of kindlin-2 for which we have very low statistics) (cf. Figure 12.2).

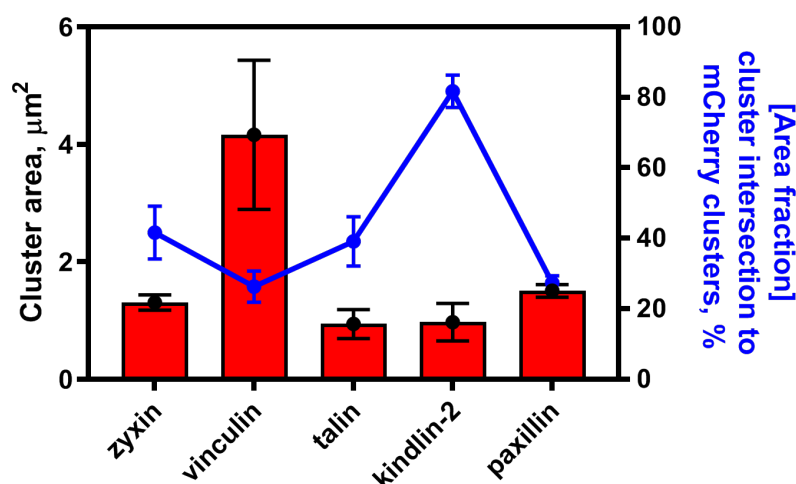


Figure 12.2: Adhesion cluster intersection.


(left axis) Total area of the clusters of mCherry labelled adhesion proteins (red bars). Bar plot (mean with SEM).

(right axis) Fraction between the area of intersection of integrin and other adhesion protein clusters (zyxin, vinculin, talin, kindlin-2, paxillin) and the area of its union (blue line graph). Line plot (mean with SEM).

These results indicate that cells adhering on RGD fluid substrates recruit a number of adhesion proteins to integrin clusters, although their clusters did not overlap completely. The 20-40% area ratio of intersection between integrin and other proteins can be explained by the recruitment of adhesion proteins to other type of integrin clusters (not β_1 -integrins).

Some of the recruited proteins like paxillin, talin and vinculin were shown to be recruited to integrin clusters on RGD-coated SLBs that were prepared differently (SLBs

were functionalized with neutravidins that carried RGD peptides on them) (han Yu et al. [2013]). The co-clustering of β_1 -integrin with kindlin-2 and zyxin have not been reported before. Vinculin and zyxin are the late adhesion proteins that do not bind integrins directly. Their presence in integrin clusters indicates the degree of adhesion maturity on RGD.

Next, we have analyzed the amounts of proteins in the zone of the overlap between integrins and the other adhesion proteins. Every **AZ** that we have analyzed comprised clusters of two proteins (integrin and another adhesion protein). Whereas for all pairs of adhesion proteins (integrin and another adhesion protein) the median amount of integrins in the **AZ** varied between 79 and 199, it is approximately an order of magnitude higher than the other adhesion proteins. The median levels of zyxin proteins in the adhesion clusters is 971, vinculin – 3006, talin – 282, kindlin-2 – 470 and paxillin – 684. We also observe that a significant fraction of the total number of detected adhesion proteins colocalizes with integrin clusters: 62% of zyxin, 42% of vinculin, 75% of talin, 91% of kindlin-2 and 48% of paxillin proteins are found in the integrin clusters, thus higher fractions than the area fractions of overlap (cf. Figure 12.3). These results demonstrate that significant numbers of detected adhesion proteins are recruited to integrin clusters 

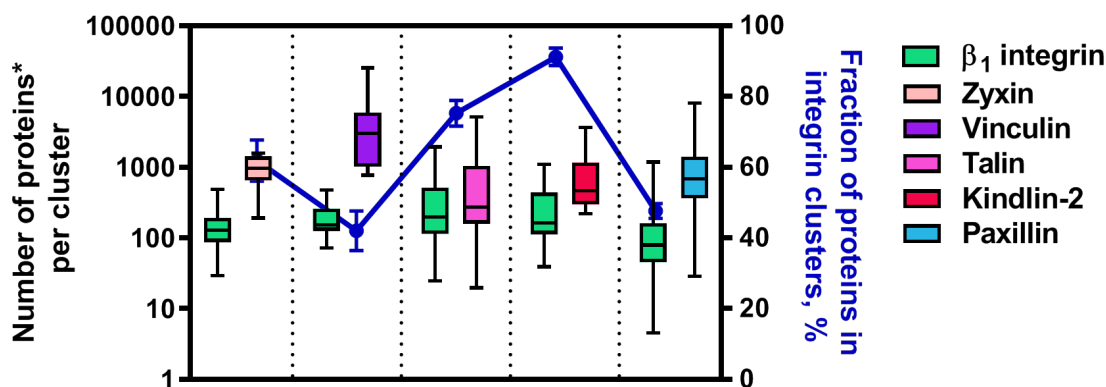


Figure 12.3: Number of adhesion proteins* in the AZ.

Adhesion proteins* = fluorescent adhesion proteins.

(left axis) Number of adhesion proteins (β_1 -integrin, zyxin, vinculin, talin, kindling-2, paxillin) in integrin clusters. Log scale. Box with whiskers (from min to max) plot.

(right axis) Fraction of the number of adhesion proteins in integrin clusters to the total number of detected adhesion proteins (blue line graph). Line plot (mean with SEM).

12.2 Adhesion protein recruitment as a function of the size of integrin cluster

In this section, we have analyzed the relation between the number of recruited adhesion proteins with the number of β_1 -integrins in the adhesion clusters. We have analyzed integrin clusters with other co-localized adhesion proteins: 99 clusters co-localized with zyxin, 90 with vinculin, 197 with talin and 905 with paxillin. We have not analyzed individual kindlin-2 clusters because we did not have big enough statistics on them.

For all adhesion proteins we observe a positive correlation between their amount and the amount of β_1 -integrins in the clusters (Pearson correlation coefficients between 0.65 and 0.93). Next, we have used a linear model to fit the paired distributions of protein number in adhesion clusters (cf. Figure 12.4, log-log scale). Clusters that contain less than 10 integrins (approximately the median value of integrins, cf. Figure 10.2A) do not recruit the adhesion proteins in the same ways as do those with more than 10 integrins. The number of adhesion proteins per cluster in them only weakly depends on the number of integrins. These clusters correspond to the very early NA clusters that are likely formed in absence of mechanotransduction (Changede et al. [2015]). On contrary, the number of adhesion proteins linearly depends on the number of integrins in clusters that contain more than 10 integrins. This suggests a more effective recruitment of the adhesion proteins to larger clusters. Moreover, we do not observe any saturation effects in the protein recruitment to the largest clusters. That might suggest that the adhesion clusters that we observe can potentially mature into larger ones.

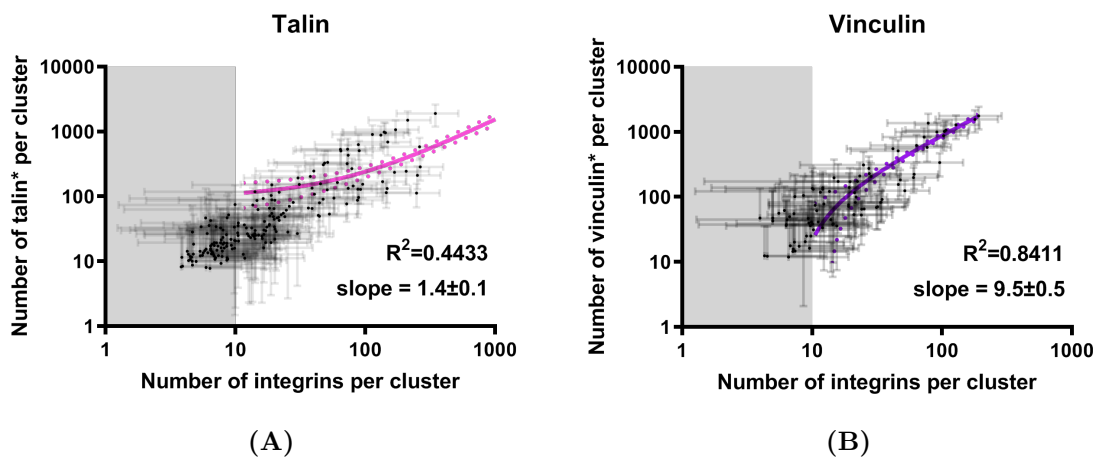


Figure 12.4: Number of adhesion proteins as a function of number of β_1 -integrins in the clusters.

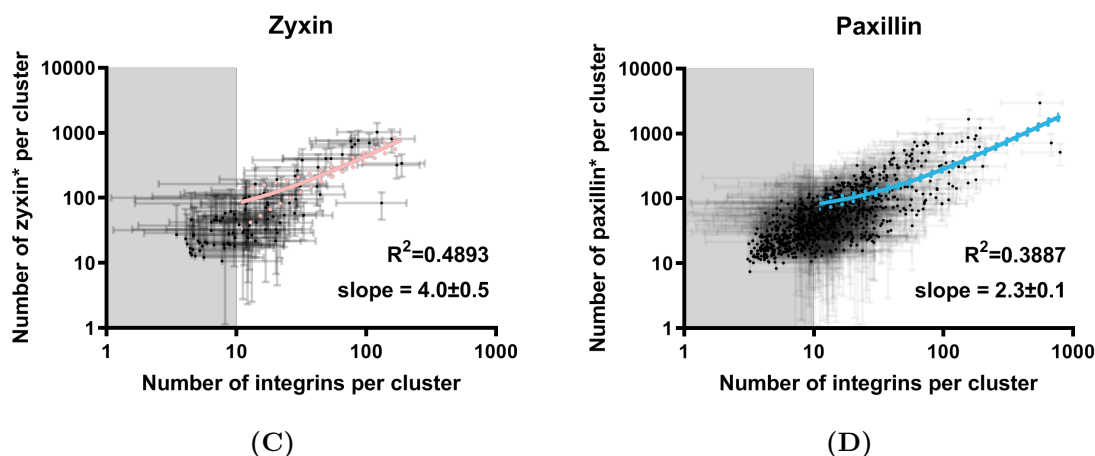


Figure 12.4: Number of adhesion proteins* as a function of number of β_1 -integrin integrins in the clusters(cont.).

Adhesion proteins* = fluorescent adhesion proteins. Log-log plots.

Error bars have been calculated according to the method described in the A. Data are fitted with a linear curve (full color lines). The slopes of the fitted curves are indicated. The goodness of the fits are indicated by R^2 values.

- A) Scatter plot for number of talin and integrin proteins in adhesion clusters.
- B) Scatter plot for number of vinculin and integrin proteins in adhesion clusters.
- C) Scatter plot for number of zyxin and integrin proteins in adhesion clusters.
- D) Scatter plot for number of paxillin and integrin proteins in adhesion clusters.

The slopes of these linear curves allow us to compare the molar ratios r between the different adhesion proteins in integrin clusters. Thus, we have measured these molar ratios r , as the numbers of adhesion proteins per one β_1 -integrin in the adhesion cluster. The mean values r vary between 1.4 and 9.5 proteins per integrin in the cluster: the lowest being for talin and the highest being for vinculin (cf. Table 12.1).

Table 12.1: Ratio between the number of adhesion proteins and integrins in clusters (from linear fits in the Figure 12.4).

	Zyxin	Vinculin	Talin	Paxillin
r	4.0	9.5	1.4	2.3
Std. Error	0.5	0.5	0.1	0.1

Noteworthy, we can deduce that an average relative ratio r is about 6 times higher for vinculin than for talin (cf. Table 12.1 and Figure 12.4C-12.4D). This might suggest there are 6 times more vinculin than talin recruited to the adhesion cluster with the same number of integrins. Interestingly, these linear fits suggest that the number of vinculin is higher than the number of talin in the clusters that contain more than 14 β_1 -integrins (cf. Figure 12.5). These clusters likely correspond to the maturing under contraction forces

NA clusters, in which the catch-bond molecular clutch connection between actin and integrins is established (Han et al. [2021]).

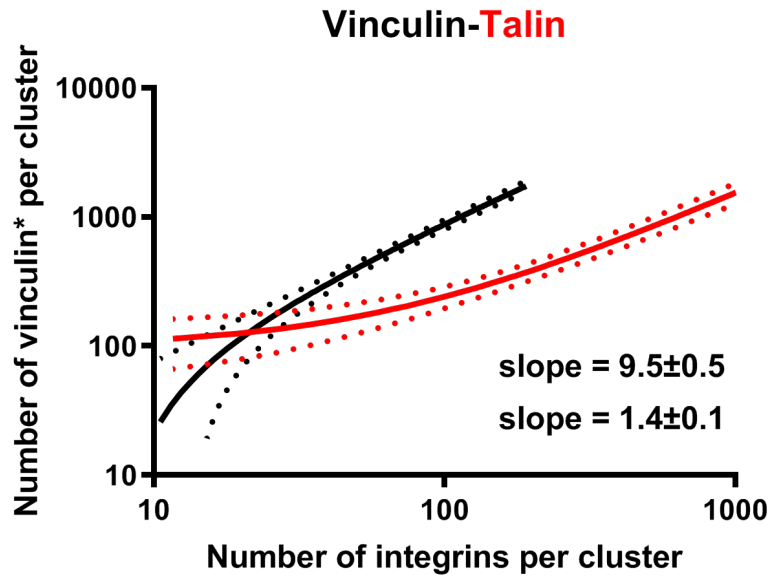


Figure 12.5: Number of talin and vinculin proteins* as a function of number of β_1 -integrins in the clusters.

Talin and vinculin proteins* = fluorescent talin and vinculin proteins. Log-log plots. Linear fits of the relations of talin-integrin and vinculin-integrin numbers in adhesion clusters.

These results suggest that cells on RGD fluid substrates are able to develop mature enough adhesion that contain not only integrin receptors but also such adhesion proteins as zyxin, vinculin, talin, kindlin-2 and paxillin. Noteworthy, zyxin and vinculin do not bind directly to integrins and are generally considered as the force transduction and actin regulation proteins (Hu et al. [2015]). Moreover, relative numbers of vinculin to integrins are higher than those of talin, suggesting a certain level of integrin activation when several vinculin bind to talin.

12.3 Role of integrin activation by Mn^{2+} on adhesion protein recruitment dynamics

Since we have already seen in the previous chapters that integrin priming by Mn^{2+} has an effect on cluster size and integrin density, we have checked the effect of Mn^{2+} treatment on the recruitment of adhesion proteins other than integrins. We have focused on paxillin since we have many more data with it than with other adhesion proteins. We have analyzed 905 and 950 clusters in cells adhering on the RGD coated fluid substrates treated respectively with and without Mn^{2+} .

First, we have compared the number of paxillin proteins in integrin clusters for both Mn^{2+} conditions (cf. Figure 12.6). On average we observe a statistically significant increase in paxillin numbers in the clusters of Mn^{2+} treated cells (**** Mann-Whitney test).

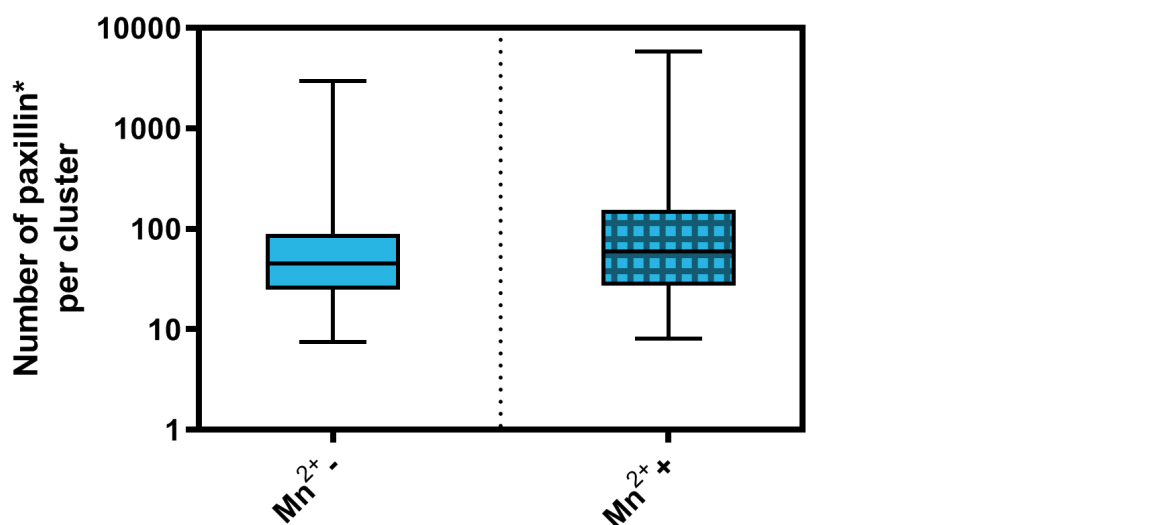


Figure 12.6: Number of paxillin proteins in adhesion clusters in cells treated with(out) Mn^{2+} .

Paxillin proteins* = fluorescent paxillin proteins.

Box with whiskers (from min to max) plot.

Next, as in the previous section, we have studied the relationship between the amount of paxillin proteins and integrins in the adhesion cluster for both Mn^{2+} conditions (cf. Figure 12.7).

RESULTS
 CHAPTER 12. LOCALIZATION OF OTHER ADHESION PROTEINS IN
 INTEGRIN CLUSTERS

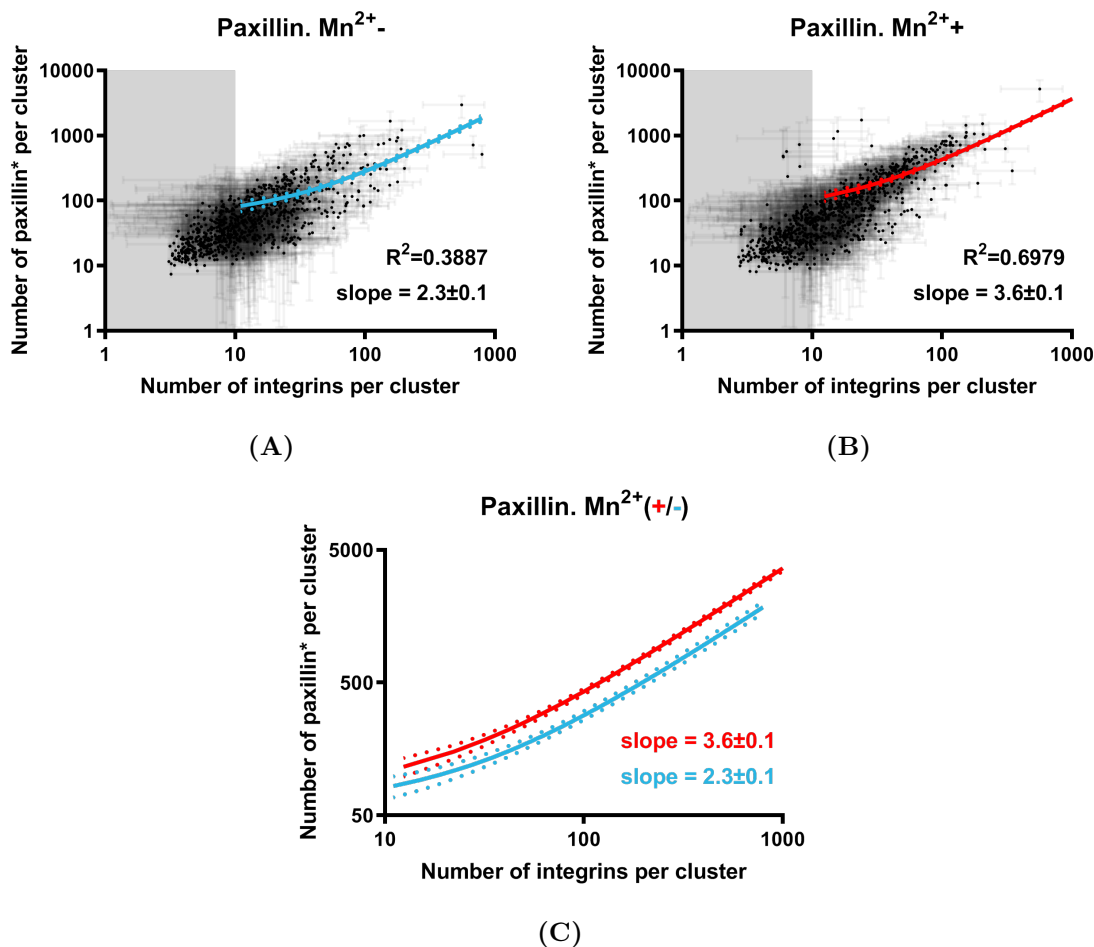


Figure 12.7: Number of paxillin proteins* as a function of number of β_1 -integrins in the clusters. Role of Mn^{2+} .

Paxillin proteins* = fluorescent paxillin proteins.

In A) and B) the error bars have been calculated according to the method described in the A. Data are fitted with a linear curve (full color lines). The slopes of the fitted curves are indicated. The goodness of the fits are indicated by R^2 values. Log-log plots.

A) Scatter plot for number of paxillin and integrin proteins in adhesion clusters for the non-treated cells adhering on RGD.

B) Scatter plot for number of paxillin and integrin proteins in adhesion clusters for the Mn^{2+} treated cells adhering on RGD.

C) Linear fits of the relations of paxillin-integrin numbers in adhesion clusters for cell treated with(out) Mn^{2+} .

By the slopes of linear regression fits we can deduce that Mn^{2+} treated cells have on average 54% more paxillin in the clusters (per number of integrins) than the non-treated ones. These results suggest that integrin priming by Mn^{2+} triggers association of integrin clusters with the actin cytoskeleton associated with paxillin recruitment.

chapter 12 conclusions:

To summarize this chapter, we have observed the recruitment of zyxin, vinculin, talin, kindlin-2 and paxillin to integrin clusters on RGD-coated SLBs. We have also examined the role of integrin activation by Mn^{2+} on the maturation of integrin-paxillin clusters. We have found the following:

- β_1 -integrin clusters have a significant overlap with the clusters of other studied adhesion proteins (both in terms of area and number of proteins).
- The number of adhesion proteins in the cluster linearly depends on the number of integrins in the cluster. More vinculin per integrin are recruited as compared to talin, paxillin or zyxin.
- Integrin activation by Mn^{2+} increases the number of paxillin per integrin in the clusters.

Part IV

Discussion, Conclusion, Perspectives


Chapter 13

Discussion

Cell adhesion on rigid and fluid substrates is very different. Unlike on glass, on fluid SLBs, cells do not develop mature FAs. Nevertheless, cells bind to functionalized SLBs, due to adhesion through elementary NA dot-like integrin clusters (Changede and Sheetz [2016]). In this thesis, we have shown that cells are able to develop mechanical forces on fluid substrates and transmit them through adhesion clusters. We have also demonstrated the role of integrin affinity to its ligands and integrin activation in the growth and maturation (recruitment of integrin adaptor proteins linking them to actin and permitting mechanotransduction between cells and substrates) of integrin clusters. We have observed that cells can deform the SLB through adhesion clusters. Moreover, cells on SLBs form integrin clusters that are morphologically different from those on (rigid) glass. This difference is likely due to the main direction of the applied force, which in the case of and as opposed to glass, does not correspond to the substrate plane.

Therefore, our work extends current views on cell adhesion proposed by the groups of Michael Sheetz and Alexander Bershadsky (Yu et al. [2011]; Changede et al. [2015]). In this part, we will discuss our main results in the scope of the previous knowledge on the subject. We will also discuss the experimental limitations that should be considered when drawing the conclusions. We will then provide a possible mechanism of cell adhesion on fluid substrates. Finally, we will discuss the open questions and propose some perspectives.

13.1 Integrin activation and clustering on rigid and fluid substrates

Cell adhesion is initiated by integrins that bind to their ligands on substrates. This binding induces an allosteric conformational change of integrin molecule straightening its ectodomains and separating its cytoplasmic tails in a process called outside-in integrin activation (cf. subsection 2.2.1 of the Introduction). Integrin activation can also be achieved by binding of adaptor proteins, integrin activators like talin and kindlin to the cytoplasmic tails and their spatial separation (inside-out activation). These processes are reciprocal and occur in a loop: binding of extracellular ligand would enhance the separation of integrin cytoplasmic domains, allowing their interaction with adaptor proteins and cytoskeleton; reciprocally, separation of the cytoplasmic tails by talin, kindlin and other integrin activators would activate integrin head for ligand binding (Hynes [2002], Calderwood [2004], Mehrbod et al. [2013]). Active integrins cluster through interactions between their ectodomains or adaptor proteins (Li et al. [2003], Cluzel et al. [2005]). Therefore, the induced integrin activation leads to the growth of adhesion clusters (Zhao et al. [2020]) and cell stabilization of the substrate (cf. chapter 8-9 of the Results). Individual integrin clusters evolve: they can disappear or grow bigger in size and recruit more integrins, and they mature by recruiting more adaptor proteins. It has been shown that the size and the maturation level of integrin clusters developed on RGD-coated SLBs is limited and they cannot mature beyond NAs (Yu et al. [2011], Changede et al. [2015]). In contrast, on glass, integrin clusters can grow bigger and recruit more integrin adaptor proteins to link integrins to actin and to become FAs. The degree of maturation of integrin adhesion clusters is associated with the ability of the cell to transmit physical forces between the cell and the substrate through clusters. Mechanical forces transmitted by actin stress fibers that connect mature FAs that are linked to rigid substrates change the cell shape from round to elongated along the main direction of the forces. On contrary, smaller NAs on soft substrates cannot transmit such forces and cells stay round during adhesion (Geiger et al. [2009], Prager-Khoutorsky et al. [2011]).

13.2 Integrin cluster growth on RGD-coated SLBs

We have characterized quantitatively the integrin clusters by measuring their areas and counting β_1 -integrins (cf. section 7.2 of the Materials and Methods). We have found that cluster formation on RGD-SLBs begins within the first minutes of cell adhesion. Small

submicron-sized clusters containing several tens of integrins are formed (cf. chapter 10 of the Results). These clusters likely correspond to the NA nano-clusters described in Changede et al. 2015. However, we find a lower number of integrins in these NAs than in those reported by Changede et al. [2015] (10 versus 50 integrins per cluster, respectively). This difference might be due to several reasons:

1. different microscopy and image processing methods were used. In particular, they used a super resolution technique, whereas we combine more conventional confocal with fluorescence calibration. Moreover, our cluster quantification relies on the assumption that the fluorescence properties of the fluorophores are similar in our calibration and in the cell adhesion experiments. The environment in these two experiments is not exactly the same, potentially leading to some systematic error preventing the comparison with other studies. However, this systematic error does not perturb the comparison of the results within our study.
2. Changede et al. have not detected directly the integrins but the fluorescent neutravidin molecules that link RGD peptides to the SLB. In contrast, we have observed specifically β_1 -integrins.
3. we have not controlled that all β_1 -integrins in detected clusters are labeled. We may have underestimated the amounts of integrins since our surface labeling procedure excludes integrins' trafficking inside the cell (Bridgewater et al. [2012], de Franceschi et al. [2015]).
4. We have used linearized RGD peptides on the SLBs, whereas Changede et al. have used cyclic ones with a slightly higher affinity to integrins (cf. Table 2.2).
5. we have used much higher densities of RGD than Changede et al. (28000 versus 2800 μm^{-2}). However, they have shown that the integrin density in the clusters does not depend on the RGD density on the SLB (Changede et al. [2015]). Moreover, with higher RGD densities on the SLBs, we nevertheless observe lower integrin densities in our clusters than Changede et al.

Despite these differences, we have not observed significant cluster growth during cell adhesion on RGD-coated SLBs, consistent with previous reports (Yu et al. [2011], han Yu et al. [2013], Changede et al. [2015]).

13.3 Integrin cluster movement in the AZ on RGD-coated SLBs

Next, we have analyzed the integrin clusters' location in the AZ during the time course of cell adhesion. We have observed that integrin clusters move towards the cell center. This centripetal movement brings them half-way between the cell edge and the cell center (cf. chapter 9, 11 of the Results). Integrin clusters that are engaged in this movement experience the counter forces from possible barriers on the cell membrane and in the cytoplasm, and friction forces from the viscous bilayer (Bennett et al. [2018]). Indeed, *in vitro* studies have shown that lipid bilayers can resist enough to the motion of biological objects such as myosin1b-actin complexes, at velocity of the order of 50 nm/s, to affect the actin polymerization rates (Pernier et al. [2019]). Thus, this resisting force could also be sufficient to trigger some mechanotransduction process in adhesive clusters, although this force will depend directly on membrane viscosity and thus lipid composition and might be low in fluid bilayers (Bennett et al. [2018]). What limits their displacement midway between the cell center and the cell edge has to be clarified, but one possibility would be the presence of the nucleus.

Since clusters move towards the cell center, they have to be subjected to forces. The most obvious ones are related to the actin cytoskeleton. Tensile forces directed towards the cell center and applied to integrin adhesive structures via contractile actin fibers were reported on rigid glass (Brockman et al. [2018]). Integrin clusters in that case, however, were morphologically different (elongated along the force axis FAs versus dot-like NAs) and not mobile as strongly attached to the glass. On RGD-SLBs, we have observed an actin-dense structure surrounding the AZ in cells (thus, not at the cell edge) but no stress fibers as observed on rigid substrates (cf. chapter 11 of the Results). But, we do not know yet how this actin structure emerges and if and how it is related to the centripetal movement of the clusters. In addition, less dense actin structures probably polymerize at the level of the clusters, and transmit forces on them through the retrograde flow via the adaptor proteins but they are not detected in our experiments.

As a future perspective, we would need to explore the role of the actomyosin in the centripetal movement of integrin clusters. We have envisioned to block myosin-II activity with drugs (i.e. blebbistatin) and to block actin polymerization with drugs (e.g. cytochalasin D or latrunculin A) to verify whether the forces implicated in the centripetal movement of integrin clusters are generated by actomyosin contractions, to evaluate the role of actin polymerization in this movement and in the maturation of the clusters (cf.

section 13.4) and eventually understand the origin of the actin ring-like structure. Actin flow was measured on mouse myoblast cells adhering on fluid DOPC RGD-SLB, and no significant effect was detected with blebbistatin (Bennett et al. [2018]). But, no actin ring-like structure around the AZ zone was detected in these experiments, and the localization of the integrin clusters in the cells was not examined.

13.4 Recruitment of integrin adaptor proteins to adhesion clusters

Next, we have observed the recruitment of adaptor proteins to integrin clusters on RGD (cf. chapter 12 of the Results). Among them are integrin activators like talin and kindlin-2, or paxillin that are presumed to directly associate with integrin cytoplasmic tails (Turner [2000]). The presence of talin, paxillin at early adhesion stages on SLBs was previously reported (han Yu et al. [2013]). In addition, we have also detected a high ratio of vinculin to talin (approximately 6 fold) in integrin clusters. This vinculin accumulation might suggest NA cluster maturation under physical load, when talin is stretched and its vinculin-binding-sites (VBSs) are exposed (Han et al. [2021]). Moreover, we have detected zyxin in the integrin clusters. This mechanosensitive adaptor protein that concentrates along the actin cytoskeleton is a sign of a later adhesion stage.

The presence of the adaptor proteins such as vinculin and zyxin in the integrin clusters indirectly reveals that a mechanotransduction mechanism possibly takes place during adhesion on RGD-SLBs. Although the integrin density in adhesion clusters on RGD-coated SLBs is lower than in FAs on glass and the cluster size smaller, these results suggest a certain degree of cluster maturation under mechanical load (cf. chapter 12 of the Results).

As a future prospective, we have to analyze the time evolution of the recruitment of integrin adaptor proteins on SLBs. Moreover, in order to better understand the degree of adhesion cluster maturation, we would study the recruitment of later adhesion markers like the vasodilator-stimulated phosphoprotein (VASP). As mentioned above, the role of actin polymerization and acto-myosin contraction in the maturation process have also to be studied.

Therefore, we have found evidence of mechanotransduction on RGD-coated SLBs, even though integrin clusters do not grow larger than NAs. Thus, we asked whether the weak affinity of RGD for integrins could limit the potential force transmission and impede

integrin cluster growth.

13.5 Role of integrin activation by ligands

To test this hypothesis, we have studied cell adhesion on SLBs coated with a different ligand, Invasin. Invasin binds to integrins with a much higher affinity than RGD, thus we expected that integrin clusters formed on Invasin could withstand higher mechanical forces. Interestingly, it takes a longer time for cells to stabilize on Invasin than on RGD: while most of the cells on RGD pass the “trembling-adhesion” transition during the first 30 minutes of adhesion, no cells on Invasin properly adhere by that time (cf. chapter 8 of the Results). This interesting observation can be explained by the lower efficiency of Invasin to activate integrins than RGD. Indeed, during cell adhesion, ligands engage with a pool of integrins of mixed conformations (active, non-active, intermediate) (cf. section 2.2 of the Introduction). After engaging with their ligands, more integrins are activated. RGDs can bind to all integrins conformations (even non-active) in practically the same way, whereas big ligands like Invasin or fibronectin can only bind to a small fraction of this pool (active integrins only) (cf. subsection 2.2.2 of the Introduction). Thus, at the very beginning of adhesion, less integrins engage with Invasin than with RGD and consequently, fewer adaptor proteins are recruited to integrin clusters on Invasin than on RGD through the outside-in signaling. Additionally, RGD bind a larger range of integrin types than Invasin (cf. section 2.2 of the Introduction). Moreover, the higher dissociation rate between RGD peptides and integrins results in a more frequent RGD-integrin unbinding-rebinding cycle leading to a higher rate of activation of the neighboring integrins in the adhesion cluster for RGD than Invasin. That might explain the lower number of integrins engaging with Invasin than with RGD, which leads to slower adhesion cluster formation and cell stabilization (cf. chapter 8-10 of the Results).

Integrin priming by manganese increases the proportion of active integrins in the early stage of adhesion resulting in faster cell adhesion on Invasin-coated SLBs. Moreover, it also increases the number of integrins in adhesion clusters on Invasin. For RGD, the manganese treatment does not drastically affect the dynamics of cell adhesion and cluster formation. These results might confirm a less efficient integrin activation on Invasin than on RGD without integrin priming by manganese. Nevertheless, after manganese treatment the overall adhesion strength or avidity on Invasin is higher than on RGD. These results might suggest that integrin cluster growth and maturation are limited by different factors on Invasin and on RGD. On Invasin, it is limited by the amount of active integrins at the early stage of cell adhesion. Moreover, Invasin is less efficient than RGD in activating the

neighboring integrins due to its high affinity for them. On RGD, integrin priming does not result in a more advanced clustering. Thus, it is probably the low affinity of individual RGD for integrins that limits cluster growth and maturation. Indeed, since the individual integrin-ligand bonds have a shorter lifetime for RGD than for Invasin, for the same number of integrin-ligand pairs, adhesion clusters can withstand higher mechanical loads on Invasin than on RGD. Consequently, these mechanical forces, probably related to the actomyosin system, can induce mechanotransduction signaling, leading to the recruitment of more adhesion proteins to the cluster and to its strengthening (cf. section 2.3 of the Introduction). Thus, in principle, mechanical forces can more likely induce integrin cluster maturation on Invasin than on RGD.

We did observe integrin cluster growth in manganese treated cells adhering on Invasin-coated SLBs (no such effect on RGD). Interestingly, it revealed a non-continuous process with step-like increases of the integrin density in the clusters (cf. chapter 10 of the Results). The appearance of integrin clusters of higher densities, reaching the densities in the FAs (Wiseman et al. [2004]) might indicate a different protein organization inside the clusters over time that probably happen sequentially during adhesion growth and maturation. For example, cluster maturation might induce the fusion of neighboring clusters through scaffolding adhesion proteins (Changde and Sheetz [2016]). This fusion should be followed by a reorganization of integrins and a higher packing. The corresponding mechanism is unclear.

As a future prospective, we could analyze the dynamics of integrin cluster maturation on Invasin-coated SLBs by studying the recruitment of integrin adaptor proteins to adhesion clusters over time. We would use non-fluorescent Invasin to coat SLBs in order to “save” a fluorescent microscopy channel for adaptor proteins. Same experiments related to acto-myosin and actin polymerization suggested above with RGD-SLBs should also be performed on Invasin-SLBs.

13.6 Membrane deformations

Manganese-treated cells on Invasin-coated SLBs are capable to transmit stronger forces than on RGD. Interestingly, these forces were directed perpendicularly and not tangentially to the bilayer. Although there is no specific reason for the physical forces acting on adhesion clusters to be perfectly tangential to the adhesion plane, the role of perpendicular components has been poorly appreciated. Nevertheless, the perpendicular components of these forces exerted at the adhesion clusters on glass are far from negligible

(Brockman et al. [2018]). According to our results, cells also exert forces perpendicular to the SLB during adhesion. Indeed, membrane deformations of SLBs and cells in the direction perpendicular to the substrate is a direct proof that cells apply mechanical forces on fluid substrates, although former papers claimed that cells cannot exert traction forces on fluid substrates in the absence of physical "barriers" in the bilayer (Yu et al. [2011], Changede and Sheetz [2016]). We have detected micron-long membrane tethers pulled out of SLBs in the perpendicular direction, towards the cell interior. Integrin enrichment at the top of the tube was also observed. The force needed to pull a membrane tether from a supported bilayer is of the order of several tens of piconewtons and can reach 100 pN (cf. section 4.1 of the Introduction). Therefore, the presence of such membrane deformation suggests that cells manage to develop clusters mature enough in terms of number of molecules, density and actin connection to be able to transmit local pulling forces of this magnitude. Interestingly, we do not observe such deformation on RGD-coated SLBs. This result corroborates our previous findings, confirming that integrin clusters mature more on Invasin than on RGD-coated SLBs.

As a future perspective, it would be informative to study actin organization in places where such deformations occur. We could use more appropriate microscopy techniques with better optical sectioning above the sample plane, such as light sheet microscopy. We could also study this phenomenon with a different assay that was developed during this thesis: cell adhesion to a giant unilamellar vesicle (GUV) held with a micropipette (cf. chapter 15), which allows to study adhesion on a fully deformable membrane.

13.7 Cluster morphology

Morphologically, we have observed integrin clusters of various shapes, from simple dot-like clusters to larger and with more complex shape structures, both on RGD and Invasin. We have also observed a local overlap of integrins and Invasins in the clusters (cf. section 11.3 of the Results). We have not observed the formation of podosome-like adhesion structures that were previously detected and characterized on RGD-SLBs (han Yu et al. [2013]). These structures are characterized by a central actin core surrounded by a ring of ligands, adhesive molecules and adaptor molecules. Such difference in the cluster morphology might be related to a better optical resolution in Yu et al. experiments than in ours. They have used structural illumination microscopy (SIM) that allowed them to resolve the inner structure of integrin clusters, which we cannot not achieve with normal confocal microscopy techniques. Another possible explanation might be related to the

fact that Yu et al. have coupled the RGD to the bilayer through neutravidin molecules that are much bigger than RGD. Integrins are not directly detected but the fluorescent neutravidins, that might be excluded from integrin clusters due to their size.

13.8 Ligand reorganization on the SLB surface

We have analyzed the ligand reorganization for the manganese treated cells adhering on Invasin-coated SLBs (cf. chapter 11 of the Results). More precisely, we have observed, on the one hand, co-clustering of integrins and Invasin and, on the other hand, Invasin depletion zones close to these clusters. Such depletion zones were not reported previously, at least on RGD-coated SLBs. Although we do not completely understand how these Invasin exclusion zones form, this phenomenon could be driven by a mechanism similar to the one controlling the organization of the immunological synapse. When a T-cell adheres on a SLB coated with peptide-bound major histocompatibility complexes (pMHC) that mimics the surface of an antigen presenting cell (APC), a large transmembrane phosphatase CD45 is excluded from the pMHC/TCR (T cell receptor) clusters to their periphery, permitting stable TCR phosphorylation and further activation of downstream immune signaling cascades (James and Vale [2012]).

Fletcher et al. have studied this protein depletion zone formation *in vitro*, at the interface between two sticky membranes containing proteins able to bind to each other (Binding Proteins, BP) (Schmid et al. [2016]). They have mixed these proteins with non-binding proteins (NBP) of different lengths (corresponding to the height above the membrane), and have observed the formation of local areas where the long non-binding proteins were excluded (cf. Figure 13.1). They have demonstrated that this protein exclusion phenomenon is size-dependent. These exclusions correspond to an energetically more favorable protein configuration between the two adhering membranes. They have found that a difference of +5 nm and more between the sizes of non-binding and binding proteins can lead to the depletion of the non-binding proteins from the adhesion zone.

In the immune synapse, the ectodomains of CD45 isoforms range between 15 and 40 nm in length, whereas the TCR-pMHC interface gap size is about 13 nm (Schmid et al. [2016]). Thus, this model can explain the exclusion of CD45 from the pMHC/TCR clusters. Invasin is a 19 nm long and 2.7 nm wide rod-shape protein (PDB: 1CWV) (Hamburger et al. [1999]). Straightened integrin ectodomains are approximately 20 nm long (Xu et al. [2016]). Thus, integrin-Invasin complex can potentially reach 40 nm in length.

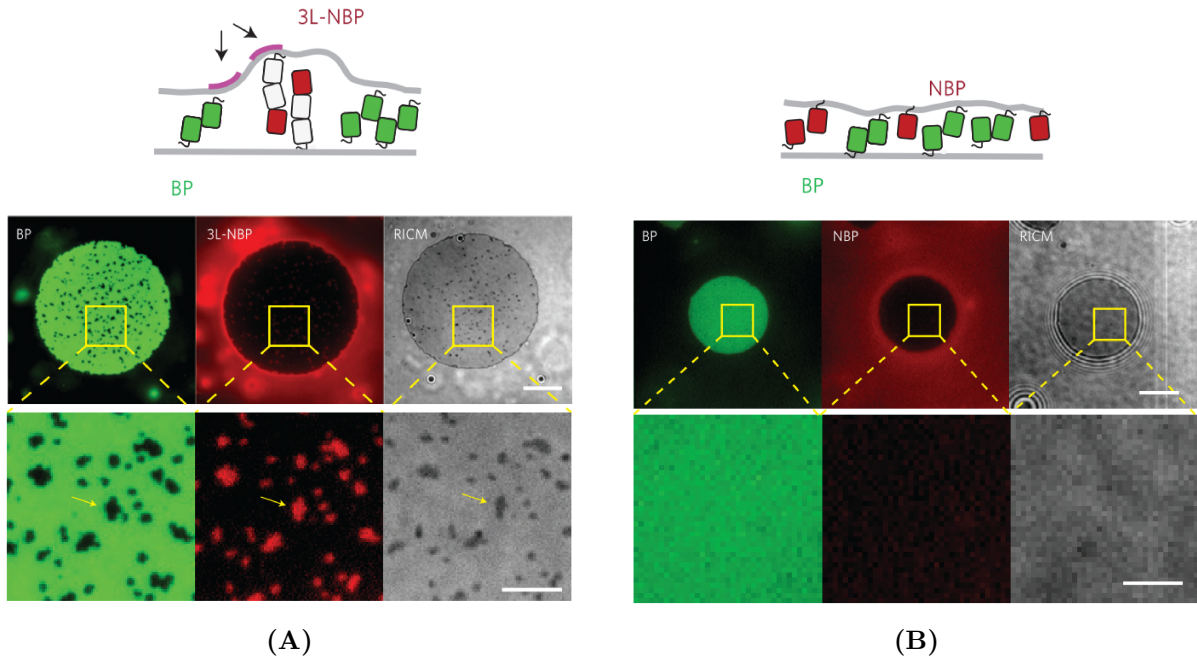



Figure 13.1: Length-dependent protein exclusion at the contact of two membranes. Representative multichannel fluorescence and RICM images of membrane interface formation between SLBs and GUVs showing the mutual exclusion of binding proteins (BP, green) and non-binding proteins (NBP, red) of different lengths: long NBPs are excluded from the BP covered areas and form clusters (shown with an arrow) (A); short NBPs are not excluded (B). Scale bars, 10 μm .

Figure adapted from Schmid et al. [2016].

Cells are surrounded by a glycocalyx, a dense layer of sugars and proteins that can extend over several tens to several hundreds of nm outside the cell, depending on cell type (Möckl [2020]). Based on the exclusion mechanism proposed by the Fletcher group, we expect the cell glycocalyx to be excluded from the adhesion clusters. A similar depletion was observed when GUVs covered with PEG-lipids mimicking a glycocalyx adhere on a SLB via streptavidin-biotin interaction (Albersdörfer et al. [1997]). In our experiments, outside of the adhesion clusters, the cell glycocalyx is in contact, on the opposing membrane, with the Invasin molecules that are long and rigid. Such asymmetric system was not considered in (Schmid et al. [2016]). It is possible that a type of transverse segregation takes place with zones depleted of Invasin but with extended glycocalyx and others depleted from glycocalyx but with not constrained Invasin molecules. A model is needed to check if this hypothesis is physically reasonable.

Interestingly, the core of the podosome-like adhesion structures observed by Han Yu et al. [2013] are also areas of ligand (neutravidin/biotin/RGD complex) exclusion. Neutravidin-RGD complex that is about 6 nm in height above the membrane (PDB:2AVI) and bound to integrin, is depleted from the center of the podosome-like structures. Yu

et al. showed by interference reflection microscopy (IRM) that in these structures, actin is enriched in the centers of the "podosome" with a tight apposition of the cell membrane and the bilayer. This suggests that actin filaments are pushing against the SLB and deplete locally the Neutravidin-RGD integrin complexes. This would correspond to a segregation mechanism, but different from the immune synapse, and still to be deciphered.

As a future perspective, we could test whether Invasin is locally depleted by the glycocalyx. We could first use IRM to estimate the distance between the SLB and the cell membrane in the Invasin holes (Holt et al. [2008]). If the cellular glycocalyx is concentrated in zones locally depleted from Invasin, the height of the gap should be higher than the tight adhesion zone corresponding to the integrin clusters or to the rest of the contact zone. If in contrary, we would observe tight adhesion zones, it could suggest that the cytoskeleton is locally pushing the cell membrane against the SLB and the Invasin molecules outside the contact zone. In order to verify this "glycocalyx exclusion" hypothesis, we could shave the cell glycocalyx with a glycosidase treatment and test whether Invasin holes change or disappear (Schmidt et al. [2020]).  verify the "exclusion by actin pushing" hypothesis, we need to study the local organization of actin in Invasin holes.

DISCUSSION

Chapter 14

Conclusion

We have studied the early stages of cell adhesion on fluid substrates, SLBs. We were specifically interested in learning how integrins that are involved in adhesion are distributed at the cell-SLB contact area. We have used a MEF cell line created by the team of David Calderwood that expresses β_1 -integrin with a Halotag in the β_1 KO background (cf. section 5.3 of the Materials and Methods). The labelled integrins were quantified using the calibration approach (cf. section 6.2 of the Materials and Methods) and integrin clusters were detected by a custom-made software (cf. section 7.2 of the Materials and Methods). We have quantified integrin clusters by measuring their areas and number of β_1 -integrins they contain. Previously, the groups of Michael Sheetz and Alexander Bershadsky have shown that **integrin clusters on fluid substrates** coated with **RGD** ligands are **less stable and mature** than **FAs on rigid substrates**. Although these clusters cannot mature beyond the level of NAs, they can have a rather high integrin density and recruit different adaptor proteins. In addition, a peculiar evolution of the NA into "podosome-like" structures was observed after 45 minutes of adhesion (han Yu et al. [2013]).

The **difference in integrin organization** between cells adhering on **fluid and rigid substrates** is striking and was explained by these authors by the inability of cells to develop high enough mechanical forces on fluid substrates to induce mechanotransduction pathways. Other studies have shown that the **viscosity forces** experienced by integrins upon dragging ligands in SLBs can influence **integrin clustering** during cell adhesion (Bennett et al. [2018]). Moreover, even if resisting forces in the SLB plane are relatively small due to the bilayer fluidity, **forces in the plane perpendicular to the bilayer** are not, since a few tens of pN up to 100 pN are needed to deform the SLB into a tube. **Our work shows that some mechanotransduction process can take place on**

fluid SLBs. We have shown that during cell adhesion on RGD-coated SLBs, relatively small integrin clusters became concentrated around the cell center, and not at the cell periphery where they originally formed, suggesting that some centripetal force acted on them. A **dense actin layer** was detected around the adhesion zone, but how it is involved in the centripetal movement of the clusters is still unclear at this stage. Additionally, we have found that **integrin adaptor proteins** like talin, kindlin-2, paxillin, and also those with a mechano-dependent recruitment like vinculin and zyxin, were **recruited in the clusters**, revealing that some pulling forces were exerted on integrins. However, the integrin clusters on fluid SLBs do not mature to an even close extent as on rigid glass. Therefore, it suggests that **integrin cluster maturation is impeded** not by the absence of physical forces that can possibly be generated by cells on SLBs (factor entirely related to the SLB mechanical properties), but by the **cells' inability to transmit the forces and to initiate the mechanotransduction and integrin cluster maturation.**

To test this hypothesis, we decided to **reinforce integrin-ligand connection** and to study cell adhesion on SLBs coated with a different cell ligand, Invasin. **Invasin** binds to integrin with much **higher affinity than RGD**, so we expected that **higher forces can be transmitted** between cells and SLBs on Invasin. Surprisingly, we have found that **cells adhere more slowly on Invasin than on RGD-coated SLBs** (cf. chapter 8 of the Results). It takes a longer time for integrins to cluster and to move towards the cell center on Invasin than on RGD. These, at first glance counter-intuitive results, can be explained by **differences in integrin activation** on these ligands. Integrins are activated more easily on RGD than on Invasin-coated SLBs. After **integrin priming**, we have seen **cluster maturation on Invasin, reaching levels comparable to FAs** (in terms of integrin densities). **Integrin densities** increase in a **step-like manner** during this maturation, suggesting the **fusion of the smaller nano-sized clusters of NAs** that are typically observed on RGD-coated SLBs (cf. chapter 10 of the Results) and further reorganization inside the cluster.

Moreover, **manganese-treated cells** are capable of **exerting physical forces** on Invasin-coated SLBs, **pulling membrane tethers** out of the bilayer (cf. chapter 11 of the Results). The fact that cells can transmit forces of the order of several tens of pN to the SLB through individual integrin clusters provides a direct **evidence of mechanotransduction** on fluid substrates. Such forces cannot build up on fluid RGD-SLB due to the weaker RGD-integrin bond. However, these forces are essentially directed perpendicularly to the SLB plane. On rigid substrates, forces are parallel to the surface on the cell periphery, but they also have a normal component on clusters closer to the cell center (Brockman et al. [2018]). The **difference in force directions** might explain the

morphological differences of adhesion structures on rigid and fluid substrates. However, while it is well-known that these forces are exerted by stress fibers on FAs, the actin structures involved in mechanotransduction on fluid surfaces and how they emerge have still to be discovered.

There are other open questions, for example, related to the formation of **podosome-like structures and Invasin holes on SLBs**. We have proposed mechanisms that could possibly explain these two ligand exclusion phenomena: exclusion under local force of actin pushing and exclusion of Invasin by cellular glyocalyx. Next, we have observed that cells exert pulling forces on SLBs (directed towards the cell) but to **quantify these forces** properly, we need to know the **surface tension of the bilayer**. Thus, to measure the forces exerted on SLBs by adhering cells, we need a way to assess or control the surface tension of the bilayer. Moreover, if cells exert **pushing forces** on the SLB (directed towards the bilayer), like in podosomes or invadopodia, we would not be able to neither measure nor even detect them with our current setup, because **cells cannot significantly deform the bilayer and of course, not the rigid substrate under it**. We describe in the last section an assay that we have designed to tackle these questions.

CONCLUSION

Chapter 15

Longer-term perspectives

We have shown that during cell adhesion on SLBs, cells are able to exert significant forces (several tens of pN) deforming the lipid bilayer. The force required to pull a membrane tether out of the SLB depends on the surface tension of the bilayer (Derényi et al. [2002]). Unfortunately, in our experimental setup, membrane tension is high due to the interaction with the solid surface and we cannot control it, thus, measure these forces generated during cell adhesion. Moreover, we can only detect pulling forces exerted by the cell but not any force directed towards the bilayer (direction that is common for the forces developed in cell protrusions like podosomes or invadopodia), since the bilayer deformation would be negligibly small.

In order to properly measure cell forces applied through integrin clusters, we propose to study cell adhesion to giant unilamellar vesicles, GUVs. For this purpose, we have designed and constructed a setup that consists of an aspirating micropipette coupled to the stage of the microscope and controlled by a micromanipulator. The micropipette holds the GUV coated with cell ligands (RGD, or Invasin) (Annex2) setting its tension in a controlled manner by aspirating it (cf. Figure 15.1A). The adhesion zone between the GUV and the dorsal part of a cell can be imaged, and integrins, ligands and membrane can be localized.

Our preliminary results show that integrins are clustered at the contact sites. Moreover, we observe ligand exclusions reminiscent of the podosome-like adhesion structures at cell-GUV contact (longer ligand than those on SLBs: a protein complex of Protein A + anti-MBP antibody + MBP-Invasin) (cf. Figure 15.1B). Moreover, we have evidence that cells can deform the GUV in both directions by either pulling on it but also by pushing on it, forming an invadopodia-like structure (cf. Figure 15.1C). These experiments should be reproduced more systematically and the tension of the GUV modulated in order to

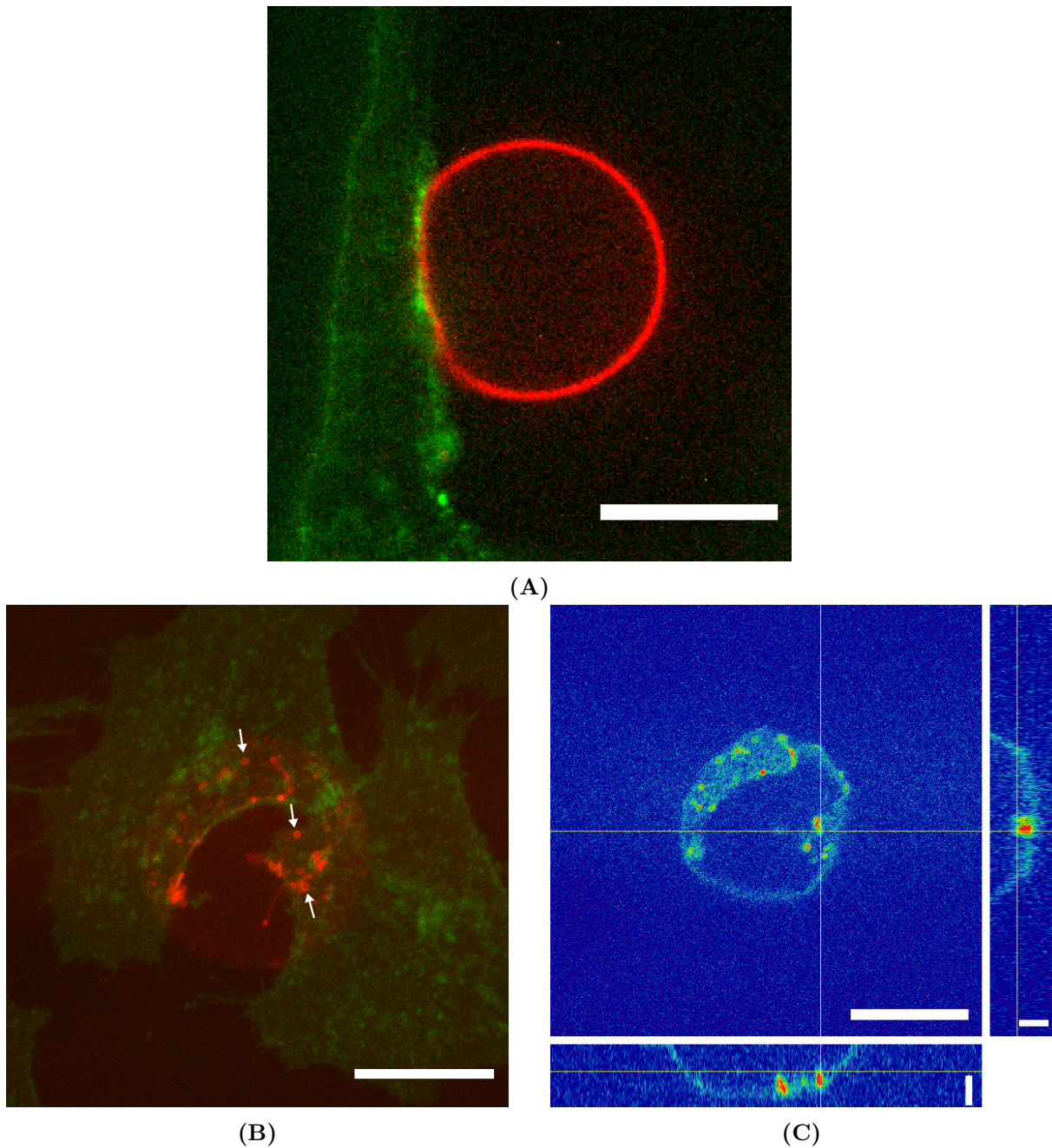


Figure 15.1: Adhesion between a cell and a GUV.

A) A GUV functionalized with Invasin (red) brought in contact to the manganese treated MEF cell with labelled β_1 -integrins (green) by a micropipette. The micropipette is out of focus holding the GUV on the right. The cell sits on an elevated micropattern. Scale bar, 10 μm .

B) A z-projection of a fluorescence image of a GUV functionalized with a protein complex (Protein A (labelled with Alexa Fluor 488) + anti-MBP antibody + MBP-Invasin) (red) brought on top of two HeLa cells (membrane dye FM-4-64, green). Protein complex containing Invasin clusters forming adhesion structures reminiscent of podosomes (shown with white arrows). Scale bar, 20 μm .

C) The orthogonal views of the z-stack of the same image as in B. Invasin-containing protein complexes shown with a pseudo color. Scale bars in the z-direction, 5 μm .

study its effect on integrin clustering and on the deformation of the GUV membrane. In the longer term, with this type of experiments, we could get more comprehensive insights about the development of the adhesion zone between 2 cells, mediated by integrins.

Appendices

Appendix A

Uncertainty estimation for protein densities and protein numbers

Here we have estimated the uncertainties δN of quantify the number of proteins in an adhesion cluster N and $\delta\rho$ of the density of proteins in it ρ . We do not measure these quantities directly in our experiments, we rather calculate them from different quantities that we observe directly in our study by the following formulas:

$$N = S \cdot \rho = S \frac{A_{fl}}{\tilde{n}} \cdot I; \quad (\text{A.1})$$

$$\rho = \frac{A_{fl}}{\tilde{n}} \cdot I, \quad (\text{A.2})$$

where S is a surface area of an adhesion cluster μm^2 , I is a fluorescence intensity AU, \tilde{n} is a factor due to inhomogeneous illumination and A_{fl} is the defined in the section 6.2 of the Materials and Methods proportionality factor of the calibration.

Therefore, the uncertainties δN and $\delta\rho$ originate from the δS , δI , $\delta\tilde{n}$ and δA_{fl} , which in its turn originates from δA_{st} , $\delta\alpha_{fl}$ and $\delta\beta_{st}$, as $A_{fl} = \frac{\beta_{st} \cdot A_{st}}{\alpha_{fl}}$:

$$\frac{\delta N}{N} = \sqrt{\left(\frac{\delta S}{S}\right)^2 + \left(\frac{\delta I}{I}\right)^2 + \left(\frac{\delta\tilde{n}}{\tilde{n}}\right)^2 + \left(\frac{\delta A_{fl}}{A_{fl}}\right)^2}, \quad (\text{A.3})$$

$$\frac{\delta\rho}{\rho} = \sqrt{\left(\frac{\delta I}{I}\right)^2 + \left(\frac{\delta\tilde{n}}{\tilde{n}}\right)^2 + \left(\frac{\delta A_{fl}}{A_{fl}}\right)^2}. \quad (\text{A.4})$$

$$\frac{\delta A_{fl}}{A_{fl}} = \sqrt{\left(\frac{\delta A_{st}}{A_{st}}\right)^2 + \left(\frac{\delta \alpha_{fl}}{\alpha_{fl}}\right)^2 + \left(\frac{\delta \beta_{st}}{\beta_{st}}\right)^2}. \quad (\text{A.5})$$

The fractional uncertainty $\frac{\delta A_{fl}}{A_{fl}}$ depends on the fluorescence calibration. δA_{st} , $\delta \alpha_{fl}$ and $\delta \beta_{st}$ are calculated based on the linear regression fits with 95% confidence intervals. Thus, for the 3 fluorophores we use in the study we obtain (cf. Table A.1):

Table A.1: Fractional uncertainties due to calibration.

Fluorophore	Alexa Fluor 488	JF549	mCherry
$\frac{\delta A_{fl}}{A_{fl}}$	42%	23.5%	26.5%

The fractional uncertainty related to the illumination correction $\frac{\delta n^*}{n^*}$ is at maximum 25%.

The fractional uncertainty $\frac{\delta S}{S}$ depends on the cluster area: it is bigger for the smaller clusters reaching 20% for the smallest we consider in our analysis, the ones at the limit of our optical resolution.

The fractional uncertainty $\frac{\delta I}{I}$ can be understood as the inverse signal to noise ratio (SNR^{-1}). As the number of photons counted by an electric device or camera follows a Poisson distribution, the $SNR = \frac{N_{ph}}{\sqrt{N_{ph}}}$, where N_{ph} is a number of detected photons. Thus, $\frac{\delta I}{I} = \frac{1}{\sqrt{I}}$ and becomes more important for the signals of lower intensity, reaching 40% for the very low signal intensities in the adhesion clusters.

Appendix B

GUV preparation

Giant unilamellar vesicles were generated by the electroformation technique (Angelova et al. [2007], Girard et al. [2004]). First, lipids solubilized in chloroform are mixed together in a glass vial at 1 mg/ml. Droplets of approximately 10 μ l of the lipid mix are carefully deposited on indium tin oxide (ITO) treated glass slides. The film was then dried in vacuum desiccator for 1 hour.

Second, the GUV formation chamber is built: the two ITO slides were sealed with paste Sigillum wax (Vitrex). The chamber is filled with the **GUV growth buffer** (300 mM sucrose) and sealed with paste Sigillum wax.

Third, for electroformation, an AC electric field provided by a pulse generator was applied for 4 h across the chamber (1 V at 10 Hz frequency) (cf. Figure B.1).

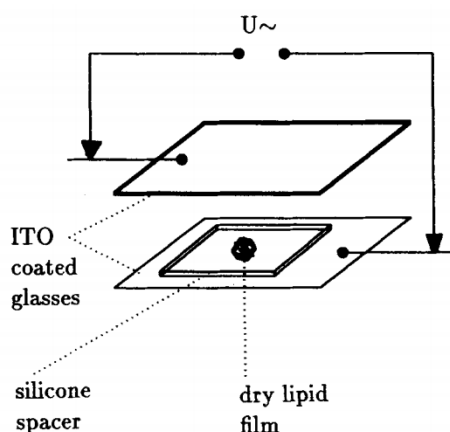


Figure B.1: Sketch of the chamber for the vesicle preparation.

Figure taken from Angelova et al. [2007].

Next, the electroformed GUVs are dissolved in the **cell buffer**: 25 mM HEPES pH 7.3; 120 mM NaCl; 7 mM KCl; 1.8 mM CaCl_2 ; 0.8 mM MgCl_2 ; 5 mM glucose (of approximately

the same osmolarity as the GUV growth buffer). For the GUV functionalization they are incubated with Invasin in the similar manner as for the SLB functionalization (cf. subsection 5.1.5 of the Materials and Methods).

Finally, fluorescently labelled GUVs are observed together with cells in the cell buffer under the microscope (cf. Figure B.2)

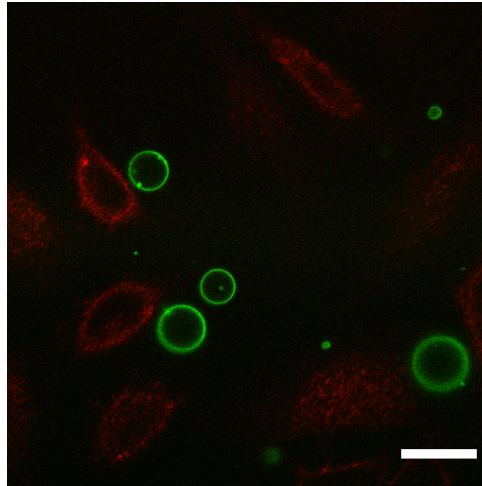


Figure B.2: GUVs added to cells in culture.

Fluorescence image of the GUVs functionalized with a protein complex (Protein A (labelled with Alexa Fluor 488) + anti-MBP antibody + MBP-Invasin) (green) and HeLa cells (membrane dye FM-4-64, red).

Scale bar, 50 μm .

Bibliography

- Akiyama, S. K. and Yamada, K. M. (1985). The interaction of plasma fibronectin with fibroblastic cells in suspension. *Journal of Biological Chemistry*, 260(7):4492–4500.
- Albersdörfer, A., Feder, T., and Sackmann, E. (1997). Adhesion-induced domain formation by interplay of long-range repulsion and short-range attraction force: A model membrane study. *Biophysical Journal*, 73(1):245–257.
- Alberts, B., Johnson, A., Lewis, J., Raff, M., Roberts, K., and Walter, P. (2008). *MOLECULAR BIOLOGY OF THE CELL*. 4 edition.
- Andersson, A.-S., Glasmästar, K., Sutherland, D., Lidberg, U., and Kasemo, B. (2003). Cell adhesion on supported lipid bilayers. *Journal of Biomedical Materials Research Part A*, 64A(4):622–629.
- Angelova, M. I., Soléau, S., Méléard, P., Faucon, F., and Bothorel, P. (2007). Preparation of giant vesicles by external AC electric fields. Kinetics and applications. *Trends in Colloid and Interface Science VI*, 131(899):127–131.
- Armond, J. W., MacPherson, J. V., and Turner, M. S. (2011). Pulling nanotubes from supported bilayers. *Langmuir*, 27(13):8269–8274.
- Bennett, M., Cantini, M., Reboud, J., Cooper, J. M., Roca-Cusachs, P., and Salmeron-Sanchez, M. (2018). Molecular clutch drives cell response to surface viscosity. *Proceedings of the National Academy of Sciences of the United States of America*, 115(6):1192–1197.
- Bergert, M., Lendenmann, T., Zündel, M., Ehret, A. E., Panozzo, D., Richner, P., Kim, D. K., Kress, S. J., Norris, D. J., Sorkine-Hornung, O., Mazza, E., Poulikakos, D., and Ferrari, A. (2016). Confocal reference free traction force microscopy. *Nature Communications*, 7.
- Biswas, K. H. and Groves, J. T. (2019). Hybrid Live Cell-Supported Membrane Interfaces for Signaling Studies. *Annual Review of Biophysics*, 48:537–562.

- Block, S. (2018). Brownian motion at lipid membranes: A comparison of hydrodynamic models describing and experiments quantifying diffusion within lipid bilayers. *Biomolecules*, 8(2).
- Boal, D. (2012). *Mechanics of the Cell*. 2 edition.
- Bouaouina, M., Harburger, D. S., and Calderwood, D. A. (2012). *Talin and Signaling Through Integrins*, volume 757 of *Methods in Molecular Biology*. Humana Press, Totowa, NJ.
- Boulbitch, A. A. (1999). Strain of a biomembrane caused by a local tangential force: Application to magnetic tweezer measurements. *Physical Review E - Statistical Physics, Plasmas, Fluids, and Related Interdisciplinary Topics*, 59(3):3402–3407.
- Bridgewater, R. E., Norman, J. C., and Caswell, P. T. (2012). Integrin trafficking at a glance. *Journal of Cell Science*, 125(16):3695–3701.
- Brockman, J. M., Blanchard, A. T., Pui-Yan, V., Derricotte, W. D., Zhang, Y., Fay, M. E., Lam, W. A., Evangelista, F. A., Mattheyses, A. L., and Salaita, K. (2018). Mapping the 3D orientation of piconewton integrin traction forces. *Nature Methods*, 15(2):115–118.
- Byron, A., Humphries, J. D., Bass, M. D., Knight, D., and Humphries, M. J. (2011). Proteomic analysis of integrin adhesion complexes. *Science Signaling*, 4(167).
- Calderwood, D. A. (2004). Integrin activation. *Journal of Cell Science*, 117(5):657–666.
- Carman, C. V. and Springer, T. A. (2003). Integrin avidity regulation: Are changes in affinity and conformation underemphasized? *Current Opinion in Cell Biology*, 15(5):547–556.
- Case, L. B. and Waterman, C. M. (2015). Integration of actin dynamics and cell adhesion by a three-dimensional, mechanosensitive molecular clutch. *Nature Cell Biology*, 17(8):955–963.
- Changede, R. and Sheetz, M. (2016). Integrin and cadherin clusters: A robust way to organize adhesions for cell mechanics. *BioEssays*.
- Changede, R., Xu, X., Margadant, F., and Sheetz, M. P. (2015). Nascent Integrin Adhesions Form on All Matrix Rigidities after Integrin Activation. *Developmental Cell*, 35(5):614–621.

- Choquet, D., Felsenfeld, D. P., and Sheetz, M. P. (1997). Extracellular Matrix Rigidity Causes Strengthening of Integrin–Cytoskeleton Linkages. *Cell*, 88(1):39–48.
- Cluzel, C., Saltel, F., Lussi, J., Paulhe, F., Imhof, B. A., and Wehrle-Haller, B. (2005). The mechanisms and dynamics of $\alpha v \beta 3$ integrin clustering in living cells. *Journal of Cell Biology*, 171(2):383–392.
- Coller, B. S. (1986). Activation affects access to the platelet receptor for adhesive glycoproteins. *Journal of Cell Biology*, 103(2):451–456.
- Cossart, P. and Sansonetti, P. J. (2004). Bacterial Invasion: The Paradigms of Enteroinvasive Pathogens. *Science*, 304(5668):242–248.
- Dahim, M., Mizuno, N. K., Li, X. M., Momsen, W. E., Momsen, M. M., and Brockman, H. L. (2002). Physical and photophysical characterization of a BODIPY phosphatidylcholine as a membrane probe. *Biophysical Journal*, 83(3):1511–1524.
- de Franceschi, N., Hamidi, H., Alanko, J., Sahgal, P., and Ivaska, J. (2015). Integrin traffic—the update. *Journal of Cell Science*, 128(5):839–852.
- del Rio, A., Perez-Jimenez, R., Liu, R., Roca-Cusachs, P., Fernandez, J. M., and Sheetz, M. P. (2009). Stretching Single Talin Rod Molecules Activates Vinculin Binding. *Science*, 323(5914):638–641.
- Delva, E., Tucker, D. K., and Kowalczyk, A. P. (2009). The desmosome. *Cold Spring Harbor perspectives in biology*, 1(2):1–18.
- Derényi, I., Jülicher, F., and Prost, J. (2002). Formation and Interaction of Membrane Tubes. *Physical Review Letters*, 88(23):238101.
- Discher, D. E., Janmey, P., and Wang, Y. L. (2005). Tissue cells feel and respond to the stiffness of their substrate. *Science*, 310(5751):1139–1143.
- Dupont, S., Morsut, L., Aragona, M., Enzo, E., Giulitti, S., Cordenonsi, M., Zanconato, F., Le Digabel, J., Forcato, M., Bicciato, S., Elvassore, N., and Piccolo, S. (2011). Role of YAP/TAZ in mechanotransduction. *Nature*, 474(7350):179–184.
- Dustin, M. L. (2014). The immunological synapse. *Cancer immunology research*, 2(11):1023–1033.
- Dustin, M. L. and Groves, J. T. (2012). Receptor Signaling Clusters in the Immune Synapse. *Annual Review of Biophysics*, 41(1):543–556.

- Elosegui-Artola, A., Trepata, X., and Roca-Cusachs, P. (2018). Control of Mechanotransduction by Molecular Clutch Dynamics. *Trends in Cell Biology*, 28(5):356–367.
- Engler, A., Bacakova, L., Newman, C., Hategan, A., Griffin, M., and Discher, D. (2004). Substrate Compliance versus Ligand Density in Cell on Gel Responses. *Biophysical Journal*, 86(1 I):617–628.
- Engler, A. J., Sen, S., Sweeney, H. L., and Discher, D. E. (2006). Matrix Elasticity Directs Stem Cell Lineage Specification. *Cell*, 126(4):677–689.
- Finkielstein, C. V. and Capelluto, D. G. S. (2016). Disabled-2: A modular scaffold protein with multifaceted functions in signaling. *Inside the Cell*, 1(1):48–58.
- Frantz, C., Stewart, K. M., and Weaver, V. M. (2010). The extracellular matrix at a glance. *Journal of Cell Science*, 123(24):4195–4200.
- Galbraith, C. G. and Sheetz, M. P. (1998). Forces on adhesive contacts affect cell function. *Current Opinion in Cell Biology*, 10(5):566–571.
- Galush, W. J., Nye, J. A., and Groves, J. T. (2008). Quantitative Fluorescence Microscopy Using Supported Lipid Bilayer Standards. *Biophysical Journal*, 95(5):2512–2519.
- Ganz, A., Lambert, M., Saez, A., Silberzan, P., Buguin, A., Mège, R. M., and Ladoux, B. (2006). Traction forces exerted through N-cadherin contacts. *Biology of the Cell*, 98(12):721–730.
- García, A. J., Schwarzbauer, J. E., and Boettiger, D. (2002). Distinct activation states of $\alpha 5 \beta 1$ integrin show differential binding to RGD and synergy domains of fibronectin. *Biochemistry*, 41(29):9063–9069.
- Garrod, D. and Chidgey, M. (2008). Desmosome structure, composition and function. *Biochimica et Biophysica Acta (BBA) - Biomembranes*, 1778(3):572–587.
- Gautreau, A., Louvard, D., and Arpin, M. (2000). Morphogenic effects of ezrin require a phosphorylation-induced transition from oligomers to monomers at the plasma membrane. *Journal of Cell Biology*, 150(1):193–203.
- Geiger, B., Spatz, J. P., and Bershadsky, A. D. (2009). Environmental sensing through focal adhesions. *Nature Reviews Molecular Cell Biology*, 10(1):21–33.
- Geiger, T. and Zaidel-Bar, R. (2012). Opening the floodgates: proteomics and the integrin adhesome. *Current Opinion in Cell Biology*, 24(5):562–568.

- Ghassemi, S., Meacci, G., Liu, S., Gondarenko, A. A., Mathur, A., Roca-Cusachs, P., Sheetz, M. P., and Hone, J. (2012). Cells test substrate rigidity by local contractions on submicrometer pillars. *Proceedings of the National Academy of Sciences*, 109(14):5328–5333.
- Giannone, G., Dubin-Thaler, B. J., Döbereiner, H. G., Kieffer, N., Bresnick, A. R., and Sheetz, M. P. (2004). Periodic lamellipodial contractions correlate with rearward actin waves. *Cell*, 116(3):431–443.
- Giannone, G., Dubin-Thaler, B. J., Rossier, O., Cai, Y., Chaga, O., Jiang, G., Beaver, W., Döbereiner, H.-G., Freund, Y., Borisy, G., and Sheetz, M. P. (2007). Lamellipodial Actin Mechanically Links Myosin Activity with Adhesion-Site Formation. *Cell*, 128(3):561–575.
- Girard, P., Pécréaux, J., Lenoir, G., Falson, P., Rigaud, J. L., and Bassereau, P. (2004). A new method for the reconstitution of membrane proteins into giant unilamellar vesicles. *Biophysical Journal*, 87(1):419–429.
- Glazier, R. and Salaita, K. (2017). Supported lipid bilayer platforms to probe cell mechanobiology. *Biochimica et Biophysica Acta (BBA) - Biomembranes*, 1859(9):1465–1482.
- Grashoff, C., Hoffman, B. D., Brenner, M. D., Zhou, R., Parsons, M., Yang, M. T., McLean, M. A., Sligar, S. G., Chen, C. S., Ha, T., and Schwartz, M. A. (2010). Measuring mechanical tension across vinculin reveals regulation of focal adhesion dynamics. *Nature*, 466(7303):263–266.
- Gumbiner, B. M. (1996). Cell adhesion: The molecular basis of tissue architecture and morphogenesis. *Cell*, 84(3):345–357.
- Guo, L., Har, J. Y., Sankaran, J., Hong, Y., Kannan, B., and Wohland, T. (2008). Molecular diffusion measurement in lipid bilayers over wide concentration ranges: A comparative study. *ChemPhysChem*, 9(5):721–728.
- Hall, A. (2005). Rho GTPases and the control of cell behaviour. *Proceedings of International Conference on Harmonics and Quality of Power, ICHQP*.
- Hamai, C., Yang, T., Kataoka, S., Cremer, P. S., and Musser, S. M. (2006). Effect of average phospholipid curvature on supported bilayer formation on glass by vesicle fusion. *Biophysical Journal*, 90(4):1241–1248.

BIBLIOGRAPHY

- Hamburger, Z. A., Brown, M. S., Isberg, R. R., and Bjorkman, P. J. (1999). Crystal structure of invasin: A bacterial integrin-binding protein. *Science*, 286(5438):291–295.
- Han, S. J., Azarova, E. V., Whitewood, A. J., Bachir, A., Groisman, A., Horwitz, A. R., Goult, B. T., Dean, K. M., and Danuser, G. (2021). Talin-vinculin precomplex drives adhesion maturation by accelerated force transmission and vinculin recruitment. *bioRxiv*, pages 1–29.
- han Yu, C., Rafiq, N. B. M., Krishnasamy, A., Hartman, K. L., Jones, G. E., Bershadsky, A. D., and Sheetz, M. P. (2013). Integrin-matrix clusters form podosome-like adhesions in the absence of traction forces. *Cell Reports*, 5(5):1456–1468.
- Hartman, N. C., Nye, J. A., and Groves, J. T. (2009). Cluster size regulates protein sorting in the immunological synapse. *Proceedings of the National Academy of Sciences of the United States of America*, 106(31):12729–12734.
- Hauck, C. R., Borisova, M., and Muenzner, P. (2012). Exploitation of integrin function by pathogenic microbes. *Current Opinion in Cell Biology*, 24(5):637–644.
- Hogg, N., Henderson, R., Leitinger, B., McDowall, A., Porter, J., and Stanley, P. (2002). Mechanisms contributing to the activity of integrins on leukocytes. *Immunological Reviews*, 186(4):164–171.
- Holt, M. R., Calle, Y., Sutton, D. H., Critchley, D. R., Jones, G. E., and Dunn, G. A. (2008). Quantifying cell – matrix adhesion dynamics in living cells using. *Journal of Microscopy*, 232(March):73–81.
- Horton, E. R., Humphries, J. D., James, J., Jones, M. C., Askari, J. A., and Humphries, M. J. (2016). The integrin adhesome network at a glance. *Journal of Cell Science*, 129(22):4159–4163.
- Hu, S., Tee, Y.-H., Kabla, A., Zaidel-Bar, R., Bershadsky, A., and Hersen, P. (2015). Structured illumination microscopy reveals focal adhesions are composed of linear subunits. *Cytoskeleton*, 72(5):235–245.
- Huet-Calderwood, C., Rivera-Molina, F., Iwamoto, D. V., Kromann, E. B., Toomre, D., and Calderwood, D. A. (2017). Novel ecto-tagged integrins reveal their trafficking in live cells. *Nature Communications*, 8(1).
- Humphries, J. D., Byron, A., and Humphries, M. J. (2006). Integrin ligands at a glance. *Journal of Cell Science*, 119(19):3901–3903.

BIBLIOGRAPHY

- Huttenlocher, A., Ginsberg, M. H., and Horwitz, A. F. (1996). Modulation of cell migration by integrin-mediated cytoskeletal linkages and ligand-binding affinity. *Journal of Cell Biology*, 134(6):1551–1562.
- Huttenlocher, A. and Horwitz, A. R. (2011). Integrins in Cell Migration. *Cold Spring Harbor Perspectives in Biology*, 3(9):a005074–a005074.
- Hynes, R. O. (1987). Integrins: a family of cell adhesion receptors. *Cell*, 48:549–554.
- Hynes, R. O. (2002). Integrins: Bidirectional, Allosteric Signaling Machines. *Cell*, 110:673–687.
- Isberg, R. R. (1991). Discrimination between intracellular uptake and surface adhesion of bacterial pathogens. *Science*, 252(5008):934–938.
- Isberg, R. R. and Barnes, P. (2001). Subversion of integrins by enteropathogenic *Yersinia*. *Journal of cell science*, 114(Pt 1):21–28.
- Isberg, R. R., Voorhis, D. L., and Falkow, S. (1987). Identification of invasins: A protein that allows enteric bacteria to penetrate cultured mammalian cells. *Cell*, 50(5):769–778.
- Isenberg, W. M., McEver, R. P., Phillips, D. R., Shuman, M. A., and Bainton*, D. E. (1987). The Platelet Fibrinogen Receptor : An Immunogold-Surface Replica. 104(June):1655–1663.
- Iskratsch, T., Wolfenson, H., and Sheetz, M. P. (2014). Appreciating force and shape — the rise of mechanotransduction in cell biology. *Nature Reviews Molecular Cell Biology*, 15(12):825–833.
- Izard, T. and Vonrhein, C. (2004). Structural basis for amplifying vinculin activation by talin. *Journal of Biological Chemistry*, 279(26):27667–27678.
- James, J. R. and Vale, R. D. (2012). Biophysical mechanism of T-cell receptor triggering in a reconstituted system. *Nature*, 487(7405):64–69.
- Jiang, G., Huang, A. H., Cai, Y., Tanase, M., and Sheetz, M. P. (2006). Rigidity sensing at the leading edge through $\alpha v \beta 3$ integrins and RPTP α . *Biophysical Journal*, 90(5):1804–1809.
- Johnson, J. M., Ha, T., Chu, S., and Boxer, S. G. (2002). Early steps of supported bilayer formation probed by single vesicle fluorescence assays. *Biophysical Journal*, 83(6):3371–3379.

- Juerg H. Beer, Springer, K. T., and Coller, B. S. (1992). Immobilized Arg-Gly-Asp (RGD) Peptides of Varying Lengths as Structural Probes of the Platelet Glycoprotein IIb/IIIa Receptor. pages 117–128.
- Kanchanawong, P., Shtengel, G., Pasapera, A. M., Ramko, E. B., Davidson, M. W., Hess, H. F., and Waterman, C. M. (2010). Nanoscale architecture of integrin-based cell adhesions. *Nature*, 468(7323):580–584.
- Kapur, J. N., Sahoo, P. K., and Wong, A. K. (1985). A new method for gray-level picture thresholding using the entropy of the histogram. *Computer Vision, Graphics, & Image Processing*, 29(3):273–285.
- Khalil, A. S., Xie, A. W., and Murphy, W. L. (2014). Context Clues: The Importance of Stem Cell–Material Interactions. *ACS Chemical Biology*, 9(1):45–56.
- Klapholz, B. and Brown, N. H. (2017). Talin – the master of integrin adhesions. *Journal of Cell Science*, 130(15):2435–2446.
- Koch, A. L. (1966). The logarithm in biology 1. Mechanisms generating the log-normal distribution exactly. *Journal of Theoretical Biology*, 12(2):276–290.
- Kong, F., García, A. J., Mould, A. P., Humphries, M. J., and Zhu, C. (2009). Demonstration of catch bonds between an integrin and its ligand. *Journal of Cell Biology*, 185(7):1275–1284.
- Koster, G., Cacciuto, A., Derényi, I., Frenkel, D., and Dogterom, M. (2005). Force barriers for membrane tube formation. *Physical Review Letters*, 94(6):16–19.
- Kuo, J. C., Han, X., Hsiao, C. T., Yates, J. R., and Waterman, C. M. (2011). Analysis of the myosin-II-responsive focal adhesion proteome reveals a role for β -Pix in negative regulation of focal adhesion maturation. *Nature Cell Biology*, 13(4):383–395.
- Lai-Cheong, J. E., Arita, K., and McGrath, J. A. (2007). Genetic Diseases of Junctions. *Journal of Investigative Dermatology*, 127(12):2713–2725.
- Lampe, P. D. and Lau, A. F. (2000). Regulation of Gap Junctions by Phosphorylation of Connexins. *Archives of Biochemistry and Biophysics*, 384(2):205–215.
- Laudanna, C., Kim, J. Y., Constantin, G., and Butcher, E. C. (2002). Rapid leukocyte integrin activation by chemokines. *Immunological Reviews*, 186:37–46.
- Lauffenburger, D. A. and Horwitz, A. F. (1996). Cell Migration: A Physically Integrated Molecular Process. *Cell*, 84(3):359–369.

- Leckband, D. E., Helm, C. A., and Israelachvili, J. (1993). Role of Calcium in the Adhesion and Fusion of Bilayers. *Biochemistry*, 32(4):1127–1140.
- Leong, J., Fournier, R., and Isberg, R. (1990). Identification of the integrin binding domain of the *Yersinia pseudotuberculosis* invasin protein. *The EMBO Journal*, 9(6):1979–1989.
- Li, H., Deng, Y., Sun, K., Yang, H., Liu, J., Wang, M., Zhang, Z., Lin, J., Wu, C., Wei, Z., and Yu, C. (2017). Structural basis of kindlin-mediated integrin recognition and activation. *Proceedings of the National Academy of Sciences of the United States of America*, 114(35):9349–9354.
- Li, R., Mitra, N., Gratkowski, H., Vilaire, G., Litvinov, R., Nagasami, C., Weisel, J. W., Lear, J. D., DeGrado, W. F., and Bennett, J. S. (2003). Activation of integrin α IIb β 3 by modulation of transmembrane helix associations. *Science*, 300(5620):795–798.
- Lin, W.-C., Yu, C.-H., Triffo, S., and Groves, J. T. (2010). *Supported Membrane Formation, Characterization, Functionalization, and Patterning for Application in Biological Science and Technology*, volume 2.
- Lo, C. M., Wang, H. B., Dembo, M., and Wang, Y. L. (2000). Cell movement is guided by the rigidity of the substrate. *Biophysical Journal*, 79(1):144–152.
- Marchi-Artzner, V., Lorz, B., Hellerer, U., Kantlehner, M., Kessler, H., and Sackmann, E. (2001). Selective Adhesion of Endothelial Cells to Artificial Membranes with a Synthetic RGD-Lipopeptide. *Chemistry*, 7(5):1095–1101.
- Mascalchi, P., Haanappel, E., Carayon, K., Mazères, S., and Salomé, L. (2012). Probing the influence of the particle in Single Particle Tracking measurements of lipid diffusion. *Soft Matter*, 8(16):4462–4470.
- Matsuyoshi, N., Hamaguchi, M., Taniguchi, S., Nagafuchi, A., Tsukita, S., and Takeichi, M. (1992). Cadherin-mediated cell-cell adhesion is perturbed by v-src tyrosine phosphorylation in metastatic fibroblasts. *Journal of Cell Biology*, 118(3):703–714.
- McConnell, H. M., Watts, T. H., Weis, R. M., and Brian, A. A. (1986). Supported planar membranes in studies of cell-cell recognition in the immune system. *BBA - Reviews on Biomembranes*, 864(1):95–106.
- Mehrbod, M., Trisno, S., and Mofrad, M. R. (2013). On the activation of integrin α IIb β 3: Outside-in and inside-out pathways. *Biophysical Journal*, 105(6):1304–1315.

- Mengaud, J., Ohayon, H., Gounon, P., Mège, R.-M., and Cossart, P. (1996). E-Cadherin Is the Receptor for Internalin, a Surface Protein Required for Entry of *L. monocytogenes* into Epithelial Cells. *Cell*, 84(6):923–932.
- Miihkinen, M., Grönloh, M. L., Vihinen, H., Jokitalo, E., Goult, B. T., Ivaska, J., and Jacquemet, G. (2020). Myosin-X is required for integrin activation at filopodia tips. *bioRxiv*, page 2020.05.05.078733.
- Mitchison, T. and Kirschner, M. (1988). Cytoskeletal dynamics and nerve growth. *Neuron*, 1(9):761–772.
- Möckl, L. (2020). The Emerging Role of the Mammalian Glycocalyx in Functional Membrane Organization and Immune System Regulation. *Frontiers in Cell and Developmental Biology*, 8(April):1–14.
- Montanez, E., Ussar, S., Schifferer, M., Bösl, M., Zent, R., Moser, M., and Fässler, R. (2008). Kindlin-2 controls bidirectional signaling of integrins. *Genes and Development*, 22(10):1325–1330.
- Moore, S. W. and Sheetz, M. P. (2011). Biophysics of substrate interaction: Influence on neural motility, differentiation, and repair. *Developmental Neurobiology*, 71(11):1090–1101.
- Morimatsu, M., Mekhdjian, A. H., Adhikari, A. S., and Dunn, A. R. (2013). Molecular tension sensors report forces generated by single integrin molecules in living cells. *Nano Letters*, 13(9):3985–3989.
- Mould, A. P., Burrows, L., and Humphries, M. J. (1998). Identification of amino acid residues that form part of the ligand-binding pocket of integrin $\alpha 5\beta 1$. *Journal of Biological Chemistry*, 273(40):25664–25672.
- Murrell, M., Oakes, P. W., Lenz, M., and Gardel, M. L. (2015). Forcing cells into shape: The mechanics of actomyosin contractility. *Nature Reviews Molecular Cell Biology*, 16(8):486–498.
- Naglea, J. F. and Tristram-Nagleb, S. (2015). Structure of lipid bilayers. *Surface and Coatings Technology*, 262(3):173–183.
- Nathalie Q. Balaban, Ulrich S. Schwarz, Daniel Riveline, Goichberg, P., Gila Tzur, Sabanay, I., Mahalu, D., Safran, S., Bershadsky, A., Addadi, L., and Geiger, B. (2001). Force and focal adhesion assembly: a close relationship studied using elastic micropatterned substrates. *Nature Cell Biology*, 3(4):466–472.

- Nye, J. A. and Groves, J. T. (2008). Kinetic Control of Histidine-Tagged Protein Surface Density on Supported Lipid Bilayers. *Langmuir*, 24(8):4145–4149.
- Palecek, S. P., Loftust, J. C., Ginsberg, M. H., Lauffenburger, D. A., and Horwitz, A. F. (1997). Integrin-ligand binding properties govern cell migration speed through cell-substratum adhesiveness.
- Panetti, T. S. (2002). Tyrosine phosphorylation of paxillin, FAK, and p130CAS: effects on cell spreading and migration. *Frontiers in bioscience : a journal and virtual library*, 7(11):143–150.
- Perez, T. D., Tamada, M., Sheetz, M. P., and Nelson, W. J. (2008). Immediate-Early Signaling Induced by E-cadherin Engagement and Adhesion. *Journal of Biological Chemistry*, 283(8):5014–5022.
- Pernier, J., Kusters, R., Bousquet, H., Lagny, T., Morchain, A., Joanny, J. F., Bassereau, P., and Coudrier, E. (2019). Myosin 1b is an actin depolymerase. *Nature Communications*, 10(1):1–7.
- Pfaff, M., Tangemann, K., Müller, B., Gurrath, M., Müller, G., Kessler, H., Timpl, R., and Engel, J. (1994). Selective recognition of cyclic RGD peptides of NMR defined conformation by alpha IIb beta 3, alpha V beta 3, and alpha 5 beta 1 integrins. *The Journal of biological chemistry*, 269(32):20233–8.
- Picas, L., Rico, F., and Scheuring, S. (2012). Direct measurement of the mechanical properties of lipid phases in supported bilayers. *Biophysical Journal*, 102(1):L01–L03.
- Pincet, F., Adrien, V., Yang, R., Delacotte, J., Rothman, J. E., Urbach, W., and Tareste, D. (2016). FRAP to characterize molecular diffusion and interaction in various membrane environments. *PLoS ONE*, 11(7):1–19.
- Pollard, T. D., Earnshaw, W. C., Lippincott-Schwartz, J., and Johnson, G. T. (2017). *Cell biology*.
- Prager-Khoutorsky, M., Lichtenstein, A., Krishnan, R., Rajendran, K., Mayo, A., Kam, Z., Geiger, B., and Bershadsky, A. D. (2011). Fibroblast polarization is a matrix-rigidity-dependent process controlled by focal adhesion mechanosensing. *Nature Cell Biology*, 13(12):1457–1465.
- Richter, R., Mukhopadhyay, A., and Brisson, A. (2003). Pathways of Lipid Vesicle Deposition on Solid Surfaces: A Combined QCM-D and AFM Study. *Biophysical Journal*, 85(5):3035–3047.

- Riveline, D., Zamir, E., Balaban, N. Q., Schwarz, U. S., Ishizaki, T., Narumiya, S., Kam, Z., Geiger, B., and Bershadsky, A. D. (2001). Focal contacts as mechanosensors: Externally applied local mechanical force induces growth of focal contacts by an mDia1-dependent and ROCK-independent mechanism. *Journal of Cell Biology*, 153(6):1175–1185.
- Roca-Cusachs, P., Conte, V., and Trepats, X. (2017). Quantifying forces in cell biology. *Nature Cell Biology*, 19(7):742–751.
- Romero, S., Grompone, G., Carayol, N., Mounier, J., Guadagnini, S., Prevost, M. C., Sansonetti, P. J., and Tran Van Nhieu, G. (2011). ATP-mediated Erk1/2 activation stimulates bacterial capture by filopodia, which precedes *Shigella* invasion of epithelial cells. *Cell Host and Microbe*, 9(6):508–519.
- Romero, S., Quatela, A., Bornschlöggl, T., Guadagnini, S., Bassereau, P., and Van Nhieu, G. T. (2012). Erratum to Filopodium retraction is controlled by adhesion to its tip [J. Cell Sci. 125, PART 21, (2012) 4999-5004]. *Journal of Cell Science*, 125(22):5587.
- Rothlein, R., Dustin, M. L., Marlin, S. D., and Springer, T. A. (1986). A human intercellular adhesion molecule (ICAM-1) distinct from LFA-1. *Journal of immunology (Baltimore, Md. : 1950)*, 137(4):1270–4.
- Rozario, T. and DeSimone, D. W. (2010). The extracellular matrix in development and morphogenesis: A dynamic view. *Developmental Biology*, 341(1):126–140.
- Sackmann, E. (1996). Supported membranes: Scientific and practical applications. *Science*, 271(5245):43–48.
- Saez, A., Buguin, A., Silberzan, P., and Ladoux, B. (2005). Is the mechanical activity of epithelial cells controlled by deformations or forces? *Biophysical Journal*, 89(6):52–54.
- Sahoo, P., Wilkins, C., and Yeager, J. (1997). Threshold selection using Renyi’s entropy. *Pattern Recognition*, 30(1):71–84.
- Sansonetti, P. (2002). Host-pathogen interactions: the seduction of molecular cross talk. *Gut*, 50(Supplement 3):iii2–iii8.
- Schiller, H. B., Friedel, C. C., Boulegue, C., and Fäsingssler, R. (2011). Quantitative proteomics of the integrin adhesome show a myosin II-dependent recruitment of LIM domain proteins. *EMBO Reports*, 12(3):259–266.

BIBLIOGRAPHY

- Schiller, H. B., Hermann, M. R., Polleux, J., Vignaud, T., Zanivan, S., Friedel, C. C., Sun, Z., Raducanu, A., Gottschalk, K. E., Théry, M., Mann, M., and Fässler, R. (2013). β 1 - And α v -class integrins cooperate to regulate myosin II during rigidity sensing of fibronectin-based microenvironments. *Nature Cell Biology*, 15(6):625–636.
- Schmid, E. M., Bakalar, M. H., Choudhuri, K., Weichsel, J., Ann, H. S., Geissler, P. L., Dustin, M. L., and Fletcher, D. A. (2016). membrane interfaces. *Nature Physics*, (March).
- Schmidt, S., Weigelin, B., te Riet, J., te Boekhorst, V., te Lindert, M., Wijers-Rouw, M., Lelli, B., Rognoni, L., Krause-Vortmeyer, M., Messent, A., Bracci, L., Gottschalk, K. E., Kissler, S., Humphries, M. J., Lefebvre, D. J., Fransen, J., and Friedl, P. (2020). Glycocalyx-mediated cell adhesion and migration. *bioRxiv*.
- Shattil, S. J., Kashiwagi, H., and Pampori, N. (1998). Integrin signaling: The platelet paradigm. *Blood*, 91(8):2645–2657.
- Sheehy, S. P. and Parker, K. K. (2011). Tissue Engineering in Regenerative Medicine. pages 77–97. Humana Press, Totowa, NJ.
- Soumpasis, D. M. (1983). Theoretical analysis of fluorescence photobleaching recovery experiments. *Biophysical Journal*, 41(1):95–97.
- Staykova, M., Holmes, D. P., Read, C., and Stone, H. A. (2011). Mechanics of surface area regulation in cells examined with confined lipid membranes. *Proceedings of the National Academy of Sciences of the United States of America*, 108(22):9084–9088.
- Sun, Z., Guo, S. S., and Fässler, R. (2016). Integrin-mediated mechanotransduction. *JCB Review*.
- Swaminathan, V., Kalappurakkal, J. M., Mehta, S. B., Nordenfelt, P., Moore, T. I., Koga, N., Baker, D. A., Oldenbourg, R., Tani, T., Mayor, S., Springer, T. A., and Waterman, C. M. (2017). Actin retrograde flow actively aligns and orients ligand-engaged integrins in focal adhesions. *Proceedings of the National Academy of Sciences of the United States of America*, 114(40):10648–10653.
- Takagi, J., Petre, B. M., Walz, T., and Springer, T. A. (2002). Global conformational arrangements in integrin extracellular domains in outside-in and inside-out signaling. *Cell*, 110(5):599–611.
- Tang, V. W. (2018). Cell–cell adhesion interface: orthogonal and parallel forces from contraction, protrusion, and retraction. *F1000Research*, 7(0):1544.

- Tran Van Nhieu, G. and Isberg, R. (1993). Bacterial internalization mediated by beta 1 chain integrins is determined by ligand affinity and receptor density. *The EMBO Journal*, 12(5):1887–1895.
- Turner, C. E. (2000). Paxillin and focal adhesion signalling. *Nature Cell Biology*, 2(12):231–236.
- Van Nhieu, G. T. and Isberg, R. R. (1991). The *Yersinia pseudotuberculosis* invasin protein and human fibronectin bind to mutually exclusive sites on the $\alpha 5\beta 1$ integrin receptor. *Journal of Biological Chemistry*, 266(36):24367–24375.
- Vicente-Manzanares, M., Ma, X., Adelstein, R. S., and Horwitz, A. R. (2009). Non-muscle myosin II takes centre stage in cell adhesion and migration. *Nature Reviews Molecular Cell Biology*, 10(11):778–790.
- Vogel, V. and Sheetz, M. (2006). Local force and geometry sensing regulate cell functions. *Nature Reviews Molecular Cell Biology*, 7(4):265–275.
- Watts, T. H. and McConnell, H. M. (1987). Biophysical aspects of antigen recognition by T cells. *Annual review of immunology*, 5:461–475.
- Wehrle-Haller, B. and Imhof, B. A. (2003). Integrin-dependent pathologies. *The Journal of Pathology*, 200(4):481–487.
- Wen, J. H., Vincent, L. G., Fuhrmann, A., Choi, Y. S., Hribar, K. C., Taylor-Weiner, H., Chen, S., and Engler, A. J. (2014). Interplay of matrix stiffness and protein tethering in stem cell differentiation. *Nature Materials*, 13(10):979–987.
- Winograd-Katz, S. E., Fässler, R., Geiger, B., and Legate, K. R. (2014). The integrin adhesome: from genes and proteins to human disease. *Nature Reviews Molecular Cell Biology*, 15(4):273–288.
- Wiseman, P. W., Brown, C. M., Webb, D. J., Hebert, B., Johnson, N. L., Squier, J. A., Ellisman, M. H., and Horwitz, A. F. (2004). Spatial mapping of integrin interactions and dynamics during cell migration by image correlation microscopy. *Journal of Cell Science*, 117(23):5521–5534.
- Wolfenson, H., Bershadsky, A., Henis, Y. I., and Geiger, B. (2011). Actomyosin-generated tension controls the molecular kinetics of focal adhesions. *Journal of Cell Science*, 124(9):1425–1432.

- Wolfenson, H., Iskratsch, T., and Sheetz, M. P. (2014). Early events in cell spreading as a model for quantitative analysis of biomechanical events. *Biophysical Journal*, 107(11):2508–2514.
- Wu, C., Keivenst, V. M., O’Toole, T. E., McDonald, J. A., and Ginsberg, M. H. (1995). Integrin activation and cytoskeletal interaction are essential for the assembly of a fibronectin matrix. *Cell*, 83(5):715–724.
- Xu, X. P., Kim, E., Swift, M., Smith, J. W., Volkmann, N., and Hanein, D. (2016). Three-Dimensional Structures of Full-Length, Membrane-Embedded Human α IIb β 3 Integrin Complexes. *Biophysical Journal*, 110(4):798–809.
- Yamada, K. M. and Sixt, M. (2019). Mechanisms of 3D cell migration. *Nature Reviews Molecular Cell Biology*, 20(12):738–752.
- Yang, B., Lieu, Z. Z., Wolfenson, H., Hameed, F. M., Bershadsky, A. D., and Sheetz, M. P. (2016). Mechanosensing Controlled Directly by Tyrosine Kinases. *Nano Letters*, 16(9):5951–5961.
- Young, L., Sung, J., and Masters, J. R. (2010). Detection of mycoplasma in cell cultures. *Nature Protocols*, 5(5):929–934.
- Yu, C. H., Law, J. B. K., Suryana, M., Low, H. Y., and Sheetz, M. P. (2011). Early integrin binding to Arg-Gly-Asp peptide activates actin polymerization and contractile movement that stimulates outward translocation. *Proceedings of the National Academy of Sciences of the United States of America*, 108(51):20585–20590.
- Zaidel-Bar, R. and Geiger, B. (2010). The switchable integrin adhesome. *Journal of Cell Science*, 123(9):1385–1388.
- Zaidel-Bar, R., Itzkovitz, S., Ma’ayan, A., Iyengar, R., and Geiger, B. (2007). Functional atlas of the integrin adhesome. *Nature Cell Biology*, 9(8):858–867.
- Zamir, E., Geiger, B., and Kam, Z. (2008). Quantitative multicolor compositional imaging resolves molecular domains in cell-matrix adhesions. *PLoS ONE*, 3(4):9–11.
- Zhao, J., Santino, F., Giacomini, D., and Gentilucci, L. (2020). Integrin-targeting peptides for the design of functional cell-responsive biomaterials. *Biomedicines*, 8(9).

